Applications of Reconstructed Nanofluidic Membrane of Layered Materials in Ionic Thermoelectricity and Moisture-Electricity-Generation

A dissertation submitted to the
Indian Institute of Technology Guwahati as
partial fulfilment of the Degree of

DOCTOR of PHILOSOPHY

Submitted by

Raktim Gogoi

Roll No: 196122024

Department of Chemistry
Indian Institute of Technology Guwahati
Guwahati-781039 Assam, India
March 2024

Dedicated to My Family

INDIAN INSTITUTE OF TECHNOLOGY

GUWAHATI

Department of Chemistry

STATEMENT

I hereby declare that the matter embodied in this thesis entitled "***Applications of Reconstructed Nanofluidic Membrane of Layered Materials in Ionic Thermoelectricity and Moisture-Electricity-Generation***" is the results of the investigations carried out by me at the Department of Chemistry, Indian Institute of Technology Guwahati, Assam, India under the guidance of Dr. Kalyan Raidongia.

In keeping with the general practice in reporting scientific observations, due acknowledgment has been made whenever the work described is based on the findings of other investigators.

Date: March, 2024 **Raktim Gogoi**

IIT Guwahati

INDIAN INSTITUTE OF TECHNOLOGY

GUWAHATI

Department of Chemistry

CERTIFICATE

This is to certify that the matter embodied in this thesis entitled **"*Applications of Reconstructed Nanofluidic Membrane of Layered Materials in Ionic Thermoelectricity and Moisture-Electricity-Generation*"** has been carried out by **Mr. Raktim Gogoi** at the Department of Chemistry, Indian Institute of Technology Guwahati, Assam, India. It has not been submitted elsewhere for the award of any degree or diploma.

Date: March, 2024
IIT Guwahati

Dr. Kalyan Raidongia
(Thesis Supervisor)
Department of Chemistry
Indian Institute of Technology Guwahati
Guwahati-781039
Assam, India

PREFACE

The present thesis with the title "Applications of Reconstructed Nanofluidic Membrane of Layered Materials in Ionic Thermoelectricity and Moisture-Electricity-Generation" is divided into six chapters. The chapter 1 describes about various pathways for the formation of 2D materials, reconstruction of these materials to obtain nanofluidic membranes and the utilization of the membranes to study the ionic thermoelectric effect and moisture enabled electricity generators.

Chapter 2 represents an elaborate study about the exfoliation of a natural clay minerals and reconstruction of the exfoliated nanosheet to obtain a freestanding nanofluidic membrane. The membrane was utilized to investigate ionic thermoelectric responses and the performance of the same was significantly enhanced through the surface functionalisation of the individual nanosheets. The performance of the functionalized clay membrane was examined under lower humidity conditions, and challenges associated with these conditions were mitigated by applying a protective coating layer to the fabricated membrane. The practical utility of the fabricated devices was thoroughly investigated through the illumination of white light, as a fire alarm system, as a self-powered sensors and as an energy harvester from hot water steam.

Chapter 3 describes about fabrication of an ionic thermoelectric material out of reconstructed V_2O_5 membrane which was further modified via the intercalation of poly(4-styrene sulfonic) acid inside the nanochannels of V_2O_5 in order to enhance the ionic thermoelectric property. This chapter specifically elucidates the importance of nanoconfinements in the directional diffusion of mobile ions under temperature gradient. These findings were verified by changing the morphologies of the V_2O_5 nanosheets into nanobelts, without altering the original chemical structure. Finally, the material was examined in various real-time scenarios to harness waste heat and convert it into a useful form of energy.

In chapter 4, a nanofluidic membrane was fabricated that can be tuned to have both positive and negative Seebeck coefficients. Through the intercalation of mobile ion generating species such as Mg-aminoclay, benzyltriethylammonium chloride salts the membrane can be tuned to have negative Seebeck coefficients. Similarly, through the intercalation of poly(4-styrene sulfonic) acid molecules the membrane can be tuned to have positive Seebeck coefficient. The acquisition of these two contrasting materials will eventually led to the fabrication of ionic thermopile that has the potential to elevate the ionic thermopower according the requirements. Additionally, an alternate path was developed to harness the waste heat from the ionic thermopile through water assisted combination of an another ion conducting membrane in to the system.

In the previous chapters it has been observed that, V_2O_5 based nanofluidic membranes can develop mobile cations and the $Ni(OH)_2$ based nanofluidic membranes can develop mobile anions in the in the presence of atmospheric water molecules. Therefore, in chapter 5 both of these two membranes were combined in order to obtain a bilayer moist electric generator (BMEG) that can generate power output continuously for reasonably prolonged period of time. This work further initiates the hybridization of a moist electric generator with that of Soret effect by creating a temperature gradient across the BMEG. The development of temperature gradient across the fabricated BMEG improves the voltage output by 34% demonstrating a new strategy for the development of MEGs. The BMEG was finally utilized in several practical applications such powering up different electronic devices and fabricating self-powered sensors.

The chapter 6 consist of overall conclusion of the work done during my PhD tenure and the future perspective of the work.

. Acknowledgements

It is a pleasant duty to convey my special thanks to many people who have supported and accompanied me during my Ph.D. tenure.

First and foremost, I would like to express my sincere gratitude to my supervisor, Dr. Kalyan Raidongia for giving me an opportunity to work under his expert supervision. This thesis would not have been possible without his limitless efforts, expert guidance, valuable suggestions, boundless support and freedom to work. He has been a continuous source of encouragement throughout my Ph.D. life and it is my good fortune to have him as my supervisor.

I convey my special thanks to my doctoral committee members, Prof. Biplab Mondal, Prof. Debasis Manna and Dr. Dipankar Srimani for their valuable advice, suggestions, constant encouragement, and constructive input on my work progress, which helped a lot in improving my thesis. I am grateful to all the faculty members of the Department of Chemistry, IIT Guwahati, for their encouragement and also to the technical staff of the Department of Chemistry for their valuable supports. I am thankful to the Central Instrument Facility (CIF) and Department of Chemistry of IIT Guwahati for various instrument facilities and to IIT Guwahati for the Scholarship.

My sincere acknowledgement goes to Dr. Yoav Green and Dr. K.K.R. Datta for the valuable comments that helped in the improvisation of the thesis work.

I wish to extend my heartfelt appreciation to my dear friends Sivangi Paul and Abhishek Sarkar from Tezpur University for their unwavering support and encouragement, which has been a constant source of strength throughout this wonderful journey, from our university days to the present.

I would also like to thank Dr. Rajkumar Gogoi, Dr. Kundan Saha, Dr. Jumi Deka, Dr. Tukhar Jyoti Konch, Mr. Arindom Bikash Neog, Ms. Trisha Dutta, Dr. Priyamjeet Deka, Mr. Shivasish Das, Ms. Barsha Rani Bora, Ms. Bipasha Saikia, Ms. Kiran Mayawad, Mr. Deepak Jyoti Deuri, Mr. Harshan Madeshwaran, Mr. Arnab Ghosh, Mr. Priyanku Garg, Ms. Sonali Roy, Mr. Bikash K. Das, Ms. Ayushi Prajapat, Ms. Nabamallika Nath, Mr. Mrityunjoy Dey, Ms. Parijat Pratim Das, Mr. Gouri S. Mandal, Mr. Monotosh Mondol, Mr. Amit Kumar Rajak, Mr. Dibakar Das, Mr. Sagar Karak, Mr. Krishnarajan Sundararajan and Mr. Ahitagni Das from Dr. Raidongia's research group (Nanofluidic Lab).

Finally, I would like to express my sincere gratitude with great honour to my family members for their limitless love, absolute support, sincere encouragement and inspiration for lifting me uphill in this phase of my life. I am fortunate and blessed to have such a caring and supportive family starting from Deta (Monoranjan Gogoi), Maa (Sumitra Gogoi) and Bhaiti (Bhagadatta Gogoi) who sacrificed and struggled to make my life smooth going for this big achievement.

Thank you very much, everyone, for your endless support and encouragement.

Raktim Gogoi

Synopsis

Chapter 1. Application of reconstructed lamellar 2D material in harnessing unwanted heat and moisture

Reliable and affordable energy is the most fundamental requirement for the survival and development of modern civilisation. Unfortunately, as per the approximation, nearly two-thirds of energy is lost as unused heat from diverse sources like thermal power plants, nuclear facilities, vehicles, and industrial plants. The economic conversion of this significant portion of waste heat into other usable forms of energy is vital to fulfilling the ever-increasing demand for energy. Therefore, developing technology or methods capable of directly converting this waste heat into functional energy forms is imperative. The thermoelectric effect emerges as an ideal solution in this scenario, as these devices can directly convert heat into electricity, along with additional advantages such as noiseless operation and minimal maintenance requirements. However, conventional thermoelectric devices relying on the Seebeck effect exhibit significantly low thermopower, necessitating a large number of thermopiles for generating practically usable electricity from waste heat. Considering these shortcomings, the focus of thermoelectricity is shifting from the thermal diffusion of electrons (and holes) to ionic thermodiffusion (the Soret effect). This newly emerging field of ionic thermoelectricity has shown the potential to fulfil the need for higher thermopower. Ionic thermoelectric devices exhibit nearly 100 times higher than that of electronic thermoelectric devices. However, the material selection for ionic thermoelectric devices is mainly localised within polyelectrolytes and ionic liquids. Moreover, the effect of confinement and ion selectivity in thermodiffusion is yet to be explored. As the enhancement of the ionic Seebeck coefficient significantly depends on the mobility difference of cations and anions, integrating ion-selective nanochannels could revolutionise the need for high thermopower ionic thermoelectric materials. In this context, the lamellar, reconstructed two-dimensional (2D) nanofluidic membranes could be an effective

ionic thermoelectric material due to higher ion selectivity and conduction, high-temperature stability, easy fabrication techniques, high scalability and cost-effectiveness.

In recent years, the atmospheric water molecules have been demonstrated to be a massive source of renewable energy. Typically, moisture-enabled electricity generators (MEG) work on the principle of absorbing water molecules by surface active materials from the atmosphere, followed by dissociation into mobile ions. The concentration gradient or evaporation-driven diffusion of these mobile ions in a charged matrix generates electricity. This technique can be further extended to two layers of oppositely charged materials developing mobile anions in one layer and a cation in the other layer, developing mobile anions in one layer and a cation in the other layer, named bilayer moist electric generator (BMEG). Considering the flexibility in designing and modifying reconstructed layered materials based on nanofluidic membranes and the presence of well-aligned ion selective nanochannels could quickly meet the necessity of MEGs.

Chapter 2. Fabrication of Robust and Versatile Ionic Thermoelectric Devices of Natural Clay Minerals

Ionic thermoelectricity has emerged as a burgeoning scientific field thanks to its advantages, such as high ionic thermopower, abundant materials, and straightforward fabrication techniques, enabling the efficient conversion of low-grade waste heat into electricity. Nonetheless, the field is limited to polyelectrolytes and ionic liquids. In this work, we have developed a thermally and chemically resilient, reconstructed lamellar 2D nanofluidic membrane composed of natural clay-based material (vermiculite) to study the ionic thermoelectric effect. Interestingly, a pristine vermiculite membrane is capable of developing Seebeck coefficients in the range of 6 ± 0.8 mV/K, which is further improved up to 14.4 ± 0.4 mV/K by simply modifying the surface functional groups (-OH) into $–SO_3H$. The surface

functionalisation improves the dissociation of protons, and the water uptake capacity of the materials, eventually facilitating the diffusion of protons under a temperature gradient. Unlike conventional ionic thermoelectric materials, clay-based membranes exhibit remarkable high-temperature resilience (~300 °C) without compromising power output performance. Additionally, these materials can effortlessly recover from any physical damage through water-assisted healing while maintaining their original ionic thermopower. One of the major hurdles in the realm of ionic thermoelectricity is their dependency on relative humidity (RH) levels. At lower RH levels, the thermoelectric response becomes quite negligible. This problem is addressed here by applying a coating layer of hydrogel (PVA, borax and LiCl) on the top of the clay membrane, thereby retaining the water uptake level at relatively lower RH levels. The material undergoes further modification with a coating of carbon nanotube (CNT) solutions specifically applied to one side. This configuration enables the generation of a temperature gradient upon exposure to white light, thereby producing a definite amount of thermovoltage. Through specific configurations, the clay-based ionic thermoelectric material can find additional applications in the areas of fire alarms, touch sensors and hot water steam-based electricity generation systems.

Chapter 3. Ionic Thermoelectric Properties of Reconstructed Lamellar Vanadium Pentoxide Membranes

In this chapter, the intercalation of a polyelectrolyte (poly(4-styrenesulfonic acid)) (PSS), containing sulfonic groups within a reconstructed layered material is being explored, following the observation of how the formation of sulfonic groups enhances the overall thermopower of a thermoelectric material in the previous chapter. The reconstructed layered material, V_2O_5, can develop an ionic thermopower of 14.5 ± 0.5 mV/K through the thermodiffusion of protons under 90 % RH. The intercalation of PSS molecules inside the V_2O_5 nanochannels has improved the thermopower up to 26.3±0.7 mV/K, attributed to the higher proton concentration

and higher water retention capability of the membranes after intercalation of PSS. The effect of nanoconfinement in the enhancement of ionic thermopower can be verified by altering the morphology of V_2O_5 nanosheets into nanobelts without modifying the chemical compositions. The V_2O_5 – PSS composite membrane, featuring V_2O_5 nanobelts, lacks nanoconfinements, resulting in a significantly lower Seebeck coefficient of 0.094 mV/K compared to the V_2O_5 – PSS composite with nanosheets morphology (26.3 mV/K). This observation specifically demonstrates the importance of 2D materials with nanofluidic channels for efficient thermodiffusion of ions. The high-temperature stability of these inorganic oxides safeguards the intercalated PSS molecules and preserves the high thermopower. A water-assisted healing property is also observed with V_2O_5 – PSS membrane, facilitating its recovery from physical damage. Finally, the practical applicability of the V2O5 – PSS device was demonstrated by harvesting electricity from direct exposure to infrared (IR) light and a hot water kettle. Through the series combination of six thermoelectric devices, ~ 1V of output thermovoltage can be generated by positioning the same near a hot water kettle, demonstrating the broad applicability of such ionic thermoelectric devices.

Chapter 4. Application of Lamellar Nickel Hydroxide Membrane as a Tunable Platform for Ionic Thermoelectric Studies

Among different ionic thermoelectric materials, materials with cations as active charge carriers have been broadly explored. Only a handful of studies report the thermodiffusion of anions, most of which are ionic liquid-based systems. However, for more sophisticated uses like crafting ionic thermopiles, high-resolution temperature sensors, and pyroelectric detectors, i-TE materials with both positive and negative Seebeck coefficients are essential. In this study, we have developed a β-$Ni(OH)_2$-based lamellar membrane that exhibits a negative Seebeck coefficient of -7.04 ± 0.3 mV/K upon adding Mg-aminoclay as a mobile –OH ion generator. The same can be enhanced further up to -13.7±0.2 mV/K by adding quaternary ammonium salt

benzyltriethyl ammonium chloride (BTAC) salt. The difference in sizes of cations and anions of the quaternary ammonium salt eventually leads to differing mobility under the temperature gradient, thereby enhancing overall ionic thermopower. The pristine β-$Ni(OH)_2$ platform can be further tuned to generate positive thermovoltages by simply intercalating poly(4-styrene sulfonic acid) (PSS) molecules inside the β-$Ni(OH)_2$ layers. The intercalation generates mobile H^+ ions that diffuse under the temperature gradient, developing a Seebeck coefficient of +12 ± 1.9 mV/K. The wide-ranging tuning of β-$Ni(OH)_2$ membrane with different active intercalating species opens up possibilities for developing ionic thermoelectric material with greater applicability. An ionic thermopile was fabricated with the combination of these positive and negative ionic thermoelectric materials that are capable of producing thermovoltage of ~1V under a temperature gradient of 12 K. Similar to the previous observations, the $Ni(OH)_2$-based membranes are also observed to be stable at elevated temperature (~200 °C) without losing its thermoelectric properties. Additionally, another ion-conducting membrane (vermiculite) was integrated towards the colder side of positive and negative ionic thermoelectric material, validating an additional pathway of the energy harvesting system.

Chapter 5. Boosting of Moisture-Electricity Conversion by Robust Oxide-Hydroxide Nanofluidic Membranes with Light and Waste Heat

The exploration of environmental moisture as a renewable energy source has recently gained considerable attention, thanks to its abundance of moisture and the convenience of moisture electric generators (MEGs). As the V_2O_5 and PSS-based composite membranes (VO-PSS) are capable of generating mobile H^+ ions and β-$Ni(OH)_2$, Mg-aminoclay and benzyl triethyl ammonium chloride-based membranes (Ni-AC-Cl) fundamentally produce mobile OH- and Cl- ions; they are combined to fabricate a bilayer moist electric generator (BMEG). The combination procedure involves the water-assisted fusion of both of these oppositely charged nanofluidic membranes. The interaction with the atmospheric water molecules eventually

generates mobile cations towards the VO-PSS layer and mobile anions towards the Ni-AC-Cl layer, thereby developing an interfacial potential responsible for overall BMEG output voltage and current. Unlike most moisture electric generators (MEGs), which exhibit transient responses over time with the continuous influx of external moisture, the fabricated BMEG can generate a sustained voltage for a prolonged period. A single BMEG can develop a potential difference of ~ 620 mV at 85 % RH level, which was further enhanced by ~34% by simply applying a temperature gradient across the BMEG. The heat flux forces the migrating ions to diffuse towards the junctions of VO-PSS and Ni-AC-Cl, thereby increasing the overall BMEG output. The same behaviour can be observed through the illumination of white light, which elevates the BMEG output by ~23 %. This class of BMEG, composed of inorganic oxides and hydroxide layers, can easily survive extreme temperatures (-195 to +200 °C), opening up doors of broader applicability. Interestingly, after a couple of months, the performance of a BMEG can be easily recovered by simply rehydrating and renewing the connections. Through the series and parallel connections of several BMEG devices, the voltage and current output can be further enhanced up to 40 V and 45 μA, respectively. The amplification of both voltage and currents can be tailored as required by adjusting the number of devices through series and parallel connections. Finally, we have demonstrated that the fabricated BMEGs can effectively power LED lights and calculators, with potential for further applications such as developing self-powered moisture sensors. Considering the easy fabrication techniques, wide operating temperature range, ease of recovering BMEG outputs, enhancement of power output though simple addition of heat flux of light illumination and reasonably good power output, BMEGs fabricated from these classes of nanofluidic membranes hold promise in the realm of energy generation from atmospheric moisture.

Conclusion:

In conclusion, we have investigated multiple reconstructed lamellar nanofluidic systems to effectively convert waste heat and ambient moisture into electrical energy that involves the intercalation of different mobile ion-generating species. Chapter 1 provides an overview of the necessity for efficiently converting waste heat into electricity, the underlying principles driving this process, and using ambient moisture to generate valuable energy. Chapter 2 showcases the application of reconstructed natural clay membrane (vermiculite) in generating thermovoltages, which were subsequently enhanced through surface functionalisation of individual vermiculite nanosheets. Chapter 3 illustrates the ionic thermoelectric properties of reconstructed lamellar pristine V2O5 membranes and the composite V2O5 membranes with the intercalation of mobile ion-generating PSS molecules. The work further demonstrates the importance of nanoconfinements for directional and organised thermodiffusion of ions and, therefore, the enhancement of overall thermovoltage. Unlike the previous two chapters, chapter 4 describes the thermodiffusion of anions instead of cations that develop negative thermovoltages under temperature gradients. β-$Ni(OH)_2$ was utilised as the base material, which was modified with Mg-aminoclay and BTAC salt to obtain negative thermopower due to the thermodiffusion of OH^- and Cl^- ions. The β-$Ni(OH)_2$ membrane (Ni-AC-Cl) was further tuned to have positive thermopower by simply intercalating PSS molecules that alters the overall Seebeck coefficient from negative to positive. Finally, in chapter 5, both the composite membranes of VO-PSS and Ni-AC-Cl were combined to harvest energy from atmospheric moisture through water-assisted joining. As the individual membrane generates ions with opposite natures in the presence of atmospheric water molecules, the combination of them develops reasonable good power output that was further enhanced through the introduction of the temperature gradient. At last, the constructed device was employed in various applications, including powering an LED, a calculator, and self-powered moisture-sensing devices.

Table of contents

Chapter 1

Harnessing electricity from waste heat and environmental moisture with reconstructed lamellar 2D material

1. Introduction

1.1. Materials with layered structure and its transition into two-dimensional form:

The history of layered materials is a narrative that unfolds across millennia, rooted in ancient observations and evolving into a cutting-edge realm of materials science. Early civilisations noted the natural layering of substances like mica and graphite. These materials often occur in layered formations within rocks and minerals.[1] However, with the recognition of graphite's lamellar structure by Benjamin Collins Brodie, a new perspective has been developed towards the groundwork for understanding layered materials at the atomic level.[2,3] Later, the structure was confirmed using single-crystal X-ray diffraction.[4] Similarly, during the 1970s, the layered structure of hydrotalcite (layered double hydroxide (LDH)), was validated with layered arrangement through X-ray diffraction analysis.[5,6] The knowledge of these layered structures has sparked a keen interest in acquiring single-layer, two-dimensional (2D) nanosheets from the corresponding layered structures using exfoliation techniques. These endeavours were fuelled by the desire to explore the unique properties of materials in their ultimate 2D form such as extraordinary electrical, mechanical and thermal properties etc. Indeed, after many unsuccessful attempts the pivotal moment arrived in 2004, when Andre Geim and Konstantin Novoselov isolated graphene using a simple scotch tape method.[7,8] Instantly, the theoretical inquiries predating the single-layer exfoliation of graphene found experimental validation, revealing outstanding electrical conductivity, thermal conductivity, mechanical strength, and optical transparency.[9–11] This quest to explore the characteristics of single-layer nanosheets established different exfoliation techniques and various 2D materials tailored for various applications that continue to this day.

Materials with layered structures, represent different layers of intralayer/covalently-bonded atomic planes sequentially divided by feeble interlayer bonding, such as van der Waals forces

or weak electrostatic interactions.[12–14] The absence of covalent bonding (or strong covalent bonding) among the atomic layers allows the disruption of weak forces (van der Waals or electrostatic), leading to the exfoliation of individual layers into atomically thin 2D nanosheets. Another process of preparing 2D nanosheets entails deliberately assembling individual atoms or molecules to form a 2D structure with specific properties. This process, commonly known as bottom-up synthesis, further encompasses multiple techniques. The details of various methodologies adopted for preparing atomically thin 2D nanosheets are discussed below with specific examples.

1.2. Exfoliation–Based Techniques:

The understanding of the feeble interactive nature among different layers in a layered material has led to the concept of disassembling them into individual 2D structures, commonly referred to as the top-down method. The goal can be achieved through different techniques, primarily encompassing mechanical exfoliation, chemical and electrochemical exfoliation and laser-assisted exfoliation. However, considering the limitations of the existing methods, efforts have been devoted towards developing advanced methodologies.

1.2.1. Mechanical exfoliation:

The mechanical exfoliation process involves physical splitting or peeling off the bulk layered materials into individual nanosheets. The major advantage of this method lies in the yield of high-purity crystals, as no chemical reactions involves during the exfoliation process. This mechanical exfoliation process also includes micromechanical cleavage, sonication and ball milling-based processes.

Micromechanical cleavage: A bulk structure of a layered material can be mechanically exfoliated by applying a normal force or a lateral force, as depicted in the schematic of Figure 1.1a.[15–17] The micromechanical cleavage, also known as the “Scotch tape method,” involves

the normal force exfoliating the layers through the breakage of van der Waals forces. The process was originally developed to synthesise atomically thin graphene sheets from highly ordered pyrolytic graphene (HOPG) in 2004.[8] Generally, a normal force is repeatedly exerted on the HOPG surface using a scotch tape until it reaches the state of single-layered graphene. Schematically the process is represented in Figure 1.1b. Indeed, high-quality graphene nanosheets are obtainable from this simple and cost-effective means. However, the labour-intensive nature of this process constrains its applicability primarily to fundamental research.[18]

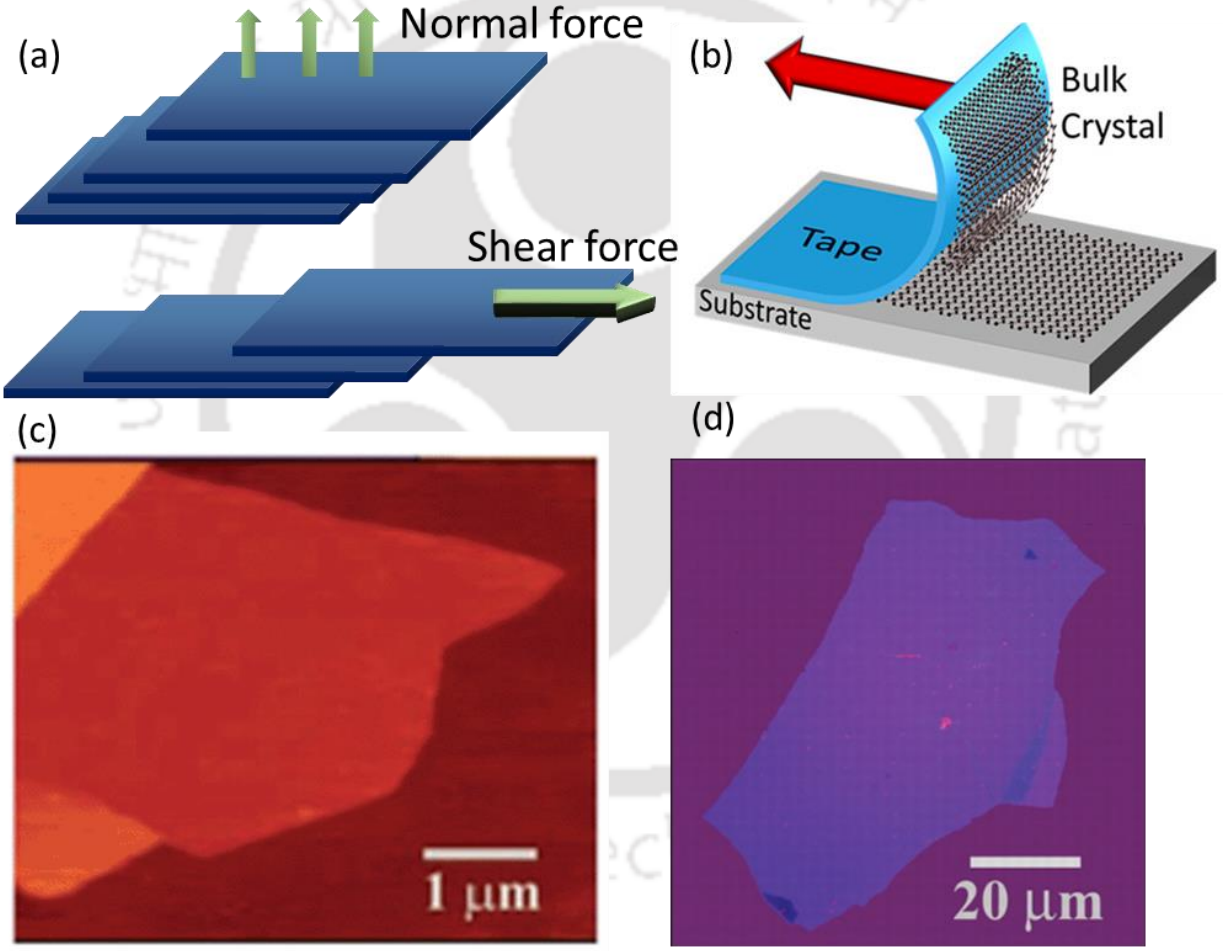

Figure 1.1: (a) Two different kinds of mechanical forces for the exfoliation of a layered material into individual nanosheets. (b) Schematic representation of the mechanical exfoliation process, known as "Scotch Tape" method. (c) AFM image of a single layer graphene nanosheet. (d) Digital photograph of a relatively large multilayer graphene flake with thickness ~3 nm on top of an oxidized Si wafer. (Images copied from (b) *ACS nano*, 13(9), pp.9781-9810 and (c)-(d) *Science*, 306(5696), pp.666-669.)

Sonication: The sonication process involves using ultrasonic waves for liquid-phase exfoliation of layered materials through the appropriate choice of solvents. For example, in order to obtain the graphene nanosheets, in 2008, Coleman's group performed this liquid-phase exfoliation of graphite powder through sonication with the specific solvent of N,N-dimethylformamide (DMF) and N-methylpyrrolidone (NMP).[19] This approach was further broadened to include the exfoliation of other classes of layered materials, such as transition metal dichalcogenides (TMDs)[20–23], hexagonal boron nitride[20,21,24,25] , Mn oxides[20] etc. Additionally, this method is recognised to be ideal for the scalable, controlled synthesis of nanosheets with the required thickness and size.

Ball milling: This process involves the shear force for lateral exfoliation of a layered material (Figure 1.1a). The impact and friction generated between the milling balls and the layered material result in the mechanical exfoliation of layers (Figure 1.2e). The desired single layer of nanosheets is achievable in the presence of specified solvents, known as wet ball milling, or in a completely dry condition, referred to as dry ball milling. In 2010, Knieke et al. and Zhao et al. performed the wet ball milling method to exfoliate the graphite by modifying the milling technique.[26,27] The modification followed the same idea of sonication mentioned above, employing N, N-dimethylformamide (DMF) as the solvent medium. Along with the graphene sheets, this process has been extended to exfoliate different layered materials such as boron nitride, MoS_2, WS_2 etc.[28–32] On the other hand, in the dry ball milling process, the layered material is combined with hard milling balls under dry conditions. For example, during the exfoliation of graphite, it was combined with water-soluble and chemically inert inorganic salt to avoid the distortion of morphologies considering graphene nanosheets. Leon et al. modified this exfoliation process of graphite by introducing melamine molecules into it, weakening the van der Waals forces among the interlayers.[33] The modification was further continued by Liu

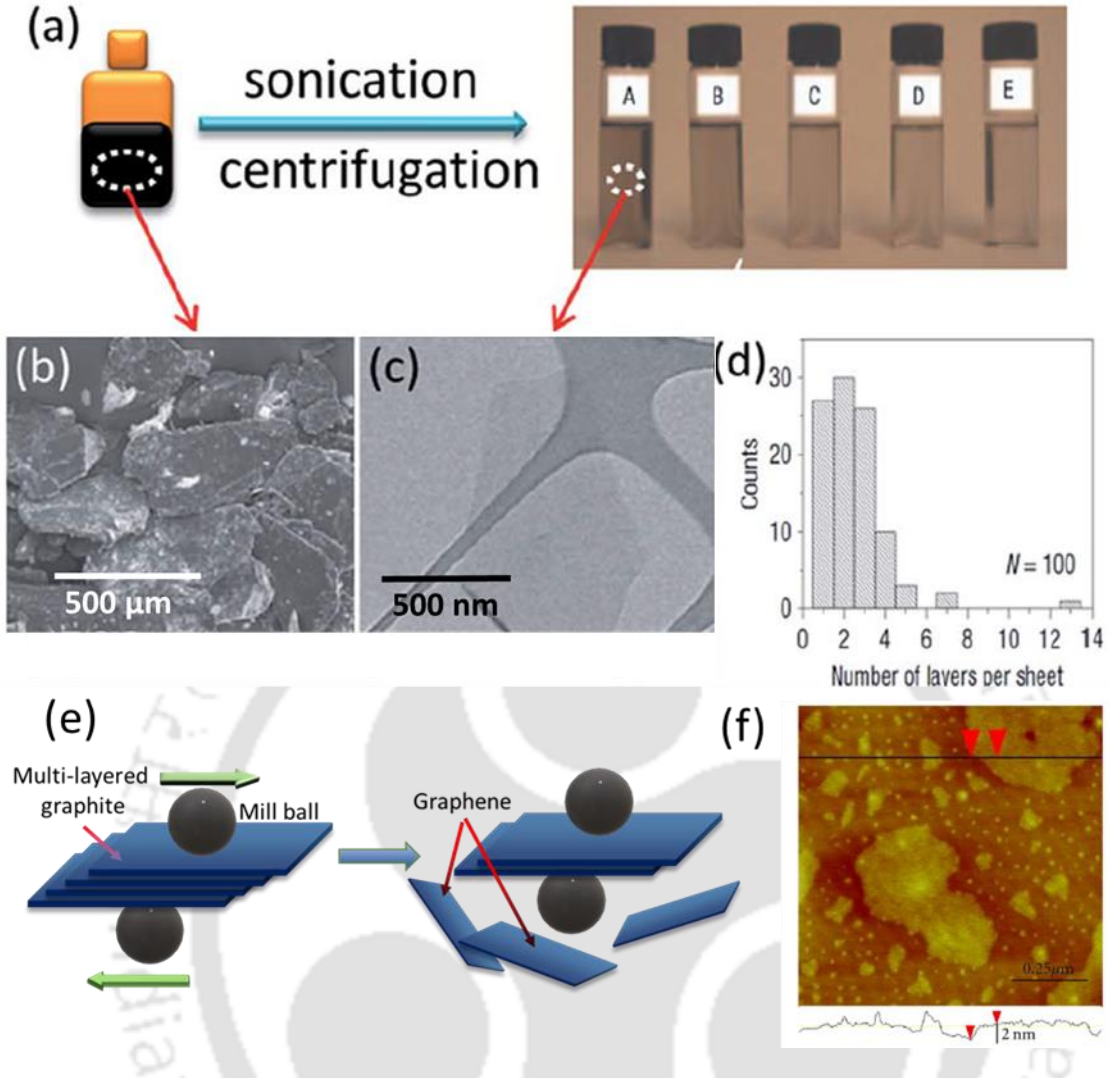

Figure 1.2: (a) Exfoliation of graphite through the sonication process. (b) SEM image of the graphite flakes in the initial state. (c) TEM image of the exfoliated graphene nanosheets. (d) Histogram of the number of layers. (e) Schematic representation of the ball milling process for the exfoliation of graphite in graphene nanosheets. (f) AFM image of the graphene nanosheets exfoliated from the ball milling process. (Images copied from (a)-(d) *Nature nanotechnology*, 3(9), pp.563-568. (f) Journal of Nanomaterials, 2010, pp.1-4.)

et al. by incorporating ammonia borane.[34] The major shortcoming of this method stems from the unavoidable formation of defects due to the high-energy collisions involving hard milling balls. However, by understanding the prerequisites, one can adopt this method as it demonstrates the potential yield of nanosheets on a large scale.

1.2.2. Chemical and Electrochemical exfoliation:

The chemical exfoliation process involves using chemical agents to selectively intercalate, weaken, or break the interlayer bonds within a layered material, separating individual layers (Schematic of Figure 1.3a). One of the popular examples is exfoliation into graphene oxide (GO) nanosheets from graphite through the modified Hummers process. The exfoliation was performed via the oxidation and intercalation of graphite layers with potassium permanganate and sulfuric acid solution. This oxidation process introduces oxygen-containing functional groups on the surface of graphite, thereby increasing the interlayer spacing among the layers. The intercalation of potassium ions and water molecules between the graphite layers further weakens the van der Waals forces that hold them together. Finally, it leads to the formation of GO nanosheets.

A number of other layered materials have been explored for exfoliation through intercalation of different chemical species. For example, the transition metal dichalcogenides (TMDs) were exfoliated by intercalating sodium, potassium and lithium ions.[35] However, achieving complete exfoliation into singular nanosheets requires the selection of suitable intercalating species based on their interactions with the layers intended for exfoliation. For instance, the complete exfoliation of MoS_2 cannot be achieved through potassium intercalation.[36] Roy Morrison pioneered the quantitative investigation of single-layer MoS_2 using XRD spectra and reported that only the n-BuLi intercalation-based process yielded the best result.[37] The lateral dimension through this exfoliation process falls in the range of 0.3-0.8 µm with a typical thickness of 1-1.2 nm, confirming the formation of individual nanosheets. To enhance flake size, Loh et al. adopted a two-step expansion and intercalation approach utilising N_2H_4 molecules to expand the layer spacing between MoS_2 sheets and subsequently intercalating with $NaC_{10}H_8$.[36] Interestingly, this resulted in single-layer MoS_2 with lateral widths around 10 µm. Therefore, the choice of the intercalating species is crucial for the desirable morphology of obtained

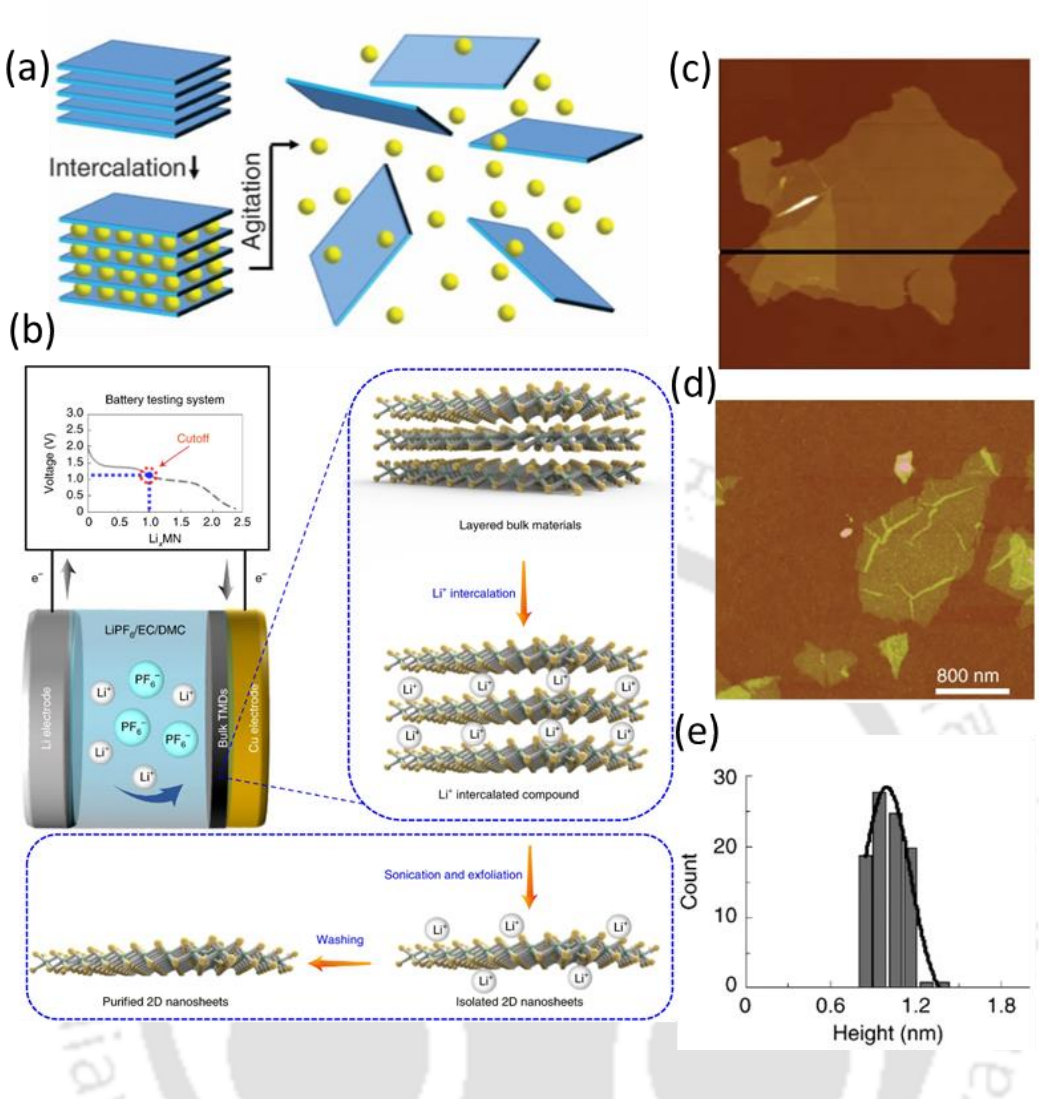

Figure 1.3: (a) Schematic representation of the exfoliation of a bulk layered crystal through the intercalation of the external species. (b) Schematic representation depicting the process of exfoliation based on electrochemical lithium-ion intercalation. (c) AFM image of the exfoliated vermiculite nanosheet. (d) AFM image of the exfoliated MoS_2 through electrochemical lithium ion intercalation. (e) Histogram to represent the height of the nanosheets shown in Figure 1.3d. (Images copied from (a) *Science*, 340(6139), p.1226419. (b), (d) and (e) *Nature protocols*, 17(2), pp.358-377. (c) *Nature communications*, 6(1), p.7602.

nanosheets. Besides the simple intercalation process, an ion exchange method can be employed for the exfoliation process, where the second set of ions of bigger sizes replaces the intercalated ions. This method is important for exfoliating different layered double hydroxides (LDHs), metal oxides, and clay minerals.[38,39] One of the clay minerals, vermiculite, undergoes exfoliation by intercalating sodium ions in the first step (Figure 1.3c). This is followed by

exchanging these sodium ions with lithium in the second step in an aqueous dispersion.[40] Additionally, the counter ions, such as Cs^+ of the metal oxide, i.e. TiO_2, can be exchanged with the protons through immersion in an acidic solution. These protons can then be swapped for voluminous organic ions, such as tetrabutylammonium cations, inducing significant swelling and exfoliation into individual nanosheets.[41,42]

This intercalation process can further be accomplished electrochemically, as depicted in Figure 1.3b. Particularly, for electrochemical lithiation, the bulk materials such as MoS_2, WS_2, TiS_2, TaS_2, ZrS_2 is integrated as cathode whereas the lithium foil as an anode.[43,44] This electrochemical process facilitates the lithium intercalation, whereas the final ultrasonication process isolates the individual nanosheets. Indeed, graphite can undergo exfoliation via electrochemical means in sulfuric acid, with a Pt wire utilised as the grounded electrode.[45] This direct intercalation or electrochemical intercalation process holds great promise in top-down synthesis by selecting appropriate solvents and intercalating species.

1.2.3. Laser-assisted exfoliation:

The energy of photons from lasers can drive exfoliation by irradiating materials and elevating the temperature at the material/laser interface. This process induces high-pressure cavities and chemical reactions, leading to plasma formation, vaporisation and condensation on the material's surface, causing detachment of the species on the surface. Laser irradiation is commonly used for surface etching and material thinning. For example, subjecting Highly Oriented Pyrolytic Graphite (HOPG) to a high-power laser (>60 mW) results in the oxidative burning of upper layers, yielding monolayer graphene.[46] MoS_2 and $MoTe_2$ can also be exfoliated similarly. However, this method has the drawback of very low efficiency, producing only one flake per bulk crystal as discarded upper layers.

1.3. Bottom-up synthesis of 2D materials:

The bottom-up approach involves constructing a material by assembling it gradually, either molecule by molecule, atom by atom, or cluster by cluster. This approach allows precise control over the nanosheets composition, structure, and properties, enabling the design of materials with tailored characteristics. Building from the molecular or atomic level often results in high purity and uniformity. This bottom-up approach can be accomplished through different methodologies such as chemical vapour deposition (CVD), hydrothermal, co-precipitation, and sol-gel methods.

1.3.1. Chemical vapor deposition (CVD):

In CVD, gaseous precursors containing the desired elements react on a heat substrate surface, producing a thin film. In a comprise way, the CVD technique encompasses different steps such

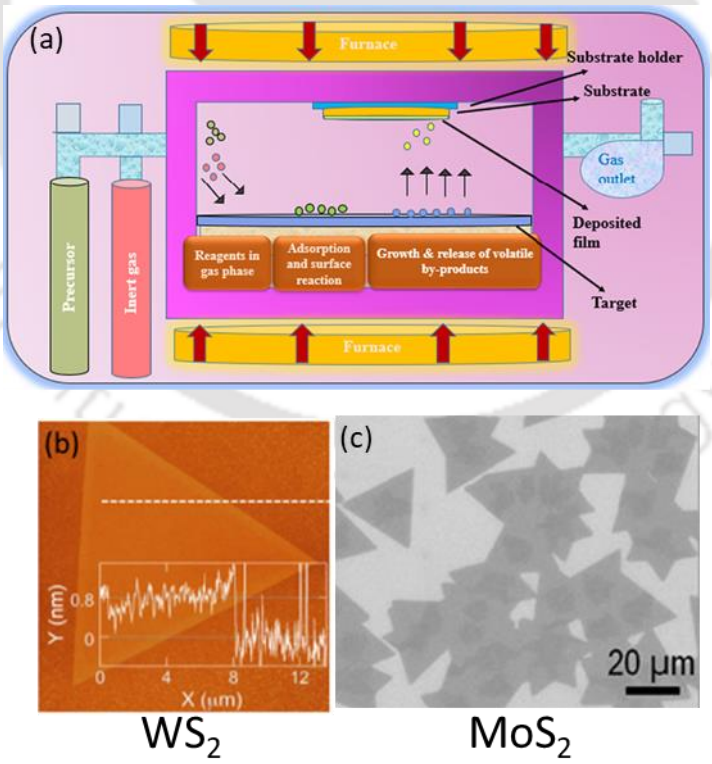

Figure 1.4: (a) Schematic representation of the CVD technique. (b) AFM image of the WS_2 nanosheet. (c) SEM image of the MoS_2 nanosheets formed through CVD technique. (Images copied from (a) *Advances in Colloid and Interface Science*, 300, p.102597. (b) *Scientific reports*, 6(1), p.35154. (c) *Chemical Vapor Deposition*, 21(10-11-12), pp.241-259.

as the precise dispensation of gas-phase reactants, the presence of a sealed reaction chamber, the expulsion of gases, the management of reaction pressure, the provision of an energy source for chemical reactions and the purification of exhaust gases (Schematic of Figure 1.4a). Moreover, this method enables the growth of nanosheets with a predetermined alignment per specific requirements. For example, vertically aligned WS_2 nanosheets were grown at a reasonably low temperature (500 °C) on the FTO substrate by A. Ahmadi et al.[47] In another work, MoS_2 nanosheets were grown on montmorillonite nanosheets at two different temperatures (500 °C and 600 °C) with different lateral dimensions.[48] Similarly, VS_2 nanosheets can be grown from VCl_3 at 550 °C, $MoSe_2$ can be grown from Se and MoO_3 on SiO_2/Si substrate and SnS_2 from $SnCl_4.5H_2O$ and S powder on an FTO substrate.[49]

1.3.2. Hydrothermal treatment:

In this process, nanosheets were grown from their precursors at an elevated temperature and pressure within an aqueous solution. This methodology offers precise control over the growth and assembly of nanosheets along with uniformity, homogeneity and scalability. For example, hydrothermal treatment of KSCN and MoO_3 can effectively produce MoS_2 nanosheets at 453 K with a few-layer thickness.[50] This hydrothermal treatment can be extended to prepare graphene oxide nanosheets from the glucose as a precursor at a temperature ranging from 160 to 220 °C.[51] Modified WS_2 nanosheets were prepared through one-pot hydrothermal treatment from $(NH_4)_2WS_4$ for W and S source and polyvinyl pyrrolidone was chosen as the modifier.[52] Although this process allows for precise control of the nanosheets with high crystallinity, sometimes the major scale production becomes very expensive, and the direct observation of crystal growth is impossible.

1.3.3. Sol-Gel method:

One frequently employed bottom-up method for synthesizing 2D nanomaterials is the sol-gel approach, chosen for its straightforwardness. Sol-gel is a fusion of two terms, "sol" refers to a colloidal solution composed of solid particles suspended in a liquid, and "gel" signifies a solid macromolecule that dissolves in a liquid. This method comprises different steps: hydrolysis in the first step, followed by polycondensation, ageing, drying and finally, calcination.[53] Various factors, such as pH, stirring speed and duration, temperature and reaction time, play a crucial role in influencing the microstructure of the nanosheets. The characteristics of the solvent and precursor used in the sol-gel method also significantly impact the final products. This method also allows precise control over materials texture and surface qualities. For instance, Manoj Pudukudy et al. have synthesised the nanosheets of spinel Co_3O_4 with this sol-gel method using the surfactant Pluronic P123 triblock copolymer.[54] Hybrid compounds incorporating exfoliated nanosheets, featuring a perovskite-related structure, have been synthesised through a sol-gel procedure. This method involves the interaction of an n-deoxy derivative of an ion-exchangeable layered perovskite, namely $HLaNb_2O_7 \cdot xH_2O$ (HLaNb) or $HCa_2Nb_3O_{10} \cdot xH_2O$ (HCaNb), with silanol-terminated poly(dimethylsiloxane) (PDMS) and tetraethoxysilane (TMOS).[55] Subsequent intentional hydrolysis, catalyzed by hydrochloric acid, completes the synthesis process. This sol-gel method is cost-effective and produces homogeneously structured materials at low processing temperatures, making it versatile for various applications. It simplifies the creation of composites and intricate nanostructures, allowing for the uniform distribution of modest amounts of dopants. The method enhances product purity, but drawbacks include a longer reaction time, health risks associated with the toxic organic chemicals, and the need for post-treatment for sample purification.

1.4. Reconstruction of layered materials:

The detailed explanation of exfoliating layered materials into individual nanosheets is covered in the previous sections. In the following section, we will delve into the reconstruction or restacking of these individual nanosheets and the intriguing properties that emerge through this process.

The reconstruction or restacking of individual exfoliated nanosheets can be achieved either through vacuum filtration or drying the nanosheet dispersion. The schematic representation of these methods is shown in Figure 1.5a and b. In a typical vacuum filtration method, the

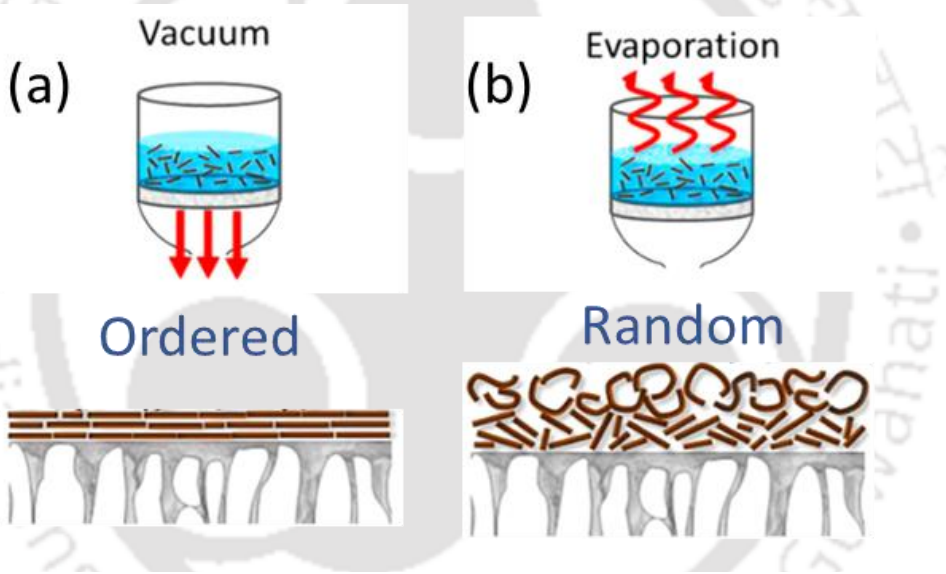

Figure 1.5: Schematic representation (a) of the reconstruction of nanosheets through vacuum filtration, (b) of reconstruction of nanosheets through evaporation method and. (Images copied from (a)-(b) *Journal of Membrane Science*, 477, pp.93-100.

dispersion of exfoliated nanosheets is allowed to pass through a supporting membrane with a definite pore diameter. The suction force generated by the vacuum pump ultimately results in the uniform arrangement of nanosheets on the supporting membrane (Figure 1.5a). In the evaporation method, the restacking process occurs through simple evaporation of the dispersed liquid. However, this method yields a rather unpredictable reassembly of nanosheets, contingent on the overall duration of evaporation (Figure 1.5b). Other than these two

methodologies, there are other techniques that can be applied for the assembly or the reconstruction of individual nanosheets, such as, spin coating of the dispersion of nanoseets with appropriate solvents[56], Langmuir-Blodgett assembly[57,58], layer by layer assembly[59,60] and self-assembly process.[61]

As individual 2D nanosheets undergo reconstruction, the channels formed through this process enable the fluid within to exhibit a distinct behaviour. The concept called nanofluidics is a descriptive study about the behaviour of this fluid inside the nanochannels. It involves the study of fluid flow, transport phenomena, and interactions between fluids and solid surfaces in confined spaces at the nanoscale. The distinct characteristics of fluids within nanochannels facilitate various technological applications, including energy conversion and storage, water purification and desalination, as well as sensing and detection, among others. The detail of this concept is elaborately discussed in the following sections.

1.4.1. Nanofluidics:

In a simple word, nanofluidics describes the behavioural properties of a fluid within nanoscale confinements. Nanofluidics, often viewed as an evolution from microfluidics, distinguishes itself as more than a mere extension. It unveils new physical phenomena and mechanisms that remain latent at microscales or in bulk, establishing a unique research frontier for exploring novel scientific insights and fluid applications. The revealed phenomena encompass nonlinear transport, such as concentration polarization and ion-current rectification, along with modified liquid properties of water, including a lower dielectric constant, higher viscosity, and enhanced proton mobility compared to bulk properties.[40,62–64] These effects primarily arise from ultrahigh surface-to-volume ratios along with surface charge, leading to the overlapping of electrical double layers (EDL) in nanochannels. The overlap of electrical double layers occurs when the channel width is comparable to or smaller than the Debye length of the EDL. This leads to the

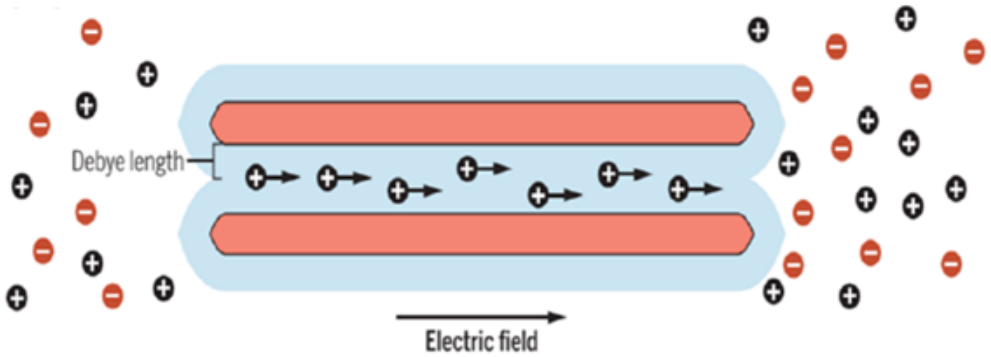

Figure 1.6: selective diffusion of ions through a nanofluidic channel. *Science*, 351(6280), pp.1395-1396

emergence of various intriguing properties under such conditions. In such conditions, the ionic conductance within nanochannels is predominantly influenced by the surface charges of the constituents. This eventually results in the elevation of ionic conductivity a few orders magnitudes higher than the bulk electrolyte concentration, particularly at a lower electrolyte concentration regime.[65–67] Due to this distinctive conductivity pattern in nanochannels, significant focus has been directed towards tailoring the geometry and surface chemistry of engineered nanofluidic channels to control molecular/ionic transport behaviours. These investigations contribute to a thorough comprehension of fundamental nanofluidic transport mechanisms and enhance various applications such as biosensing and biomedical analysis[68], desalination and water purification[69], molecular separation[70] and nanofluidic energy conversion and storage.[71,72] The later sections, of this thesis focus on different energy harvesting techniques using nanofluidic phenomenon.

1.4.2. Energy harvesting techniques:

The unique transport phenomena of ions through the EDL overlapping nanochannels enabled several energy harvesting techniques such as nanofluidic reverse electrodialysis (NRED), streaming potential, moisture-enabled energy harvesting systems and ionic thermoelectricity.[71,72] All these methods for harvesting energy rely on a fundamental principle

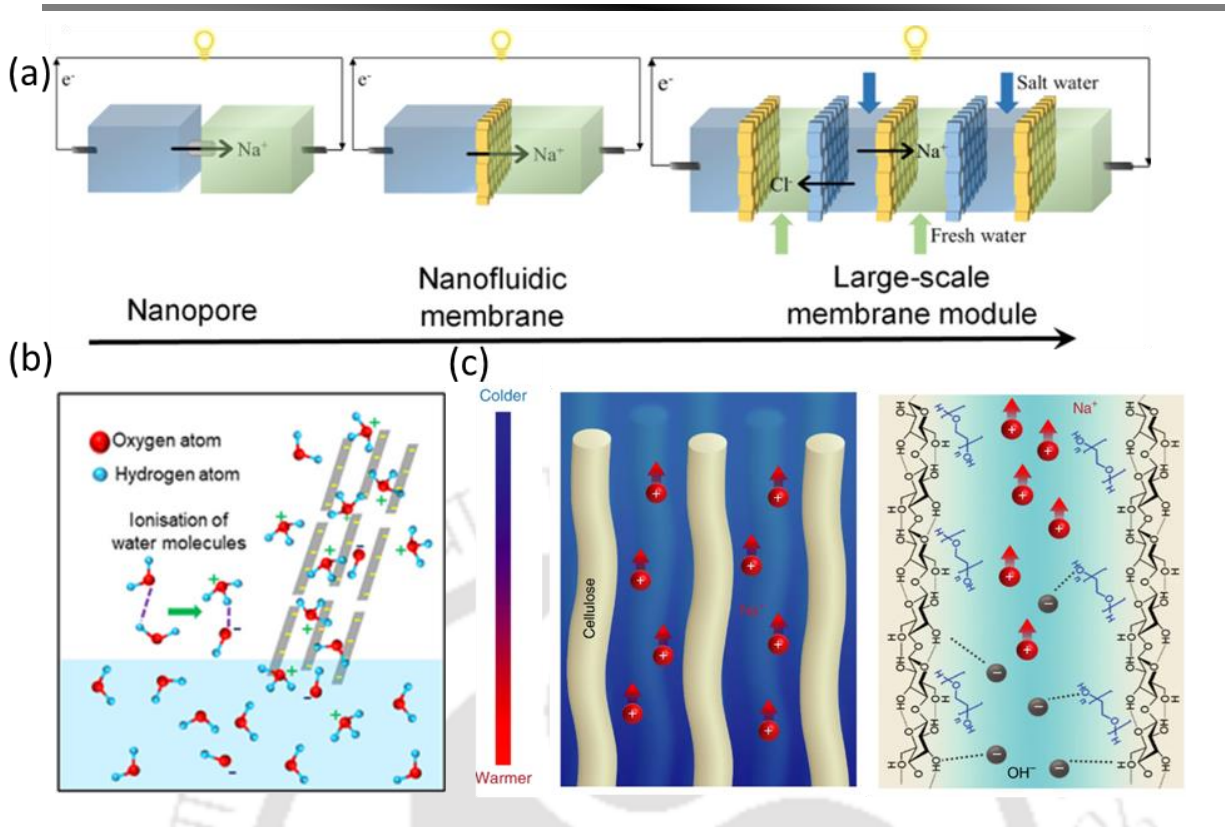

Figure 1.7: (a) Schematic representation of the nanofluidic reverse electrodialysis representing a system with single nanopore (left), with a nanofluidic membrane (middle) and consisting of several number of devices with cation selective and anion selective nanofluidic membranes (right). (b) Schematic representation of an energy harvesting system thorough evaporation induced streaming potential utilizing a nanofluidic membrane as an active material. (c) Schematic representation of the improved ion mobility and selectivity within the cellulosic membrane in the presence of nanofluidic channels and the migration of ions under the influence of temperature gradient. (Images copied from (a) *ACS nano*, 15(4), pp.5838-5860. (b) *ACS Applied Energy Materials*, 4(8), pp.8410-8420. (c) *Nature materials*, 18(6), pp.608-613..

of permselectivity: enabling only counterions to diffuse through electrically charged nanochannels while repelling co-ions (schematic representation of Figure 1.6). Therefore, in a system of NRED, when a nanofluidic membrane separates two compartments of salt solutions with different concentrations, the ions will naturally be driven towards the solution with a low concentration (uphill ion). However, the nanofluidic membrane permits only the passage of counterions, disrupting electroneutrality and consequently generating electric potential and current flow. The schematic representation of an NRED is shown in Figure 1.7a. The second approach, known as streaming potential, represents the building of potential difference across

an energy harvesting system as a liquid, predominantly water, passes through the nanochannel, diffusing the counterions in the process (Figure 1.7b).[72] Primarily, when water comes in contact with the active material of streaming potential comprising of nanofluidic channels, undergoes dissociation into H^+ and OH^- ions. Depending on the surface charge of the nanochannels, the counterion diffuses. However, due to capillary evaporation, the channels create a gradient of counterions across the active material, thereby generating potential difference and electric current. Similar diffusion behaviour with counterions can be observed through the nanochannels when a temperature gradient is applied across the active material. In this scenario, the driving force is the temperature gradient, and the counterions are internally formed that diffuse across the temperature gradient (Soret effect), generating a definite amount of energy output (Figure 1.7c). The final form of energy harvesting system, moisture-enabled electricity generation, depends on the generation of counterions inside the nanochannels of the active material in the presence of moisture.[71] In simple words, if two active materials with contrasting surface charge behaviour are physically attached, a potential gradient can be observed. This can be attributed to generating mobile cations in one layer and the mobile anions in the counter layer. The diffusion of these cations and anions through the nanochannels will eventually generate a diffusive electrical current and potential gradient. In the later sections, we will mainly focus on the techniques and materials for ionic thermoelectricity and moisture-enabled electricity generation processes.

1.5. Thermoelectricity:

The need for an alternative energy source other than the predominantly consumed fossil fuels is all known. Consequently, humankind must explore renewable energy sources such as solar, wind, rain, wave and geothermal energy. In this quest of exploration, it has come to the realisation that another abundant energy source could be the massive heat dissipated into the environment from various sources. For example, an internal combustion engine can be operated

only with an efficiency of 30-40% and nearly 60% of the energy is wasted as unwanted heat.[73] Similarly, different industrial sectors, such as thermal power plants, nuclear power plants, waste incinerators, food processing, steel industries, etc., only utilise half of their initial energy and half is wasted through heat. Along with these primary contributors of unwanted heat, households are equipped with appliances such as ovens, electric or gas stoves, electric kettles, and other equipment capable of producing heat during their operations. Therefore, technology or a method is essential to directly convert this waste heat into useful forms of energy. In this context, the ideal solution would be the thermoelectric effect, which has the potential to transform heat flow into electricity directly, provided it attains sufficient efficiency.

1.5.1. Electronic Thermoelectricity:

The discovery of the Seebeck effect in the year 1821 by Thomas Johann Seebeck is the beginning of today's thermoelectric materials.[74] The observation was that when two different metal electrodes were connected in a loop, and a temperature gradient was maintained, a potential difference was generated across the circuit (Figure 1.8a). This observation is the fundamental principle underlying the behaviour of all thermoelectric materials, where the migration of charge carriers (electrons and holes) eventually generates the output voltage under the temperature gradient. Peltier observed the complete opposite effect in the year 1834 where heat is either absorbed or released when an electric current is passed through the junction of two different metals (Figure 1.8b).[75]

The quantification of this Seebeck effect is possible with the expression in equation 1 where the generation of voltage (ΔV) across the two dissimilar material is assumed to be directly proportional with the temperature gradient (ΔT).

$$\Delta V = S\Delta T \quad \text{---------- (1)}$$

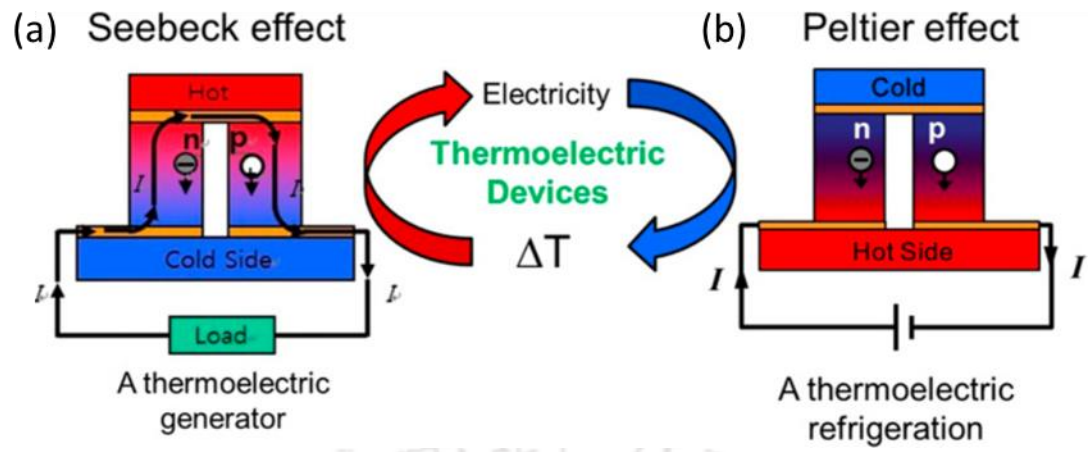

Figure 1.8: Schematic representation of the thermoelectric effects (a) Seebeck effect and (b) Peltier effect. (Images copied from *Frontiers in Chemistry*, 9, p.762896.

The term S here is named as Seebeck coefficient. Apart from the Seebeck coefficient, the effectiveness of a thermoelectric material relies on two additional factors: thermal conductivity and electrical conductivity. For optimal functionality, sustaining a consistent temperature gradient across the thermoelectric material is preferable throughout the entire operational duration. Therefore, a material with lower thermal conductivity (κ) is desirable to minimise the heat flow across the thermoelectric material. Another factor that could greatly impact operational performance is the dissipation of energy through Joule heating, primarily observed with materials with higher resistivity. In other words, a material exhibiting superior electrical conductivity (σ_e) is expected to demonstrate enhanced performance in generating thermovoltages. Combining these parameters, a dimensionless expression was formulated known as the figure of merit (ZT) of a thermoelectric material:

$$ZT = \frac{S_e^2 \sigma}{\kappa} T \quad \text{----------(2)}$$

In addition to this widely acknowledged parameter, another metric is employed to compare the performance of materials known as the power factor (PF) with the expression of $S_e^2 \sigma$ with the

dimension of (mW/m*K^2). The maximum power generation efficiency (η) now can be calculated with the help of this figure of merit as expressed below[76,77]:

$$\eta = \left(\frac{T_{hot}-T_{cold}}{T_{hot}}\right)\left[\frac{\sqrt{1+ZT_m}-1}{\sqrt{1+ZT_m}+\left(\frac{T_{cold}}{T_{hot}}\right)}\right] \quad \text{----------(3)}$$

where,

$$T_m = \frac{T_{hot}-T_{cold}}{2} \quad \text{----------(4)}$$

The initial part of the equation (3) $(T_{hot}-T_{cold})/T_{hot}$ is the Carnot efficiency and the remaining part represents the reduced efficiency that is dependent on ZT_m, T_{hot} and T_{cold}. Over an extended period of time the ZT values of thermoelectric materials that has been developed fallen within the range of 1.0 suggesting the conversion efficiency nearly about 10%. Additionally, theoretical insights propose that achieving a ZT value of 3.0 could lead to a conversion efficiency of up to 30%, which opens the possibility of creating more practical systems, including economically viable home refrigerators comparable to traditional models. Therefore, ZT value is crucial in analysing and upgrading the thermoelectric materials as per the requirements.

Identifying thermoelectric (TE) characteristics in semiconducting materials with a figure of merit close to 1.0 in the 1950s paved the way for developing today's advanced thermoelectric materials.[78] Since then, efforts to enhance the performance of TE materials have led to the development of various material classes such as BiTe series, CuSe series, SnSe series, GeTe/PbTe series, different metal oxides, composites of organic and inorganic materials, half-Heusler alloys etc. Indeed, the majority of commercially accessible thermoelectric (TE) materials consist of Bi_2Te_3, serving as a primary benchmark for the development of other classes of TE materials. The nanostructuring of this Bi_2Te_3 has further elevated the ZT value

upto 1.35.[73] Additional research has explored alternative materials, including skutterudite (ZT = 1.5), SrTe (ZT = 2.2), and SnSe (ZT = 2.6).[78] A notable study from 2019 reached an impressive ZT exceeding 5 by employing a Heusler metal alloy, currently standing at the forefront of advancements in this field.[79]

Thermoelectric materials and their devices are attractive for several reasons, including their ability to directly convert heat into electricity, the absence of any moving parts, no maintenance requirements leading to cost savings, operation without the need for a working fluid, and, notably, their noiseless operation. It was understood that the generation of thermovoltage is influenced by the electrons in the vicinity of the Fermi level, resulting in a Seebeck coefficient that falls within the range of only 10-100 μVK^{-1}. For example, the Seebeck coefficient of a metal copper wire is observed to be ~10 μVK^{-1}, suggesting that to achieve a voltage of 1 mV, a temperature gradient of 100 K has to be applied. Considering other semiconducting materials as well with the Seebeck coefficient in the range of 600 μVK^{-1}, only ~60 mV can be achieved with the temperature gradient of 100 K, which is still far from real-time practical implementation. By employing both series and parallel connections of numerous devices, it becomes feasible to augment the overall power output. However, the emphasis should be on developing these materials through cost-effective and scalable methods and the incorporation of straightforward fabrication techniques to enable the large-scale production of such materials.

1.5.2. Shift from electronic to ionic:

The primary hurdle of a significantly lower Seebeck coefficient associated with the TE materials can be overcome by altering the charge carriers from electrons to ions, termed ionic thermoelectricity (i-TE). The goal can be achieved through two distinct approaches: (a) employing a system with a redox couple or an electrochemically driven system and (b) utilising a system without a redox couple.

1.5.2.1. System with a redox couple:

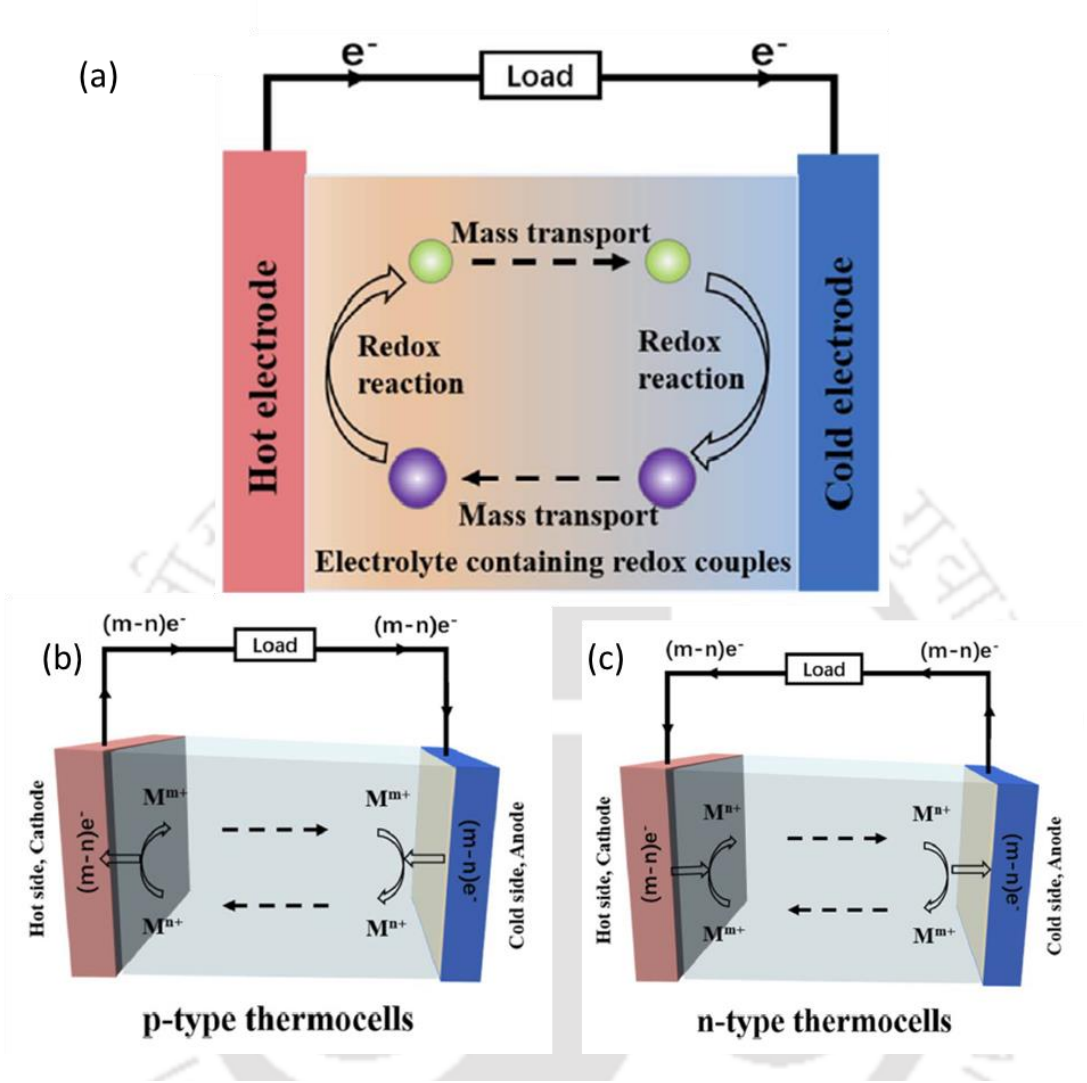

Figure 1.9: Schematic representation of (a) working principle of a thrmogalvanic cell, (b) p-type thermogalvanic cell and (c) n-type thermogalvanic cell. (Images copied from *Journal of Materials Chemistry A*, 10(39), pp.20730-20755.)

In a completely different system, thermal energy can be converted into electrical energy by integrating a redox couple, commonly referred to as a thermogalvanic cell.[80] The basic working principle behind the conversion method is fundamentally based on reversible redox reactions at the hot and cold electrodes and the diffusion of redox couple along with the electrolyte through convection. Figure 1.9a is the general representation of a thermogalvanic cell that encompasses an electrolyte with an active redox couple and two electrodes. The temperature

gradient induced voltage is developed by the entropy enhancing reaction on the hot side and entropy reducing reaction on the cold side. It is important to mention that, there are only a limited number of redox pairs that exhibited reversible redox behaviour under a temperature gradient. Based on the overall potential developed across the two electrodes, a thermogalvanic cell is categorised as p-type ($\frac{V_{hot}-V_{cold}}{T_{hot}-T_{cold}} < 0$) and n-type ($\frac{V_{hot}-V_{cold}}{T_{hot}-T_{cold}} > 0$) and schematically it is represented in Figure 1.9b and c. In general, inside a p-type thermocell, oxidation occurs across the hot electrode developing a negative potential while inside an n-type thermocell, reduction occurs across the hot electrode resulting a positive potential. For example, some elaborately studied p-type redox couples includes $Fe(CN)_6]^{4-}/[Fe(CN)_6]^{3-}$, $[FeBr_4]^{2}/[FeBr_4]^{-}$, and $[FeCl_4]^{2-}/[FeCl_4]^{-}$ and n-type redox couples includes $Co(bpy)_3]^{3+}/[Co(bpy)_3]^{2+}$, Fe^{3+}/Fe^{2+}, Zn^{2+}/Zn, Cu^{2+}/Cu, and I^{-}/I_3^{-}.[80]

Similar to the e-TE materials the performance of a thermogalvanic cell can be assessed through the Seebeck coefficient, which is primarily determined by the entropy disparity within the redox couple and the quantity of electrons participating in the redox reaction. For instance, the Seebeck coefficient can be expressed as:

$$S_e = \frac{\partial V}{\partial T} = \frac{\Delta S}{nF} = \frac{(S_B + \hat{S}_B) - (S_A + \hat{S}_A) - n\bar{S}_e}{nF} \quad \text{----------(5)}$$

Here, n denotes the quantity of electrons engaged in the reaction, F stands for the Faraday constant, A and B signify the oxidized and reduced species, respectively. The partial molar entropies and the Eastman entropies are represented by S_A, S_B and $\hat{S}_A$, $\hat{S}_B$ respectively. The Eastman entropy is associated with the interaction among the ions with their solvated shell within the solution. However, its significance is minimal when compared to the magnitudes of S_A and S_B. The residual term $\bar{S}_e$ denotes the entropy associated with electrons being conveyed

in the external circuit and the magnitude is in the range of ~ μVK^{-1}, therefore, can be easily disregarded. Therefore, the final equation will have the expression of:

$$S_e = \frac{\partial V}{\partial T} = \frac{\Delta S}{nF} = \frac{(S_B)-(S_A)}{nF} \quad \text{----------(6)}$$

Optimization:

The performance of a thermogalvanic cell can be optimized using the parameters such as choosing suitable electrolyte in thermocell, modifying electrode materials and incorporating separators or membranes.

Choice of electrolyte:

Most of the electrolytes that has been studied in the realm of thermocell can be categorised either as aqueous electrolytes, ionic liquids or quasi-solid state electrolytes. As the entropy of a thermocell is directly related to the entropy difference of redox species (equation 6), their interaction with the electrolyte is crucial. For example, most redox couples with complex structures exhibit a larger Seebeck coefficient (S_e) than those with simple structures. In another study, the Seebeck coefficient was enhanced from 1.43 mVK^{-1} to 2.9 mVK^{-1} by simply mixing methanol with the aqueous mixture of $[Fe(CN)_6]^{4-}$/ $[Fe(CN)_6]^{3-}$ due to the restructuring of solvation shell within the electrolyte environment.[81] The concentration gradient of the redox species (ΔC) across the two electrodes further determines the change of S_e within an electrolyte. One perfect example of a system contributing to both ΔS and ΔC was studied by the group of Boyang Yu et al. In this study, an aqueous system of $[Fe(CN)_6]^{4-}$/ $[Fe(CN)_6]^{3-}$ was analysed with the addition of guanidinium cations (Gdm^+).[82] The UV-vis study of this composition confirms the enhancement of entropy difference in the system after the addition of Gdm^+. This is evident from the shift in the peak position of $[Fe(CN)_6]^{4-}$ upon the addition of Gdm+, while the position of $[Fe(CN)_6]^{3-}$ remained the same. The concentration gradient (ΔC) originated from

the crystallisation and precipitation of $[Fe(CN)_6]^{4-}$ towards the cold side of the thermocell in the presence of Gdm^+ and redissolution towards the hot side. These factors simultaneously contribute to the overall improvement of S_e from 1.4 mVK^{-1} to 3.73 mVK^{-1}.

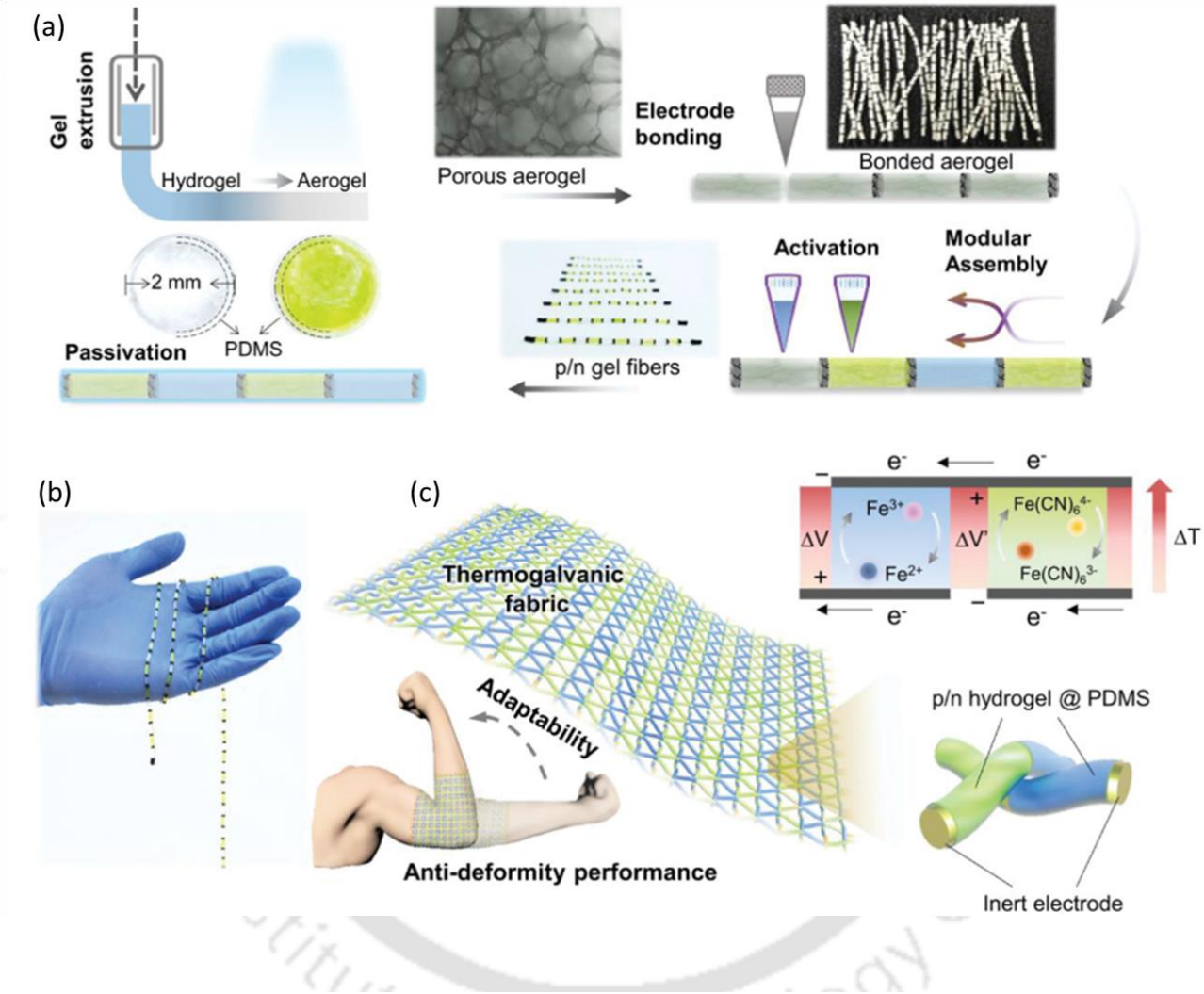

Figure 1.10: (a) Schematic representation of the fabrication process with the alteration of p and n type thermocells. (b) Digital photograph of the hydrogel fibre with the length of 1 m. (c) Thermogalvanic fabric woven out of hydrogel based fibres. (Images copied from *Advanced Energy Materials*, 11(44), p.2102219.)

Apart from the aqueous electrolytes, different classes of ionic liquids have been extensively studied due to their advantages, such as high-temperature tolerance, reasonably lower thermal conductivity, high ionic conductivity and non-inflammability. Some of the examples include the work by Katayama et al. with the redox couple of $[Fe(CN)_6]^{4-}$/ $[Fe(CN)_6]^{3-}$ within the ionic

liquid 1-butyl-1-methylpyrrolidinium bis(tri-fluoromethylsulfonyl)amide (BMPTFSA) (S_e = -1.49 mVK^{-1}).[83] Similarly, the combination of $[Co(bpy)_3]^{3+}/[Co(bpy)_3]^{2+}$ as a redox couple within different ionic liquids $[C_2mim][NTf_2]$, $[C_4mpyr][NTf_2]$, $[C_2mim][B(CN)_4]$, and [C2mim][eFAP] improves the Seebeck coefficient from 1.5–2.2 mV K^{-1}.[84] The remaining form of electrolyte, i.e. quasi solid state electrolyte, is known for its higher flexibility and lower thermal conductivity, allowing the fabrication of wearable devices. For example, in one of the recent work, a flexible thermocell was fabricated out of polyacrylamide hydrogel with the addition of polydimethylsiloxane (PDMS)/carbon nanotube (CNT) composites as shown in Figure 1.10.[85] The entire thermocell can be structured in rope-like forms that can efficiently transforming body heat into valuable energy.

Modification of electrode materials:

Unlike the electronic thermoelectric (e-TE) material, a thermogalvanic cell is dependent on the redox reactions involved on the hotter and colder sides. Therefore, the nature of the electrodes incorporated in a thermocell has an important role. These popularly known electrodes are mostly based on carbon, conductive polymer, and metal-based materials. They are chosen according to their high surface area and catalytic activities. Carbon-based materials offer a high specific surface area and fast redox electron transport, improving the overall efficiency of a thermogalvanic cell. For example, when multiwalled carbon nanotubes (MWCNTs) with a high specific surface area of 278 m^2g^{-1} and high conductivity of 100 Scm^{-1} were incorporated in a thermocell, the overall efficiency was found to improve as compared to the traditional Pt foils with a current density of 55.7 Am^{-2} and a voltage output of 70.4 mV under a temperature gradient of 60 K.[86] There are some other reported literature based on the flexible carbon materials as electrodes for wearable devices that can effectively utilise the body heat in cold weather environments.

The other form of electrodes is composed of conductive polymers, recognised for their flexibility in modifications, ease of fabrication using printing techniques, and resistance to the formation of insulating layers, unlike the oxide layers found on the surface of metal electrodes. As an illustrative example, the conductive polymer PEDOT was previously studied as an electrode in the form of a film with the ionic liquid $[C_2\,mim][B(CN)_4]$ as an electrolyte and $Co^n(bpy)_3(NTf_2)_n$ as the redox couple. Further elaborate studies were carried out by Crispin *et al.* through the deposition of poly(3,4-ethylenedioxythiophene)-tosylate (PEDOT–Tos) onto an insulator along with the variation of electrode thickness and its performance related to it.[87] The final form of electrodes are pure metal-based materials such as Cu, Ni, Pt, W, etc., and their properties primarily depend on the redox behaviour at different electrolyte environments. These metal electrodes have been studied elaborately with different electrolytes and redox couples. However, the device's performance is significantly influenced by the carefully designed pore size, thickness, and morphology of the electrodes. Optimising micro- and electronic structures through different engineering strategies, such as vacancy creation via elemental doping, phase and interlayer engineering, and heterostructure construction, can further enhance the output power density. All of the above-mentioned strategies are based on two similar electrodes. However, the impact of dissimilar electrodes remains unexplored, holding significant potential for future research.

Addition of a Separators:

The performance of a thermogalvanic cell can be additionally optimised through the integration of a separator, thereby maintaining a definite amount of temperature and concentration gradient for a sufficiently elongated period. In the works performed by MacFarlane et al., polyvinylidene fluoride (PVDF) membrane was incorporated as a separator with the redox couple of I^-/I_3^- in an aqueous solution.[88] This modification within the thermocell has significantly reduced the heat dissipation around the electrodes, eventually improving the open

circuit voltage from 1.3 mV to 2.8 mV under the temperature gradient of 12 K. Similar observations were reported by Zhang et al. with the separator of PVDF and Fe^{3+}/Fe^{2+} based PVA-gel where the Seebeck coefficient was effectively improved from 0.58 mVK^{-1} to 0.79 mVK^{-1}.[89] The thermal conductivity was reduced from 1.22 $Wm^{-1}K^{-1}$ to 0.93 $Wm^{-1}K^{-1}$. However, as compared to the number of studies related to the electrolyte and the electrode materials, the separator-based studies are very limited.

Thermogalvanic cells are quite effective for directly converting low-grade waste heat into electricity. However, the constrained variety of naturally occurring redox couples suitable for reversible redox reactions restricts their broader applications. Additionally, this approach of energy conversion involves redox chemistry, which accelerates the degradation of the electrode materials and, therefore, has a definite lifetime. Other factors limit its broader applicability, such as lower Seebeck coefficient, leakage and packaging issues of the electrolytes, and limited availability of high-temperature stable electrode and electrolyte materials. There is a final approach for direct conversion of heat into electricity known as thermodiffusion, details of which are discussed below.

1.5.2.2. Thermodiffusion:

Other than the electronic thermoelectricity (electrons and holes are the charge carriers) and thermogalvanic cell, the temperature gradient-induced thermovoltages can be generated from the thermodiffusion of cations and anions in an aqueous solution. Here, the Seebeck coefficient or the ionic thermopower is calculated from the ratio of temperature-induced thermovoltage with the temperature gradient across the electrolyte (equation 1). In previous studies, the Seebeck coefficients were measured to be within the 0.1-1 mVK^{-1} range with diverse aqueous salt solutions. However, with the ongoing research on different electronic materials, polyelectrolytes, ionic liquids, and organic polymer-based materials, the Seebeck coefficient

has been improved to several orders of magnitudes. The following sections provide detailed insights into the origin of the thermodiffusion effect, the progressive evolution of this approach leading to advanced ionic thermoelectric materials, the integration of this effect with redox couples, a transition to two-dimensional materials, and a discussion on areas requiring improvement for future advancements.

Soret effect and its relation with ionic thermoelectricity:

Subjecting a fluid comprising multiple atomic or molecular species to a temperature gradient leads to a non-uniform composition. This observation was initially studied by Soret in the 19th century and is known as the Soret effect.[90] In other words, under a steady state condition of net zero current, when a temperature gradient is subjected within a salt solution inside a tube with concentration c, there will be a concentration gradient of Δc:

$$\Delta c = -c\, S_T \Delta T \quad \text{----------(7)}$$

S_T is known as the Soret coefficient, which could be either positive or negative based on the diffusion of solute particles. In a classical thermodynamic system, the Soret coefficient is related to the "heat of transport" Q^*:

$$S_T = \frac{Q^*}{k_B T^2} \quad \text{----------(8)}$$

Now, using the Born model that was proposed in the year 1920, the Seebeck coefficient (S) can be defined as:

$$S = \frac{Q^*}{N_A |q| T} \quad \text{----------(9)}$$

In the above equation, N_A represents the Avogadro's constant and q represents the unit ion charge. Further, this equation is suitable only to represent single molecular or atomic species. In the presence of dual ion electrolytes, the equation 9 can be modified into:

$$S = \frac{w_+ Q_+^* - w_- Q_-^*}{eT} \quad \text{----------(10)}$$

Here, Q_+^* and Q_-^* represents the heat of transport of individual cations and anions respectively and $w_\pm = n_\pm / (n_+ + n_-)$ represents the weight factor. The term Q^*/T appearing in the equation 9 represents the Eastman entropy and is defined as the combination of both transport and partial molar entropy. Therefore, much larger Seebeck coefficients (S) observed in most of the ionic thermoelectric systems can be attributed to the difference between the electronic Eastman entropy and that of ionic Eastman entropy.

Therefore, all of the mathematical formulations mentioned above delineate the diffusion of atomic, molecular or ionic entities propelled by Eastman entropy, commonly recognised as the Soret effect, occurring under the influence of a temperature gradient. Establishing a concentration gradient among the ionic entities (cations and anions) between the hotter and cooler sides generates a distinct voltage, quantified by the Seebeck coefficient. This phenomenon is commonly referred to as ionic thermoelectricity. The intricate development of this emerging field is thoroughly explored in the subsequent sections.

Emerging materials for ionic thermoelectricity:

Similar to the Seebeck effect in e-TE materials, the Soret effect contributes to the concentration gradient of ionic species in a temperature non-equilibrium system as shown in schematic of Figure 1.11a. Considering equation 10, if the thermodiffusion is restricted to only specified ions (either cations or anions), the contribution to the Seebeck coefficient experiences a significant increase. Conversely, if the contribution from Q^* is comparable for both cations and anions, the thermovoltage will drop to zero. Therefore, when exposed to a specific temperature gradient, the approach is to design an ionic thermoelectric (i-TE) material with a substantial mobility contrast between oppositely charged ions. An ideal i-TE material would be one that will facilitate the selective diffusion of only one type of ion (either cation or anion)

while the other remains stationary in its initial position. Different classes of materials have been explored in searching for an ideal i-TE material, including asymmetric polyelectrolytes, polyelectrolytes with conducting polymers, ionic liquids, different hybrid materials and materials with ionic confinements.

The i-TE material, similar to the e-TE material, can be categorised into p-type and n-type based on the majority charge carriers of cations and anions, respectively. The findings of both p-type and n-type materials hold significant importance in developing ionic thermopiles, enabling the efficient conversion of waste heat into electricity. However, the i-TE materials with n-type characteristics are very limited in the existing literature, highlighting the necessity for extensive efforts in future advancements in this field.

So far, optimising an ionic thermoelectric (i-TE) material performance relies on the steady-state Seebeck coefficients involving the slopes related to different saturated stable thermovoltages with the applied temperature gradients. The device fabrication procedure could be both vertical or horizontal depending on the material's properties, as shown in Figure 1.11b and c. In brief, as shown in Figure 1.11b, in a vertically oriented setup, the i-TE material is sandwiched between two electrodes that are directly connected with the heat source towards one side and the heat sink towards the other (mostly Peltier devices). The temperature gradient across the two electrodes is measured using thermocouples along with the thermovoltages with different measuring instruments. In a horizontally oriented setup (Figure 1.11c), both the i-TE material and electrodes are placed on a stage made of two Peltier devices serving as a heat source and heat sink, and the voltage is measured across the temperature gradient. Comprehending the factors influencing optimisation, various classes of iTE materials have arisen, and these will be explored in the following sections.

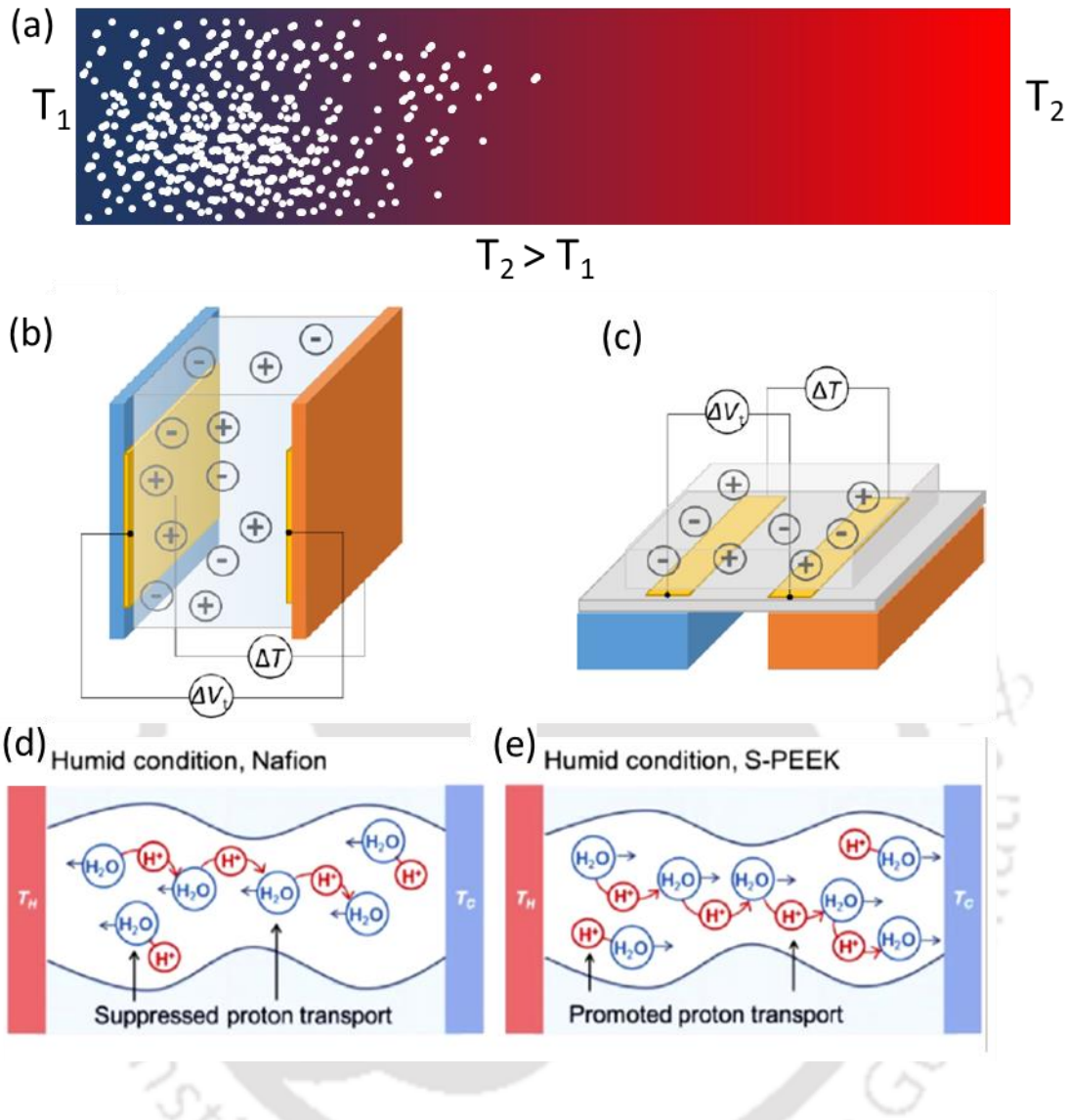

Figure 1.11: (a) Schematic illustration to represent the generation of concentration gradient of ions or molecules under a temperature gradient. Schematic representation of two different orientation of the experimental setup (b) vertical structure and (c) horizontal structure. Schematic representation of the thermodiffusion of the ions and the water molecules (d) in the opposite direction (example: nafion), (e) in the same direction (example: S-PEEK) (Images copied from (d)-(e) *Organic Electronics*, 54, pp.231-236.)

Polyelectrolytes:

Polyelectrolytes are ideal candidates for thermodiffusion of ions as only one type of ion is affixed to the immobile surface of its opposite counterpart. Various polyelectrolytes have been elaborately studied till now in this field of ionic thermoelectricity, and the initial work was

studied by Chang et al. with the polyelectrolyte of Nafion-Ag and PSS-Ag.[91] The performance of these polyelectrolytes is dependent on the relative humidity (RH) level as water molecules absorbed by the polyelectrolytes build a percolated path for ionic diffusion. Later, elaborate studies were carried out by Kim et al. with the polyelectrolytes Nafion, S-PEEK and poly(diallyldimethylammonium chloride) (PDDAc).[92] The observation was that, at higher humidity, the water molecules diffused along with the solvated ions (with S-PEEK) (Figure 1.11e) or opposite to the diffused ions (Nafion), as shown in Figure 1.11d. However, the Seebeck coefficient associated with the PDDAc polyelectrolyte was attributed to the disparity in water absorption capacity of the polyelectrolyte between the hot and cold sides, leading to differences in the dissociation of Cl^- ions. In a recent study, the i-TE property of poly(4-styrenesulfonic acid)(PSSH) was reanalysed with the addition of graphene oxide (GO) nanosheets. An upward shift from 7.9 mVK^{-1} to 12.6 mVK^{-1} was observed after the modification due to the lubricating influence of the GO nanosheets facilitating the diffusion of water molecules and, consequently enhancing the mobility of protons.[93]

The water molecules in these polyelectrolytes greatly influence the i-TE properties, restricting their applicability to humid environments exclusively. Furthermore, utilising these polyelectrolytes in high-temperature applications would be impractical, as these materials are susceptible to losing water molecules through evaporation at elevated temperatures, resulting in a significant decline in their performance. However, considering room temperature applications and high humid conditions, polyelectrolyte materials can perform well in the realm of ionic thermoelectricity.

Ionic liquids:

Unlike polyelectrolyte-based systems which are water-based, ionic liquids are organic salts that exist in a liquid state at near room temperature; therefore, both the cations and anions are

mobile. Here, Instead, the i-TE effect arises due to the mobility difference of cations and anions, the komsotropic effect, and ion-electrode interaction and cation-anion interactions. The initial studies were carried out by Bonetti et al. in 2011, followed by numerous subsequent works afterwards.[94] In the year 2019, Zhao et al. reported a work related to quasi-solid state ionic liquid polymer gel composed of poly(hexafluoropropylene) (HFP), poly(vinylidene fluoride) (PVDF) and the ionic liquid [EMIM][TFSI].[95] Interestingly, adding polyethylene glycol (PEG) has altered the Seebeck coefficient from -4 mVK^{-1} to +14 mVK^{-1} by changing the interaction between the ionic liquid and the polymer matrix. This work has even demonstrated the combination of 18 pairs of p and n-types legs through printing that enhances the overall Seebeck coefficient upto 333 mVK^{-1}. In a recent work, Yongjie et al. has successfully improvised the ionic Seebeck coefficient (32.7 mVK^{-1}) of carbonized pomelo peel (CPP) filled with BMIM:Cl through ion-electron coupling.[96]

As ionic liquids do not rely on water, their effectiveness in high-temperature and prolonged operations makes them viable candidates for use as i-TE materials. Additionally, through the fine-tuning of ion-polymer interactions, the majority of charge carriers can be altered from p-type to n-type or vice versa. However, the high cost of the ionic liquids limits its broader applicability. Furthermore, the ionic conductivity of ionic liquid-based systems is at least two-thirds lower in magnitude compared to systems based on conventional polyelectrolytes.

Hybrid systems:

The careful studies of the interactions among active ions and the surrounding environments can greatly improve the efficiency of i-TE materials in hybrid systems. For instance, Zhao et al. have reported a work related to water-free polyelectrolytes with the combination of NaOH and polyethene oxide (PEO).[97,98] The Seebeck coefficient was observed to be ~11 mVK^{-1} and cannot be explained through the heat of transport of Na^+ and OH^- ions. In the end, through

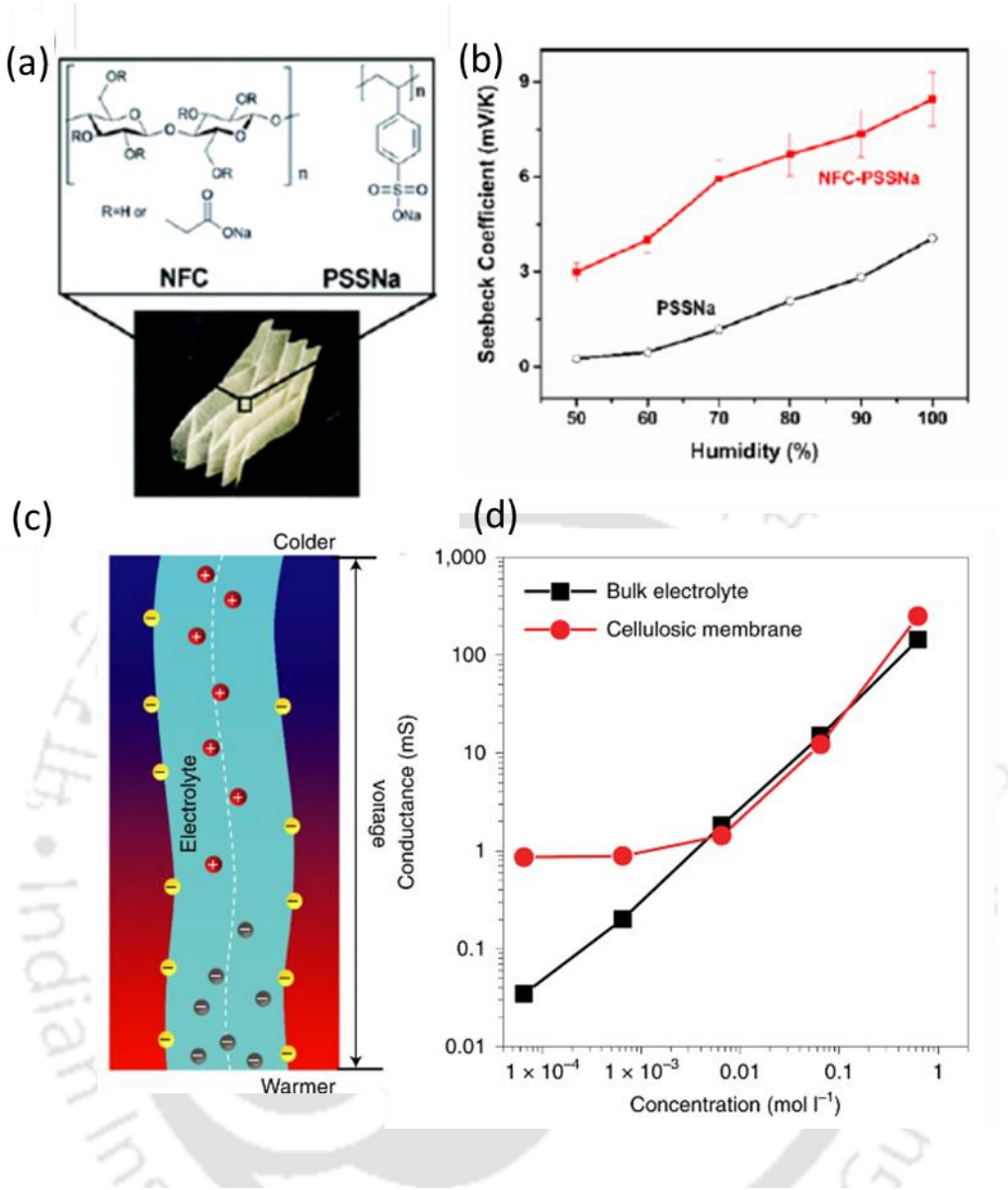

Figure 1.12: (a) Digital photograph to represent the flexibility of NFC-PSSNa paper and the chemical structure of the nanofibrillated cellulose (NFC) and polystyrene sulfonate sodium (PSSNa). (b) Comparison of the Seebeck coefficients of PSSNa with NFC-PSSNa at different relative humidity. (c) Schematic representation illustrating the configuration of the ionic device following the infusion of electrolyte into the nanofluidic cellulosic membrane. When subjected to a temperature gradient, the surface-charged nanofibers govern the movement of ions through nanofluidic effects, resulting from the combined impact of strong confinement and the charged boundaries of the cellulose nanochannels. (d) The surface charge governed ionic conductivity plot of cellulosic membrane. (Images copied from (a)-(b) *Journal of materials chemistry A*, 5(32), pp.16883-16888. (c)-(d) *Nature materials*, 18(6), pp.608-613.)

chemical analysis, they concluded the formation of polyanions due to PEO deprotonation, which eventually generated large thermovoltages. In another work, the improvement of the i-

TE performance of PSSNa was observed by simply integrating the same with nanofibrillated cellulose (NFC), particularly at lower humidity levels, as shown in Figure 1.12a and b and is attributed to the better water retention capacity of NFC, which enables the formation of percolation path along the fibres.[99] The hybrid materials offer additional benefits, including exceptional stretchability and flexibility, high tensile strength, robustness, and, in some cases, a self-healing capability. A work with similar properties was presented by Zico Alaia Akbar et al. with the composition of polyaniline, poly(2-acrylamido-2-methyl-1-propanesulfonic acid) and phytic acid. This composite polymer exhibits remarkable stretchability, reaching approximately 750%, and a self-healable nature.[100,101] This polymer further demonstrates the outstanding recoverability from deformation (50% strain) with a Seebeck coefficient of 8.1 mVK^{-1} from the diffusion of protons and an ionic power factor of 1.6 $mWm^{-1}K^{-1}$. The interaction among the active ionic species and the electrodes can also determine the direction of the Seebeck coefficient (n-type or p-type). Such an example was reported by Cheng et al. with the polymer composite of poly(vinylidene fluoride-co-hexafluoropropylene) (PVDF-HFP), propylene carbonate and sodium trifluoromethanesulfonimide (NaTFSI). With this composite polymer the thermovoltages were reported with Cu and a-CNT electrodes. The distinct interactions of the active ions Na^+ and $TFSI^-$ with Cu and a-CNT electrodes eventually generate a wide range of thermopower ranging from 20.2 mVK^{-1} to 10.2 mVK^{-1}.[102]

The performance of an i-TE system can be further enhanced by integrating a redox couple into a thermodiffusion process. Within this hybrid system, both the thermogalvanic and thermodiffusion processes occur simultaneously. One such example was reported by Cheng-Gong Han et al. with a gelatin polymer matrix with additional ion providers KCl and a redox couple of [$Fe(CN)_6^{4-}/Fe(CN)_6^{3-}$]. A Seebeck coefficient of 4.8 mVK^{-1} was observed solely from the thermogalvanic effect, while the thermodiffusion of KCl yielded a Seebeck coefficient of 6.7 mVK^{-1}. When these thermodiffusion and thermogalvanic effects were combined, the

Seebeck coefficient was elevated to 17 mVK^{-1}.[103] In a similar work, Ziquan Zhou has incorporated Li_2SO_4 and the same redox couple with the double network gel of polyacrylamide (PAM) and carboxymethyl cellulose (CMC).[104] Here as well, the individual effect of thermodiffusion and thermogalvanic developed Seebeck coefficient of 2.91 and 3.63 $mVK^{-1,}$ respectively, and the combined effect of these two upraised it to 11.58 mVK^{-1}. There are numerous other studies dealing with the synergistic combination of these two effects that clearly describe the potential for advanced futuristic applications.

Shift towards the nanoconfinement:

The theoretical and experimental understanding of the nanoconfinements illuminated avenues for diverse energy harvesting approaches. Yet, within the realm of ionic thermoelectricity, a noticeable gap exists in the exploration and understanding of this field. There are a handful of theoretical studies exploring the nanoconfinement effect that significantly enhances the thermopower of thermoelectric materials. The improved thermoelectric properties were theoretically elucidated by considering the coupling of ion steric effects in the electrical double layer (EDL), along with the formation of a surface charge density gradient under a temperature gradient that leads to an increase in electrophoretic ionic mobility compared to classical thermophoretic mobility.[105] Xin Qian et al. further studied the confinement effect by solving the Poisson-Nernst-Plank equation with the addition of the perturbation method.[106] The collective insights from these theoretical studies contribute to a better understanding of the positive implications of introducing confinements, which will be instrumental in developing confined ionic thermoelectric materials.

Similar to the theoretical investigations, scarcity can also be observed in the experimental studies on the confinement effect. One example was reported by Tian Li et al. with the one-dimensional confinement of cellulosic membrane.[107] The surface-charged governed ionic

conductivity plot shown in Figure 1.12c and d confirmed the presence of confinements. This system's active component comprised the previously reported composite mixture of NaOH and PEO. However, the application involved the infiltration of this mixture into the cellulosic membrane. This slight modification of nanoconfinement inclusion has improved the Seebeck coefficient up to 24 mVK^{-1} through the selective diffusion of Na^{+} ions. Guodong et al. have fabricated an ionic hydrogel through the confinement of ionic liquid [EMIm][DCA] inside the functionalised biopolymer.[108] The confinement has improved the ionic conductivity up to 79 $mScm^{-1}$ with the maximum Seebeck coefficient of 11.55 mVK^{-1}. However, the experimental understanding is limited to only these two individual works. Considering their availability, cost-effectiveness, and ease of fabrication, 2D self-standing lamellar restacking membranes could be ideal candidates for nanoconfinement-based ionic thermoelectric systems.

1.6. Moisture-enabled electricity generator (MEG):

In pursuing sustainable and innovative energy solutions, harnessing ambient environmental factors has emerged as a promising frontier. Among these, moisture-enabled electricity generation stands out as a captivating avenue due to the ubiquitous presence of moisture in the atmosphere.[109] The journey started in 2001, with the idea that electricity could be generated by passing flowing water through carbon nanotubes.[110] However, it took numerous efforts to enhance the output voltage from few microvolts to 1V.[111,112] Now in the following sections, as we explore the mechanisms, materials, and applications behind moisture-enabled electricity generation, we embark on a journey towards environmentally friendly energy solutions that harness the natural resources surrounding us.

1.6.1. The basic principle of MEGs:

Depending on the ion diffusion technique, a MEG fundamentally can be fabricated with a pair of electrodes and a hygroscopic material with different surface functional groups (-COOH, -

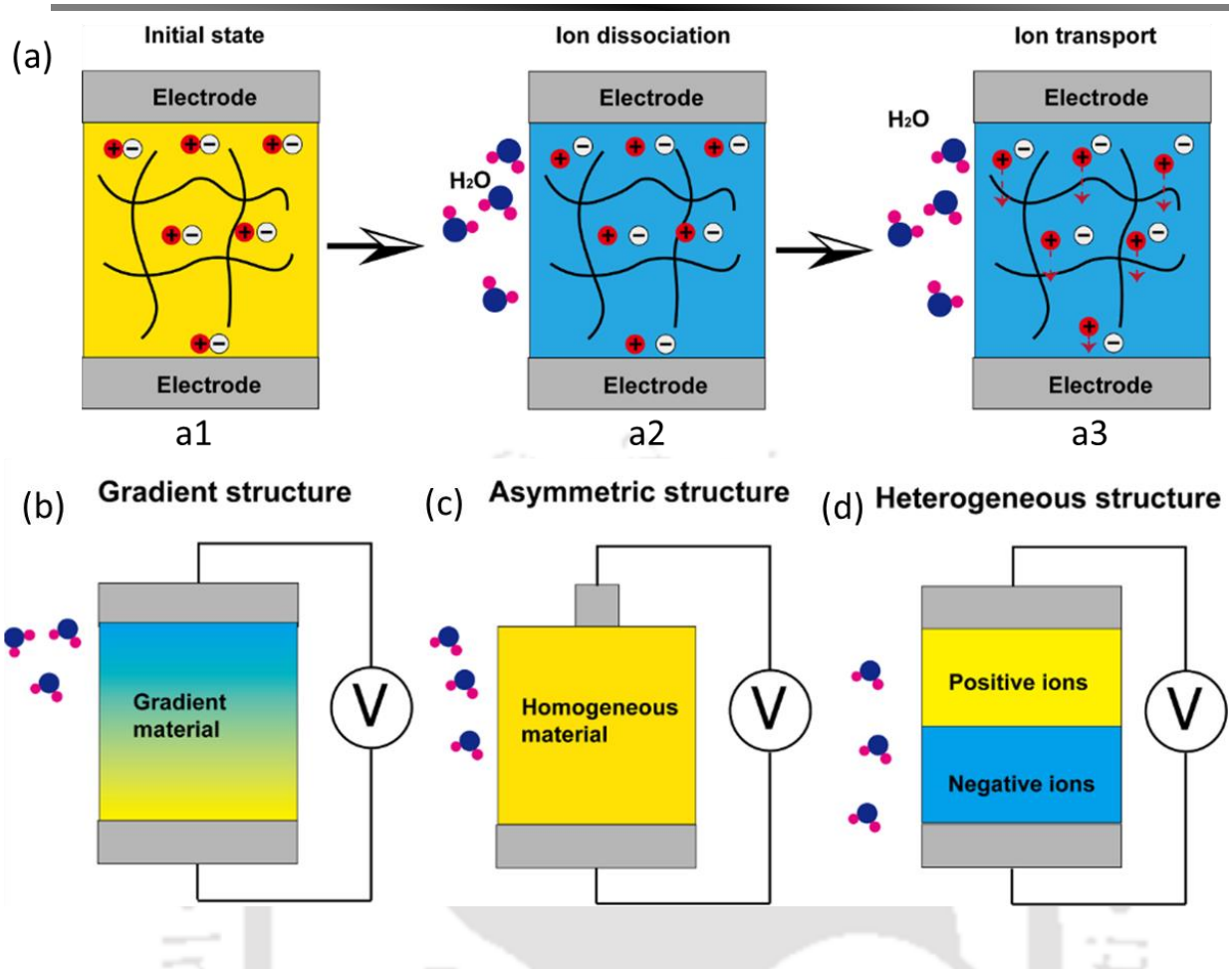

Figure 1.13: (a) Schematic representation showing the generation of electricity from moisture utilizing a gradient based material. Schematic of three different types of MEG (b) material with a gradient structure, (c) homogeneous material with an asymmetric structure and (d) heterogeneous structure with two contrasting materials. (Images copied from *EScience*, 2(1), pp.32-46)

OH, -SO_3H, etc.) shown in Figure 1.13a. At its core, the energy generation process begins with the absorption of water molecules from the atmosphere by the integrated hygroscopic material. This initial step triggers the dissociation of functional groups, releasing mobile cations and anions. Subsequently, the diffusion of these ions occurs, driven by the uneven distribution of moisture, material asymmetry, or the heterogeneous structure of the material that eventually leads to the generation of an electrical field across the gradient (Figure 1.13a).[113] By comprehending this operational principle, three distinct fabrication techniques for Moist-Electric Generation (MEG) have been devised that include a gradient material with similar

electrodes (Figure 1.13b), homogeneous material with asymmetric structure (Figure 1.13c) and a heterogeneous structure integrating two oppositely charged materials (Figure 1.13d).

1.6.2. Gradient Material:

A material with a gradient structure results from the uneven distribution of surface functional groups, eventually creating a gradient of dissociated mobile ions in the presence of atmospheric water molecules.[114] Qu et al. carried out the initial studies using the gradient structure of graphene oxide (GO) film.[115] The inhomogeneous distribution of oxygen-containing groups across the film developed a moisture-induced voltage of ~35 mV with a power density of 4.2 mWm^{-2}. Following the successful fabrication of MEG, several modifications have been implemented involving GO structures, including 3D assembly of GO, enhancing the power density to 1 $mWcm^{-2}$.[116] Additionally, the directional reduction of GO foam has been employed to elevate the voltage output to 450 mV[117], and a composite mixture of porous GO and sodium polyacrylate has been utilised, resulting in a voltage output of 600 mV.[118] In another work, ~275 mV of voltage and 7.6 µA cm^{-2} of current density were recorded from the asymmetric distribution of citric acid inside an A4 printer paper.[119] The energy conversion process was propelled by the self-sustained ionic gradient established within the paper through inhomogeneous ionisation of organic acids. This fabrication process further allows for developing flexible, self-powered wearable sensors. Lianhui et al. fabricated one such device through a gradient distribution of hydroxyl groups with a porous polydopamine layer.[120] The asymmetric distribution of the mobile H^+ ions across the layer eventually developed an output voltage of 0.52 V and a power density of 0.246 $mWcm^{-2}$.

Although the asymmetric distribution of active components can yield a reasonable amount of energy, fabricating such gradient structures is often complex, limiting their widespread applications.[113] Additionally, many Moist-Electric Generators (MEGs) with higher

performance exhibit transient responses, requiring continuous pulses of external moisture for optimal performance. Consequently, exploring alternative designs for MEGs becomes crucial, as discussed below.

1.6.3. Asymmetric structure:

In this fabrication process, a homogeneous material is integrated with a pair of asymmetric electrodes. In other words, one of the electrodes can either function as an active electrode, releasing mobile ions or facilitating moisture contact with the hydrogel, resulting in an uneven water distribution within the hydrogel. Once the atmospheric water molecules come in contact with the hydrogel, it starts releasing the mobile ions from the surface functional groups that diffuse with the water molecules towards the other side of the electrode, eventually generating voltages and currents. For example, in a work demonstrated by Tong Xu et al., the active material poly(4-styrene sulfonic acid) (PSSA) was sandwiched between two gold electrodes.[121] The top electrode was constructed with perforations, enabling direct exposure of external moisture to the active PSSA membrane. This exposure led to the generation of mobile cations at the upper section, gradually diffusing towards the lower portion of the electrode over time. This experimental arrangement has generated a voltage output of ~0.8 V with a current density of ~0.1 mA cm^{-2}. The performance of the PSSA membrane was further improved by creating a composite of PSSA with polyacrylonitrile (PAN) and integrating it with an Al electrode.[122] The Al electrode is responsible for the generation of Al^{3+} ions when reacts with the H^+ ions of PSSA, therefore maintaining a higher concentration gradient of cation across the MEG material, eventually generating a voltage output of 1.1 V. Similar to this work, Liangti Qu et al. have utilised ZnO as an active electrode on the top of GO.[123] The ZnO molecules actively dissociate water molecules into H^+ and OH^- ions, followed by the chemisorption of the ion on the surface. The second layer of the water molecules is physically adsorbed with the preceding layer of water molecules while the chemisorbed OH^- ions promote dissociation of the water

molecules into H_3O^+ ions that eventually form a built-in potential across the ZnO and GO layer, forming a potential difference of ~400 mV.

1.6.4. Heterogeneous structure:

The final type of Moist-Electric Generator (MEG) comprises two layers of contrast surface properties generating mobile cations in one layer and mobile anions in its counterpart. The opposite nature of these mobile ions is responsible for generating electric potential and current flow. Although this class of bilayer moist electric generators (BMEG) are superior in terms of simplicity and flexibility of fabrication process comprising various ways of integrating the active components, adaptability in various applications, consistency in the generation of mobile ions ensuring a more reliable and stable output, there are only handful of works have been reported so far. For example, the Qu group has fabricated a BMEG composed of a polycation layer (polydiallyl dimethyl ammonium chloride, PDDA) integrating with a polyanion layer (composite mixture of polystyrene sulfonic acid and polyvinyl alcohol).[124] A single BMEG device is capable of producing 1.38 V at 85 % RH originated from the heterogeneous distribution of H^+ ions in the polyanion layer and Cl^- ions in the polycation layer (Figure 1.14a). The voltage output was further enhanced to 1000 V by combining multiple devices. Similarly, a BMEG was fabricated from natural wood with aligned nanochannels.[125] The anion layer of the wood was prepared through delignification followed by a carboxylation process introducing several functional groups (Figure 1.14b and c). Correspondingly, the cation layer was fabricated through the quaternisation process after delignification, introducing quaternary ammonium groups inside the nanochannels. Upon the amalgamation of these two layers containing cations and anions, an output voltage of ~0.57 V was observed, accompanied by a volumetric power density of 0.71 μW cm^{-3}. Combining two hydrogel layers with opposite surface charges, 0.36 $nW.cm^{-2}$ of power density can be generated for nearly 40 hours.[126] Poly

(sodium4-styrene sulfonate) (PAAS) was chosen as the active component for the polyanionic part generating mobile Na^+ ions, and 3-acrylamidopropyl [trimethylammonium] chloride (DMAPAA-Q) was chosen for polycationic part generating Cl^- as a diffusive ion. These are the only reported publications related to distinct bilayers in a MEG, and they slowly emerge as

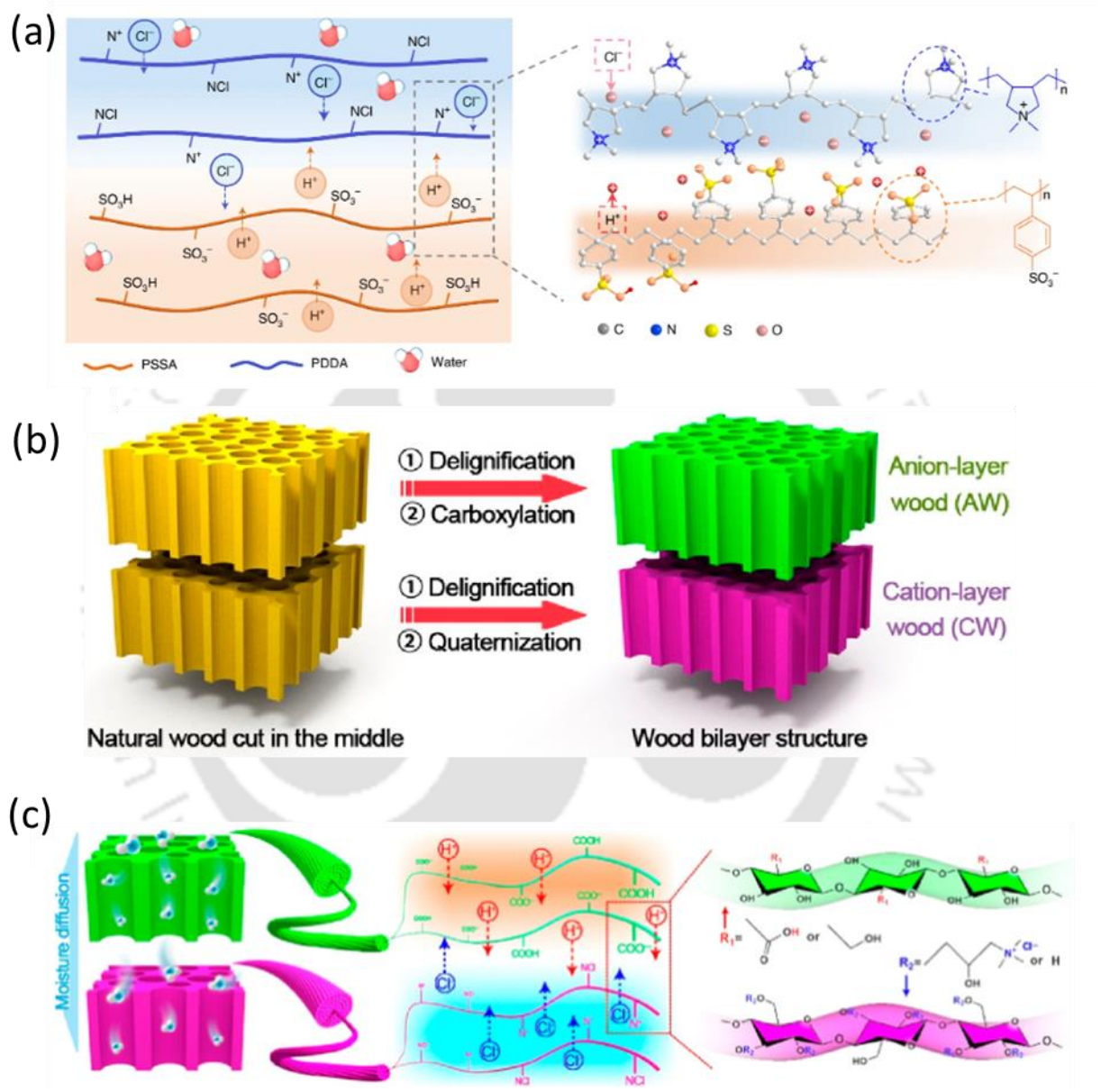

Figure 1.14: (a) Schematic representation of a BMEG composed of polystyrene sulfonic acid and polydiallyl dimethyl ammonium chloride that shows the dissociation of H^+ and Cl^- ions in the presence of atmospheric water molecules. Schematic representation of (b) the fabrication of a bilayer wood membrane and (c) the mechanism for the diffusion of dissociated ions in the presence of atmospheric water molecules. (Images copied from (a) *Nature Nanotechnology*, 16(7), pp.811-819. (b)-(c) *Nano Letters*, 22(16), pp.6476-6483.)

promising and efficient solutions, showcasing a harmonious integration of cation and anion layers that culminate in a notable output voltage and substantial volumetric power density.

1.7. Conclusion:

In conclusion, the multifaceted realm of thermoelectricity unfolds a diverse landscape of phenomena, each offering unique opportunities and challenges for advancing energy conversion technologies. Electronic thermoelectricity, governed by the Seebeck effect, stands as a foundational pillar, exploiting the intrinsic temperature dependence of charge carriers to yield electrical power. The thermogalvanic effect, rooted in electrochemical processes occurring at the electrode-electrolyte interface, provides an alternative avenue for harnessing thermal gradients. This electrochemical approach offers advantages in specific scenarios, opening avenues for innovation and efficiency. On a parallel track, ionic thermoelectricity introduces ionic species into the equation, redefining the possibilities of efficient energy conversion specifically with the ionic thermopower. The interplay between ions, electrolytes, and electrodes brings forth a distinct set of characteristics, paving the way for applications in diverse contexts, including electrochemical cells and thermoelectric devices.

In a noteworthy convergence, the combination of the thermogalvanic effect and ionic thermodiffusion in hybrid systems marks a paradigm shift. This synergistic approach capitalizes on the strengths of both phenomena, presenting opportunities for enhanced performance, adaptability, and versatility in thermoelectric applications that includes flexibility and the robustness of the material. The exploration of these hybrid systems holds promise for addressing the evolving demands of energy conversion and sustainable power generation.

As the landscape of thermoelectricity continues to evolve, researchers are propelled toward further exploration, seeking novel materials, methodologies, and synergies that will shape the future of this field. In this quest of searching, the materials with nanoconfinement effect have

found their own importance. From electronic thermoelectricity to the intricacies of ionic interactions, the journey towards more efficient, sustainable, and innovative energy conversion technologies remains vibrant and dynamic. The collaborative efforts of scientists, engineers, and researchers worldwide contribute to the collective endeavour of unlocking the full potential of thermoelectricity, ushering in an era of greener, more sustainable energy solutions.

Although this realm of energy generation from the moisture surrounding every corner of the earth is comparatively a young research field, the landscape of Moist-Electric Generators (MEG) has witnessed a truly transformative journey from material advancement to structural transformations. The integration of a gradient structure within the active hygroscopic material represents a significant breakthrough that provided a roadmap for the future improvements. Additionally, the incorporation of asymmetric electrodes has brought about a sophisticated dimension to MEG, fostering improved directional ion migration and elevating voltage outputs. The recent exploration of distinct bilayers in an MEG adds a promising chapter to this narrative, showcasing the potential of harmoniously integrated cation and anion layers, resulting in substantial voltage and volumetric power density. The amalgamation of gradient structures, asymmetric electrodes, and bilayer configurations represents a holistic and multifaceted approach, offering nuanced solutions to the challenges of energy harvesting from environmental moisture. This collective exploration propels the field toward enhanced efficiency, sustainability, and adaptability, opening new avenues for cutting-edge energy harvesting technologies that leverage the abundant and renewable resource of moisture in our surroundings.

1.8. References:

1 W. A. Deer FRS, R. A. Howie and J. Zussman, 2013.

2 S. K. Tiwari, R. K. Mishra, S. K. Ha and A. Huczko, *ChemNanoMat*, 2018, **4**, 598–620.

3 P. P. Brisebois and M. Siaj, *J. Mater. Chem. C*, 2020, **8**, 1517–1547.

4 A. W. Hull., *Phys. Rev.*, 1917, **10**, 661–696.

5 L. Liu, W. An, F. Gu, L. Cui, X. He and M. Fan, *Green Chem.*, 2023, **25**, 6149–6169.

6 B. R. Shaw, Y. Deng, F. E. Strillacci, K. A. Carrado and M. G. Fessehaie, *J. Electrochem. Soc.*, 1990, **137**, 3136.

7 A. K. Geim and K. S. Novoselov, *Nat. Mater.*, 2007, **6**, 183–191.

8 K. S. Novoselov, A. K. Geim, S. V Morozov, D. Jiang, Y. Zhang, S. V Dubonos, I. V Grigorieva and A. A. Firsov, *Science (80-.).*, 2004, **306**, 666–669.

9 G. Xin, T. Yao, H. Sun, S. M. Scott, D. Shao, G. Wang and J. Lian, *Science (80-.).*, 2015, **349**, 1083–1087.

10 M. Sang, J. Shin, K. Kim and K. J. Yu, *Nanomaterials*, 2019, 9.

11 Q. Zheng, Z. Li, J. Yang and J.-K. Kim, *Prog. Mater. Sci.*, 2014, **64**, 200–247.

12 J. Zhou, Z. Lin, H. Ren, X. Duan, I. Shakir, Y. Huang and X. Duan, *Adv. Mater.*, 2021, **33**, 2004557.

13 M. S. Stark, K. L. Kuntz, S. J. Martens and S. C. Warren, *Adv. Mater.*, 2019, **31**, 1808213.

14 Z. Li, C. Xiao and Y. Xie, *Appl. Phys. Rev.*, 2022, **9**, 11303.

15 S. Bohm, A. Ingle, H. L. M. Bohm, B. Fenech-Salerno, S. Wu and F. Torrisi, *Philos. Trans. R. Soc. A Math. Phys. Eng. Sci.*, 2021, **379**, 20200293.

16 M. G. Sumdani, M. R. Islam, A. N. A. Yahaya and S. I. Safie, *J. Nanoparticle Res.*, 2021, **23**, 253.

17 M. Yi and Z. Shen, *J. Mater. Chem. A*, 2015, **3**, 11700–11715.

18 K. E. Whitener and P. E. Sheehan, *Diam. Relat. Mater.*, 2014, **46**, 25–34.

19 Y. Hernandez, V. Nicolosi, M. Lotya, F. M. Blighe, Z. Sun, S. De, I. T. McGovern, B. Holland, M. Byrne, Y. K. Gun'Ko, J. J. Boland, P. Niraj, G. Duesberg, S. Krishnamurthy, R. Goodhue, J. Hutchison, V. Scardaci, A. C. Ferrari and J. N. Coleman, *Nat. Nanotechnol.*, 2008, **3**, 563–568.

20 R. J. Smith, P. J. King, M. Lotya, C. Wirtz, U. Khan, S. De, A. O'Neill, G. S. Duesberg, J. C. Grunlan, G. Moriarty, J. Chen, J. Wang, A. I. Minett, V. Nicolosi and J. N. Coleman, *Adv. Mater.*, 2011, **23**, 3944–3948.

21 J. N. Coleman, M. Lotya, A. O'Neill, S. D. Bergin, P. J. King, U. Khan, K. Young, A. Gaucher, S. De, R. J. Smith, I. V Shvets, S. K. Arora, G. Stanton, H.-Y. Kim, K. Lee, G. T. Kim, G. S. Duesberg, T. Hallam, J. J. Boland, J. J. Wang, J. F. Donegan, J. C. Grunlan, G. Moriarty, A. Shmeliov, R. J. Nicholls, J. M. Perkins, E. M. Grieveson, K. Theuwissen, D. W. McComb, P. D. Nellist and V. Nicolosi, *Science (80-.).*, 2011, **331**, 568–571.

22 G. Cunningham, M. Lotya, C. S. Cucinotta, S. Sanvito, S. D. Bergin, R. Menzel, M. S. P. Shaffer and J. N. Coleman, *ACS Nano*, 2012, **6**, 3468–3480.

23 Y. Yao, Z. Lin, Z. Li, X. Song, K.-S. Moon and C. Wong, *J. Mater. Chem.*, 2012, **22**,

13494–13499.

24 Y. Lin, T. V Williams and J. W. Connell, *J. Phys. Chem. Lett.*, 2010, **1**, 277–283.

25 P. May, U. Khan, J. M. Hughes and J. N. Coleman, *J. Phys. Chem. C*, 2012, **116**, 11393–11400.

26 C. Knieke, A. Berger, M. Voigt, R. N. K. Taylor, J. Röhrl and W. Peukert, *Carbon N. Y.*, 2010, **48**, 3196–3204.

27 W. Zhao, M. Fang, F. Wu, H. Wu, L. Wang and G. Chen, *J. Mater. Chem.*, 2010, **20**, 5817–5819.

28 M. A. Ibrahem, T. Lan, J. K. Huang, Y.-Y. Chen, K.-H. Wei, L.-J. Li and C. W. Chu, *RSC Adv.*, 2013, **3**, 13193–13202.

29 Y. Garcia-Basabe, L. M. Daminelli, S. G. Hernández, M. S. Cardoso, R. O. R. R. da Cunha, J. J. S. Acuña and D. R. G. Larrudé, *J. Mater. Res.*, 2023, **38**, 2958–2968.

30 C. Han, Y. Zhang, P. Gao, S. Chen, X. Liu, Y. Mi, J. Zhang, Y. Ma, W. Jiang and J. Chang, *Nano Lett.*, 2017, **17**, 7767–7772.

31 S. Bellani, F. Wang, G. Longoni, L. Najafi, R. Oropesa-Nuñez, A. E. Del Rio Castillo, M. Prato, X. Zhuang, V. Pellegrini, X. Feng and F. Bonaccorso, *Nano Lett.*, 2018, **18**, 7155–7164.

32 M. A. Islam, P. Serles, B. Kumral, P. G. Demingos, T. Qureshi, A. Meiyazhagan, A. B. Puthirath, M. S. Bin Abdullah, S. R. Faysal, P. M. Ajayan, D. Panesar, C. V. Singh and T. Filleter, *Appl. Phys. Rev.*, 2022, **9**, 41301.

33 V. León, M. Quintana, M. A. Herrero, J. L. G. Fierro, A. de la Hoz, M. Prato and E. Vázquez, *Chem. Commun.*, 2011, **47**, 10936–10938.

34 L. Liu, Z. Xiong, D. Hu, G. Wu and P. Chen, *Chem. Commun.*, 2013, **49**, 7890–7892.

35 Q. Zhang, L. Mei, X. Cao, Y. Tang and Z. Zeng, *J. Mater. Chem. A*, 2020, **8**, 15417–15444.

36 J. Zheng, H. Zhang, S. Dong, Y. Liu, C. Tai Nai, H. Suk Shin, H. Young Jeong, B. Liu and K. Ping Loh, *Nat. Commun.*, 2014, **5**, 2995.

37 P. Joensen, R. F. Frindt and S. R. Morrison, *Mater. Res. Bull.*, 1986, **21**, 457–461.

38 E. L. Crepaldi, P. C. Pavan and J. B. Valim, *Chem. Commun.*, 1999, 155–156.

39 R. Zhu, L. Zhu, J. Zhu and L. Xu, *Appl. Clay Sci.*, 2008, **42**, 224–231.

40 J.-J. Shao, K. Raidongia, A. R. Koltonow and J. Huang, *Nat. Commun.*, 2015, **6**, 7602.

41 R. Ma and T. Sasaki, *Adv. Mater.*, 2010, **22**, 5082–5104.

42 T. Tanaka, Y. Ebina, K. Takada, K. Kurashima and T. Sasaki, *Chem. Mater.*, 2003, **15**, 3564–3568.

43 Z. Zeng, Z. Yin, X. Huang, H. Li, Q. He, G. Lu, F. Boey and H. Zhang, *Angew. Chemie Int. Ed.*, 2011, **50**, 11093–11097.

44 J. Xiao, D. Choi, L. Cosimbescu, P. Koech, J. Liu and J. P. Lemmon, *Chem. Mater.*, 2010, **22**, 4522–4524.

45 C.-Y. Su, A.-Y. Lu, Y. Xu, F.-R. Chen, A. N. Khlobystov and L.-J. Li, *ACS Nano*, 2011, **5**, 2332–2339.

46 W. Zheng and L. Y. S. Lee, *Matter*, 2022, **5**, 515–545.

47 A. Ahmadi, M. Z. Shoushtari and M. Farbod, *J. Mater. Sci. Mater. Electron.*, 2019, **30**, 6342–6349.

48 J. Zhang, T. Liu, L. Fu and G. Ye, *Chem. Phys. Lett.*, 2021, **781**, 138972.

49 J. Yuan, J. Wu, W. J. Hardy, P. Loya, M. Lou, Y. Yang, S. Najmaei, M. Jiang, F. Qin, K. Keyshar, H. Ji, W. Gao, J. Bao, J. Kono, D. Natelson, P. M. Ajayan and J. Lou, *Adv. Mater.*, 2015, **27**, 5605–5609.

50 X. Zhang, Z. Lai, C. Tan and H. Zhang, *Angew. Chemie Int. Ed.*, 2016, **55**, 8816–8838.

51 L. Tang, X. Li, R. Ji, K. S. Teng, G. Tai, J. Ye, C. Wei and S. P. Lau, *J. Mater. Chem.*, 2012, **22**, 5676–5683.

52 S. Wang, J. Zhao, H. Yang, C. Wu, F. Hu, H. Chang, G. Li, D. Ma, D. Zou and M. Huang, *Acta Biomater.*, 2017, **58**, 442–454.

53 N. Abid, A. M. Khan, S. Shujait, K. Chaudhary, M. Ikram, M. Imran, J. Haider, M. Khan, Q. Khan and M. Maqbool, *Adv. Colloid Interface Sci.*, 2022, **300**, 102597.

54 M. Pudukudy and Z. Yaakob, *Chem. Pap.*, 2014, **68**, 1087–1096.

55 S. Tahara, Y. Takeda and Y. Sugahara, *Chem. Mater.*, 2005, **17**, 6198–6204.

56 H. Yano, N. Sakai, Y. Ebina, R. Ma, M. Osada, K. Fujimoto and T. Sasaki, *ACS Appl. Mater. Interfaces*, 2021, **13**, 43258–43265.

57 F. Kim, S. Kwan, J. Akana and P. Yang, *J. Am. Chem. Soc.*, 2001, **123**, 4360–4361.

58 S. Acharya, J. P. Hill and K. Ariga, *Adv. Mater.*, 2009, **21**, 2959–2981.

59 H. K. Choi, A. Lee, M. Park, D. S. Lee, S. Bae, S.-K. Lee, S. H. Lee, T. Lee and T.-W. Kim, *ACS Nano*, 2021, **15**, 829–839.

60 J. Zou and F. Kim, *Nat. Commun.*, 2014, **5**, 5254.

61 Z. Sun, T. Liao, Y. Dou, S. M. Hwang, M.-S. Park, L. Jiang, J. H. Kim and S. X. Dou, *Nat. Commun.*, 2014, **5**, 3813.

62 Y. Xu and B. Xu, *Small*, 2015, **11**, 6165–6171.

63 N. R. Tas, J. Haneveld, H. V Jansen, M. Elwenspoek and A. van den Berg, *Appl. Phys. Lett.*, 2004, **85**, 3274–3276.

64 S. Liu, Q. Pu, L. Gao, C. Korzeniewski and C. Matzke, *Nano Lett.*, 2005, **5**, 1389–1393.

65 R. K. Gogoi, A. B. Neog, T. J. Konch, N. Sarmah and K. Raidongia, *J. Mater. Chem. A*, 2019, **7**, 10552–10560.

66 T. J. Konch, R. K. Gogoi, A. Gogoi, K. Saha, J. Deka, K. A. Reddy and K. Raidongia, *Mater. Chem. Front.*, 2018, **2**, 1647–1654.

67 T. J. Konch, T. Dutta, A. B. Neog, R. Gogoi and K. Raidongia, *J. Phys. Chem. C*, 2021, **125**, 17939–17949.

68 K. M. Weerakoon-Ratnayake, C. E. O'Neil, F. I. Uba and S. A. Soper, *Lab Chip*, 2017, **17**, 362–381.

69 P. Deka, V. K. Verma, B. Yurembam, A. B. Neog, K. Raidongia and S. Subbiah, *Sustain. Energy Technol. Assessments*, 2021, **44**, 101093.

70 A. Piruska, M. Gong, J. V Sweedler and P. W. Bohn, *Chem. Soc. Rev.*, 2010, **39**, 1060–1072.

71 J. Deka, K. Saha, R. Gogoi, G. K. Dutta and K. Raidongia, *ACS Appl. Electron. Mater.*, 2021, **3**, 277–284.

72 K. Saha, J. Deka and K. Raidongia, *ACS Appl. Energy Mater.*, 2021, **4**, 8410–8420.

73 D. Zhao, A. Würger and X. Crispin, *J. Energy Chem.*, 2021, **61**, 88–103.

74 K. Uchida, H. Adachi, T. Kikkawa, A. Kirihara, M. Ishida, S. Yorozu, S. Maekawa

and E. Saitoh, *Proc. IEEE*, 2016, **104**, 1946–1973.

75 V. A. Drebushchak, *J. Therm. Anal. Calorim.*, 2008, **91**, 311–315.

76 G. J. Snyder and A. H. Snyder, *Energy Environ. Sci.*, 2017, **10**, 2280–2283.

77 J. He and T. M. Tritt, *Science (80-.).*, 2017, **357**, eaak9997.

78 M. A. Zoui, S. Bentouba, J. G. Stocholm and M. Bourouis, *Energies*, 2020, 13.

79 B. Hinterleitner, I. Knapp, M. Poneder, Y. Shi, H. Müller, G. Eguchi, C. Eisenmenger-Sittner, M. Stöger-Pollach, Y. Kakefuda, N. Kawamoto, Q. Guo, T. Baba, T. Mori, S. Ullah, X.-Q. Chen and E. Bauer, *Nature*, 2019, **576**, 85–90.

80 X. He, H. Sun, Z. Li, X. Chen, Z. Wang, Y. Niu, J. Jiang and C. Wang, *J. Mater. Chem. A*, 2022, **10**, 20730–20755.

81 T. Kim, J. S. Lee, G. Lee, H. Yoon, J. Yoon, T. J. Kang and Y. H. Kim, *Nano Energy*, 2017, **31**, 160–167.

82 B. Yu, J. Duan, H. Cong, W. Xie, R. Liu, X. Zhuang, H. Wang, B. Qi, M. Xu, Z. L. Wang and J. Zhou, *Science (80-.).*, 2020, **370**, 342–346.

83 T. MIGITA, N. TACHIKAWA, Y. KATAYAMA and T. MIURA, *Electrochemistry*, 2009, **77**, 639–641.

84 T. J. Abraham, D. R. MacFarlane and J. M. Pringle, *Energy Environ. Sci.*, 2013, **6**, 2639–2645.

85 T. Ding, Y. Zhou, X.-Q. Wang, C. Zhang, T. Li, Y. Cheng, W. Lu, J. He and G. W. Ho, *Adv. Energy Mater.*, 2021, **11**, 2102219.

86 R. Hu, B. A. Cola, N. Haram, J. N. Barisci, S. Lee, S. Stoughton, G. Wallace, C. Too, M. Thomas, A. Gestos, M. E. dela Cruz, J. P. Ferraris, A. A. Zakhidov and R. H.

Baughman, *Nano Lett.*, 2010, **10**, 838–846.

87 K. Wijeratne, M. Vagin, R. Brooke and X. Crispin, *J. Mater. Chem. A*, 2017, **5**, 19619–19625.

88 S. W. Hasan, S. M. Said, M. F. M. Sabri, A. S. A. Bakar, N. A. Hashim, M. M. I. M. Hasnan, J. M. Pringle and D. R. MacFarlane, *Sci. Rep.*, 2016, **6**, 29328.

89 C. Bai, Z. Wang, S. Yang, X. Cui, X. Li, Y. Yin, M. Zhang, T. Wang, S. Sang, W. Zhang and H. Zhang, *ACS Appl. Mater. Interfaces*, 2021, **13**, 37316–37322.

90 J. K. Platten, *J. Appl. Mech.*, 2005, **73**, 5–15.

91 W. B. Chang, C. M. Evans, B. C. Popere, B. M. Russ, J. Liu, J. Newman and R. A. Segalman, *ACS Macro Lett.*, 2016, **5**, 94–98.

92 S. L. Kim, J.-H. Hsu and C. Yu, *Org. Electron.*, 2018, **54**, 231–236.

93 M. Jeong, J. Noh, M. Z. Islam, K. Kim, A. Sohn, W. Kim and C. Yu, *Adv. Funct. Mater.*, 2021, **31**, 1–7.

94 M. Bonetti, S. Nakamae, M. Roger and P. Guenoun, *J. Chem. Phys.*, 2011, **134**, 114513.

95 D. Zhao, A. Martinelli, A. Willfahrt, T. Fischer, D. Bernin, Z. U. Khan, M. Shahi, J. Brill, M. P. Jonsson, S. Fabiano and X. Crispin, *Nat. Commun.*, 2019, **10**, 1093.

96 Y. He, S. Li, R. Chen, X. Liu, G. O. Odunmbaku, W. Fang, X. Lin, Z. Ou, Q. Gou, J. Wang, N. A. N. Ouedraogo, J. Li, M. Li, C. Li, Y. Zheng, S. Chen, Y. Zhou and K. Sun, *Nano-Micro Lett.*, 2023, **15**, 101.

97 D. Zhao, H. Wang, Z. U. Khan, J. C. Chen, R. Gabrielsson, M. P. Jonsson, M. Berggren and X. Crispin, *Energy Environ. Sci.*, 2016, **9**, 1450–1457.

98 D. Tordera, D. Zhao, A. V Volkov, X. Crispin and M. P. Jonsson, *Nano Lett.*, 2017, **17**, 3145–3151.

99 F. Jiao, A. Naderi, D. Zhao, J. Schlueter, M. Shahi, J. Sundström, H. Granberg, J. Edberg, U. Ail, J. Brill, T. Lindström, M. Berggren and X. Crispin, *J. Mater. Chem. A*, 2017, **5**, 16883–16888.

100 B. Kim, J. Na, H. Lim, Y. Kim, J. Kim and E. Kim, *Adv. Funct. Mater.*, 2019, **29**, 1807549.

101 Z. A. Akbar, J. W. Jeon and S. Y. Jang, *Energy Environ. Sci.*, 2020, **13**, 2915–2923.

102 H. Cheng, X. He, Z. Fan and J. Ouyang, *Adv. Energy Mater.*, 2019, **9**, 1901085.

103 C.-G. Han, X. Qian, Q. Li, B. Deng, Y. Zhu, Z. Han, W. Zhang, W. Wang, S.-P. Feng, G. Chen and W. Liu, *Science (80-.).*, 2020, **368**, 1091–1098.

104 Z. Zhou, Y. Wan, J. Zi, G. Ye, T. Jin, X. Geng, W. Zhuang and P. Yang, *Mater. Today Sustain.*, 2023, **21**, 100293.

105 W. Zhang, X. Liu, K. Jiao, Q. Wang, C. Yang and C. Zhao, *Nano Lett.*, 2023, **23**, 8264–8271.

106 X. Qian, T.-H. Liu and R. Yang, *Mater. Today Phys.*, 2022, **23**, 100627.

107 T. Li, X. Zhang, S. D. Lacey, R. Mi, X. Zhao, F. Jiang, J. Song, Z. Liu, G. Chen, J. Dai, Y. Yao, S. Das, R. Yang, R. M. Briber and L. Hu, *Nat. Mater.*, 2019, **18**, 608–613.

108 G. Fan, K. Liu, H. Su, Y. Luo, Y. Geng, L. Chen, B. Wang, Z. Mao, X. Sui and X. Feng, *Chem. Eng. J.*, 2022, **434**, 134702.

109 W. Lu, W. L. Ong and G. W. Ho, *J. Mater. Chem. A*, 2023, **11**, 12456–12481.

110 P. Král and M. Shapiro, *Phys. Rev. Lett.*, 2001, **86**, 131–134.

111 Y. Liang, F. Zhao, Z. Cheng, Y. Deng, Y. Xiao, H. Cheng, P. Zhang, Y. Huang, H. Shao and L. Qu, *Energy Environ. Sci.*, 2018, **11**, 1730–1735.

112 Y. Huang, H. Cheng, C. Yang, P. Zhang, Q. Liao, H. Yao, G. Shi and L. Qu, *Nat. Commun.*, 2018, **9**, 4166.

113 Z. Sun, X. Wen, L. Wang, D. Ji, X. Qin, J. Yu and S. Ramakrishna, *eScience*, 2022, **2**, 32–46.

114 Z. Feng, G. Hu, R. Zhu, S. Zhang, C. Liu, P. Guan, M. Li, T. Wan, H. Xu and D. Chu, *ACS Appl. Nano Mater.*, 2022, **5**, 12224–12244.

115 F. Zhao, H. Cheng, Z. Zhang, L. Jiang and L. Qu, *Adv. Mater.*, 2015, **27**, 4351–4357.

116 F. Zhao, Y. Liang, H. Cheng, L. Jiang and L. Qu, *Energy Environ. Sci.*, 2016, **9**, 912–916.

117 H. Cheng, Y. Huang, F. Zhao, C. Yang, P. Zhang, L. Jiang, G. Shi and L. Qu, *Energy Environ. Sci.*, 2018, **11**, 2839–2845.

118 Y. Huang, H. Cheng, C. Yang, H. Yao, C. Li and L. Qu, *Energy Environ. Sci.*, 2019, **12**, 1848–1856.

119 L. Yang, L. Zhang and D. Sun, *ACS Appl. Mater. Interfaces*, 2022, **14**, 53615–53626.

120 L. Li, Z. Chen, M. Hao, S. Wang, F. Sun, Z. Zhao and T. Zhang, *Nano Lett.*, 2019, **19**, 5544–5552.

121 T. Xu, X. Ding, Y. Huang, C. Shao, L. Song, X. Gao, Z. Zhang and L. Qu, *Energy Environ. Sci.*, 2019, **12**, 972–978.

122 Z. Sun, L. Feng, X. Wen, L. Wang, X. Qin and J. Yu, *Mater. Horizons*, 2021, **8**, 2303–

2309.

123 Y. Yang, J. Wang, Z. Wang, C. Shao, Y. Han, Y. Wang, X. Liu, X. Sun, L. Wang, Y. Li, Q. Guo, W. Wu, N. Chen and L. Qu, *Nano-Micro Lett.*, 2023, **16**, 56.

124 H. Wang, Y. Sun, T. He, Y. Huang, H. Cheng, C. Li, D. Xie, P. Yang, Y. Zhang and L. Qu, *Nat. Nanotechnol.*, 2021, **16**, 811–819.

125 T. Cai, L. Lan, B. Peng, C. Zhang, S. Dai, C. Zhang, J. Ping and Y. Ying, *Nano Lett.*, 2022, **22**, 6476–6483.

126 W. Lu, T. Ding, X. Wang, C. Zhang, T. Li, K. Zeng and G. W. Ho, *Nano Energy*, 2022, **104**, 107892.

Chapter 2

Fabrication of Robust and Versatile Ionic Thermoelectric Devices of Natural Clay Minerals

Summary

Ionic thermoelectric (i-TE) materials are gaining attraction as an effective solution for converting low-grade waste heat into usable energy, thanks to their ability to leverage high Seebeck coefficients, simple fabrication techniques and the abundance of materials used in their construction. In this chapter, we describe the fabrication of an ionic thermoelectric material by reconstructing exfoliated layers of lamellar natural clay minerals. The performance of the clay mineral-based i-TE material was further improved through the surface functionalisation of individual clay nanosheets. The thermoelectric properties of the composite membranes (functionalised and unfunctionalised vermiculite nanosheets) were thoroughly investigated at different temperature gradients, leading to the findings of Seebeck coefficients. The clay mineral-based i-TE material demonstrated remarkable high-temperature stability (300 °C) and water-assisted healing properties. Along with waste heat, clay-i-TE devices can also convert abundant sunlight energy into electricity. When photothermal materials like carbon nanotubes (CNT) were drop cast on one side of the thermoelectric device, light illumination with different intensities generated temperature gradients across the device, producing thermovoltages. Therefore, i-TE materials could be an alternative way to convert light into electricity. The performance of the i-TE device in low-humidity conditions could be drastically improved by coating them with polyvinyl alcohol (PVA), borax, and LiCl-based hydrogel. Finally, the potential practical applications of clay-based i-TE devices were showcased in various fields, including fire alarms, touch sensors, and generating electricity from hot water steam.

2.1. Introduction:

With the growing concern for environmental sustainability and longevity regarding conventional energy sources, there is an urgent need for alternative approaches to energy generation.[1] Ionic thermoelectricity offers a promising solution by tapping into the vast reservoir of waste heat produced by industrial processes, transportation systems, and electronic devices. By converting this wasted thermal energy into electricity, ionic thermoelectric devices can significantly reduce reliance on fossil fuels, mitigate greenhouse gas emissions, and enhance overall energy efficiency.[2] This newly emerging field of research is based on the principle called the Soret effect, which describes the diffusion of molecules, atoms or ions under the influence of temperature gradient. Fundamentally, the potential difference is developed due to the mobility difference of cations and anions in an i-TE material. Therefore, an ion-selective material (cation or anion) holds promise for achieving greater ionic thermopower than conventional i-TE materials.[3–6] In that context, 2D lamellar nanofluidic membranes could be an ideal alternative to i-TE materials owing to their high selectivity towards a specific class of ions depending on the surface zeta potentials. The overlapping of EDLs within the nanochannels of these nanofluidic membranes allows selective diffusion of ions, eventually enhancing the overall ionic conductivity and facilitating organised diffusion of ions. For example, the reconstructed lamellar nanofluidic membranes of vermiculite and V_2O_5 are known for their higher proton conduction.[7–9] Similarly, an anion-selective nanofluidic membrane composed of CoAl LDH exhibited a notable OH^- ion conductivity with the value of ~ 2 mS cm^{-1}.[10] All these intriguing characteristics of nanofluidic membranes based on 2D materials hold promise for creating another category of i-TE materials as these materials not only enhance overall thermopower but also can withstand extreme temperatures and recovery from physical damages.

2.2. Scope of the present investigation:

The field of ionic thermoelectricity is primarily confined to several classes of polyelectrolytes and ionic liquids that come with complex fabrication techniques and higher expenses. [11,12]Considering the selectivity in ionic diffusion exhibited by 2D lamellar nanofluidic membranes, these materials hold promise in ionic thermoelectricity as the selectivity of ionic thermodiffusion significantly influences the ionic thermopower. Therefore, this study provides a new platform of ionic thermoelectric materials that is entirely based on inorganic 2D reconstructed lamellar materials. These classes of materials allow selective and organised diffusion of ions, simple fabrication techniques, cost-effective and scalable synthesis of materials, along with high thermal and chemical stability.[13,14] This study of lamellar nanofluidic membranes additionally demonstrates a way of improvising the ionic thermopower through surface functionalisation of individual nanosheets, opening the possibility for surface tuning according to the necessities. One of the significant hurdles related to ionic thermoelectricity is their dependency on relative humidity levels. At lower relative humidity levels, these ionic thermoelectric materials typically exhibit a notable depletion in ionic thermopower. In this study, a methodology was developed that significantly improves the water retention capacity of ionic thermoelectric material at lower humidity levels.[15] The presence of water molecules preserves the percolation pathways, aiding in the retention of the Seebeck coefficient. This methodology involves coating of i-TE material with a layer of polyvinyl alcohol (PVA) based hydrogel. Additionally, owing to the high-temperature stability and water-assisted healable nature, these i-TE materials have broader scopes in areas like fire alarms, hot water steam to electricity conversion, and touch sensing applications.

Material structure and properties: Vermiculite is naturally occurring hydrous phyllosilicate mineral that consist of two tetrahedral sheets for each octahedral sheet. Each tetrahedral sheet is composed of silicon and oxygen atoms arranged in a tetrahedral structure, while each

octahedral sheet consists of magnesium, aluminium, and oxygen atoms arranged in an octahedral configuration. These layers are held together by weak electrostatic forces, allowing the layers to expand or contract when water molecules are absorbed or removed, respectively. This property gives vermiculite its characteristic ability to swell and exfoliate when exposed to heat. This can be utilized in various applications such as, nanofluidic ionic transport, different energy harvesting approaches, fireproofing, construction and insulation, packaging and shipping, water filtration etc.

2.3. Experimental section:

Materials: Vermiculite, hydrogen peroxide, toluene, (3-Mercaptopropyl)trimethoxysilane (MPTMS) and carbon nanotubes were purchased from Sigma-Aldrich. Lithium chloride was purchased from Sisco Research Laboratories Pvt. Ltd., Borax was purchased from Avra Synthesis Pvt. Ltd. and polyvinyl alcohol was purchased from Loba Chemie.

Exfoliation of vermiculite: The bulk vermiculite clay underwent exfoliation via a two-step ion exchange process. Initially, 300 mg of bulk vermiculite was refluxed in a saturated sodium chloride solution for 24 hours, followed by multiple washes with DI water. Subsequently, the Na-exchanged vermiculite was again refluxed with a 2M LiCl solution for 24 hours, followed by further washing with DI water. Once the washing process was completed, the sample underwent characterization and was utilized to prepare freestanding membranes.

Functionalisation of vermiculite nanosheets: A two-step process was employed to introduce SO_3H groups onto vermiculite nanosheets. Initially, thiol (-SH) groups were incorporated by reacting exfoliated vermiculite nanosheets with (3-Mercaptopropyl)trimethoxysilane (MPTMS) and toluene (in a weight ratio of 1:2:20) for 24 hours at 110 °C. Upon completion of the reaction, the resulting product underwent thorough washing with absolute ethanol and deionized water.[16] Subsequently, the washed product was air-dried for 24 hours at room

temperature before being treated with 30% H_2O_2 for 24 hours to convert the thiol groups into -SO_3H groups. The resulting product was again washed with deionized water and ethanol, followed by drying for further characterization and membrane preparation.

Membrane preparation: Freestanding membranes composed of vermiculite were fabricated using a vacuum filtration method. Initially, an aqueous dispersion containing exfoliated vermiculite nanosheets was prepared, with 20 ml of the dispersion (concentration: 5 mg/ml) subjected to vacuum filtration through PTFE membranes with a pore diameter of 100 nm. After drying at 40°C, the resulting freestanding membrane was carefully separated from the PTFE membrane.

For the preparation of composite membranes labelled as FV_30, FV_50, and FV_70, varying ratios of aqueous dispersions containing both pristine and functionalized vermiculite nanosheets were combined (in ratios of 70:30, 50:50, and 30:70, respectively). Subsequently, these mixtures were vacuum filtered through PTFE membranes with a pore diameter of 100 nm and dried at 40°C before peeling off.

Thermoelectric device fabrication: The construction of the thermoelectric device involves several steps. Initially, the prepared freestanding membrane, with dimensions of 2 cm x 0.8 cm, was cut and positioned atop a stage composed of two glass slides connected by adhesive tapes. Copper wires were then affixed to the membrane using a conductive silver paste, spaced at a distance of 1.5 cm. Another stage, featuring two Peltier devices, one serving as a heat source and the other as a heat sink, was assembled, as depicted in Figure 2.1d. The thermoelectric device was situated atop these Peltier devices to measure thermoelectric voltages. Two K-type thermocouples (Testo 735) were affixed to the glass slides to monitor the temperature gradient. To establish the desired temperature gradient (ΔT), a DC voltage was applied to the Peltier devices using a regulated DC power supply unit (METARAVI TM – RPS

30005). The thermovoltages produced by the i-TE devices were subsequently measured using a 2450 Keithley Sourcemeter instrument.

Preparation of hydrogel: The hydrogel comprising polyvinyl alcohol (PVA) and sodium tetraborate was prepared as reported earlier.[17] A mixture of equal-weight percentages of aqueous PVA and aqueous sodium tetraborate solution was combined in a volumetric ratio of 10:1. Concurrently, 150 mg of LiCl was introduced into the prepared solution. The mixture was stirred for 3 hours at 60°C, followed by successive freezing (at -20 °C) and thawing cycles at room temperature.

Upon hydrogel formation, a segment measuring 1 cm x 0.8 cm was excised and applied as a coating atop a rectangular FV_70 membrane measuring 2 cm x 0.8 cm. Care was taken to ensure that the coated hydrogel layer did not directly contact the copper electrodes.

Nanofluidic device fabrication: To assemble the nanofluidic device, rectangular vermiculite (1.5 cm x 0.5 cm x 0.004 cm) and FV_70 (1.5 cm x 0.5 cm x 0.0045 cm) membrane pieces were embedded within a freshly prepared PDMS elastomer. Reservoirs for DI water and electrolytes were sculpted at each end of the nanofluidic device, allowing the fluids to access the nanofluidic channels within the membranes. The membranes were hydrated by positioning them adjacent to reservoirs filled with DI water for 12 hours. Subsequently, approximately 0.3 ml of HCl electrolyte with varying concentrations (ranging from 10^{-6} M to 1 M) were introduced into the reservoirs and left for around 6 hours. After the pre-soaking period, I-V curves were recorded.

Experiments related to light illumination: The experiments involving light exposure were performed using a halogen light source. A portion of the FV_70 device was coated with a carbon nanotube (CNT) solution, ensuring that the CNT solution did not contact the Cu

electrodes. The intensity of the light exposure was adjusted by modifying the distance between the device and the light source.

Device fabrication of real-time applications: To generate thermovoltage directly from an open flame, the device was constructed following the same procedure described for ionic thermoelectric devices. This involved connecting two glass slides (2.5 cm x 2.5 cm) using adhesive tape, maintaining a gap of approximately 2 mm between them. The FV_70 membrane (2 cm x 0.8 cm) was then positioned atop this stage composed of the two glass slides. Thermovoltage was generated by exposing one of the glass slides directly to the open flame.

For experiments involving hot steam, steam emitted from a custom-made vent of an electric kettle was directed onto one end of the i-TE devices, ensuring that the hot vapour made contact with the desired section of the device.

2.4. Characterizations: The morphological features were investigated using a field emission scanning electron microscope (FESEM) (Zeiss, model: Sigma). Composition analysis was carried out using energy-dispersive X-ray analysis using the same FESEM instrument. X-ray diffraction (XRD) patterns were obtained using an X-ray diffractometer (Rigaku, model: Micromax-007HF). Infrared spectroscopic analysis was performed using a Perkin Elmer instrument (Spectrum Two). Atomic force microscopy (AFM) with the Oxford Cypher model was utilized to determine the height of individual nanosheets. The zeta potentials of different dispersions were measured using the Zetasizer instrument (Malvern, Nano-ZS90). The nanosheets were further examined using a Field Emission Transmission Electron Microscope (FETEM) (JEOL, Model: 2100F). Thermal images were captured using the Testo 872 thermal camera. The functionalization of nanosheets was characterized via X-ray photoelectron spectroscopy (Model: PHI 5000 versa probe III).

2.5. Results and Discussion:

2.5.1. Characterization of exfoliated clay minerals:

The process of exfoliating bulk vermiculite crystals into individual flakes involved a two-step ion-exchange method that follows a previously reported procedure (details are in the experimental section 2.3.).[7,8] Confirmation of vermiculite exfoliation into individual 2D nanosheets was achieved through the examination of atomic force microscopy (AFM) images, transmission electron microscopy (TEM) images, and X-ray diffraction (XRD) patterns. Figure 2.1a displays a representative AFM image of the exfoliated 2D sheet, along with a photo inset depicting the stable aqueous dispersion. Additionally, Figure 2.1b inset presents a photo of freestanding nanofluidic membrane prepared by restacking 2D nanosheets of vermiculite from the aqueous dispersion using the vacuum filtration method. The lamellar structure of restacked vermiculite is evident from the cross-sectional FESEM image shown in Figure 2.1b. The plot in Figure 1c illustrates the ionic conductivity versus concentration of HCl for the nanofluidic device fabricated from a vermiculite membrane. The presence of molecularly thin 2D nanofluidic channels is confirmed by the extended surface-charge-governed ionic conductivity regime (ranging from 10^{-6} to 10^{-2} M) observed in the plot of Figure 2.1c. At lower HCl concentrations (10^{-6} to 10^{-2} M), the ionic conductivity remains relatively constant regardless of increasing HCl concentration at the reservoir compared to the bulk HCl concentration. The existence of 2D nanofluidic channels in the vermiculite membrane, as supported by the XRD pattern, cross-sectional FESEM image, and surface-charge-governed conductivity regime, underscores the efficient transport of ions, prompting further exploration in the field of ionic thermoelectricity.

2.5.2. i-TE properties of clay minerals:

To assess the thermoelectric characteristics of the freestanding vermiculite membrane, a setup was constructed with two Peltier devices: one serving as the heat source and the other as the heat sink. By utilizing these Peltier devices (as depicted schematically in Figure 2.1d), the desired temperature gradient (ΔT) could be maintained. Thermoelectric devices, fabricated from rectangular strips (2 × 0.8 × 0.004 cm) of the freestanding vermiculite membrane, were positioned on the top of these two Peltier devices and exposed to various ΔT conditions. After applying an 8 K ΔT across the vermiculite device, the output thermovoltage gradually increased over time and eventually reached a saturation level (~38 mV) after approximately 280 seconds (Figure 2.1f). Similarly, after removing the temperature gradient (ΔT = 0), the thermovoltage gradually decreased and returned to approximately 0 mV (Figure 2.1f). The consistent repetition of this cycle for multiple iterations confirms that the temperature gradient is responsible for the observed output voltages. Furthermore, as depicted in Figure 2.1e, the thermovoltage exhibited a proportional increase with rising ΔT values. It is found that the time required to achieve the saturation voltage at 12 K, ΔT is higher than 4 K, ΔT. Although the rate of increment of the thermovoltage (slope), at the temperature gradient of 12 K (0.368 mV/sec) is higher as compared to 4 K, ΔT (0.24 mV/sec) which can be attributed to the higher temperature gradient that eventually promotes the diffusion of ions through the nanochannels, with that rate of increment, to attain a saturation voltage of 60 mV requires higher amount of time compared to the saturation voltage of 15 mV with the rate of 0.24 mV/sec. Therefore, the overall time necessary for the saturation level at 12 K, ΔT is higher as compared to 4 K temperature gradient. The slope calculated from Figure 2.1g corresponds to a Seebeck coefficient of approximately 6 mV/K for the vermiculite i-TE device. Previous reports have indicated the presence of surface hydroxyl groups on the exfoliated vermiculite nanosheets, which was experimentally confirmed by infrared spectroscopy (Figure 2.2e) and the negative

zeta potential (-38.5 ± 2.96 mV) of the aqueous dispersion. When exposed to atmospheric water molecules, the surface hydroxyl groups present on the vermiculite nanosheets enable the

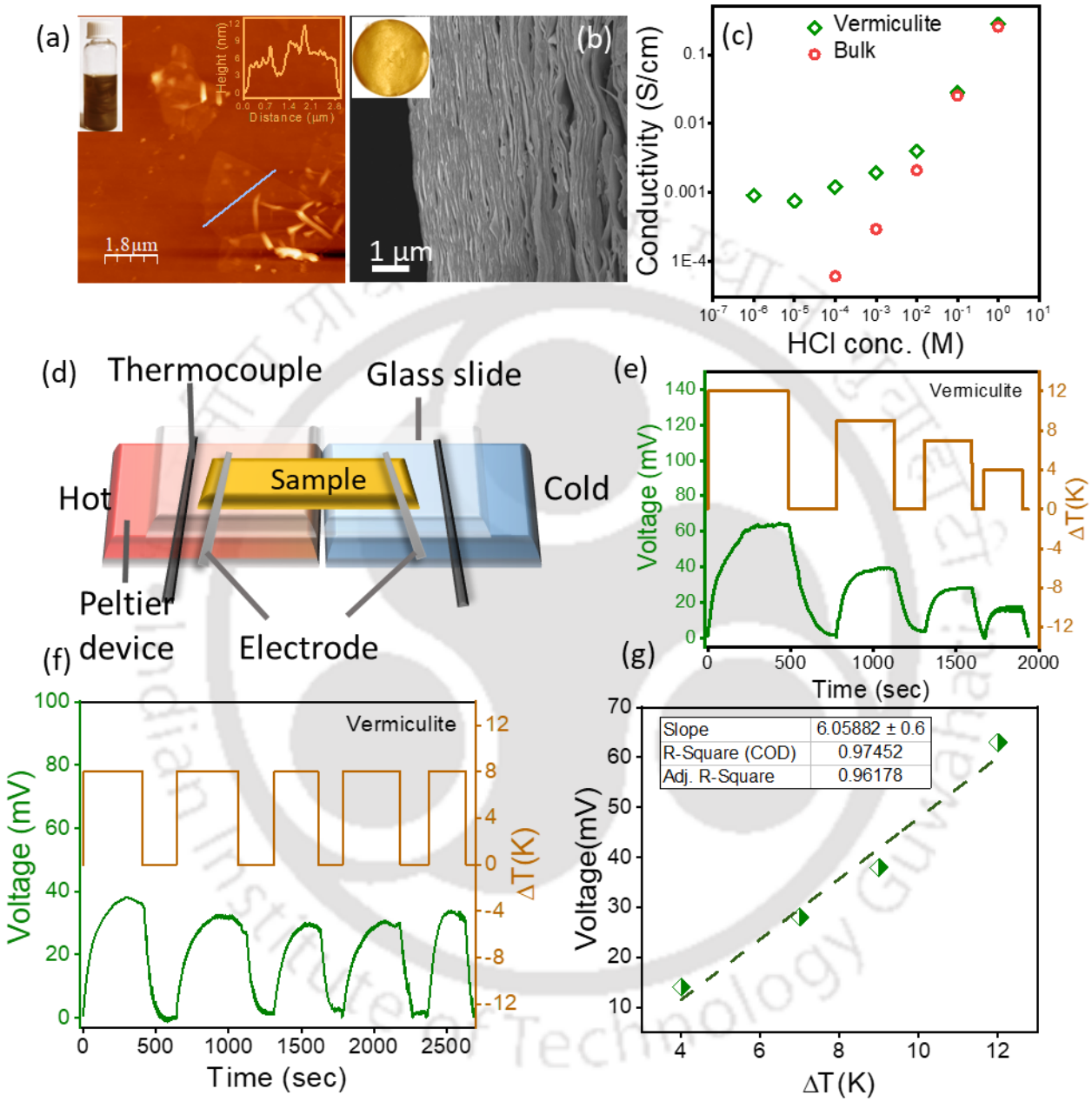

Figure 2.1: (a) AFM image and aqueous dispersion (at the inset) of vermiculite nanosheets. (b) Cross-sectional FESEM image and digital photograph (at the inset) of vermiculite membrane. (c) Concentration (HCl) vs conductivity plot showing surface charge governed ionic conductivity behaviour of vermiculite membrane. (d) Schematic of the experimental setup used for thermoelectric measurements. (e) Generation of thermovoltages from vermiculite membrane at different temperature gradients. (f) Generation of thermovoltages in pristine vermiculite based i-TE device at ΔT = 8 K. (g) The linear increment of thermovoltages with respect to increasing ΔT values.

generation of mobile protons, which then migrate in response to the temperature gradient, generating the observed thermovoltages.

2.5.3. i-TE devices of modified clay minerals:

Clays, as naturally occurring refractory materials, have served as barriers in fireplaces, ovens, and furnaces for millennia. Interestingly, natural clay minerals possess the potential to convert waste heat into electricity, as mentioned in the previous section. The integration of ionic thermoelectricity (i-TE) into clay minerals could offer a direct means to convert domestic waste heat into usable electricity. However, enhancing the Seebeck coefficient could broaden the application scope of clay-based i-TE devices. Materials rich in $–SO_3H$ groups already demonstrated elevated levels of both ionic conductivity and ionic Seebeck coefficients[18].[12] Therefore, the surface of vermiculite was modified with $–SO_3H$ groups, as explained in the experimental section 2.3. Initially, exfoliated 2D vermiculite sheets were functionalized with –SH groups via treatment with (3-Mercaptopropyl)trimethoxysilane (MPTMS), followed by a reaction with hydrogen peroxide. The generation of $–SO_3H$ groups on the surface of vermiculite nanosheets is depicted schematically in Figure 2.2a. The appearance of a peak in the XPS spectrum at a binding energy of 168.70 eV corresponding to sulfur atoms (as shown in Figure 2.3c) was absent in the case of pristine vermiculite, indicating the presence of S atoms in the $–SO_3H$ form. The high resolution XPS O1s spectra was elaborately analysed in order to find out conversion of Si-OH groups into $–SO_3H$ groups (Figure 2.2g). It is observed that the total % of–Si-OH group in the pristine membrane decreased from 6.19% to 3.8% suggesting the sulfonation reaction of the Si-OH groups. Additionally, EDX elemental analysis also confirmed the presence of S atoms in the functionalized vermiculite membrane however, no S atoms were observed in case of pristine vermiculite membrane (Figures 2.4 and 2.5). Notably, following functionalization, the zeta potential values of pristine vermiculite flakes increased from -38.5 ± 2.96 mV to -49.2 ± 1.97 mV (as shown in Figure 2.6a), while retaining their

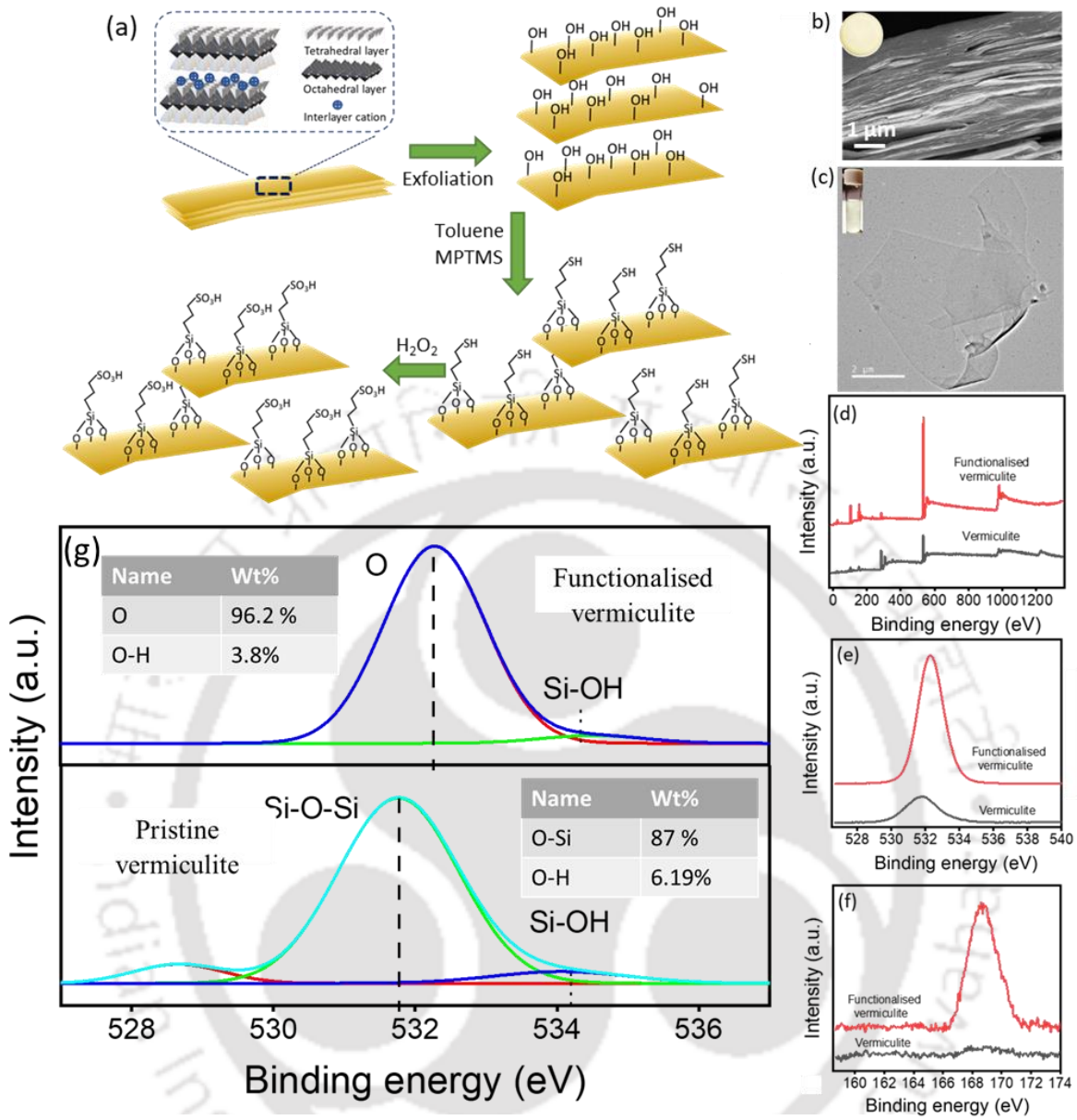

Figure 2.2: (a) Schematic representation of the functionalisation process of vermiculite nanosheets. (b) Cross-sectional FESEM image and the digital photograph (at the inset) of FV_70 membrane. (c) TEM image of the and aqueous dispersion (at the inset) of vermiculite nanosheets. (d) Wide scan XPS spectra of vermiculite and functionalized vermiculite nanosheets. High resolution XPS spectra of (e) O1s and (f) S2p of the vermiculite and functionalized vermiculite samples. (g) High resolution O1s XPS spectra of pristine and functionalised vermiculite.

atomically thin 2D morphology, as observed in the FETEM image in Figure 2.2c. This increase in zeta potential values further affirmed the formation of $–SO_3H$ groups on the surface of the vermiculite nanosheets (Figure S2c). Similarly, the pH of the aqueous dispersion (2 mg/mL) of functionalized vermiculite was measured at 3.5, compared to a pH of 6.5 for pristine vermiculite.

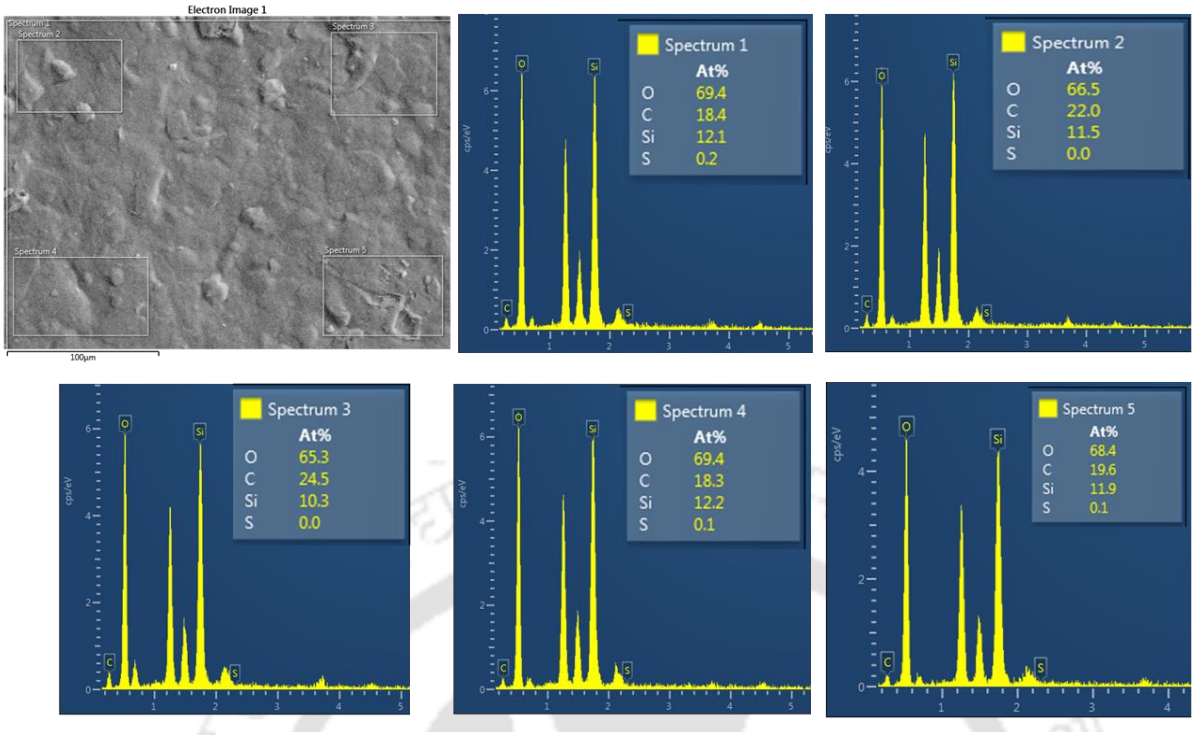

Figure 2.3: EDX analysis of pristine vermiculite membrane

To enhance the ionic thermoelectric properties, freestanding membranes were fabricated by vacuum filtering uniform blends of pristine and functionalized vermiculite dispersions in weight-to-weight ratios of 30:70 (FV_70), 50:50 (FV_50), and 70:30 (FV_30). The inset in Figure 2.2b depicts a digital image of the freestanding composite membrane (FV_70). The

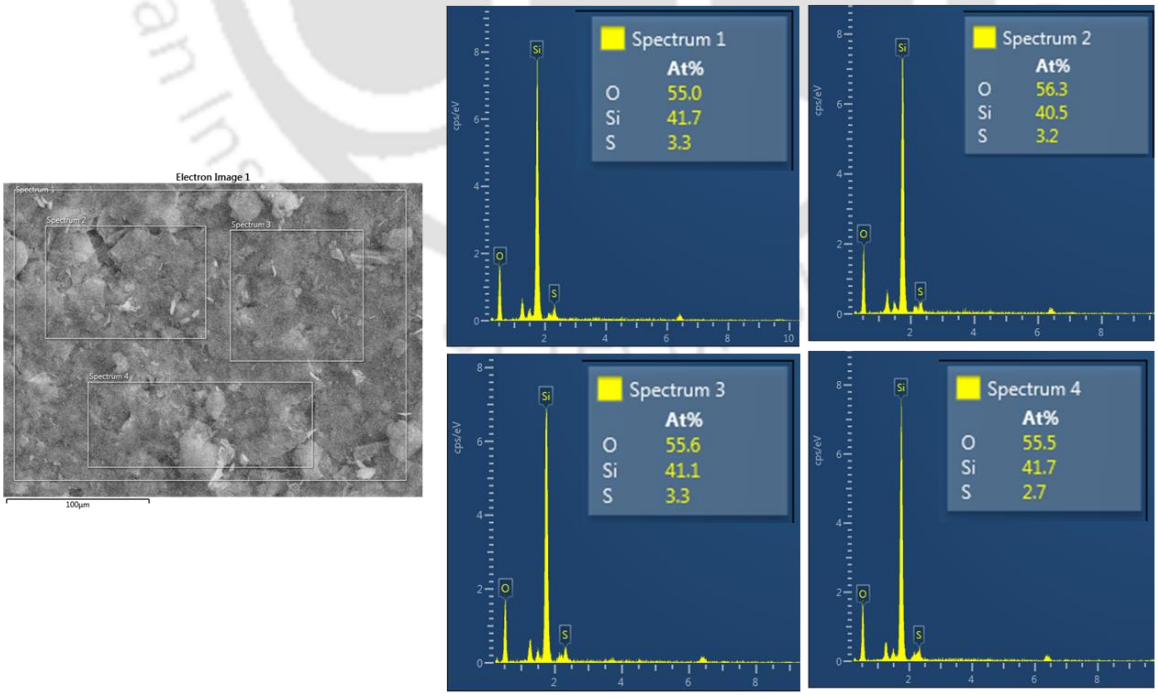

Figure 2.4: EDX analysis of functionalized vermiculite membrane

lamellar nature of nanosheets was evident from the cross-sectional FESEM image in Figure 2.2b and validated by the pXRD pattern in Figure 2.5a. The pXRD pattern in Figure 2.5a further shows the enlargement of d-spacing from 1.438 (pristine vermiculite) nm to 1.47 nm (FV_70) after incorporating functionalised vermiculite nanosheets. The schematic representation of the enlargement of d-spacing due to functionalisation process is included in Figure 2.5 d. Further, in the FT-IR spectra shown in Figures 2.5b and c, the presence of Si-OH groups in vermiculite is indicated by a band at 960 cm^{-1}. This peak undergoes a notable shift towards 985 cm^{-1} and 1080 cm^{-1} for FV_70 and functionalized vermiculite (FV_100), respectively. Additionally, the sulfonic groups exhibit distinct peaks in the range of 1100 cm^{-1} to 1200 cm^{-1}, which may overlap with the vermiculite peaks, resulting in a more intense peak at 1080 cm^{-1}. When observing the IR peak of functionalized vermiculite, the band at 960 cm^{-1} can still be observed with much lower intensity. This reduction in intensity can be attributed to the remaining unfunctionalized –Si-OH groups. Finally, the presence of 2D nanofluidic channels in the composite membranes was confirmed by the surface charge governed ionic conductivity plot of concentration (of HCl) versus ionic conductivity, as illustrated in Figure 2.6b.

Thermoelectric devices composed of the composite membranes were constructed according to the procedures outlined in experimental section 2.3 and analyzed using the setup discussed previously (depicted in Figure 2.1d). As illustrated in Figure 2.6c, an increase in thermovoltage was observed immediately upon application of the temperature gradient (ΔT = 5K) across the thermoelectric device of FV_70, stabilizing after approximately 350 seconds. Subsequently, upon removal of the temperature gradient (ΔT = 0 K), the thermovoltage returned to nearly zero. This cyclic behaviour was consistently reproduced multiple times, affirming that the voltage originated from the temperature gradient across the membrane. Similarly, the

thermovoltages exhibited an incremental trend with increasing temperature gradient across the membrane, as shown in Figure 2.6d.

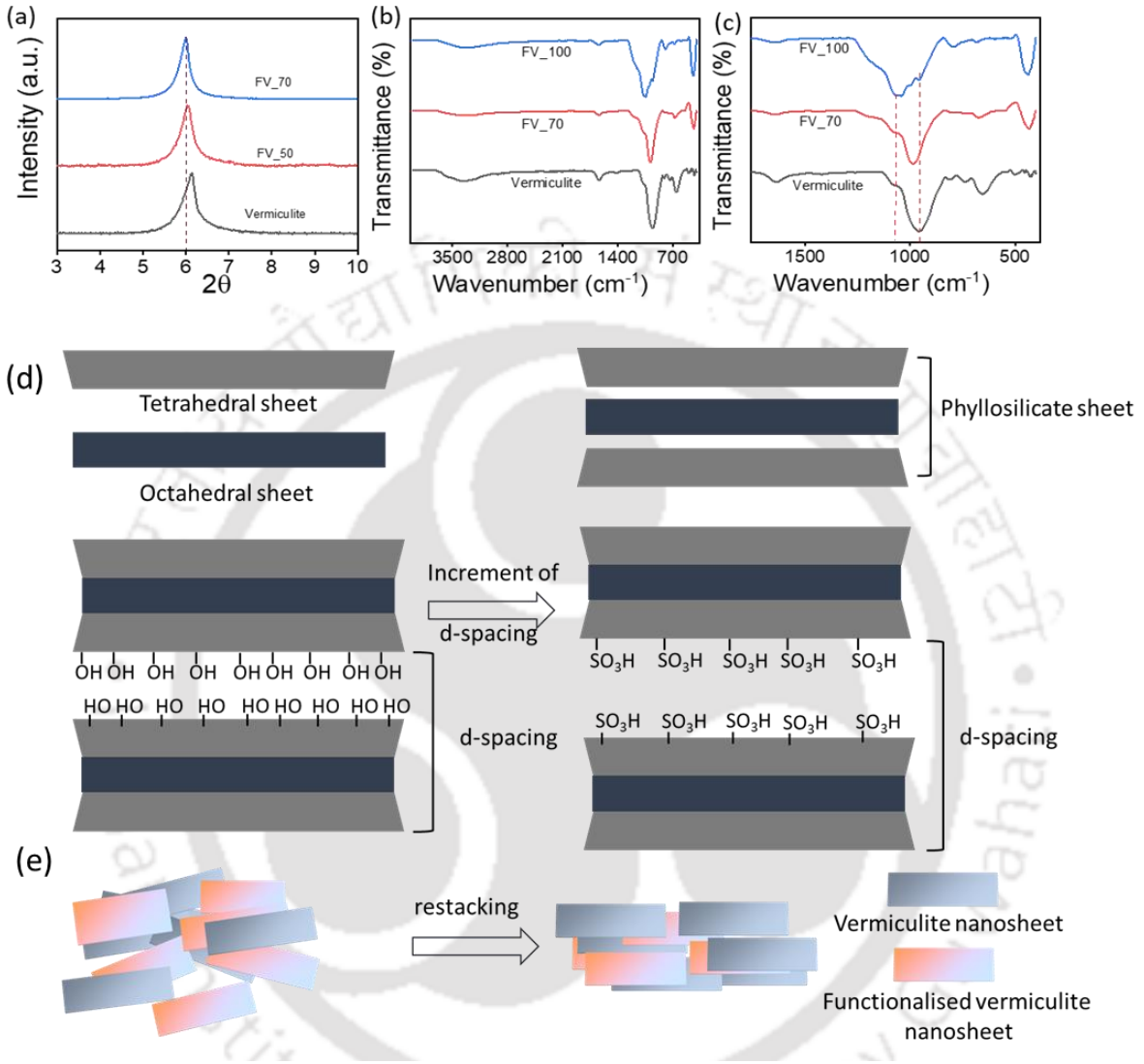

Figure 2.5: (a) pXRD pattern vermiculite, FV_50 and FV_70 membrane. (b) FT-IR spectra of vermiculite, FV_70 and functionalised vermiculite. (c) The enlarged version of Figure 2.5b. (d) Schematic representation of structure of vermiculite and increment of d-spacing after the functionalisation process. (e) Restacking of vermiculite and functionalised vermiculite nanosheets through vacuum filtration process.

The sustained voltage stability over an extended duration of 10000 seconds with a temperature gradient of 6 K was maintained across the FV_70 device as depicted in Figure 2.6e. Throughout this temperature gradient, a nearly constant voltage was consistently recorded. However, under

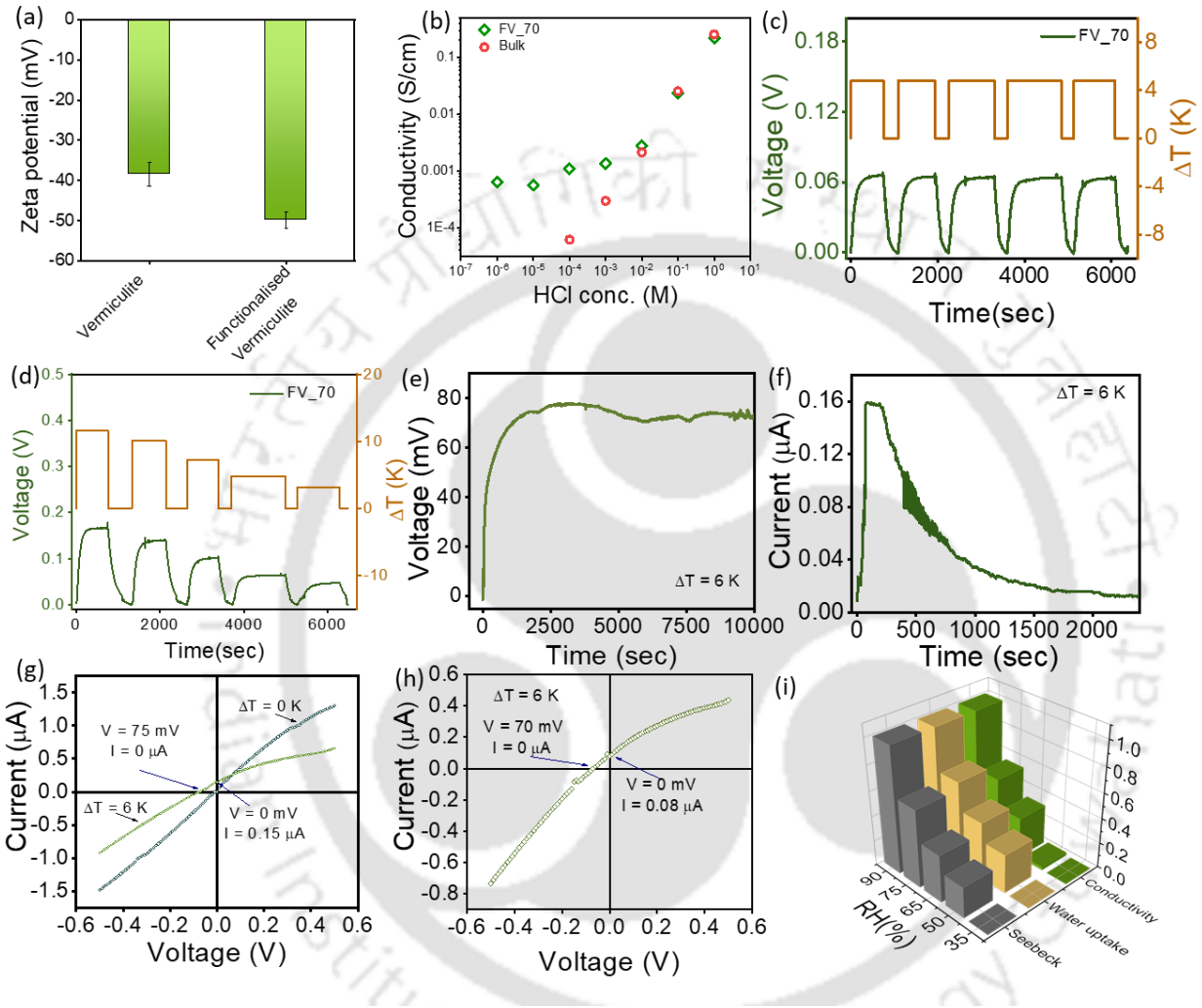

Figure 2.6: (a) The zeta potential values of aqueous dispersion of pristine and functionalised vermiculite clay. (b) The concentration (HCl) vs conductivity plot of FV_70 membrane showing surface charge governed ionic conductivity. (c) Generation of thermovoltages from FV_70 membrane at a constant temperature gradients of 4.8 K. (d) Generation of thermovoltages at different ΔT values of FV_70 membrane (e) Generation of thermovoltage from FV_70 membrane for a period of 10000 seconds at a temperature gradient of 6 K. (f) Generation of thermal current from FV_70 membrane for a period of ~2400 seconds at a temperature gradient of 6 K. (g) *I-V* curves of FV_70 membrane without and with the temperature gradient of 6 K. (h) I-V curve of FV_70 after ~2000 seconds of continuous temperature gradient (ΔT = 6 K). (i) A bar diagram for simultaneous increment of Seebeck coefficient, water uptake and ionic conductivity values of FV_70 membrane. Each of these values were normalised with the maximum value (ionic conductivity: 0.31 S/m, water uptake: 18.6 % and Seebeck coefficient: 14.4 mV/K).

a constant ΔT of 6 K, the current values gradually increased, peaked after approximately 75 seconds, and then began to decline over time (as depicted in Figure 2.6f). This phenomenon is attributed to the depletion of ion concentration and the dehydration of nanochannels within the hot zone. The temperature-induced diffusion of ions across the two ends of the composite membrane is further evident when comparing the I-V curves obtained at ΔT = 0 K and 6 K. At ΔT = 0 K, a linear I-V curve passing through the origin signifies the uniform distribution of ionic species across the FV_70 strip (as shown in Figure 2.6g). Conversely, at ΔT = 6 K, variations in ionic concentrations at the membrane's ends occur as ions migrate from the hot zone to the cold zone, causing the I-V curve to deviate from the origin. The I-V curve recorded at ΔT = 6 K intersected the X-axis at 75 mV (representing open-circuit voltage) and the Y-axis at 0.15 μA (indicating short-circuit current), as depicted in Figure 2.6g. The transient behaviour of the current was further examined by recording the I-V curve after ~2000 seconds. (depicted in Figure 2.6h). An open-circuit voltage of around 70 mV was noted from the X-intercept of the I-V curve, while a short-circuit current of 0.08 μA was observed from the Y-intercept of the curve.

Thermoelectric measurements were similarly conducted on FV_50 and FV_30 devices, as illustrated in Figure 2.7a, b, c and d. The Seebeck coefficients of the membranes were derived from the plots of ΔV versus ΔT, presented in Figure 2.7e. Notably, the FV_70 exhibited the highest Seebeck coefficient of 14.4 ± 0.4 mV/K, nearly two-fold increment as compared to the pristine vermiculite membrane. This enhancement can be attributed to the increased water uptake capacity and higher concentration of H^+ ions dissociated from the $–SO_3H$ groups (as depicted in Figure 2.7f) within the functionalized vermiculite membrane. Experimental observations reveal that at a relative humidity (RH) of 90%, pristine vermiculite can absorb atmospheric water molecules up to 10% of its weight, whereas $–SO_3H$ functionalized vermiculite membranes can absorb water molecules up to 19 wt% of their own weight under

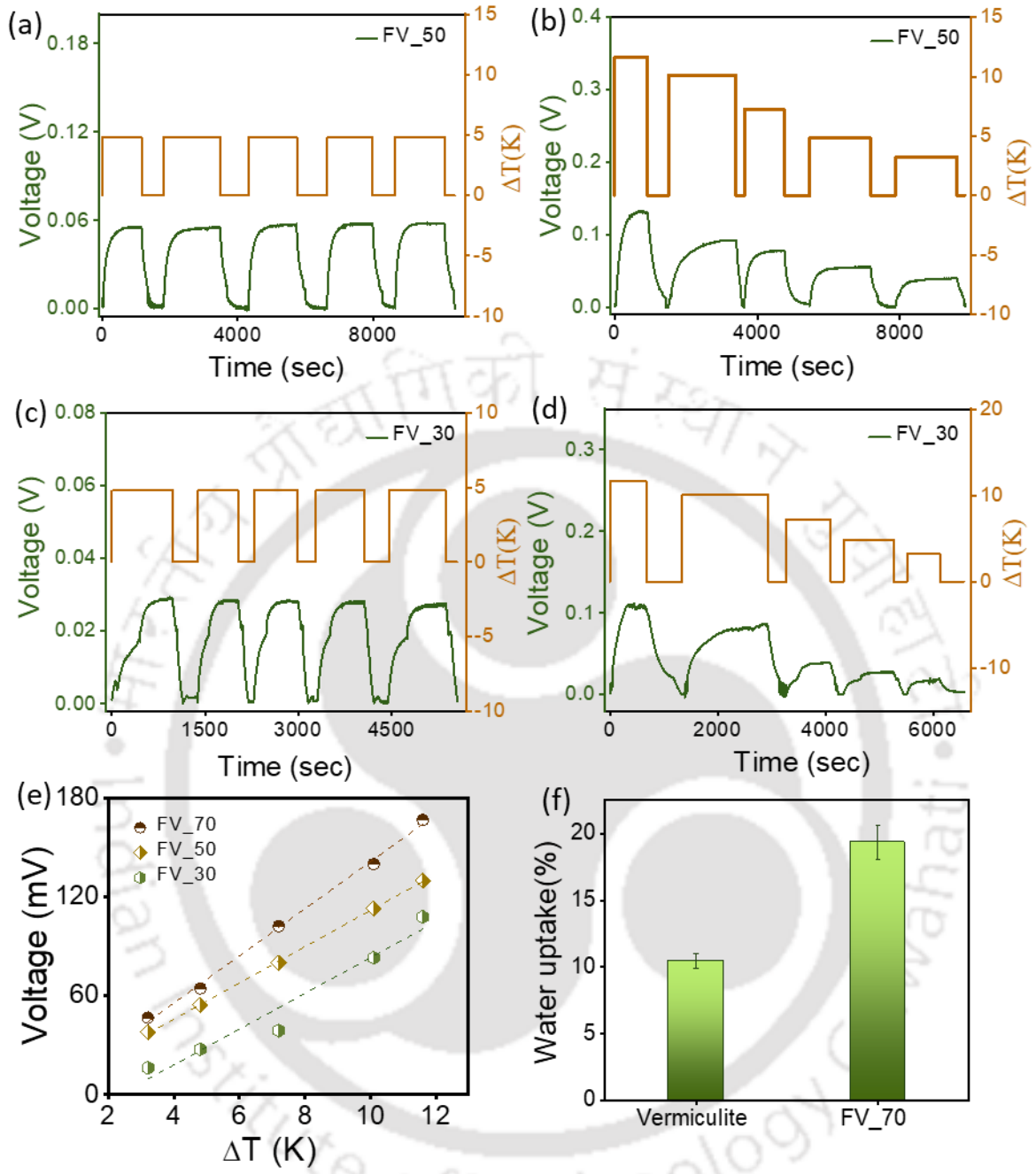

Figure 2.7: Generation of thermovoltages at ΔT = 5 K for (a) FV_50 and (c) FV_30 devices. Generation of thermovoltages at different ΔT values from (b) FV_50 and (d) FV_30 devices. (e) Linear increment of thermovoltages with temperature gradients for FV_70, FV_50 and FV_30 membranes. (f) Water uptake capacity of pristine vermiculite and FV_70 membrane.

similar conditions (Figure 2.7f). Furthermore, the dissociation of H^+ ions from the $–SO_3H$ groups is more facile than that of the surface hydroxyl groups of pristine vermiculite. This proposition is corroborated by the concurrent increase in the ionic Seebeck coefficient and

ionic conductivity with rising relative humidity levels (depicted in Figure 2.6i). As the relative humidity level increases, the water uptake of FV_70 also escalates, hydrating more nanofluidic channels, thereby facilitating proton dissociation. Consequently, the ionic conductivity and overall Seebeck coefficient value experience an increment.

2.5.4. Harvesting light energy with fabricated i-TE devices:

One of the significant advantages of ionic thermoelectric materials over the electronic TE materials is their ability to convert the abundant light energy into electricity. To showcase the potential of solar energy harvesting, one end of the FV_70 membrane was coated with carbon nanotubes (CNT), as depicted in the schematic of Figure 2.8a (details are provided in experimental section 2.3). CNTs, recognized as efficient photothermal materials, effectively can convert light into heat.[19,20] When the CNT-coated FV_70 device was exposed to varying light intensities (1500, 3000, and 6000 lux), the CNT-coated end of FV_70 heated up, resulting in non-zero temperature gradients (ΔT) across the two ends (0.7 °C, 1.1 °C, and 1.7 °C), as determined from corresponding thermal images displayed in Figure 2.8f. Concurrent with the light-induced ΔT, the i-TE devices generated thermovoltages, measured using a source meter instrument. As depicted in Figure 3b, ~5 mV of voltage was developed under a light intensity of 1500 lux, which increased up to 17 mV under the light intensity of 6000 lux, eventually diminishing to zero once the light was turned off. Figure 2.8b further demonstrates the consistent generation of voltage induced by light across numerous cycles of light illumination. Additionally, by positioning the thermoelectric device on a cooler substrate at 10 °C, the output voltages were enhanced to around 58 mV under light with an intensity of 6000 lux, aiding in the maintenance of the temperature gradient, as depicted in Figure 2.8g and h.

To enhance the light-to-electricity conversion efficiency, the FV_70 device was enclosed in a box, allowing light to illuminate only the CNT-coated region (as illustrated in the schematic of

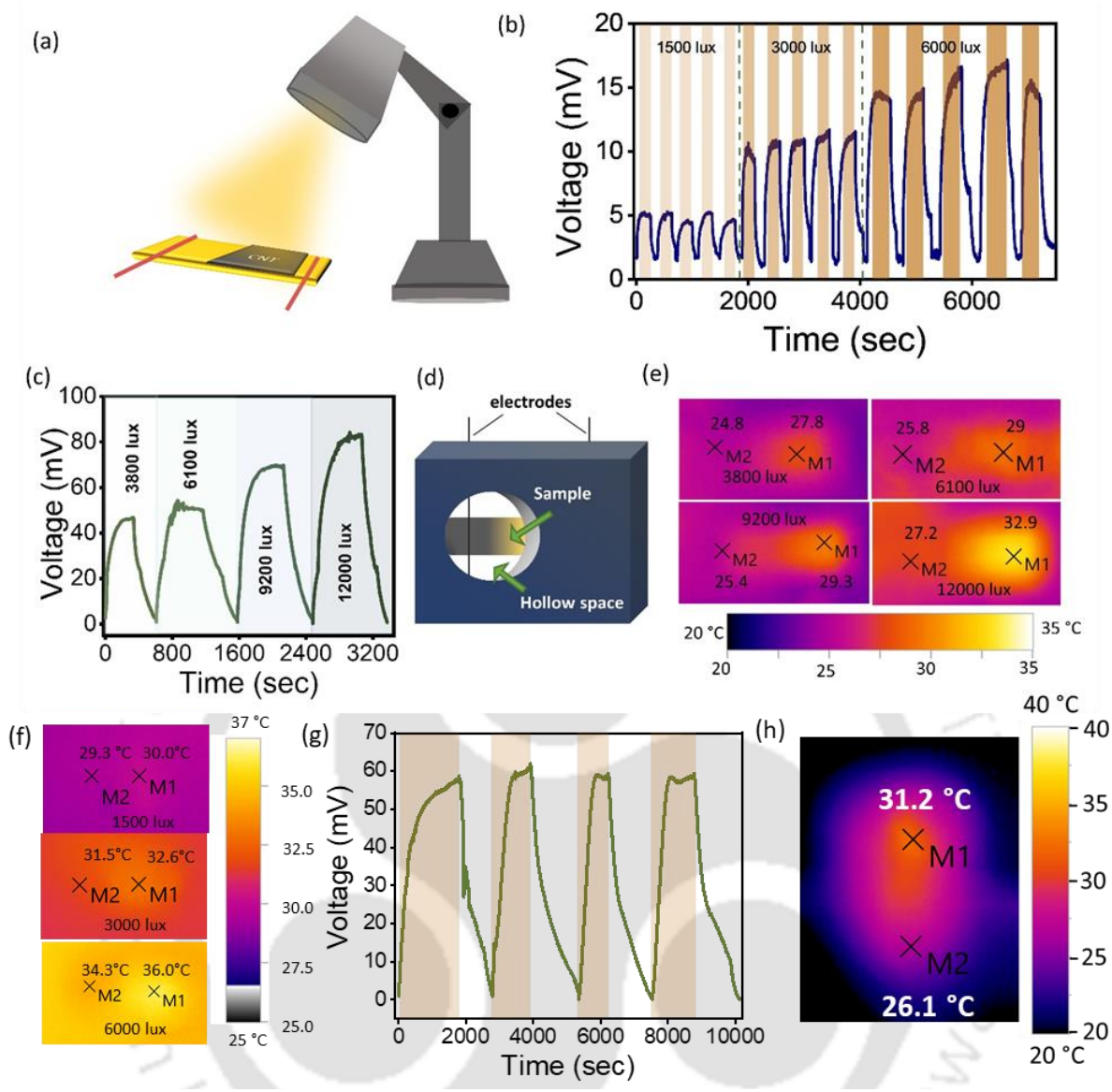

Figure 2.8: (a) Schematic representation of the light illumination process over CNT coated FV_70 membrane. (b) Generation of voltages after illumination of white light with different intensities over CNT coated FV_70 membrane and the respective (f) thermal images of CNT-coated FV_70 membranes after illumination of white light. (c) Generation of voltages, and (e) thermal images of CNT coated FV_70 membrane at different light intensities when the white light was selectively illuminated over the CNT coated region. (d) Schematic of the device used for selective illumination of white light. (g) Generation of voltages, and (h) Thermal image of CNT coated FV_70 membrane upon illumination of light with intensity 6000 lux, the temperature of bottom surface was maintained at ~10 °C

Figure 2.8d). Figure 3c illustrates the resulting output voltages under varying light intensities of 12000, 9200, 6100, and 3800 lux, with the FV_70 device generating temperature gradients of 3, 3.2, 3.9, and 5.7 °C respectively (shown in Figure 2.8e). Notably, a peak output voltage of ~82 mV was recorded under a light intensity of 12000 lux, establishing a temperature

gradient of 5.7 °C. This versatility in voltage output corresponding to different light intensities also endows the fabricated device with the capability to function as a versatile light sensor, thereby significantly broadening its potential applications.

2.5.5. High-temperature stability of clay-based i-TE materials:

Clay materials are widely recognized for their remarkable resilience in high-temperature environments.[8,21] Their remarkable thermal and chemical resilience makes clay minerals highly promising for thermoelectric applications, particularly when exposure to occasional heat shocks is anticipated. Many of the recently developed ionic thermoelectric devices rely on soft organic materials such as polyelectrolytes or hydrogels, which cannot withstand high-temperature shocks. Consequently, there is a pressing need for new ionic thermoelectric materials that offer high-temperature stability. Interestingly, i-TE devices constructed from clay minerals exhibit remarkable thermal stability, showing no signs of degradation even after exposure to 300 ºC for 5 minutes (as illustrated in Figure 2.9a). The chemical stability of these membranes, both pre- and post-heat shocks, is apparent from the unaltered FT-IR spectra depicted in Figure 2.9b. However, a decrement in intensity of peak ~670 cm^{-1} was observed. The peak at ~ 660 cm^{-1} to 790 cm^{-1} of the IR spectrum of vermiculite (or functionalized vermiculite) is attributed Si-O (730 cm^{-1}) and R-O-Si (R = Al, Mg, Fe; 675 cm^{-1}) groups, therefore, a reduction in peak intensity in this regime can be assigned to partial loss of crystallinity of the clay layers. The thermal stability of vermiculite membranes was also confirmed by the TGA analysis (Figure 2.9f). In Figure 2.9c, the thermoelectric properties of the FV_70 device before and after heat shock are compared, revealing no significant difference. The corresponding thermovoltage vs time plots are presented in Figure 2.9e. The calculated Seebeck coefficient after heat shock (13.5±1.4 mV/K) closely resembles the value obtained before heat shock (14.4±0.5 mV/K), as depicted in Figure 2.9d. Thanks to its robust thermal

stability, this category of ionic thermoelectric materials holds immense potential for expanding its application in energy generation.

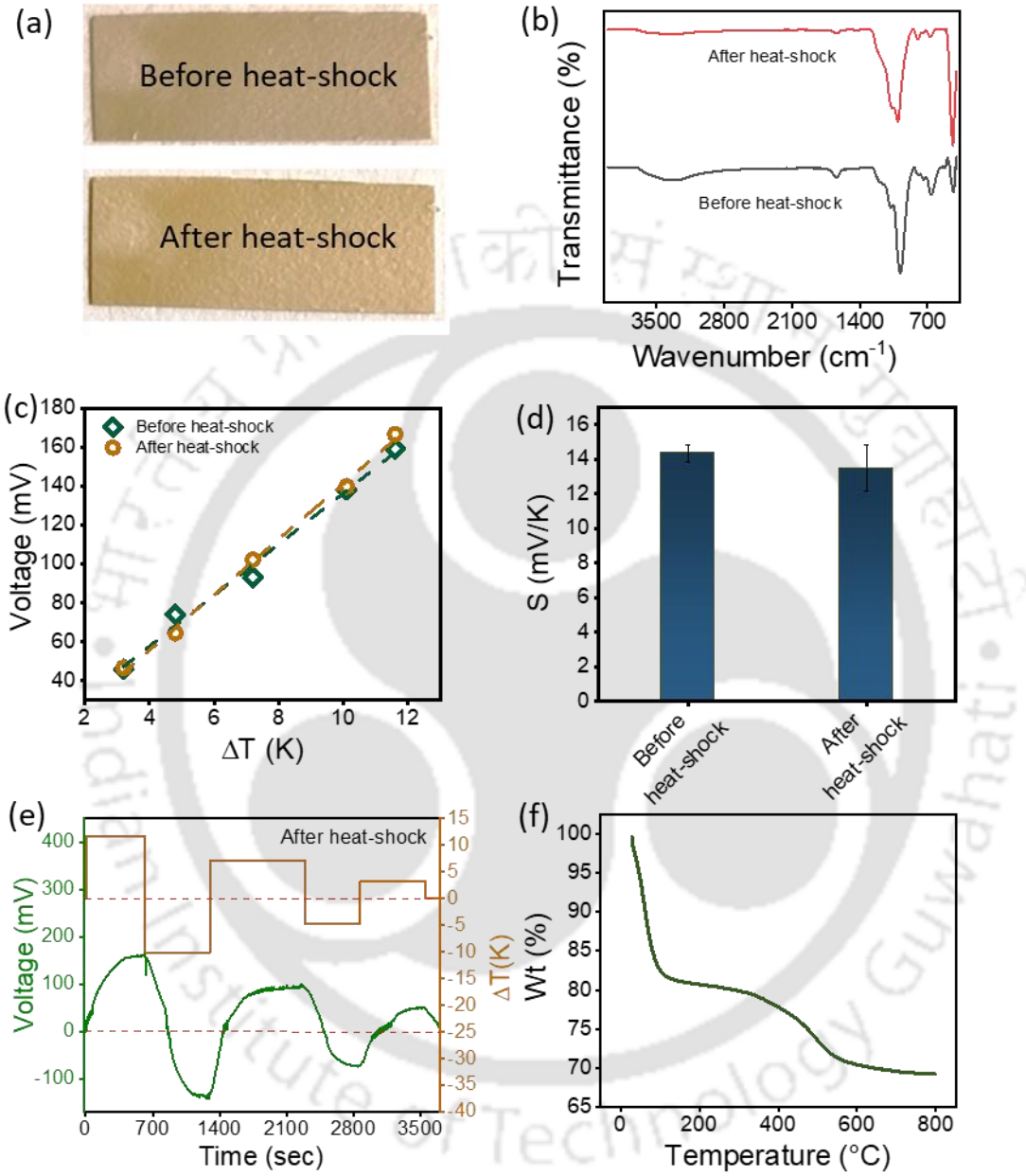

Figure 2.9: (a) Digital photograph, (b) IR spectra, (c) linear increment of thermovoltages generated, and (d) the bar diagram of Seebeck coefficients of FV_70 device before and after heat-shock at 300 °C for 5 minutes. (e) The generation of thermovoltages of FV_70 device after the heat-shock at 300 °C. (f) TGA plot of functionalised vermiculite membrane.

2.5.6. Water-assisted healing of clay-based i-TE devices:

The FV_70 membranes possess an intriguing ability to self-repair any physical or mechanical damage when exposed to a trace amount of liquid water. This property was previously reported in pristine vermiculite membranes.[22] This self-healing process is visually depicted in Figure 2.10a, where two rectangular segments of FV_70 seamlessly fuse upon introducing a small droplet of water (20 µL) between them. Notably, this water-assisted healing property restores the membrane's physical integrity and reinstates its thermoelectric properties, as illustrated in Figures 2.10b and c. Figure 2.10b illustrates the generation of thermovoltages across various temperature gradients with the healed FV_70 membrane. Additionally, the Seebeck coefficient (13.3 mV/K) calculated from the slope of ΔT versus ΔV for the healed FV_70 device (Figure 2.10c) closely resembles that of the pristine device, suggesting successful reconstruction of the majority of ion channels after the physical restoration.

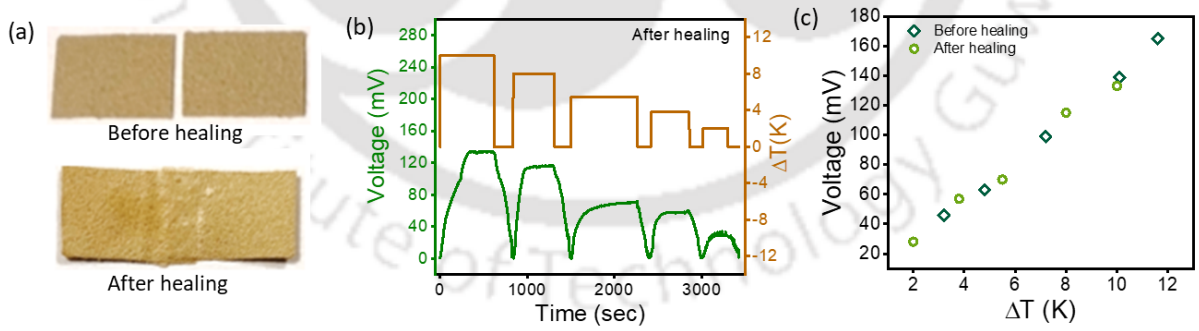

Figure 2.10: (a) Digital image, (b) thermovoltages generation, and (c) linear increment of thermovoltages of the FV_70 membrane before and after water assisted healing process.

2.5.7. Humidity tolerance of clay-based i-TE devices:

One of the major hurdles related to i-TE materials is their major dependency on relative humidity levels.[4,15] The effectiveness of these devices diminishes as the humidity level decreases, that leads to the drying out of water channels essential for ionic transport, consequently slowing down the dissociation and diffusion of ions. The whole process significantly diminishes the ionic thermopower of i-TE devices, and particularly, the FV_70

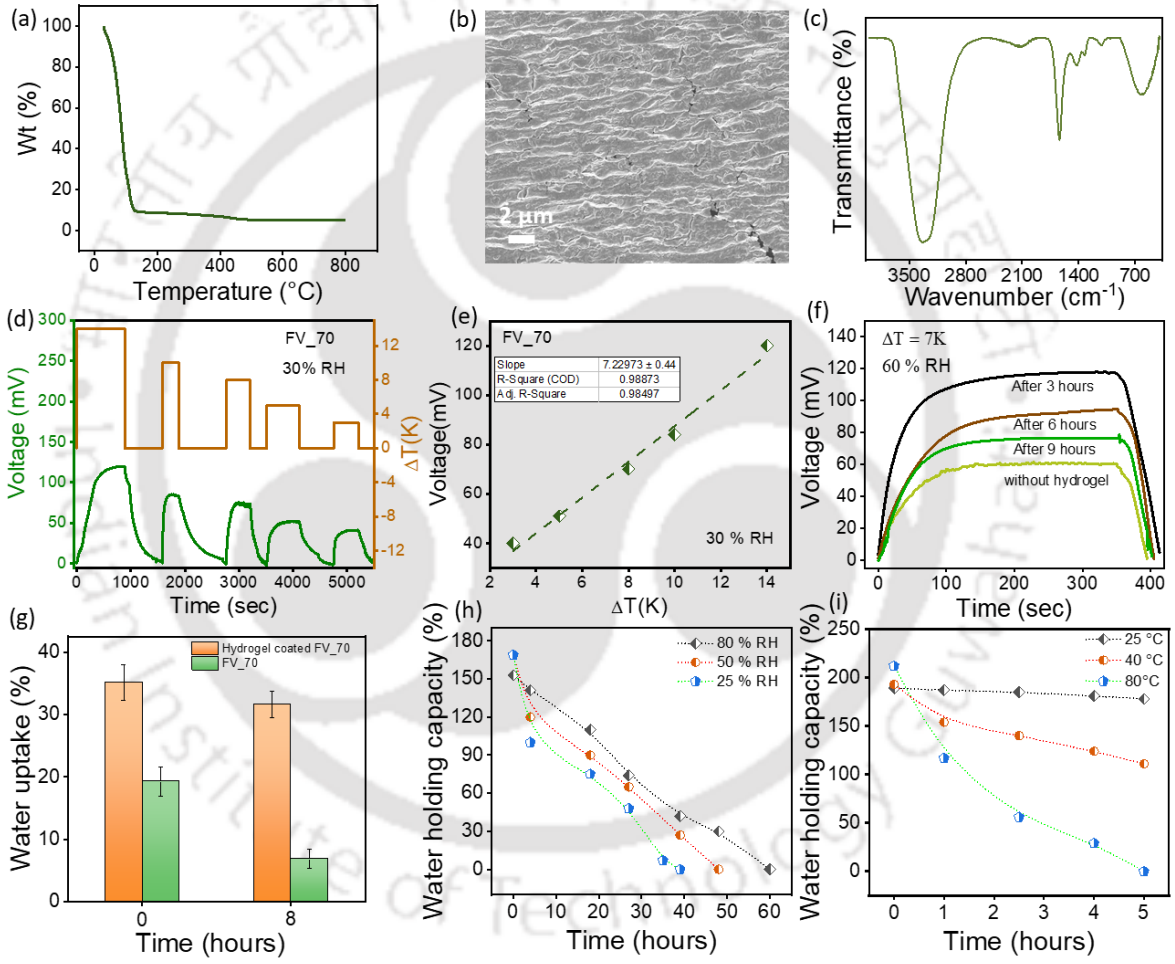

Figure 2.11: (a) TGA plot, (b) FESEM image, and (c) FT-IR spectrum of the prepared hydrogel. (d) Generation of thermovoltages, and (e) linear increment of the thermovoltages generated from hydrogel coated FV_70 membrane at 30 % RH. (f) Thermovoltages of hydrogel coated and bare FV_70 membrane at different intervals of time at 60 % RH and at $\Delta T = 7$ K. (g) Bar diagrams showing water uptake capacity vs time of FV_70 membrane with and without the hydrogel coating at RH 60 %. (h) Varying water content of the hydrogel as a function of time at different RH%. (i) Water holding capacity of the hydrogel with time at different temperatures.

membrane loses its ability to show thermoelectric responses at 30% RH level. This dependency of ionic thermopower on the RH level is shown in Figure 2.6i.

This significant challenge can be addressed by a coating of hydrogel on top of i-TE material that serves as a substantial water reservoir. Numerous polymeric hydrogels have the potential to boast water-holding capacities, effectively preventing the dehydration of ionic channels. To validate this approach, a hydrogel was synthesised using polyvinyl alcohol (PVA), borax, and LiCl (details are in experimental section 2.3, and the characterizations are shown in Figure 2.11 a, b and c). In brief, 2 grams of the hydrogel can retain up to 3.5 grams of water at an RH level of 80%, equivalent to nearly 170% of its dry weight. The water-holding capabilities of the polymeric hydrogel were examined at various relative humidity levels, as depicted in Figure 2.11h. The prepared hydrogel can retain water molecules for a duration of ~ 60 hours at a relative humidity of 80 %. It can even retain the water-holding capacity for a duration of ~40 hours at a RH level of 25 %. Additionally, the water-holding capacity of the hydrogel was analysed at different temperatures, as illustrated in Figure 2.11i. Notably, the hydrogel can be effortlessly rehydrated after complete dehydration by simply immersing it in DI water. Consequently, the diminishing power output of i-TE devices caused by the gradual dehydration of nanochannels can be prohibited by employing hydrogel coatings, thereby enhancing their practical effectiveness.

A layer of hydrogel with the dimension 1 cm x 0.8 cm was utilized for coating the FV_70 membrane and i-TE properties were studied at different dehydrating conditions. Notably, with the hydrogel coating, the FV_70 device not only displays ionic thermoelectric responses at 30% RH but also exhibits a commendable Seebeck coefficient with the value of 7 mV/K (Figure 2.11e). Figure 2.11d illustrates the respective thermovoltages of the FV_70 device under different ΔT conditions. The retrieval of thermovoltages in FV_70 membrane under relatively lower humidity levels is attributed to the hydration of the nanochannels within the

FV_70 membrane, facilitated by water molecules from the hydrogel (Figure 2.11g). Figure 2.11g specifically illustrates the water retention capability of the FV_70 membrane under 60% RH conditions, comparing the initial value with measurements taken after 8 hours, both with and without the hydrogel coating. Figure 2.11f compares the thermovoltage of the FV_70 device coated with hydrogel, subjected to a ΔT of 7 K at 60% RH, with a similar uncoated device over various time intervals. After 3 hours, the voltage reached nearly 118 mV, declining to around 94 mV after 6 hours and approximately 76 mV after 9 hours.

2.5.8. Applicability of clay-based i-TE devices:

Ensuring the scalability of output potential is crucial for the practical application of energy harvesting devices. To verify the linear scalability of FV_70 devices, different numbers of i-

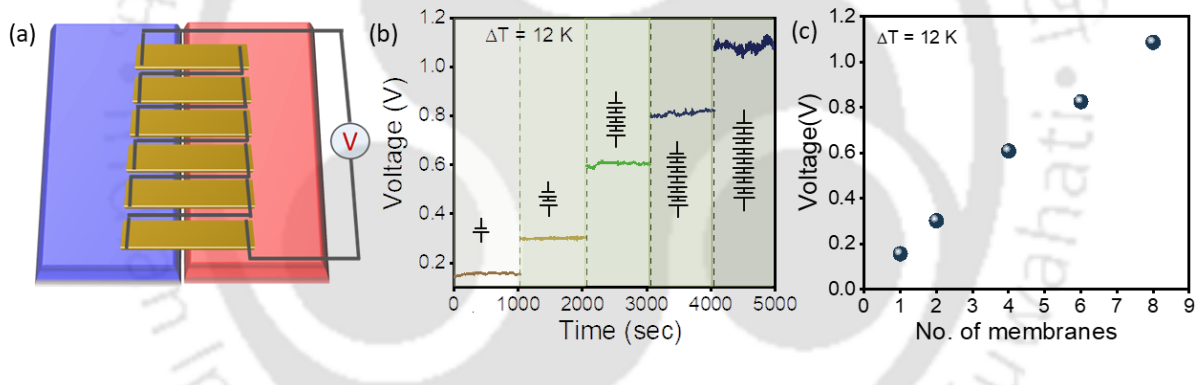

Figure 2.12: (a) Schematic representation, (b) generation of thermovoltages, and (c) linear increment of the voltages of different number of FV_70 devices in series connection.

TE devices were connected in series, as illustrated in the schematic diagram in Figure 2.12a. The linear increment in output voltages with the increasing number of FV_70 devices, maintained at ΔT = 12 K can be observed in Figure 2.12c. An output voltage of 1.08 V was achieved with eight numbers of such FV_70 devices (as shown in Figures 2.12b and c), indicating the feasibility of achieving any desired output voltage by connecting the different numbers of i-TE devices.

Clay-based i-TE devices offer a unique opportunity for developing fire alarm systems, considering their remarkable high-temperature stability, as demonstrated in Figure 2.9. While commonly explored i-TE devices cannot withstand open fire, vermiculite, known for its

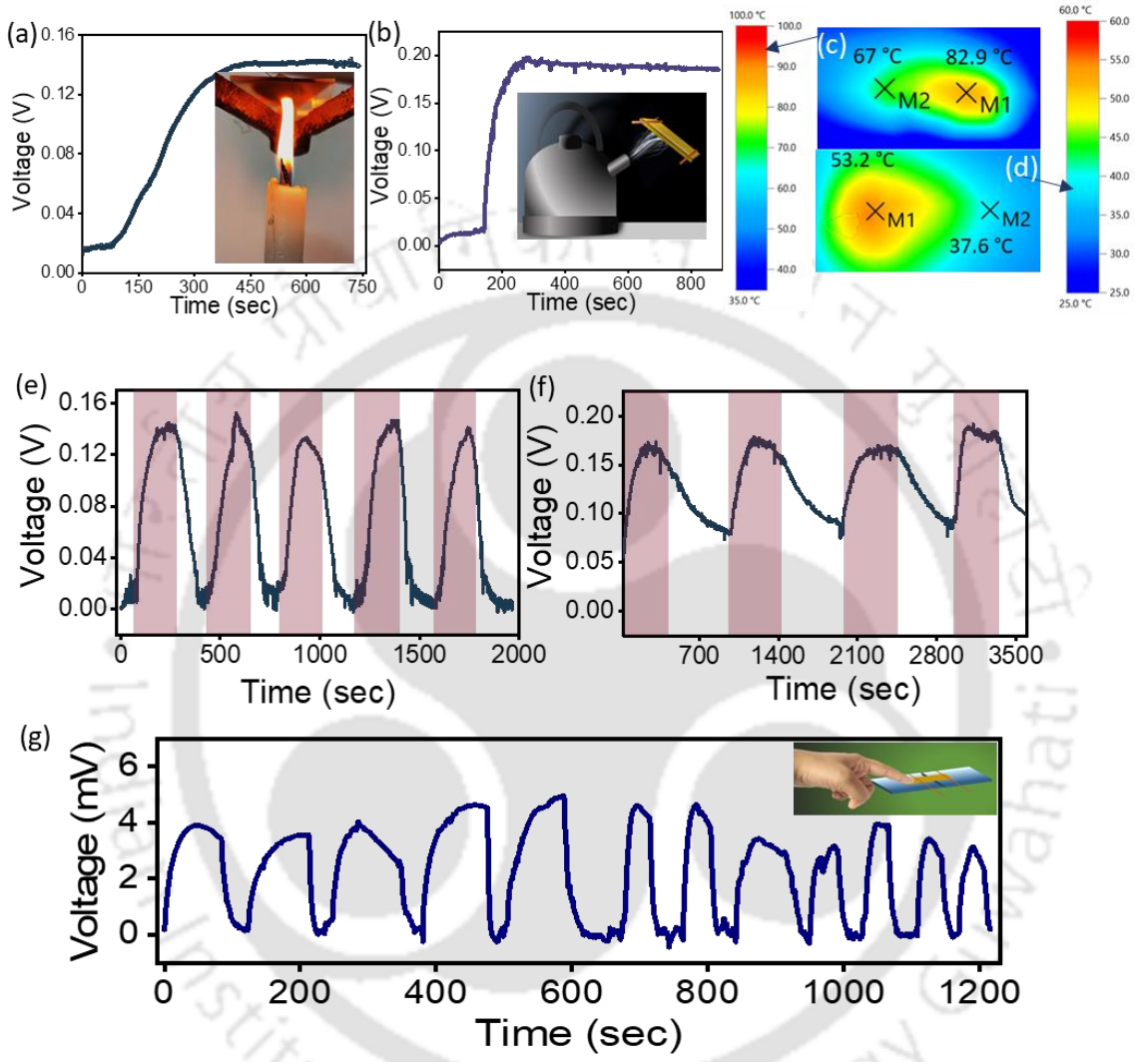

Figure 2.13: (a) Generation of voltage when the thermoelectric device was directly exposed to open flame, the insight represents the digital photograph of experimental setup. (b) Generation of voltage from the thermoelectric device when one part of it is exposed to hot water steam, the inset represents the experimental setup. Thermal images of FV_70 membranes when it is exposed to (c) open flame and (d) hot steam. Generation of thermovoltages from FV_70 for multiple numbers of iterations when exposed to (e) open flame and (f) hot water steam. (g) Responses of the thermoelectric device when one end of the membrane is in contact with the hand.

exceptional temperature resilience, presents a promising alternative. To evaluate its suitability for such demanding applications, an FV_70 device was subjected directly to an open flame exposure, as depicted in Figure 2.13a (refer to experimental section 2.3 for details). An output

voltage of approximately 141 mV was recorded when one section of the FV_70 device faced direct flame exposure, generating a temperature gradient of 15.9 °C (Figure 2.13a and Figure 2.13c). By setting a specific voltage threshold in a millivolt signal alarm, a fire alarm system can be established, activating the alarm when the voltage exceeds the predetermined limit. Notably, the FV_70 device sustained multiple exposures to open fire without significant reduction in its output voltage, as illustrated in Figure 2.13e.

Likewise, clay-based i-TE devices also offer a promising avenue for harvesting electricity from steam, presenting opportunities for large-scale industrial applications. Industrial processes such as petroleum refining, steel manufacturing, and cement production emit vast quantities of waste heat in the form of steam. Harnessing even a fraction of this energy could yield substantial benefits. To explore the feasibility of steam energy harvesting, one end of an FV_70 i-TE device was exposed to steam, as illustrated in the inset of Figure 2.13b. The directional exposure to steam created a temperature gradient of 15.6 °C (Figure 2.13d) across the FV_70 devices, resulting in a voltage output of approximately 190 mV (Figure 2.13b). A continuous generation of ionic thermovoltage was recorded for ~900 seconds without showing any physical damage to the membrane. Moreover, clay-based i-TE devices can withstand exposure to hot water steam for multiple cycles without a notable performance decrease, as demonstrated in Figure 2.13f. This successful demonstration of generating thermovoltages from hot water steam suggests potential futuristic applications of i-TE devices in recovering electrical energy from the substantial steam emissions of large-scale industrial processes. The successful generation of thermovoltages from hot water steam opens up exciting possibilities for the future application of i-TE devices.

The potential of clay-based i-TE devices in touch sensing applications can also be explored due to their high sensitivity towards ionic thermovoltages. Figure 2.13g illustrates how human touch can generate a temperature gradient that induces ionic thermovoltages across the FV_70

devices. Alongside human touch, these devices produce periodic electrical voltage pulses that cease once the contact is released. Therefore, such heat-sensitive, low-cost, biocompatible i-TE devices could be an alternative for future healthcare applications.

2.6. Conclusions:

In summary, we have showcased the potential of naturally abundant and thermally stable clay minerals in crafting highly functional i-TE devices, thereby expanding the practical applications of ionic thermoelectricity. Furthermore, enhancement of the ionic thermopower of pristine clay devices is achievable through the surface functionalisation of vermiculite nanosheets. For instance, we achieved an almost twofold increment in ionic thermopower by transforming the surface -OH group of vermiculite-based i-TE devices into $–SO_3H$ groups. With the abundance of natural clay minerals and the diverse possibilities for surface modifications, these clay materials hold promise for numerous exciting opportunities in studying and producing ionic thermoelectric materials. Moreover, our experimentation with CNT drop-casted clay membranes demonstrates the potential for converting light energy into electricity. With the recent advancements in novel photothermal and i-TE materials, a synergistic integration of the two could revolutionise the harnessing of abundant sunlight into electrical energy via ionic thermoelectricity. Additionally, we have illustrated how an effective combination of hydrogels and ion channels can address the primary challenge of i-TE devices, particularly their compatibility at low-humidity conditions. The PVA, borax, and LiCl-based hydrogel significantly enhanced the performance of clay-based i-TE devices under low humidity conditions. Notably, due to the robustness of clay minerals, these devices can withstand higher temperature shocks, including exposure to open flames, thus paving the way for their utilization in fire alarm systems. Likewise, our demonstration of generating thermovoltages from hot water steam underscores the potential of i-TE devices in harvesting electrical energy from large-scale industrial water steam generators. Furthermore, the water-

assisted healing of clay-based i-TE devices ensures their resilience and suitability for challenging environments. In essence, the versatility of clay-based i-TE devices across multiple domains holds great promise for expanding the application horizons of i-TE technology.

2.7. References:

1 C. Forman, I. K. Muritala, R. Pardemann and B. Meyer, *Renew. Sustain. Energy Rev.*, 2016, **57**, 1568–1579.

2 S. Sun, M. Li, X.-L. Shi and Z.-G. Chen, *Adv. Energy Mater.*, 2023, **13**, 2203692.

3 Z. A. Akbar, J. W. Jeon and S. Y. Jang, *Energy Environ. Sci.*, 2020, **13**, 2915–2923.

4 D. Zhao, H. Wang, Z. U. Khan, J. C. Chen, R. Gabrielsson, M. P. Jonsson, M. Berggren and X. Crispin, *Energy Environ. Sci.*, 2016, **9**, 1450–1457.

5 D. Zhao, A. Würger and X. Crispin, *J. Energy Chem.*, 2021, **61**, 88–103.

6 M. A. Rahman and M. Z. Saghir, *Int. J. Heat Mass Transf.*, 2014, **73**, 693–705.

7 R. K. Gogoi and K. Raidongia, *Adv. Mater.*, 2017, **29**, 1–8.

8 J.-J. Shao, K. Raidongia, A. R. Koltonow and J. Huang, *Nat. Commun.*, 2015, **6**, 7602.

9 K. Saha, J. Deka and K. Raidongia, *ACS Appl. Energy Mater.*, 2021, **4**, 8410–8420.

10 T. J. Konch, T. Dutta, A. B. Neog, R. Gogoi and K. Raidongia, *J. Phys. Chem. C*, 2021, **125**, 17939–17949.

11 C. Sinistri, 1966, **21**, 753–755.

12 S. L. Kim, H. T. Lin and C. Yu, *Adv. Energy Mater.*, 2016, **6**, 1600546.

13 S. A. Suvorov and V. V Skurikhin, *Refract. Ind. Ceram.*, 2003, **44**, 186–193.

14 K. Saha, J. Deka, R. K. Gogoi, K. K. R. Datta and K. Raidongia, *ACS Appl. Nano*

Mater., 2022, **5**, 15972–15999.

15 F. Jiao, A. Naderi, D. Zhao, J. Schlueter, M. Shahi, J. Sundström, H. Granberg, J. Edberg, U. Ail, J. Brill, T. Lindström, M. Berggren and X. Crispin, *J. Mater. Chem. A*, 2017, **5**, 16883–16888.

16 Z. Guo, J. Chen, J. J. Byun, R. Cai, M. Perez-Page, M. Sahoo, Z. Ji, S. J. Haigh and S. M. Holmes, *J. Energy Chem.*, 2022, **64**, 323–334.

17 A. Vinod, Y. V. Reddy Bhimavarapu, M. Hananovitz, Y. Stern, S. Gulec, A. K. Jena, S. Yadav, E. J. Gutmark, P. K. Patra and R. Tadmor, *ACS Appl. Polym. Mater.*, 2022, **4**, 8527–8535.

18 M. Jeong, J. Noh, M. Z. Islam, K. Kim, A. Sohn, W. Kim and C. Yu, *Adv. Funct. Mater.*, 2021, **31**, 1–7.

19 P. Garg, A. Bikash Neog, K. Mayawad, A. Kumar Rajak, P. Deka, R. Kumar Gogoi and K. Raidongia, *Chem. Eng. J.*, 2024, **480**, 148181.

20 B. Han, Y. L. Zhang, Q. D. Chen and H. B. Sun, *Adv. Funct. Mater.*, , DOI:10.1002/adfm.201802235.

21 F. J. Osuna, J. R. Chaparro, E. Pavon and M. D. Alba, *Ceram. Int.*, 2023, **49**, 5279–5291.

22 R. K. Gogoi and K. Raidongia, *J. Mater. Chem. A*, 2018, **6**, 21990–21998.

Chapter 3

Ionic Thermoelectric Properties of Reconstructed Lamellar Vanadium Pentoxide Membranes

Summary

Owing to the several advantages of two-dimensional (2D) materials, such as selective permeability, tunable pore size and surface property, chemical stability and durability, along with the scalability and relatively easy fabrication techniques, these materials have been elaborately studied in the realm of different energy harvesting techniques. In this Chapter, a lamellar V_2O_5 membrane was reconstructed out of exfoliated V_2O_5 nanosheets to study the ionic thermoelectric responses. A reasonably good ionic thermoelectric behaviour was observed from a pristine V_2O_5 membrane that exhibited an ionic Seebeck coefficient of 14.5±0.5 mV/K at 90% RH level. The ionic thermopower was significantly enhanced (~80% improvement, ionic Seebeck coefficient ~ 26.3±0.7 mV/K) by intercalating poly(4-styrenesulfonic acid) (PSS) molecules between 2D sheets of V_2O_5. The importance of nanoconfinement in the enhancement of overall ionic thermopower was verified by altering the morphology of V_2O_5 from nanosheet to nanobelts. Unlike organic or polyelectrolyte materials-based ionic thermoelectric materials, the V_2O_5-based system can easily sustain exposure to high temperatures (~200 °C, 5 minutes) without deteriorating its physical and chemical structure. These materials also retain their ionic thermoelectric properties. The retention of ionic thermoelectric properties of the V_2O_5-PSS membrane after heat shock justifies the protection of PSS molecules present in between the interlayer spaces, as the pristine PSS molecules are incapable of withstanding at such a high temperature. Moreover, the V_2O_5-based

thermovoltage generation from direct exposure to a hot water kettle or to an IR light, displaying its potential for developing a new class of ionic thermoelectric materials.

3.1. Introduction:

Recently, due to the attainment of higher ionic thermopower and the adoption of relatively simpler fabrication techniques have garnered significant attention for i-TE materials, leading to a notable shift in focus away from traditional e-TE materials. Till now, ionic liquids, polyelectrolytes, hydrogels and hybrid of these materials have been extensively studied in the realm of ionic thermoelectricity.[1–3] However, each of these material classes comes with its own set of drawbacks such as polyelectrolyte-based materials entail complex synthesis processes, limited stability, and a restricted operable temperature range; ionic liquid-based systems face higher expenses, lack long-term stability, and exhibit low ionic conductivity; similarly, hydrogel-based systems encounter issues such as swelling and shrinking, limited thermal stability, and restricted scalability.[4–7] In this context, the emergence of a new class of i-TE material would be highly welcomed if engineered to tackle these unresolved challenges. Understanding the nature and mechanistic insight of the origin of i-TE properties, the 2D nanofluidic membranes can potentially mitigate certain aspects of these challenges. Depending on several properties of these 2D materials, such as the surface charge or the presence of surface functional groups, tunability of the nanochannels, intercalation of external active species or surface functionalisation, the i-TE can be chosen and accordingly modified for enlargement of ionic thermopower. These 2D material-based nanofluidic systems have already been utilized for several other applications such as water purifications, light-induced ionic transport, chemical reactions in nanofluidic confinements, energy extraction from humidity gradients, concentration gradients, pressure-driven flow, etc.[8–15] High-temperature stability, scalability, cost-effectiveness, and easy fabrication techniques also help to explore these materials in emerging fields.[16–19] Therefore, the 2D material-based nanofluidic systems could emerge as an

alternative class of material, addressing the current challenges and enhancing the overall efficiency of i-TE materials in ionic thermoelectricity.

3.2. Scope of the present investigation:

The efficiency of an ionic thermoelectric (i-TE) material is primarily dependent on the selective diffusion of ions under the temperature gradient.[20–22] In that context, polyelectrolytes constituting a mobile ion and an immobile counterpart are of primary importance. Similar selectivity towards ions of specific charge polarities is observed with the lamellar nanofluidic membrane of 2D materials (like V_2O_5).[18] This work, therefore, demonstrates the utilization of a reconstructed lamellar nanofluidic membrane as an i-TE material and the intercalation of a polyelectrolyte constituting mobile H^+ ions in between the nanochannels of the nanofluidic membrane for the enhancement of i-TE performance. The polyelectrolyte is capable of enhancing ionic thermopower by ~3 fold through intercalation of ionic charge carriers inside the nanofluidic channels. Therefore, a path was developed to determine the importance of nanoconfinement in the enlargement of overall ionic thermopower by changing the morphology of V_2O_5 nanosheets into nanobelts. The study further demonstrates a mechanistic insight to investigate the origin of ionic thermovoltages by carefully exposing the D_2O molecules to the active material. Interestingly, the intercalated polyelectrolyte molecules were observed to be effectively shielded by the V_2O_5 nanosheets even at elevated temperatures, preserving the initial thermoelectric properties. This underscores the significance of hybrid materials in exploring i-TE properties. Additionally, this study demonstrates the water-assisted healing property of both pristine and composite nanofluidic membranes, broadening its future applicability. An experimental set up was further designed to harvest energy directly from a light source and the direct exposure of a hot water kettle.

Material structure and properties: The bulk form of vanadium pentoxide, V_2O_5, exhibits an orthorhombic crystal structure, specifically belonging to the P_{mmn} space group. This crystal lattice is defined by lattice parameters: a = 11.51 Å, b = 4.37 Å, and c = 3.56 Å. Within this structure, the physical layers are aligned along the (010) direction and comprise distorted V_2O_5 pyramids. These pyramids share edges and corners, with each elementary cell containing two units of V_2O_5, totalling 14 atoms. Additionally, there are six planar layers of atoms, consisting of four oxygen layers and two vanadium layers. The bulk structure of V_2O_5 can be exfoliated into individual layers and reconstructed to impart unique properties. V_2O_5 finds applications across various fields, including electrochemical energy storage, catalysis, gas sensors, electrochromic devices, biomedical applications, and energy generation.

Poly(4-styrenesulfonic) acid (PSS) is a polymer containing sulfonic groups (-SO_3H) typically attached to the benzene ring of the polystyrene backbone. The presence of sulfonic groups renders PSS ion-conductive and highly hygroscopic. Its ion-conductive nature enables its use in ion exchange resins, membrane separation processes, fuel cells, and various energy harvesting techniques.

3.3. Experimental section:

Materials: Vanadium pentoxide, V_2O_5, was purchased from SRL Pvt., Ltd, Poly (4-styrenesuphonic acid) (PSS) and hydrochloric acid were purchased from Sigma Aldrich co., Ltd, Hydrogen Peroxide was purchased from Finar., Ltd, Conductive Silver Paste was purchased from Alfa Aesar Co., Ltd.

Exfoliation of bulk V_2O_5 crystals: Bulk V_2O_5 crystals were exfoliated by treating the same with hydrogen peroxide (H_2O_2) in an ice bath (0 - 5 °C). Typically, 2.38 g of V_2O_5 was dispersed in 25 ml of deionized water. Slowly, 25 ml of 50% H_2O_2 was added to the V_2O_5 dispersion, resulting in vigorous bubbling and the formation of a brown precipitate, which

gradually turned into a gel. Subsequently, the prepared gel was diluted with 150 ml of deionized water and sonicated for 30 minutes to produce a 15 mg/mL dispersion of V_2O_5.

Fabrication of V_2O_5 Membrane (VO-M): The VO-Ms were fabricated using the previously prepared aqueous dispersion of V_2O_5. A 10 ml solution containing V_2O_5 at a concentration of 15 mg/mL was filtered under vacuum through a PTFE membrane with a pore size of 100 nm. Subsequently, the filtered material was dried under ambient conditions to obtain a freestanding V_2O_5 membrane.

Fabrication of V_2O_5 – PSS composite membrane (VO-PSS-M): For the fabrication of composite thin film membrane, 10 mL of the V_2O_5 dispersion at a concentration of 15 mg/mL was combined with a suitable quantity of PSS polymer (5%, 10%, 18%, or 31% wt % of PSS) and subjected to sonication for 20 minutes. Subsequently, the resulting solution was similarly filtered under vacuum through a PTFE membrane with a pore size of 100 nm and then dried to yield freestanding composite membranes.

Preparation of PSS membrane: A pure Poly(4-styrenesulphonic acid) membrane was created by drop-casting 3 mL of an 18 wt% polymeric solution in H_2O (M_w=75000) onto a glass slide measuring 7.5 cm × 2.5 cm. The drop-casting solution was then dried inside a hot air oven to produce a flexible polymeric membrane with uniform thickness.

Exchange of H^+ ions with D^+ ions for VO-M and VO-PSS-M: D_2O-exposed VO-M and VO-PSS-M were prepared by keeping both of the membranes inside a closed chamber with desiccants (RH = 10 %) for 24 hours and after that both of them were exposed with D_2O vapours (RH = 80 %).

Preparation of V_2O_5 nanobelts: V_2O_5 nanobelts were prepared from the V_2O_5 nanosheets through hydrothermal treatment. Typically, 15 mL of the nanosheet dispersion was placed in a

23 mL autoclave at 180°C for 18 hours, resulting in a green-colored product. The sample underwent several washes with DI water and ethanol before its utilization.

Fabrication of V_2O_5 nanobelts based membrane: The freestanding membrane of V_2O_5 nanobelts were prepared through vacuum filtration of 15 mL (10 mg/mL) aqueous dispersion of V_2O_5 nanobelt using a 100 nm pore size PTFE membrane. After completion of the process the membrane was dried in ambient atmosphere and peeled off to obtain the freestanding membrane.

Preparation of V_2O_5 nanobelt – PSS composite Membrane (VO-NB-PSS): Composite membranes comprising V_2O_5 nanobelts and PSS were fabricated by blending 15 mL of a 10 mg/mL aqueous dispersion of V_2O_5 nanobelts with 18 wt% PSS polymer. The mixture underwent sonication for 20 minutes before being vacuum-filtered through a 100 nm pore size PTFE membrane and dried in an open atmosphere.

i-TE device fabrication: Devices were constructed atop a stage comprising two glass slides (2.5 cm x 2.5 cm) to maintain an air gap of approximately 2 mm, thus preventing undesired heat transfer. Rectangular strips of suitable dimensions (2 cm x 0.8 cm) were cut from either the freestanding VO-M or the various composite membranes. These strips were affixed onto the appropriately positioned glass slides using adhesive tape. Two copper electrodes, separated by a distance of 1.5 cm, connected the membranes using conductive silver paste.

The ionic thermoelectric device was positioned above two Peltier devices, causing one side of the device to become warmer and the other side cooler. The temperature differential was measured using a Testo 735 temperature sensing instrument equipped with a K-type thermocouple. The Peltier devices were activated by a DC regulated power supply (METARAVI TM – RPS 30005), while the outputs of the device were monitored using a Keithley Sourcemeter (2450) instrument.

Current-voltage measurements: The I-V curves of the VO-M were obtained within the voltage range of -1 V to 1 V, both without and with a temperature gradient applied across the membrane. For measurements conducted without any temperature gradient, the initial data set was collected from 0 V to 1 V with a delay of 1 second. Subsequently, after a waiting period of 20 minutes to allow the device to return to its original state, the second data set was obtained from 0 V to -1 V with the same delay. Each scan comprised 101 points. Upon completion of the measurements, these two data sets were merged and presented. The measurements were taken in a similar way with the temperature gradient of 15 K at different intervals of time.

3.4. Characterizations: The morphologies of both pure V_2O_5 and the composites were examined using a field emission scanning electron microscope (FESEM) (Zeiss, model: Sigma). Additionally, energy-dispersive X-ray analysis was performed using the same FESEM instrument to analyse the elemental composition. The interlayer spacing in V_2O_5 and V_2O_5 nanochannel composites was determined using an X-ray diffractometer (XRD) (Rigaku, model: Micromax-007HF), providing insights into their structural characteristics. The mechanical strength of VO and VO-PSS composite membranes was assessed using a 5 kN universal testing machine (UTM) (Zwick Roell, model: Z005TN), allowing for the measurement of their physical durability and robustness. IR spectroscopy was conducted using a Perkin Elmer instrument (Spectrum Two) to analyse the chemical bonds present in the samples, while thermal stability was evaluated through thermogravimetric analysis (TGA) (Netzsch, Model: STA449F3A00). The surface morphology of the V_2O_5 composite was characterized using atomic force microscopy (AFM) (Oxford, model: Cypher), providing detailed information about the topography and structure at the nanoscale. The ζ potential of the aqueous dispersion of nanosheets was measured using a Zetasizer instrument (Malvern, Nano-ZS90), aiding in the understanding of their stability and colloidal behavior. Furthermore, compositional analysis was carried out using X-Ray Photoelectron Spectroscopy (XPS)

(Thermo Fisher Scientific Pvt. Ltd., UK, model: ESCALAB Xi+), offering insights into the elemental composition and chemical states of the materials.

3.5. Results and Discussion:

3.5.1. Characterisations of exfoliated nanosheets:

In order to study i-TE properties, a freestanding VO-M membrane was prepared through the restacking of exfoliated 2D nanosheets of V_2O_5. The formation of V_2O_5 nanosheets were confirmed from the AFM image shown in Figure 3.1a. A digital photograph of the freestanding VO-M and VO dispersion is shown in Figure 3.1b. The exfoliated 2D flakes of V_2O_5 were characterized (Figure 3.1a to 3.1f) and demonstrated to exhibit a high negative zeta potential (-44.5 ± 0.8 mV, Figure 3.1i). The lamellar structure of the reconstructed VO-M is evident from the cross-sectional Field Emission Scanning Electron Microscopy (FESEM) image in Figure 3.1d and X-ray diffraction (XRD) pattern in Figure 3.1f.

In order to study the ionic conductivity of VO-M, a device was fabricated by affixing two Cu electrodes on either side of a rectangular piece of VO-M using conductive Ag paste. These measurements were performed in a humidity-controlled chamber where the relative humidity levels (RH %) were adjusted using a desiccant (Silica Gel) and water vapours. Notably, the conductivity values were observed to rise with the increasing relative humidity (RH%) in the atmosphere (Figure 3.1h).[23] The dependency of ionic conductivity on RH level can be ascribed to the hygroscopic nature of VO-M. The gravimetric analysis of VO-M's water-absorption characteristics demonstrated an elevation of water intake with increasing humidity levels, as illustrated in Figure 3.1h, which correlates with the enhanced conductivity observe in Figure 3.1h. This phenomenon is attributed to the formation of additional pathways facilitating proton migration across the membrane. The rationale behind this lies in the increased proportion of fully hydrated channels within the membrane as RH increases. For instance, assuming that all

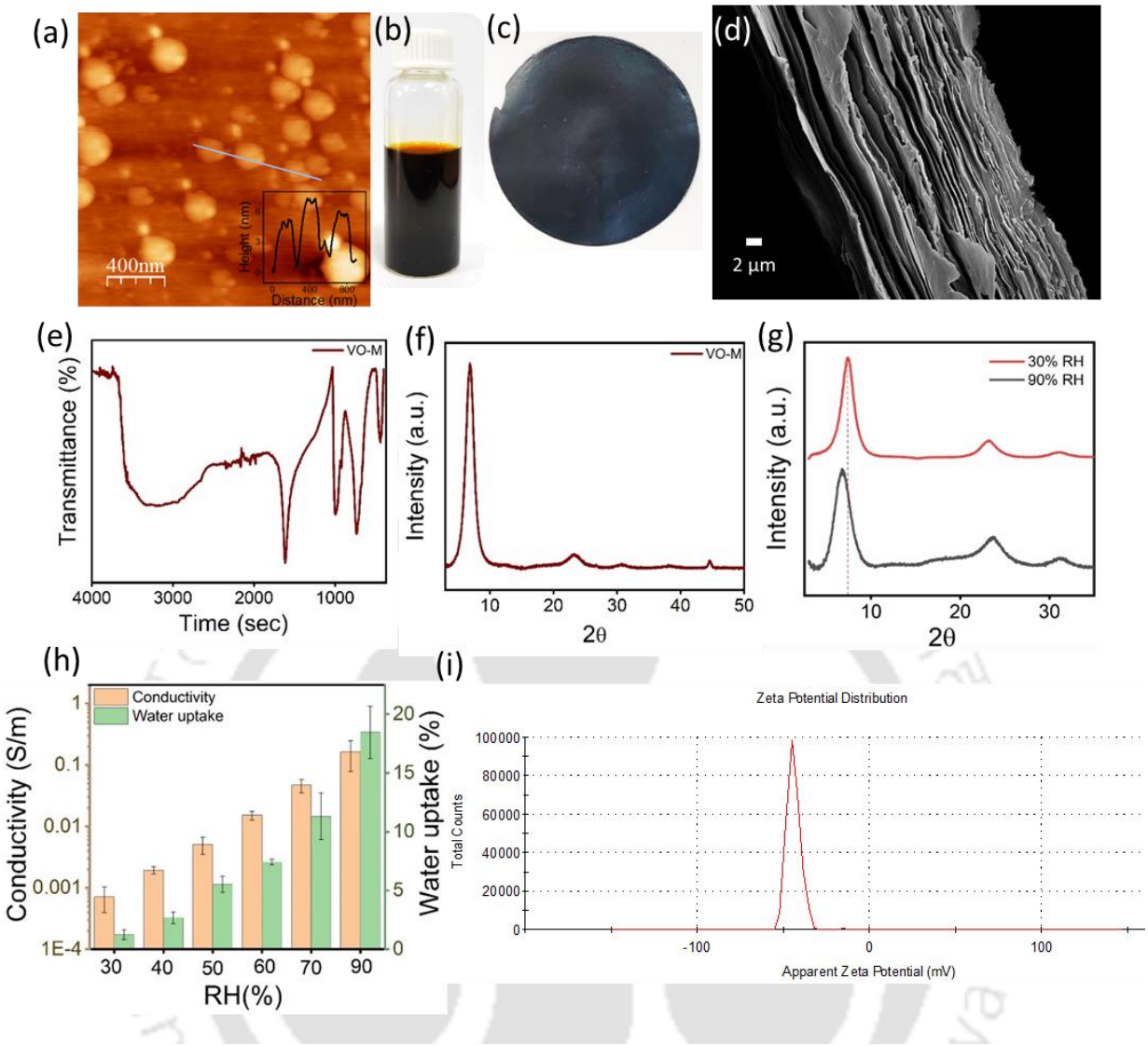

Figure 3.1: (a) AFM image of V_2O_5 nanosheets (inset shows height profile of the flakes). The AFM image (and height profile) of V_2O_5 flakes reveal the average height of the flakes to be ~ 6 nm with lateral dimensions in the range of a few hundred nanometres. (b Digital photograph of an aqueous dispersion of V_2O_5 flakes, obtained by exfoliating bulk crystals of V_2O_5, (by treating them with ice cold hydrogen peroxide solutions). (c) Digital photograph of a freestanding VO-M. (d) Cross-sectional FESEM image of VO-M. (e) FT-IR spectrum of VO-M. (f) pXRD pattern of VO-M, the intense (100) reflection indicate lamellar stacking of the V_2O_5 nanosheets. (g) pXRD pattern for VO-M at different relative humidity (RH) levels. The shift in the 2θ value corresponding to (100) reflection reveal increase in the interlayer space with the increasing RH levels. (h) Ionic conductivity, and water uptake values of VO-M membranes at different relative humidity (RH) levels. (i) Zeta potential distribution curve of aqueous dispersion of V_2O_5 nanosheets. The average zeta potential is -44.5 ± 0.8 mV.

absorbed water molecules form an interconnected network of water channels, at RH = 90%, nearly 80% of the nanochannels in VO-M will be fully hydrated. Detailed calculations are given below:

Calculation of the percentage of VO nanochannels saturated with atmospheric water:

To obtain an approximate assessment of the nanochannels filled with water in VO-M under specific atmospheric conditions, we correlate the weight increase of dehydrated VO-M upon exposure to high humidity levels, such as RH = 90% at room temperature, with its geometry.

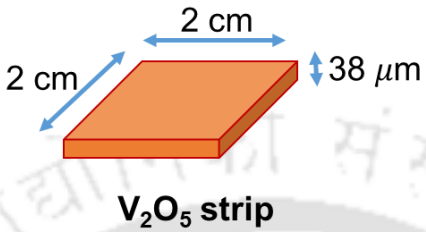

Initially, the total available free space within a VO-M strip of known dimensions was determined using the following equation.

Total free volume in V_2O_5 strip (V_{free}) = Total Volume between the V_2O_5 slabs (V_{inter}) + Volume of Void/Imperfections (V_{void})

V_{inter} represents the theoretical gap between the layers of V_2O_5 flakes for the specified geometry, assuming perfect packing of 2D sheets covering the entire geometry. V_{void} denotes the empty space within a VO-M strip resulting from imperfections in packing and horizontal gaps between the packed 2D flakes.

Measured volume of the V_2O_5 strip (V_{meas}) = *length* × *width* × *thickness* = 1.52×10^{-8} m^3

Measured weight of the V_2O_5 strip in dry condition (W_{dry}) = 46.7×10^{-6} Kg

Calculated Volume of the V_2O_5 strip (V_{cal}) = W_{dry}/Density of V_2O_5 = 1.39×10^{-8} m^3

$V_{void} = V_{meas} - V_{cal} = 1.3 \times 10^{-9}$ m^3

$V_{void}\ \% = \frac{V_{void}}{V_{meas}} \times 100 = 8.5\ \%$

Calculation of Total Volume between the V_2O_5 slabs (V_{inter})

Total number of layers in a VO-M strip (*N*) can be calculated from the ratio of total thickness to thickness of one layer, obtained from XRD pattern.

N (Thickness of the membrane / Interlayer spacing's (from XRD)) = 29343

Space between two V_2O_5 slabs (d_{one}) = Interlayer spacing's d (from XRD) – Thickness of one slab of V_2O_5 = 1.295 nm (at 90% RH) – 0.58 nm = 0.715 nm

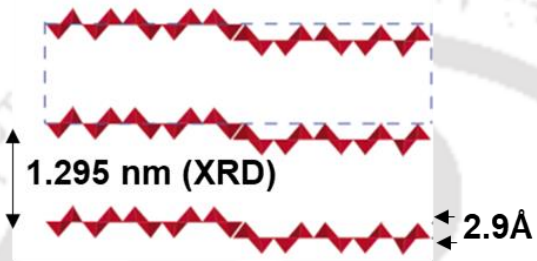

Volume between two V_2O_5 slabs (V_{one}) = $Length \times width \times d_{one}$ = 2.86×10^{-13} m^3

V_{inter} (Total volume between the V_2O_5 slabs) = $N \times V_{one}$ = 8.39×10^{-9} m^3

$V_{free} = V_{inter} + V_{void}$ = 9.69×10^{-9} m^3

The total moisture content in the VO-M was estimated by taking the weight difference of the membrane at RH = 20% and 90%. At each RH condition, strip was kept for ~24 hours before measuring the weight.

Moisture content in V_2O_5 strip (M_{wt}) = Weight of the V_2O_5 strip (at RH = 90%) – Weight of the V_2O_5 strip (at RH = 20%) = 7.72 mg

Volume of water in V_2O_5 strip at RH = 90% (V_{water}) = M_{wt} /water density = 7.72×10^{-9} m^3

Percentage of free volume occupied by water = $V_{water}/ V_{free} \times 100$ = 79.67 %

3.5.2. i-TE properties of VO-Ms:

In order to measure i-TE responses a rectangularly cut VO-M was placed on a stage composed of two glass slides (2.5 cm x 2.5 cm). Subsequently, the fabricated i-TE device was positioned

over two Peltier devices, with one serving as the heat source and the other as the heat sink (Figure 3.2a). When the temperature gradient was generated with the Peltier devices an open

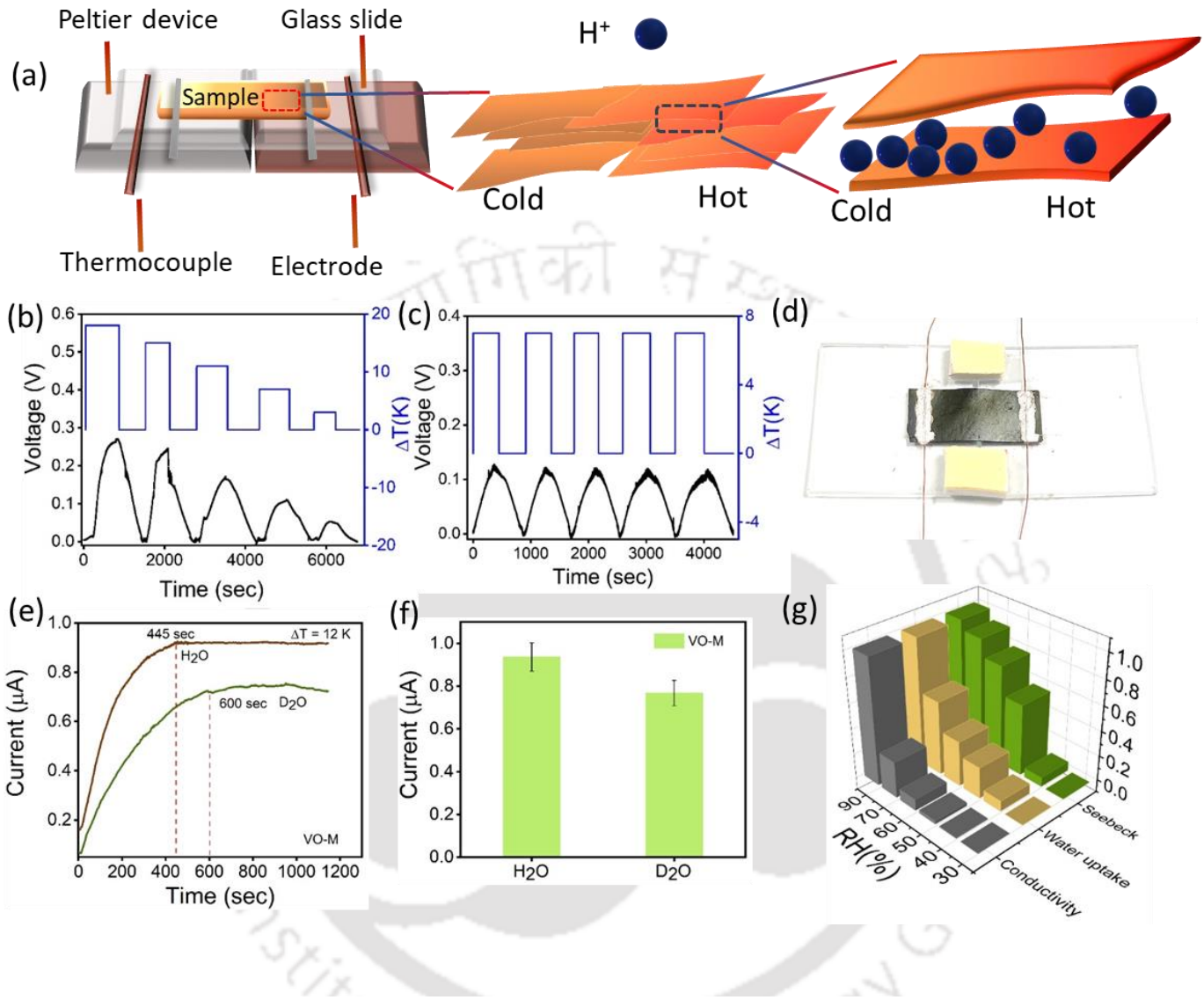

Figure 3.2: (a) Schematic diagram illustrating the measurement setup of ionic thermoelectricity and diffusion of ions under temperature gradient. The inset in the middle depicts the lamellar nature of the nanofluidic membrane. The inset in the upper right corner depicts the expected motion of ions in the direction of the temperature gradient through a 2D nanofluidic channel. (b) Time-dependent thermovoltages for the VO membrane for decreasing temperature gradients with varying periodicity. (c) Time-dependent thermovoltages for the VO-M for a periodic temperature gradient between $\Delta T=0$ and 7 K. (d) Digital photo of a typical ionic conductivity and TE device. (e) Generation of thermal current for H_2O exposed VO-M and D_2O exposed VO-M membrane. (f) A bar diagram to compare the thermal current of H_2O exposed VO-M and D_2O exposed VO-M membrane. (g) A bar chart of the ionic conductivity, water uptake, and the Seebeck coefficient with different RH (%) of VO-M. Each column has been normalized by its maximal value (Ionic conductivity 0.162 [S/m], Water uptake 18.461 [%] and Seebeck coefficient 14.5 [mV/K])

circuit voltage and a short circuit current was developed. Figure 3.2b and c depicts the open-circuit voltage observed across the two ends of a rectangular piece of VO-M (2 cm x 0.8 cm x 0.0040 cm). This VO-M was subjected to a periodic temperature gradient (ΔT = 7 K) with a period of approximately 15 minutes, under ambient conditions (T = 25 °C, RH = 90%). The VO-M exhibited a notable and repetitive maximal output voltage of ~111 mV. Following the cessation of the temperature gradient (ΔT = 0), the open circuit voltage gradually decreased and reached zero after approximately 450 seconds, equivalent to half the period. To verify the correlation between the observed open-circuit voltage in the VO-M and the ionic thermoelectric effect, five different temperatures were consequently applied and resultant voltages were measured (Figure 3.2b). The consistent and reproducible nature of these results further substantiates the involvement of the ionic thermoelectric mechanism.

The ionic thermopower or the ionic Seebeck coefficient (S) in all the experiments are calculated from the equation given below:

$$S = \frac{\Delta V}{\Delta T}$$

Here, ΔV denotes the maximum voltage difference attained for a given temperature gradient (ΔT) within the investigated time frame (approximately 450 seconds for ΔT = 7K). As depicted in Figure 3.2g, the Seebeck coefficient demonstrates an increasing trend with rising relative humidity (RH) values. Notably, the water uptake of dehumidified VO-M, ionic conductivity (as shown in Figure 1e), and Seebeck coefficient exhibit a parallel trend, suggesting that the atmospheric water-induced ionic mobility of VO-M may be the potential mechanism for the origin of ionic thermopower in VO-M.

Figure 3.2a schematically represents a potential scenario of ionic diffusion through the nanochannels under the influence of a temperature gradient. This proposition is based on previous finidings, where it is demonstrated that the dissociation of surface hydroxyl groups

within hydrated nanofluidic channels of V_2O_5 yields a high concentration of H^+ ions.[18] Additionally, previous studies have reported an increase in the ionic conductivity of VO-M membranes due to the coordinated hopping of H^+ ions through the negative surface charges of the V_2O_5 flakes.

To gain further insight of the mechanism, H^+ ions in VO-M were predominately replaced by the D^+ ions by subjecting it to dehydration followed by rehydration with D_2O molecules (details are provided in experimental section 3.3). As anticipated, the temperature gradient-induced current of VO-M was observed to be lower with D_2O compared to H_2O (Figure 3.2e and f). Subsequently, upon dehydration and re-exposure to H_2O, the thermal current reverted to its original values. Under identical conditions, the ratio of thermal current obtained with H_2O-exposed VO to that with D_2O-exposed VO (H_2O-VO/D_2O-VO) was calculated to be 1.22. This finding suggests that ion migration (H^+/D^+) plays a critical role in the thermoelectric characteristics of VO-M and VO-PSS-M.[24,25]

Steady-state response: In this part of this work, the current-voltage (I-V) curves were characterised representing the steady-state responses. The detail of the experimental procedure is explained in the experimental section of 3.3. For comparative purposes, we recorded I-Vs of VO-M both without (Figure 3.3c) and with a temperature gradient (Figure 3.3d, e and f). To elucidate the effect of temperature gradient (ΔT) on I-Vs, we increased ΔT to 15 K for these experiments. In the absence of the temperature gradient, the I-V response is linear and passes through the origin. However, in the presence of the temperature gradient (ΔT= 15 K), the response exhibits a nonlinear I-V curve that deviates from the origin. Specifically, a non-zero current (3.56 μA) is observed at zero voltage (ΔV= 0), and a non-zero voltage (269 mV) is measured at zero current (ΔI= 0). The deviation of the I-V curve from the origin suggests the formation of ionic concentration gradients at the two ends of the system (i.e., the electrodes),

which are at different temperatures. This, eventually results in the generation of electrical current and voltage across the system.[26,27]

Time transient response: As the Figure of 3.2b and c suggest that the measurements of temperature-induced voltage do not stabilize within the 450-second timeframe, prolonged experiments were conducted to measure the time-dependent voltage (Figure 3.3a) and current (Figure 3.3b) under a temperature gradient of 15 K that clarifies the time scale needed to achieve the saturation. It is important to note that each of these measurements was conducted

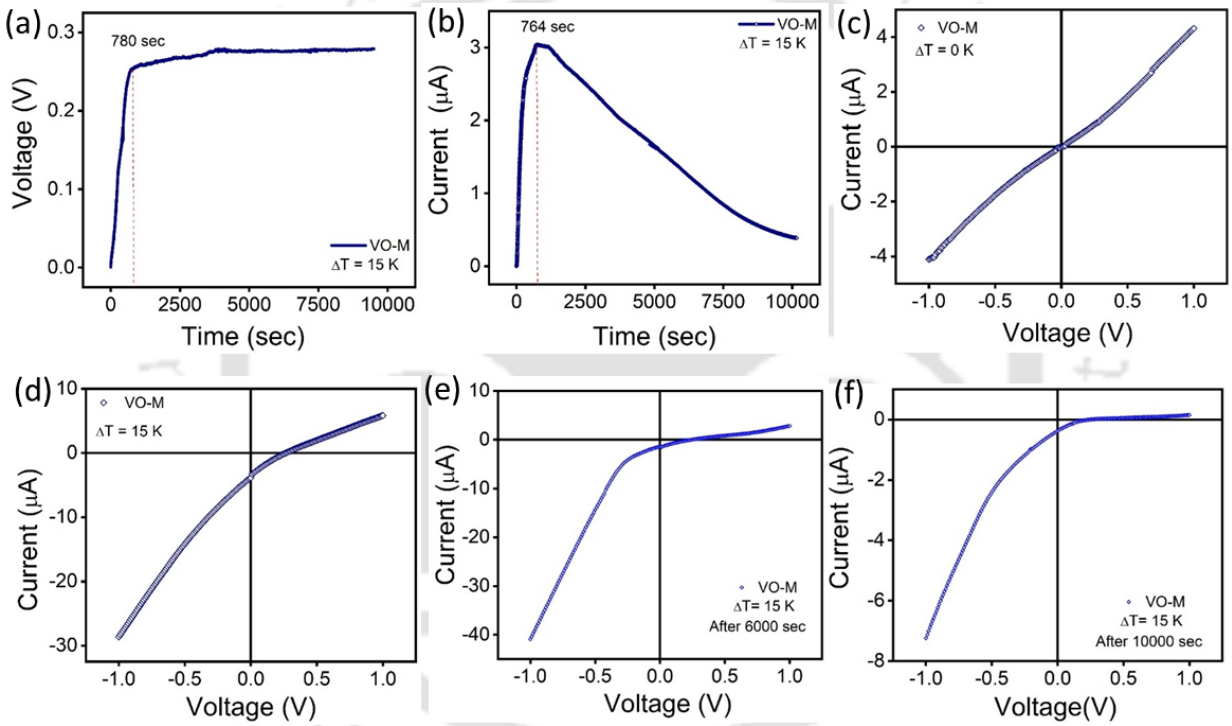

Figure 3.3: Generation of (a) voltage for VO-M and (b) current under 15 K temperature gradient for prolonged periods. I-V curve of VO-M membrane (c) without temperature gradient (d) at temperature gradient of ΔT=15 K. (e) I-V curve of VO-M membrane after ~6000 seconds with the continuous temperature gradient of 15 K across the membrane (f) I-V curve of VO-M membrane after ~10000 seconds with the continuous temperature gradient of 15 K across the membrane.

as separate experiments. In Figure 2c, where ΔT=15 K, the resulting voltage gradually increased, reaching 260 mV around 780 seconds, before appearing to stabilize into what seems to be a steady-state, remaining constant for the duration of 10,000 seconds. Conversely, the

current reaches the saturation after ~764 seconds with a maximal value of 3.04 µA, after which it steadily declines. This gradual decrease in current can be attributed to the dehydration of VO-M channels, depletion of ionic concentration in the hot zone, and saturation of ion accumulating areas in the cold zone. The stability of the output voltage and the gradual decline in output current during extended exposure of VO-M to a temperature gradient are also evident from the I-V curves recorded after 10,000 seconds of applying the temperature gradient (Figure 3.3f). Wang et al. studied a comparable finding with PSSNa-based ionic thermoelectric materials, suggesting that thermodiffused ions are unable to penetrate the external surface. Instead, these ions are presumed to accumulate around the metal electrodes, creating an electric double layer.

3.5.3. Modification of VO-M nanochannels with PSS:

Membrane fabrication and characterizations: The PSS polyelectrolyte has been extensively studied in the field of ionic thermoelectricity due to its higher proton conductivity and higher hygroscopic nature. Additionally, PSS has been utilized to augment the power output of PEDOT:PSS, leveraging the thermodiffusion of both protons and holes to generate thermovoltage. Therefore, as a demonstration, various quantities of PSS were employed to modify the nanofluidic channels of V_2O_5 membranes, resulting in the creation of VO-PSS composite membranes (VO-PSS-M).

For the fabrication of VO-PSS membranes varied quantities of aqueous PSS dispersion (5, 10, 18, 31 wt%) were typically mixed with a fixed amount of V_2O_5 (150 mg, 10 ml at 15 mg/ml). The respective freestanding membranes were named as VO-PSS-5-M, VO-PSS-10-M, VO-PSS-18-M, and VO-PSS-31-M. A representative digital photo and cross-sectional FESEM

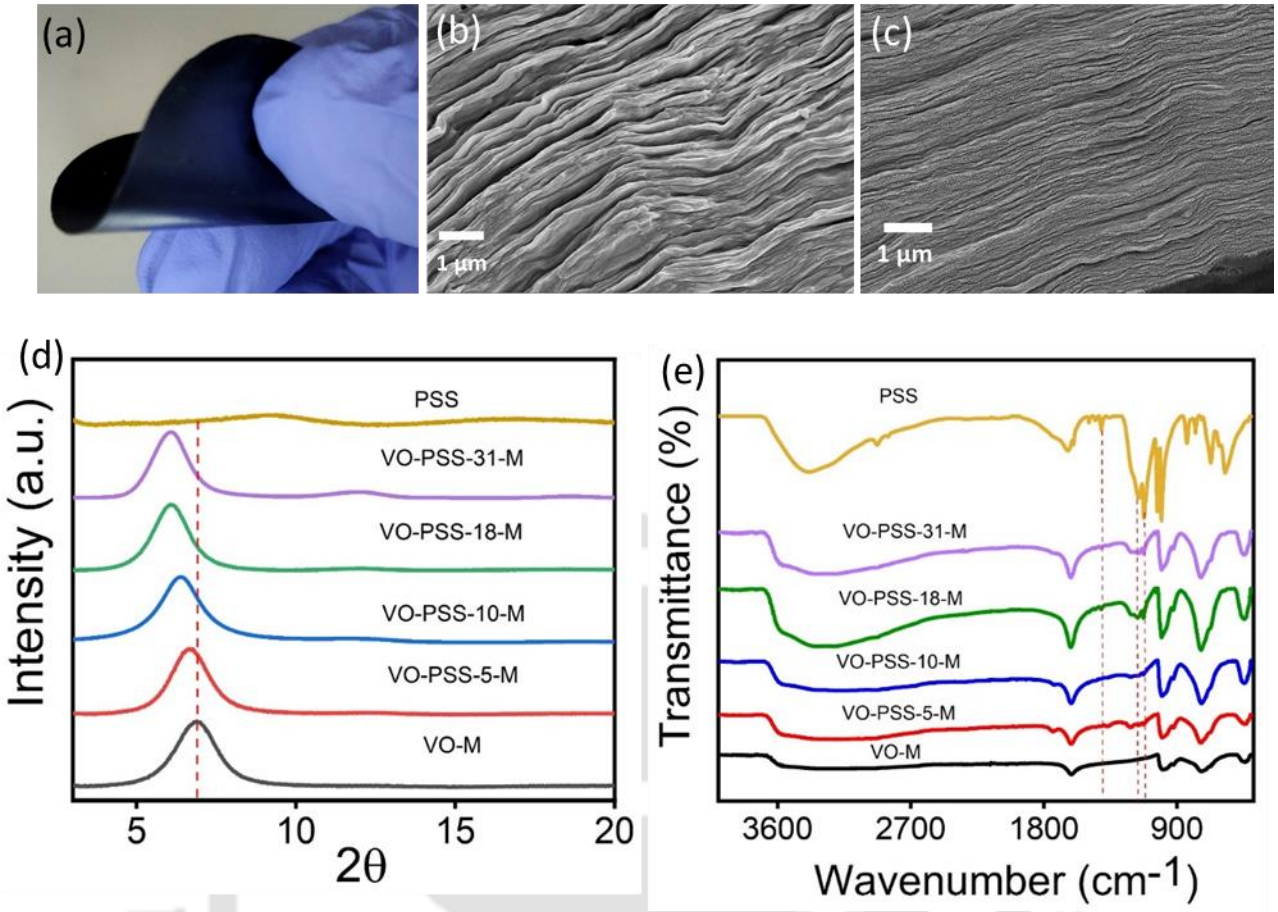

Figure 3.4: (a) Digital photograph, and (b) cross-sectional FESEM image of VO-PSS-18-M. (c) cross-sectional FESEM image of VO-PSS-31-M. (d) pXRD patterns and (e) FT-IR spectra of VO-M, PSS and different VO-PSS-M

image of VO-PSS-18-M and VO-PSS-31-M are depicted in Figure 3.4a and 3.4b and 3.4c respectively. The pXRD analysis in Figure 3.4d demonstrates a consistent increase in the interlayer spacing of the lamellar membranes as the PSS content rises, indicating successful intercalation of PSS between V_2O_5 nanosheets. Fourier-transform infrared (FT-IR) data for both composites and pure V_2O_5 membrane nanosheets were collected in the range of 400–4000 cm^{-1} (Figure 3.4e). Pure PSS displays distinct IR peaks at 1179, 1124, 1034, and 1009 cm^{-1} attributed to the R—SO_3^- groups. These same peaks are also evident in the FT-IR spectra of VO-PSS membranes, showing no discernible alteration. The unchanged peak positions of pure PSS and composite membranes indicate that the chemical structure of the components

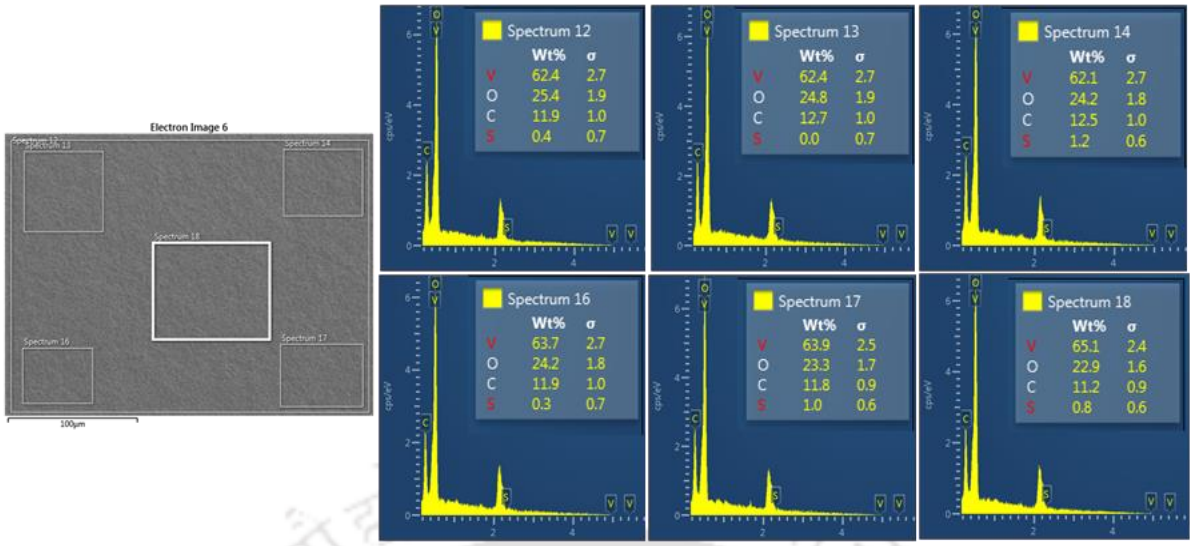

Figure 3.5: EDX analysis carried out under a FESEM instrument. Insets shows the wt% of carbon, sulphur, vanadium, and oxygen atoms in the VO-PSS-31-M membrane.

remained unaffected during the intercalation process. The systematic increase in the intensity of characteristic peaks for R—SO_3^- correlates with the growing mass loading of PSS. The intercalation of PSS molecules can be further confirmed from the EDX analysis and EDX mapping shown in Figure 3.5 and 3.6 respectively. The XPS analysis (Figure 3.7a to 3.7d) further indicates the unchanged shifts in the binding energies of V2p ($V2p_{3/2}$ and $V2p_{1/2}$ levels

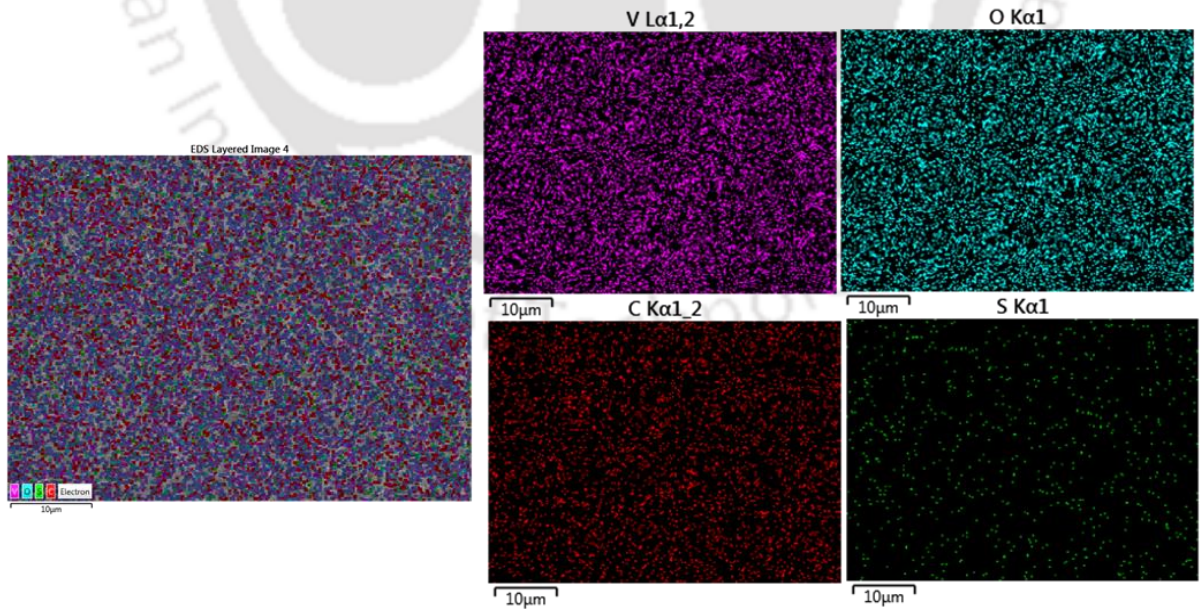

Figure 3.6: Elemental mapping of the vanadium, oxygen, carbon, and sulphur, atoms of VO-PSS-31-M membrane recorded under FESEM (EDX analysis), showing homogenous distribution of the elements all throughout the membrane.

at ~517.7 eV and ~525.2 eV, respectively) and O1s levels (~530.4 eV) following the intercalation of PSS into the interlayer space. This finding further confirms the absence of any chemical modification or degradation during the intercalation process. The tensile strength

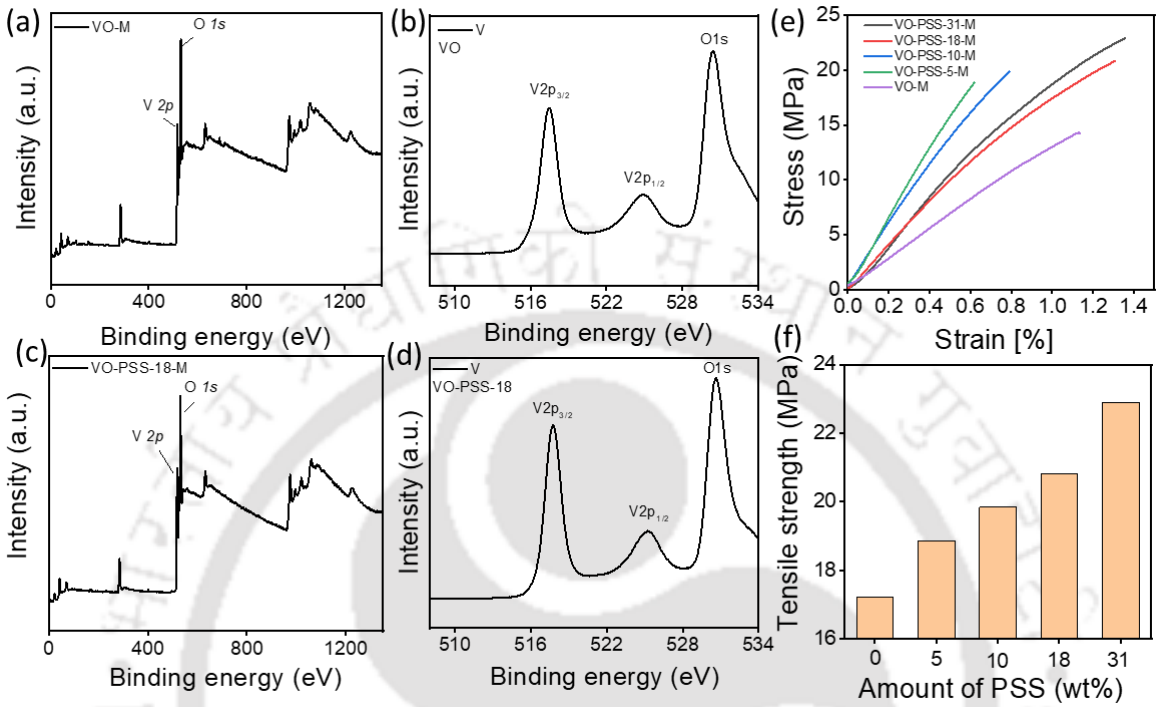

Figure 3.7: Wide scan XPS spectra for (a) VO-M (c) VO-PSS-18-M membrane. High resolution XPS spectra of V2p and O1s regions for (b) VO-M (d) for VO-PSS-18-M membrane. (e) Stress-strain curve for different composites of VO-M and PSS membrane (f) increase of tensile strength with respect to mass loading of PSS.

values, derived from the breaking point (representing the ultimate stress the material can endure), exhibited a systematic increase with the escalating mass loading of PSS (Figure 3.7e and f). The tensile strength of the pure VO-M membrane, initially at 17.21 MPa, rose to 22.9026 MPa with the addition of 31% PSS (VO-PSS-31-M). Despite the absence of observed chemical interaction or bonding, the synergistic combination of VO and PSS is evident from the enhanced mechanical properties of VO-PSS membranes compared to those of individual VO and PSS membranes.

Ionic thermoelectric properties: Similar to the VO-M, with the VO-PSS composite membrane as well temperature gradient induced ionic thermovoltages were observed. Figures

3.8a and 3.8b illustrate the measured thermovoltage of all VO-PSS-18 under a constant temperature gradient (7K) and varying temperature gradients at RH = 90% and the Figure 3.8c presents a comparable bar chart similar to that shown in Figure 3.2g (for the VO-M), specifically for VO-PSS-18-M. This chart reveals similar trends observed in Figure 1e, that includes the simultaneous increase in water uptake, ionic conductivity, and Seebeck coefficient across different RH levels. Interestingly, an 80% enlargement in the ionic Seebeck coefficient was observed from 14.5 mV/K to 26.3 mV/K after intercalation of 18 wt% of PSS molecules.

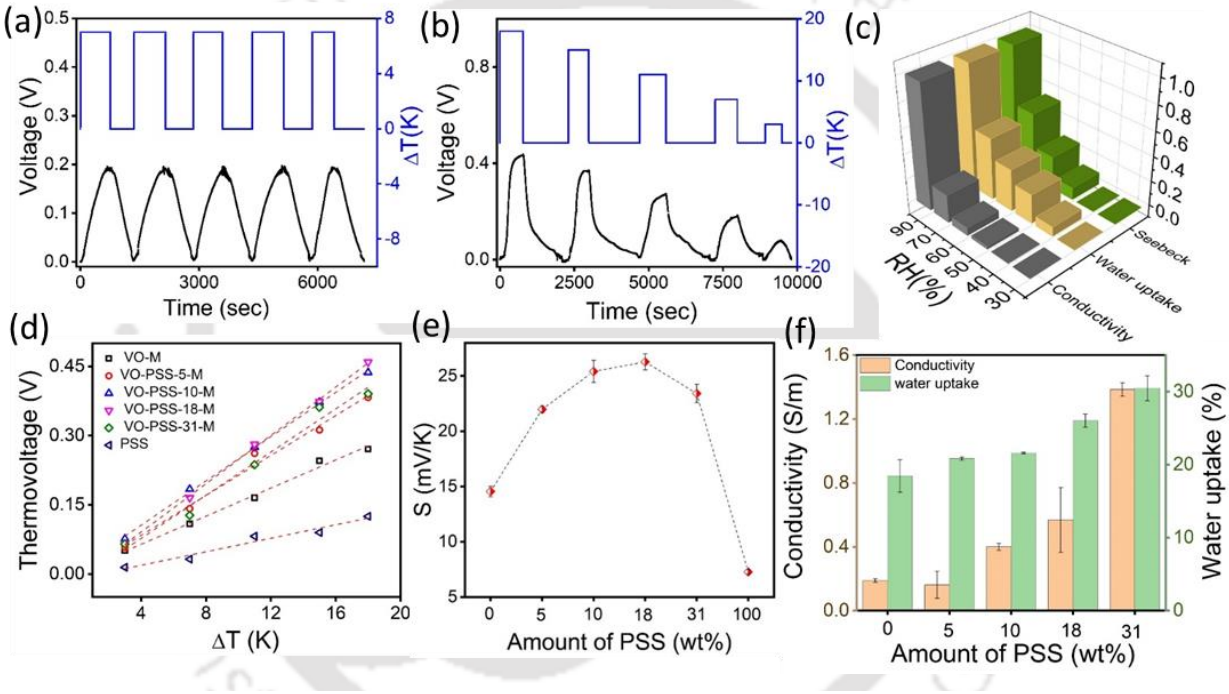

Figure 3.8: (a) Generation of thermovoltage of VO-PSS-18-M membrane under varying temperature gradient between 0 to 7 K. (b) Generation of thermovoltage of VO-PSS-18-M membrane as function of temperature gradient. (c) A bar chart of the ionic conductivity, water uptake, and the Seebeck coefficient with different RH (%) of VO-PSS-18-M. Each column has been normalized by its maximal value (Ionic conductivity 0.57 [S/m], Water uptake 26.01 [%] and Seebeck coefficient 26.3 [mV/K]). (d) Linear increment of thermovoltage with respect to temperature gradient, (e) Seebeck coefficients, and (f) Ionic conductivities and water uptake of membranes with different compositions of VO and PSS

Similar ionic thermoelectric responses were recorded for other composite membranes and depicted in Figure 3.9. The ionic Seebeck coefficients for all the composite membranes were calculated from the slopes of linear increment (ionic thermovoltages with respect to the

temperature gradients) (Figure 3.8d) and is represented in Figure 3.8e. As evident from Figure 3.8e, even a 5 wt% addition of PSS elevates the Seebeck coefficient from 14.5 mV/K to 21.6 mV/K. The Seebeck coefficient demonstrates an increasing trend with the rising PSS content until it peaks at 26.3 mV/K for 18 wt% of PSS (VO-PSS-18-M). Subsequently, a further increase in the wt% of PSS results in a slight decline in the Seebeck coefficient. As PSS has been extensively explored for generating thermovoltage, the calculated Seebeck coefficient value closely aligns with that reported in recent literature (7.3±0.2 mV/K).[28] For comparative purposes, Figure 3e also presents the Seebeck coefficient of a pure PSS membrane fabricated using the drop-casting method. The collaborative impact of VO-M and PSS becomes apparent as all composite membranes exhibit superior Seebeck coefficient values compared to those of pure membranes. The improvement in the Seebeck coefficient in composite membranes can be attributed to the amalgamation of high proton conductivity and the hygroscopic nature (water uptake) of the composite.

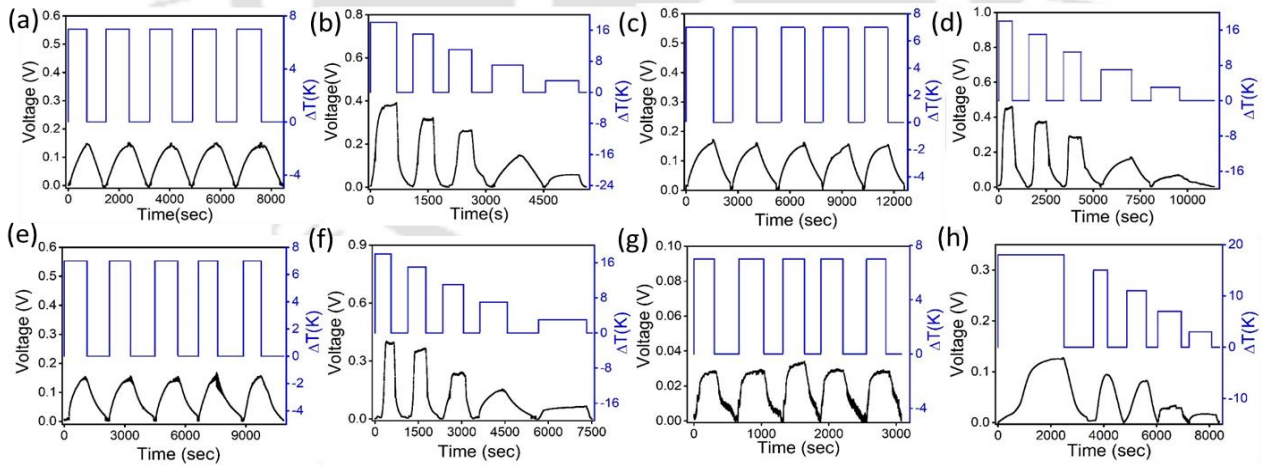

Figure 3.9: Generation of thermovoltages at the temperature gradient of 7K for (a) VO-PSS-5-M (c) VO-PSS-10-M (e) VO-PSS-31-M and (g) PSS membranes. Thermovoltages generated at different temperature gradients for (b) VO-PSS-5-M, (d) VO-PSS-10-M, (f) VO-PSS-31-M and (h) PSS membranes

To validate our hypothesis regarding the relationship between water uptake and membrane conductance, we conducted measurements of ionic conductivity and water uptake (%) at 90% RH across varying amounts of PSS (wt%). Figure 3.8f illustrates a bar diagram showcasing the correlation between the increase in water uptake and the rise in ionic conductivity of the composite membranes compared to VO-M and with the increase of PSS loading. However, it's noteworthy that despite the gradual augmentation in water content and ionic conductivity, membranes with PSS content exceeding that of VO-PSS-18 exhibited a decrease in the Seebeck coefficient (Figure 3.8e). This decline in Seebeck coefficient values with higher PSS contents could be attributed to the relaxation of nanofluidic confinement. However, comprehensive experimental and theoretical investigations are required to elucidate the interplay between ionic charge carriers and nanofluidic confinement in determining the characteristics of ionic TE.

Similar to the process described for VO-M, the exchange of H^+ ions with D^+ ions were conducted for VO-PSS-18-M as well. The H_2O-VO-PSS/D_2O-VO-PSS ratio (thermal current) of the thermal currents were calculated as 1.26 (Figure 3.10b), thus affirming the contribution of protons to the generation of thermoelectric properties. As the migration of H^+ ions are primarily responsible for the generation of ionic thermovoltages, we tried to enhance the performance of the best-performing VO-PSS membrane (VO-PSS-18-M) by introducing additional H^+ ions with a drop of 20 µL of H_2SO_4 (0.1 M). With the assistance of these additional H^+ ions from H_2SO_4, the Seebeck coefficient of VO-PSS-18-M increased from 26.3 ± 0.7 mV/K to 28.2 ± 0.5 mV/K (Figure 3.10c and d), which additionally supports the hypothesis regarding the role of H^+ ion migration in the origin of thermoelectric properties.

Additionally, the activation energy necessary for the thermal migration of ions from the hot zone to the cold zone of the VO-PSS-M was determined by measuring the maximum thermal current (I_{max}) under various temperature gradients. In this experiment, the temperature of the cold zone remained constant (25 °C), while the temperature of the hot side was systematically

increased from 30 to 45 °C. It was observed that I_{max} increased with the rising temperature (T)

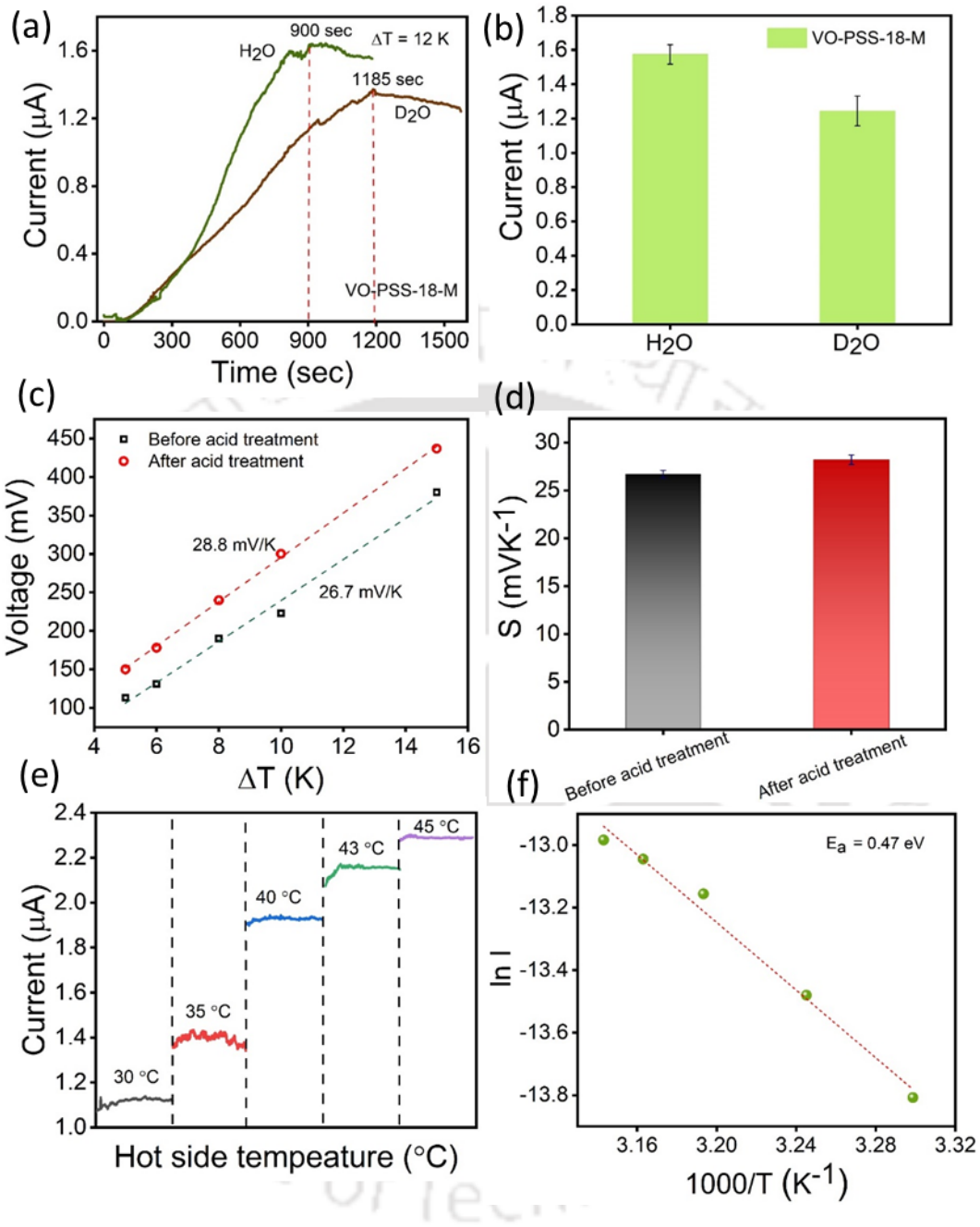

Figure 3.10: (a) Generation of thermal current for H_2O exposed and D_2O exposed VO-PSS-18-M membrane at 12 K temperature gradient. (b) A bar diagram to compare the thermal current of H_2O exposed and D_2O exposed VO-PSS-18-M membrane. (c) Generation of thermovoltage with different temperature gradient before and after the treatment of VO-PSS-18-M with H_2SO_4 showing the improvement of Seebeck coefficient. (d) A bar diagram to compare the Seebeck coefficient of VO-PSS-18-M membrane before and after acid treatment. (e) Generation of thermal current at different temperature gradient where the cold side temperature was fixed at 25 ºC and the hot side temperature was varied from 30 ºC to 45 ºC (f) ln I vs. 1/T plot where I represents the thermal current and T represents the temperature at the hot side of measurements in Figure 3.9e.

on the hot side. By plotting ln(I) against 1/T in an Arrhenius plot (Figure3.10e and f), the activation energy required for the temperature gradient-induced transport of H^+ ions was calculated to be 0.47 eV.

3.5.4. Importance of nanoconfinements:

To explore the impact of nanoscale 2D confinement in the enhancement of thermovoltages, membranes of pristine V_2O_5 and V_2O_5-PSS composites were prepared by transforming the

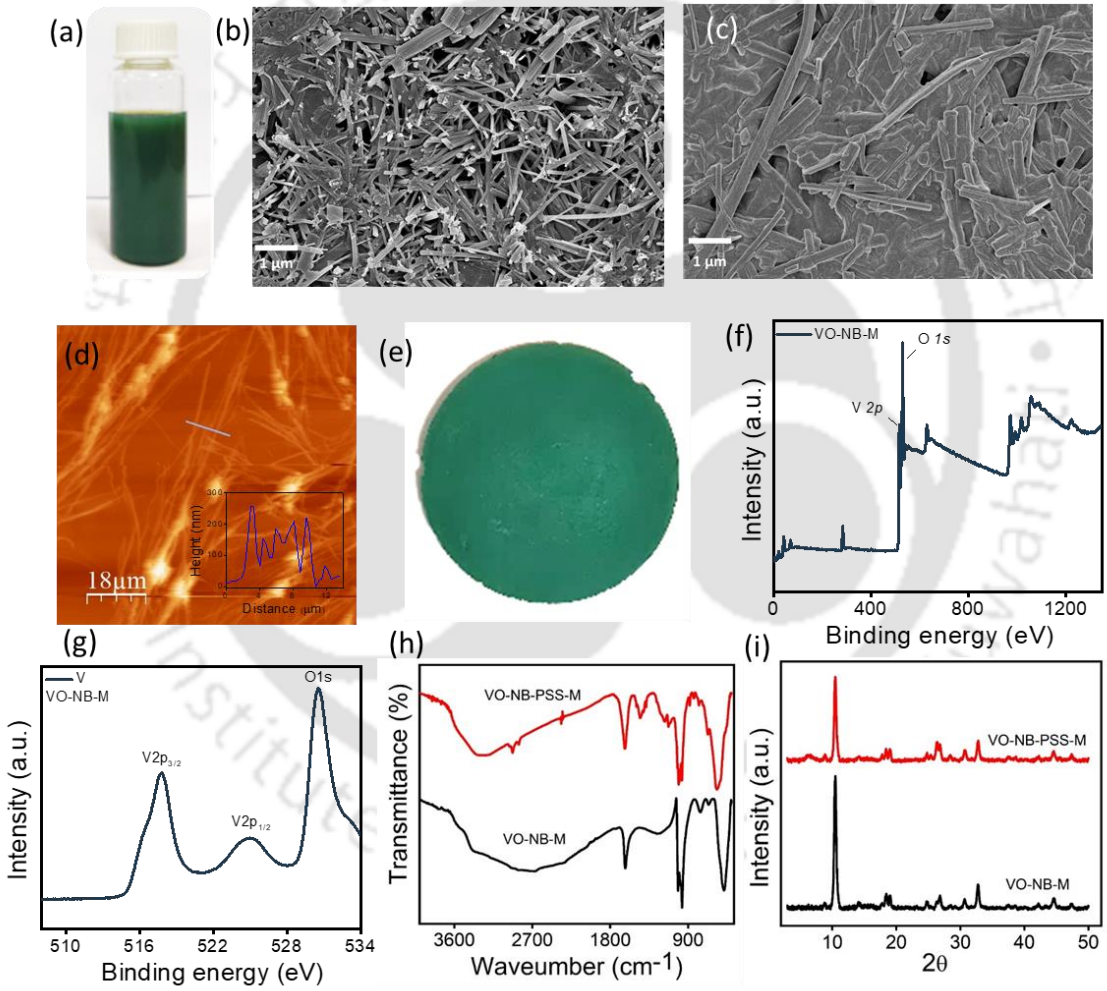

Figure 3.11: (a) A digital photograph of the dispersion of VO-NB revealing changing colour of the V2O5 dispersion from dark brown to green. (b) FESEM image of VO-NB-M. (c) FESEM image of VO-NB-PSS-M. (d) AFM image of VO-NB-M. (e) A digital photograph of the VO-NB-M. (f) Wide scan XPS spectra for VO-NB-M membrane. (g) High resolution XPS spectra of V2p and O1s regions for VO-NB-M membrane. (h) FT-IR image of VO-NB-M and VO-NB-PSS-M membrane. (i) pXRD pattern of VO-NB-M and VO-NB-PSS-M membrane.

morphology of V_2O_5 2D sheets into V_2O_5 nanobelts (VO-NB), following a procedure outlined in previous literature.[29,30] Briefly, hydrothermal treatment of the aqueous dispersion of V_2O_5 nanosheets at 180°C for 18 hours yielded a dispersion of V_2O_5 nanobelts as can be seen from the digital photograph of Figure 3.11a. The morphological changes of these V_2O_5 nanosheets into nanobelts are easily observable from the FESEM image (Figure 3.11b) and AFM image (Figure 3.11d). Figure 3.11c represents the FESEM image of the composite of V_2O_5 nanobelts and PSS, and Figure 3.11e represents the digital photograph of the freestanding membrane of VO-NB. The resulting VO-NB-M membrane exhibited a disordered and chaotic structure, lacking a predefined path for ionic transport, as observed in the FESEM image. The XPS

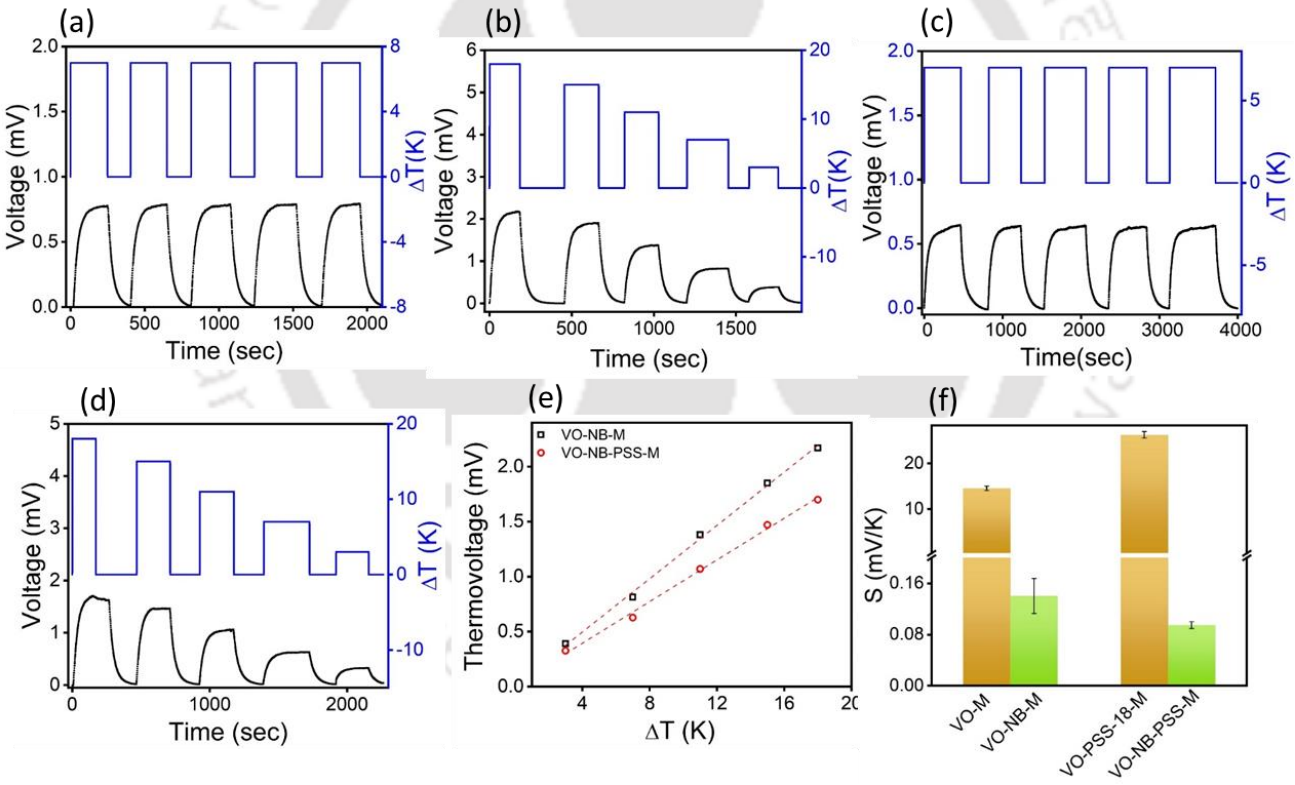

Figure 3.12: Generation of thermovoltage for VO-NB-M membrane (a) at ΔT = 7 K for multiple cycle, and (b) at different ΔT values. Generation of thermovoltage for VO-NB-PSS-M membrane (c) at ΔT = 7 K for multiple cycle, and (d) at different ΔT values. (e) Thermovoltage vs ΔT plot of VO-NB-M and VO-NB-PSS-M membrane. (f) Comparison of Seebeck coefficient of VO-M, with VO-NB-M and VO-PSS-18-M with VO-NB-PSS-M.

spectra shown in Figure 3.11f and 3.11g confirms the morphological change without altering

the chemical composition. The membranes were further characterized with FT-IR spectra and pXRD pattern as shown in Figure 3.11h and 3.11i.

Interestingly, it is observed that, in spite of having similar chemical composition, the thermovoltage associated with VO-NB-M was significantly lower compared to VO-M. While VO-M exhibited a thermovoltage of ~111 mV under similar conditions (ΔT = 7 K), VO-NB-M demonstrated a minimal thermovoltage of 0.8 mV (Figure 3.12a) (Seebeck coefficient = 0.094.7±0.005.2 mV/K). Figure 3.12f compares the Seebeck coefficient of VO-M and VO-NB-M with that of VO-PSS-18-M and VO-NB-PSS-M, underscoring the significance of well-defined 2D nanofluidic channels in achieving high ionic TE performance. The respective thermovoltages for pristine VO nanobelts and VO nanobelts and PSS composite were represented in Figure 3.12b to 3.12d and the linear increment of these thermovoltages is represented in Figure 3.12 e. The importance of precisely oriented nanochannels for ion movement is further emphasized by measuring thermovoltage perpendicular to the lamellar stacking of 2D sheets, following a method similar to prior studies. As anticipated, VO-PSS-18-M displayed a minimal thermovoltage of ~29 mV in the vertical direction compared to ~186 mV in the horizontal direction under similar conditions (ΔT = 8 K, RH = 90%), as shown in Figure 3.13a. This anisotropic behaviour of VO-PSS-M membranes is attributed to well-defined nanochannel orientation that is relatively absent in the perpendicular direction. Materials with such distinct ionic thermoelectric properties are scarcely reported in the literature and hold significant potential for technological applications.

3.5.5. High temperature stability:

It has been observed that, the majority of ionic thermoelectric materials studied so far are based on organic polymers. Despite their impressive performance under ambient conditions, these polymeric materials are often mechanically fragile or unstable at higher temperatures, and

many cannot withstand occasional high temperature shocks. However, the reconstructed layered materials have the potential to withstand at extremely high temperatures. Layered

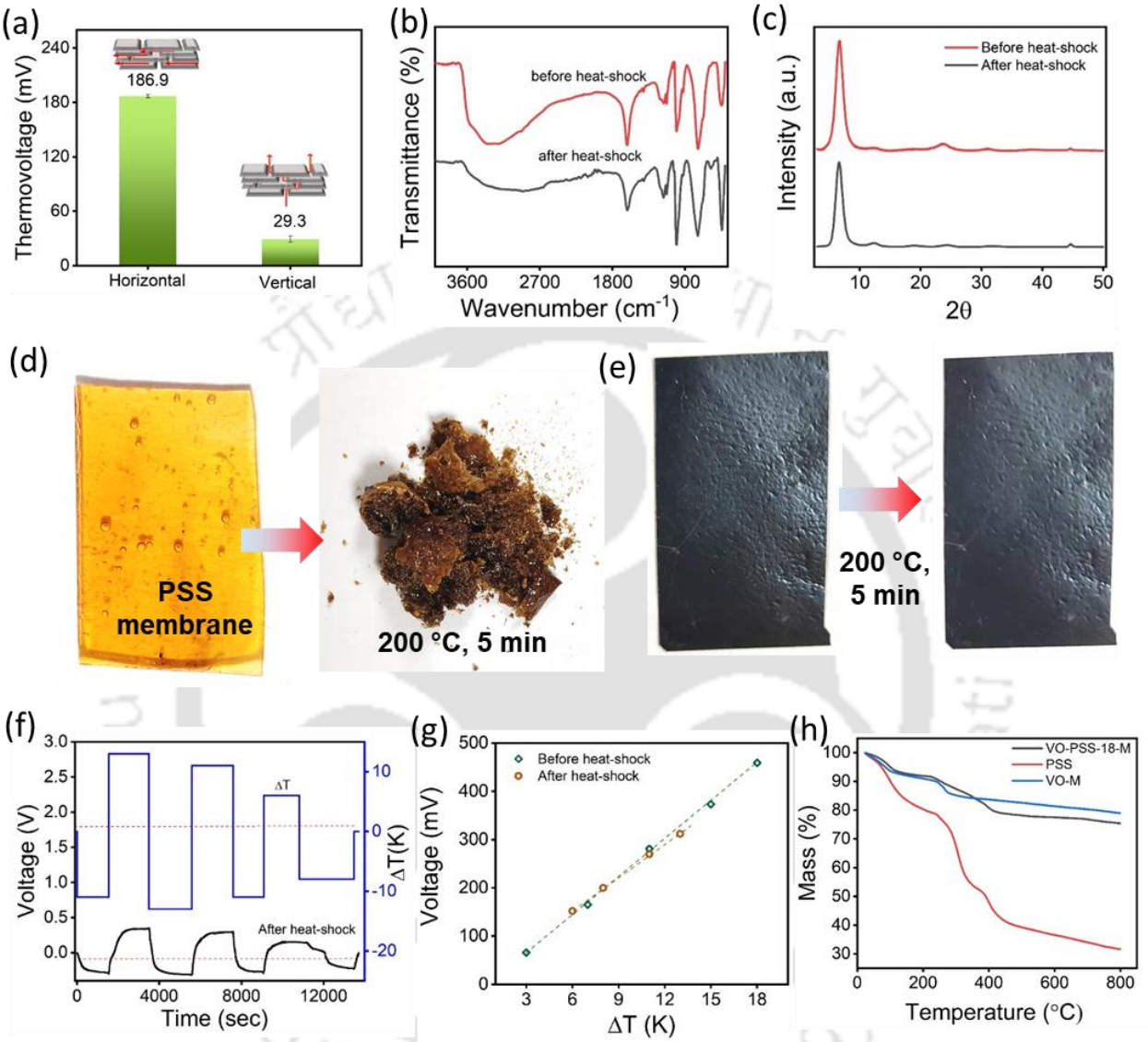

Figure 3.13: (a) Comparison of the thermovoltages originated from parallel and perpendicular directional movement of ions to the lamellar stacking of 2D sheets. (b) IR spectrum and (c) XRD pattern of VO-PSS-18-M before and after heat shock. Digital photograph of (d) PSS membrane and (e) VO-PSS-18-M membrane before and after heat shock (f) Generation of thermovoltage of VO-PSS-18-M membrane at different temperatures after heat shock. (g) Linear increment of thermovoltage with temperature gradient of VO-PSS-18-M membrane before and after the heat shock. (h) TGA curves of VO-M, PSS and VO-PSS-18-M membrane carried out under Ar atmosphere.

materials such as boron nitride, natural clay minerals, and V_2O_5 can endure temperatures exceeding hundreds of degrees Celsius. This resilience makes them suitable for harvesting waste heat from sources prone to frequent thermal shocks. To assess the resilience to sudden temperature fluctuations, the membranes were exposed to a "heat shock" by placing them inside a muffle furnace at 200 ºC for 5 minutes. A pristine PSS membrane was found to disintegrate into pieces under such an exposure (Figure 3.13d) while the VO-M demonstrated remarkable durability, withstanding the high temperature and safeguarding the polymeric materials within its interlayer space (Figure 3.13e). The unchanged FT-IR spectra and pXRD pattern shown in Figure 3.13b and c verifies the chemical stability of these composite membranes after the heat-shock. The enhanced thermal stability of PSS within the VO-M interlayer space was further confirmed by Thermogravimetric Analysis (TGA) (Figure 3.13h). Notably, the Seebeck coefficient remained stable at around 24.1±1.7 mV/K even after the heat shock and the respective thermoelectric properties were shown in Figure 3.13f and g. However, it was not feasible to measure the thermovoltage of the pure PSS membrane following similar heat treatment as it disintegrates into pieces. Ionic thermoelectric materials exhibiting such robust thermal stability hold promise for expanding their practical applications and fostering new scientific inquiries.

3.5.6. Water-assisted healing properties:

Another intriguing characteristic of V_2O_5-based membranes is their ability to recover from physical damages with the assistance of a small amount of liquid water. As shown in Figure 3.14a1, two rectangular strips of VO-PSS-18-M membrane (1 cm x 0.8 cm in size) are brought into contact with each other. A small droplet of water (10 μL) is placed at the junction. Upon evaporation of the water droplets, the pieces of VO-PSS-18-M merge into a single strip (Figure 4.14a2). The healed membrane is as flexible as the pristine membrane and Figure 4.14a3 represents a digital photograph of the same. In Figure 4.14c the mechanical property of the

healed membrane is compared with the pristine one. The tensile strength of the VO-PSS-18 membrane was calculated to be 20.835 MPa, while the healed membrane exhibited a slightly

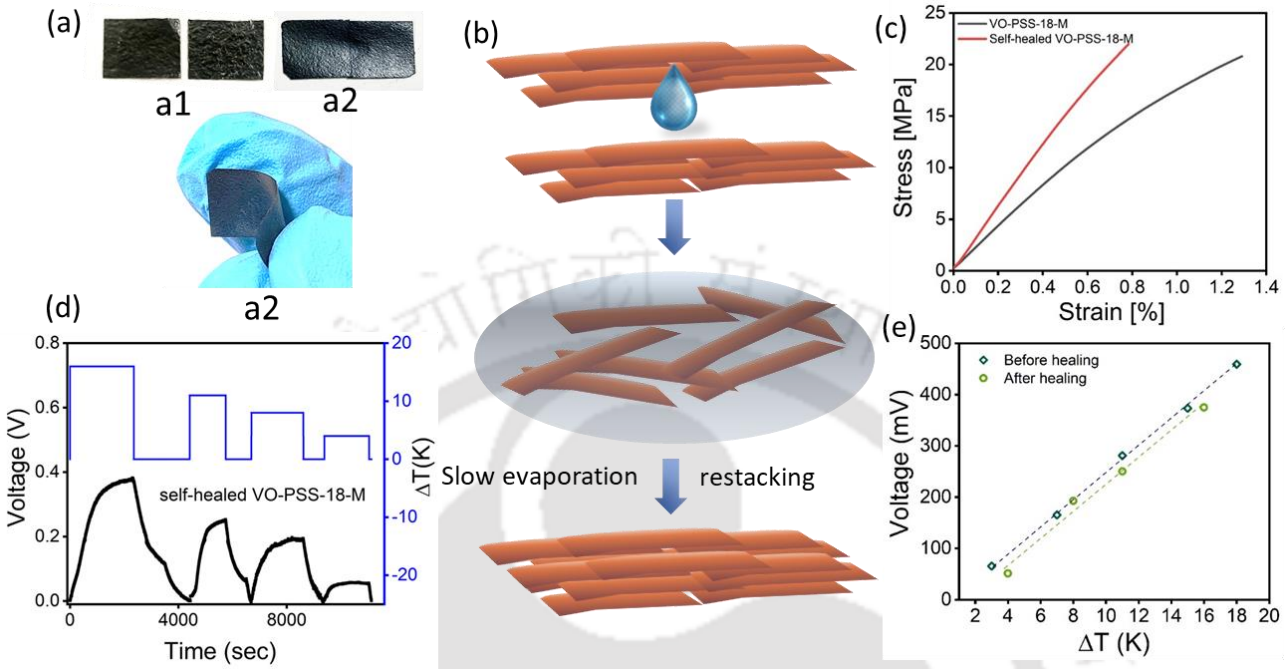

Figure 3.14: (a) Digital photographs of VO-PSS-18-M membrane before and after healing. (b) Schematic illustration of the self-healing nature of VO-PSS-18-M membrane. (c) Stress vs stain curve of VO-PSS-18-M membrane before and after healing. (d) Generation of thermovoltages at different temperature gradient for self-healed VO-PSS-18-M membrane. (e) Linear increment of thermovoltage with temperature gradient before and after the healing process.

higher value of 21.99 MPa, possibly due to increased thickness in the healed region. In order to compare the thermoelectric properties, the thermovoltages were recorded for the healed membrane as shown in Figure 3.14d. Interestingly, both membranes showed similar Seebeck coefficient values (pristine = 26.3 mV/K, healed = 26.4 mV/K), indicating that the healing process not only restored the physical integrity but also maintained its i-TE properties (Figure 3.14e).

The mechanism of water-assisted healing is depicted in Figure 3.14b. Initially, the attractive interactions between V_2O_5 and PSS components hold the membrane together through hydrogen bonding and van der Waals forces. When exposed to liquid water, the hydration energy

overcomes these interactions, causing the components to disperse. As water evaporates, the hydration energy decreases, allowing attractive interactions to dominate and leading to the reorganization of the flakes into a lamellar structure, effectively fusing the broken pieces. Expansion of the PSS and V_2O_5 layers, along with the relaxation of their stacking arrangement, can be observed in the stress-strain plot of VO-PSS-18-M when comparing conditions with and without liquid water, as depicted in Figure 3.15b. Additionally, individual VO-M and PSS membranes were also tested for healing under 95% RH at 25 ºC. While both VO-PSS-18-M and VO-M membranes exhibited healing behaviour, the pristine PSS membrane did not and remained with the solution state, further indicating the role of V_2O_5 nanosheets in the healing process (Figure 3.15a1, a2 and a3).

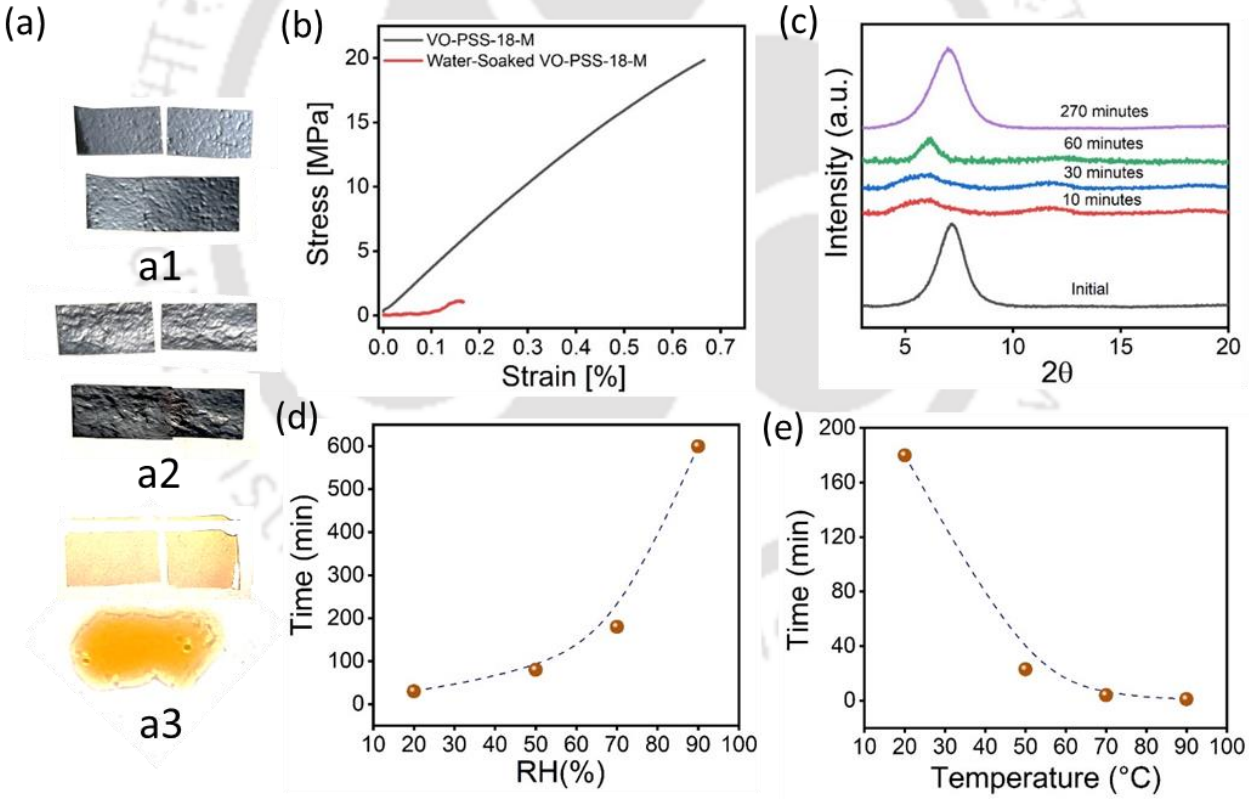

Figure 3.15: (a) Digital images to represent the self-healing behaviour of VO-M (a1) and VO-PSS-18-M (a2), however the figure a3 represents the PSS membrane still in a solution state at 95 % RH during the healing process. (b) Comparison of the mechanical strength for VO-PSS-18-M with that of water-soaked VO-PSS-18-M through stress-strain plot. (c) In-situ pXRD plot of VO-PSS-18-M with different time interval after introducing a water droplet over it. Time requirement for healing process of VO-PSS-18-M at different (d) equilibrium temperature of the membrane and (e) relative humidity (%).

To gain deeper insights of the mechanism behind the healing process, an in situ XRD patterns were recorded with addition of a water droplet over VO-PSS-18-M at regular intervals of time. As illustrated in Figure 3.15c with the addition of the water droplet, the (100) reflection representing the interlayer spacing shifted towards higher d values, transitioning from d = 1.23 nm to 1.49 nm. Additionally, the intensity of the reflection significantly diminishes, indicating the swelling of both PSS and V_2O_5 layers and the loosening of the stacking arrangement. As evaporation continues, the concentration of V_2O_5 layers increases, reverting to a stacked arrangement, thereby sandwiching the PSS molecules, ultimately filling up the damaged region. Consequently, towards the end of the evaporation process (around ~270 minutes), the (100) reflection shifted back to its original position (1.25 nm) and regained its intensity, indicating the completion of the healing process.

The mechanism of the healing process reveals that the healing time primarily depends on the evaporation rate of the drop-casted water droplet. Therefore, self-healing experiments were conducted at various relative humidity and temperature conditions. Initially, 20 µL of water was applied to the damaged region, and the healing time was measured at different relative humidity levels within a closed chamber. Figure 3.15d illustrates that at lower relative humidity levels (20% RH), the healing process occurs rapidly, completing within approximately 30 minutes, while it slows down with higher relative humidity levels. This variation is attributed to the higher evaporation rate at lower relative humidity, facilitating faster healing. Furthermore, the healing process was investigated at different equilibrium temperatures across the membrane. Broken pieces of VO-PSS-18-M were positioned on a glass plate and heated to specific temperatures (50, 70, and 90 ºC). Once the equilibrium temperature was reached, a 20 µL water droplet was applied to the broken region, and the healing time was recorded. As depicted in Figure 3.15e, the healing time decreases with increasing temperature. For instance, at elevated temperatures (~90 °C), the rapid evaporation of water leads to the fusion of broken

pieces within a short period (~1 minute). Figure 3.15e further illustrates the exponential decrease in healing time for the VO-PSS-18-M membrane at different temperatures.

3.6. Practical applications:

In order to find out the practical utility, a device was fabricated as shown in Figure 3.16b where light can be selectively exposed to one part of VO-PSS-18-M. Being a photothermal material, it experienced a temperature increase of approximately 343K upon exposure to infrared (IR) light with an intensity of 15000 lumens. By simply exposing one end of the VO-PSS-18-M

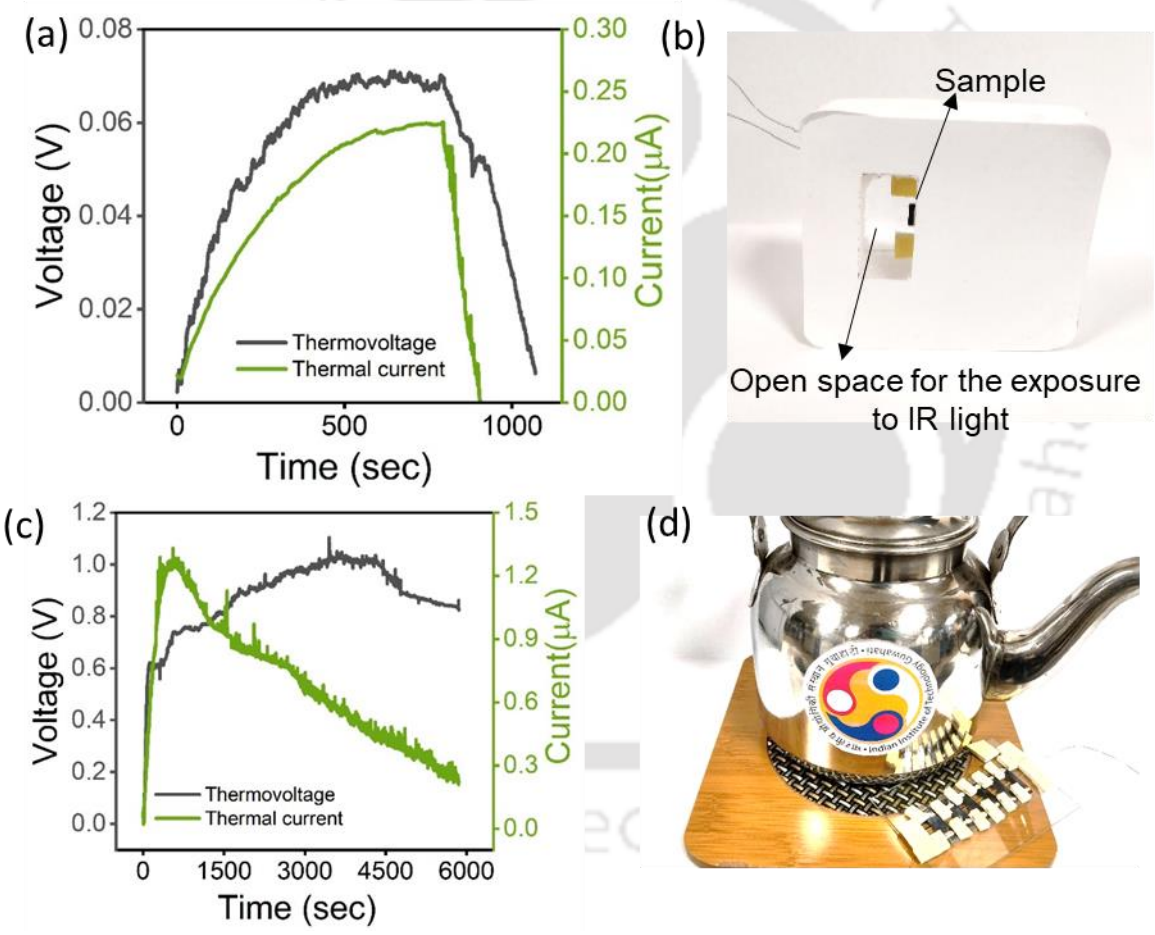

Figure 3.16: Generation of current and voltage (a) when one side of VO-PSS-18-M was exposed to IR light to create a temperature gradient across the membrane, (c) when an array of six thermoelectric devices made of VO-PSS-18-M were connected in series and kept on a table coaster beside a hot electric kettle. (b) A digital photograph of the experimental setup for pointed exposure of IR light towards one part of the VO-PSS-18-M. (d) A digital photograph to represent the experimental set-up of Figure 3.15c.

strips, (1cm x 0.8 cm), to IR light of 15000 lumens, we were able to generate an open circuit potential and current of approximately 70 mV and 0.2 µA, respectively, from a temperature gradient of about 4K (Figure 3.16a and 3.16b). Considering the wide range of photothermal materials available in the literature, incorporating suitable composites of ionic conductors and photothermal materials could offer an alternative means of harnessing solar energy.

Additionally, an array of six VO-PSS-18-M devices were connected in series and placed near a hot water kettle on a table coaster (typically used for holding containers of hot food). As illustrated in Figure 3.16c and d, simply placing a kettle of hot water on the VO-PSS-18-M integrated table coaster allowed us to achieve a voltage of approximately 1 V for nearly 1 hour, generating a temperature gradient of approximately 9K. This voltage gradually declined as the kettle cooled. With this setup, we could also achieve a maximum current of 1 µA. This demonstration opens up new possibilities for harvesting waste energy in domestic settings.

3.7. Conclusion:

In this study we emphasized the importance of systems with nanofluidic channels for harnessing low-grade heat using the concept of Soret effect. Using reconstructed vanadium oxide (VO-M) as an example, we demonstrate its suitability for studying ionic thermoelectric (i-TE) effects. Under a temperature gradient, VO-M exhibits respectable amount of thermopower, attributed to H^+ ion migration within its nanofluidic channels. This thermal migration is confirmed by non-linear I-V responses, indicating non-uniform ionic environments. The decline in thermal current following the exposure to D_2O molecules eventually validates the migration of H^+ ions under the temperature gradients. Modifying VO-M with PSS molecules enhances the overall i-TE performance, with VO-PSS-18-M showing an 80% increase in ionic thermopwoer. The importance of well-defined nanofluidic channels is highlighted by minimal thermovoltages observed with 1D nanobelts of V_2O_5 and from the

measurements performed by changing towards the perpendicular direction of the 2D channels. In contrast to fragile organic polymer-based materials, VO-M offers exceptional stability towards high temperature and can be recovered from physical damages with trace amount of water. Finally, exploring a wide array of 2D materials and their potential modifications in reconstructed layered materials could pave the way for a new platform to investigate ionic thermoelectricity, along with a plethora of application opportunities.

3.8. References:

1 K. Jiang, S.-H. Hong, S.-H. Tung and C.-L. Liu, *J. Mater. Chem. A*, 2022, **10**, 18792–18802.

2 M. Jeong, J. Noh, M. Z. Islam, K. Kim, A. Sohn, W. Kim and C. Yu, *Adv. Funct. Mater.*, 2021, **31**, 1–7.

3 M. Fu, Z. Sun, X. Liu, Z. Huang, G. Luan, Y. Chen, J. Peng and K. Yue, *Adv. Funct. Mater.*, 2023, **33**, 2306086.

4 Z. Liu, H. Cheng, Q. Le, R. Chen, J. Li and J. Ouyang, *Adv. Energy Mater.*, 2022, **12**, 2200858.

5 J. Xu, H. Wang, X. Du, X. Cheng, Z. Du and H. Wang, *ACS Appl. Mater. Interfaces*, 2021, **13**, 20427–20434.

6 K. Liu, J. Lv, G. Fan, B. Wang, Z. Mao, X. Sui and X. Feng, *Adv. Funct. Mater.*, 2022, **32**, 2107105.

7 G. Fan, K. Liu, H. Su, Y. Luo, Y. Geng, L. Chen, B. Wang, Z. Mao, X. Sui and X. Feng, *Chem. Eng. J.*, 2022, **434**, 134702.

8 P. Deka, V. K. Verma, B. Yurembam, A. B. Neog, K. Raidongia and S. Subbiah, *Sustain. Energy Technol. Assessments*, 2021, **44**, 101093.

9 J. Yang, X. Hu, X. Kong, P. Jia, D. Ji, D. Quan, L. Wang, Q. Wen, D. Lu, J. Wu, L. Jiang and W. Guo, *Nat. Commun.*, 2019, **10**, 1171.

10 K. Saha, J. Deka, S. Hens, S. Saikia and K. Raidongia, *J. Mater. Chem. A*, 2018, **6**, 22931–22939.

11 J. Deka, K. Saha, R. Gogoi, G. K. Dutta and K. Raidongia, *ACS Appl. Electron. Mater.*, 2021, **3**, 277–284.

12 T. J. Konch, T. Dutta, A. B. Neog, R. Gogoi and K. Raidongia, *J. Phys. Chem. C*, 2021, **125**, 17939–17949.

13 S. Hong, J. K. El-Demellawi, Y. Lei, Z. Liu, F. Al Marzooqi, H. A. Arafat and H. N. Alshareef, *ACS Nano*, 2022, **16**, 792–800.

14 G. Yang, D. Liu, C. Chen, Y. Qian, Y. Su, S. Qin, L. Zhang, X. Wang, L. Sun and W. Lei, *ACS Nano*, 2021, **15**, 6594–6603.

15 K. Saha, J. Deka and K. Raidongia, *ACS Appl. Energy Mater.*, 2021, **4**, 8410–8420.

16 N. Kostoglou, K. Polychronopoulou and C. Rebholz, *Vacuum*, 2015, **112**, 42–45.

17 A. Nag, K. Raidongia, K. P. S. S. Hembram, R. Datta, U. V Waghmare and C. N. R. Rao, *ACS Nano*, 2010, **4**, 1539–1544.

18 R. K. Gogoi, A. B. Neog, T. J. Konch, N. Sarmah and K. Raidongia, *J. Mater. Chem. A*, 2019, **7**, 10552–10560.

19 J.-J. Shao, K. Raidongia, A. R. Koltonow and J. Huang, *Nat. Commun.*, 2015, **6**, 7602.

20 H. Wang, D. Zhao, Z. U. Khan, S. Puzinas, M. P. Jonsson, M. Berggren and X. Crispin, *Adv. Electron. Mater.*, , DOI:10.1002/aelm.201700013.

21 C.-G. Han, X. Qian, Q. Li, B. Deng, Y. Zhu, Z. Han, W. Zhang, W. Wang, S.-P. Feng,

G. Chen and W. Liu, *Science (80-.).*, 2020, **368**, 1091–1098.

22 B. Lei, S. Bai, S. Ju, C. Yin, C. Chen and J. Zhang, *Mater. Res. Express*, 2021, **8**, 62001.

23 Y. Fang, H. Cheng, H. He, S. Wang, J. Li, S. Yue, L. Zhang, Z. Du and J. Ouyang, *Adv. Funct. Mater.*, 2020, **30**, 2004699.

24 T. E. DeCoursey and V. V Cherny, *J. Gen. Physiol.*, 1997, **109**, 415–434.

25 N. K. Roberts and H. L. Northey, *J. Chem. Soc. Faraday Trans. 1 Phys. Chem. Condens. Phases*, 1974, **70**, 253–262.

26 L.-J. Cheng and L. J. Guo, *Nano Lett.*, 2007, **7**, 3165–3171.

27 X. L. Deng, T. Takami, J. W. Son, E. J. Kang, T. Kawai and B. H. Park, *Sci. Rep.*, 2014, **4**, 4005.

28 S. L. Kim, H. T. Lin and C. Yu, *Adv. Energy Mater.*, 2016, **6**, 1600546.

29 Y. Zhang, Y. Wang, Z. Xiong, Y. Hu, W. Song, Q. Huang, X. Cheng, L.-Q. Chen, C. Sun and H. Gu, *ACS Omega*, 2017, **2**, 793–799.

30 R. K. Gogoi, A. B. Neog, N. Sarmah and K. Raidongia, *J. Mater. Chem. A*, 2019, **7**, 21157–21167.

Chapter 4

Application of Lamellar Nickel Hydroxide Membrane as a Tunable Platform for Ionic Thermoelectric Studies

Summary

All our previous works are primarily based on the thermodiffusion of cations under temperature gradients inside the nanofluidic channels of reconstructed 2D material. This study focuses on establishing a nanofluidic platform that can be fine-tuned to thermodiffuse both cations and anions by incorporating suitable ion-generating species. First, a lamellar membrane of β-$Ni(OH)_2$ (Ni-M) was fabricated by using a bottom-up synthesis method. Negative ionic Seebeck coefficient of Ni-M was tuned from (-7.04 ± 0.3 mV/K to -13.7±0.2 mV/K) by simple incorporation of Mg-aminoclay and benzyltriethyl ammonium chloride salt. Similarly, when doped with cation-generating species such as poly(4-styrene sulfonic acid) (PSS), it exhibits positive ionic Seebeck coefficient (up to +12 ± 1.9 mV/K). The positive and negative ionic thermoelectric (i-TE) materials, prepared by doping Ni-M, are assembled into ionic thermopiles generating thermovoltages up to 1 V (at ΔT = 12 K). The dependency of these ionic Seebeck coefficients on the nature of migrating ion was additionally demonstrated by carrying the anionic parts of the quaternary ammonium salts. The nanofluidic systems based on Ni-M demonstrate an additional pathway for electricity harvesting by connecting the colder zones of the positive and negative i-TE materials with another ion-conducting membrane. Finally, in contrast to organic polymer-based i-TE systems, the Ni-M-based system exhibits consistent performance even after being exposed to high temperatures (~200 °C, 5 minutes).

4.1. Introduction:

The development of ionic thermoelectric materials capable of exhibiting ionic thermopower in both positive and negative directions holds significant promise for advancing various technological applications. Traditionally, thermoelectric materials have focused primarily on exploiting electron transport for generating electrical energy from temperature differentials. However, the emergence of ionic thermoelectric (i-TE) materials opens new avenues for harnessing the potential of both cations and anions for contribution to thermopower. By incorporating suitable dopants or modifiers, such as ion-generating species, these materials can be tailored to exhibit either positive or negative ionic Seebeck coefficients, enabling the construction of thermopiles and other complex i-TE systems capable of generating significant thermovoltages. Although the theoretical understandings of these aspects are comparatively transparent considering fine tuning of ionic Seebeck coefficient both in positive and negative directions, however, in the real time scenario, only a handful of work are so far reported. Some of them includes polyvinyl alcohol and sodium hydroxide based hydrogel (-37.61 mV/K)[1], PDDAC (-19 mV/K)[2], bisulfate transport in hydrogels (-25 mV/K)[3], $FeCl_3$ doped poly(3-hexylthiophene) films (-15 mV/K)[4], liquid crystalline ionogels (-5.9 mV/K)[5], calcium ion (Ca^{2+}) coordinated bacterial cellulose (CaBC) (-27.2 mV/K)[6] and PEDOT:PSS (-18.2 mV/K).[7]

2D materials based nanofluidic systems have not yet been explored in the development of n-type ionic thermoelectric materials so far (with negative thermopower) which can have the potential of opening up new doors towards developing both p-type and n-type ionic thermoelectric materials. As per our previous findings, it is suggested that the development and enlargement of ionic Seebeck coefficients towards positive directions through the surface functionalisation and intercalation of mobile cation generating species, a novel opportunity has emerged to create functional materials capable of being adjusted to exhibit ionic thermopower in both positive and negative directions.

4.2. Scope of the present investigation:

The field of ionic thermoelectricity is getting its momentum due to several advantages as compared to traditional thermoelectricity due to several advantages such as higher ionic Seebeck coefficient, ease of fabrication, possibility of scalable approach etc. Yet, the majority of reported i-TE materials rely on the thermodiffusion or thermophoretic mobility of cations, (positive Seebeck coefficients).[8–12] However, for sophisticated applications like fabricating ionic thermopile[13–16], high-resolution temperature sensors[16,17], and pyroelectric detectors[13], i-TE materials with both positive and negative Seebeck coefficients are indispensable. In this study, a platform was constructed from lamellarly stacked 2D nanosheets capable of being tuned in both positive and negative directions as required. A methodology was thoroughly investigated that demonstrated the possibility of enhancing ionic thermopower by incorporating mobile ion generating species into the system. For instance, the incorporation of Mg-aminoclay molecules into the platform generated mobile OH^- ions in the presence of atmospheric water molecules thereby generating a negative ionic thermopower which was further elevated by the introduction of both Mg-aminoclay and benzyltriethylammonium chloride salt (capable of generating mobile Cl^- ions). The thermopower can be easily altered towards the positive direction by simple incorporation of poly (4-styrenesulfonic acid). The fabrication of i-TE materials in both positive and negative directions allowed to design an ionic thermopile capable of enhancing the overall ionic thermovoltages. An alternative route of harvesting electricity was further demonstrated by simple incorporation of an another ion conducting membrane towards the colder side of positive and negative i-TE materials. Finally, similar to the other inorganic i-TE materials, this fabricated system also showed stability at elevated temperature without losing its ionic thermopower.

Material structure and properties: Nickel(II) hydroxide exhibits two recognized polymorphic forms, designated as α and β. The α structure comprises layers of $Ni(OH)_2$ with

intercalated anions or water molecules, whereas the β form adopts a hexagonal close-packed arrangement of Ni^{2+} and OH^- ions. In the presence of water, the α polymorph tends to undergo recrystallization into the β form. Additionally, various γ nickel hydroxides have been identified, characterized by crystal structures featuring significantly larger inter-sheet distances. Nickel hydroxide finds applications in diverse fields such as rechargeable nickel-metal hydride batteries as an active material in the positive electrode, catalysis, supercapacitors, water treatment processes, sensors, and more.

Mg-aminoclay, a synthetic clay with the approximate composition $R_8Si_8Mg_6O_{16}(OH)_4$, where R = $CH_2CH_2NH_2$, features layers of magnesium ions (Mg^{2+}) sandwiched between layers of negatively charged silicate $(SiO_4)^{4-}$ tetrahedra. These layers are held together by electrostatic forces, with the positively charged magnesium ions balancing the negative charge of the silicate layers. Owing to its unique properties, Mg-aminoclay finds numerous applications across various fields, including its use as an adsorbent, in catalysis, drug delivery processes, flame retardants, soil amendments, and more.

4.3. Experimental section:

Materials: Nickel (II) acetate tetrahydrate ($Ni(CH_3CO_2H)_2.4H_2O$) and Magnesium chloride ($MgCl_2$) were purchased from SRL Pvt. Ltd., Liquor Ammonia solution and Poly (4-styrenesuphonic acid) (PSS) were purchased from Sigma-Aldrich, 3-aminopropyltriethoxysilane was purchased from Thermo Fischer Scientific. Ethanol was purchased from Changshu Hongheng Fine Co. Ltd. Poly (4-styrenesuphonic acid) (PSS) were purchased from Sigma Aldrich co. Benzyltrietylammoium chloride, Benzyltrietylammoinum bromide and Benzyltriethylammonium hydroxide were purchased from Avra Synthesis Ptv. Ltd. Vermiculite clay was purchased from Sigma Aldrich. The copper electrodes were purchased from the local market. Silver paste was purchased from Alfa-Aesar Pvt. Ltd.

Preparation of $Ni(OH)_2$ nanosheets: 0.35 grams of Nickel (II) acetate tetrahydrate ($Ni(CH_3CO_2H)_2.4H_2O$) were dissolved in 30 ml of deionized (DI) water, followed by the gradual addition of 670 microliters of 25% aqueous ammonia with continuous stirring. The solution was then stirred for 24 hours. A green precipitate formed, ~~which~~ was then separated from the solution by centrifugation and washed several times with DI water. Subsequently, the prepared $Ni(OH)_2$ was transferred into DI water to create a dispersion with a concentration of 10 mg/ml.

Preparation of $Ni(OH)_2$ membrane: $Ni(OH)_2$ membranes were fabricated from the initial $Ni(OH)_2$ dispersion through vacuum filtration. Specifically, 15 milliliters of the (10 mg/ml) $Ni(OH)_2$ dispersion were subjected to vacuum filtration using a PTFE membrane support with a pore diameter of 0.1 µm. The resulting membrane was then dried in ambient conditions to yield a free-standing $Ni(OH)_2$ membrane.

Preparation of Mg-Aminoclay: To prepare Mg-Aminoclay, 1.68 grams of Magnesium chloride ($MgCl_2$) were dissolved in 40 grams of ethanol. Subsequently, 2.6 milliliters of 3-aminopropyltriethoxysilane were added dropwise with vigorous stirring. The solution was then stirred for 24 hours. The resulting white product was separated from the solution via centrifugation and washed multiple times with ethanol. Finally, it was dried at 40°C in air.

Preparation of $Ni(OH)_2$ and Mg-aminoclay composite membrane: Composite membranes containing $Ni(OH)_2$ and Mg-aminoclay were fabricated via vacuum filtration of composite mixtures with same compositions. Initially, varying amounts of Mg-aminoclay (30 mg, 50 mg, 100 mg and 200 mg) were mixed with 15 ml of 10 mg/ml $Ni(OH)_2$ dispersion and sonicated for 20 minutes. Subsequently, the respective composite dispersions were subjected to vacuum filtration using a PTFE support with a pore diameter of 100 nm. Finally, the membranes were dried under ambient conditions to obtain free-standing membranes.

Preparation of $Ni(OH)_2$ and Benzyltriethylammonium chloride composite (BTAC) membrane: To fabricate the composite membrane comprising $Ni(OH)_2$ and BTAC salt, initially, 7 ml of $Ni(OH)_2$ dispersion (10 mg/ml) was vacuum-filtered using a PTFE membrane with a pore size of 100 nm, forming a layer of $Ni(OH)_2$ nanosheets. Onto this layer, a mixture of 8 ml $Ni(OH)_2$ dispersion (10 mg/ml) and 200 mg BTAC salt was vacuum-filtered again and left to dry in ambient conditions, resulting in a free-standing Ni-Cl-M membrane.

Preparation of $Ni(OH)_2$, Mg-aminoclay and different quaternary ammonium salt composite membranes: To prepare the composite membranes of $Ni(OH)_2$, Mg-aminoclay, and various quaternary ammonium salts, 15 ml of $Ni(OH)_2$ dispersion (10 mg/ml) was mixed with 100 mg of Mg-aminoclay and sonicated for 20 minutes. Subsequently, this dispersion was divided into two equal portions. Specific amounts of Benzyltriethylammonium chloride (BTAC) (100 mg, 150 mg, 200 mg, and 250 mg) were added to one portion of the dispersion, while the other portion, containing only $Ni(OH)_2$ and Mg-aminoclay, underwent vacuum filtration through a PTFE membrane with a pore diameter of 0.1 µm. Upon nearing completion of the filtration process, the fraction with added salt was poured onto the filtered portion and subjected to vacuum filtration before drying to yield a free-standing composite membrane. During the vacuum filtration, it's notable that not all of the BTAC salt remained within the $Ni(OH)_2$ membrane. Based on ion chromatography experiments of Cl^- ions, approximately ~30% of the BTAC salts were found to be retained within the composite membrane, which was considered when calculating the weight percentages of the BTAC salts.

Following the same procedure, composite membranes of $Ni(OH)_2$ (150 mg), Mg-aminoclay (100 mg), Benzyltriethylammonium bromide (200 mg), and $Ni(OH)_2$ (150 mg), Mg-aminoclay (100 mg), Benzyltriethylammonium hydroxide (200 mg) were also prepared.

Preparation of $Ni(OH)_2$ and Poly(4-styrenesulfonic) acid composite membrane: To prepare the composite membranes of $Ni(OH)_2$ and Poly(4-styrenesulfonic acid), 15 ml of $Ni(OH)_2$ dispersion (10 mg/ml) was combined with 1 ml of Poly(4-styrenesulfonic acid) solution (Molecular weight ~75,000) and sonicated for 30 minutes. The resulting composite mixture was then vacuum-filtered through a PTFE support with a pore diameter of 100 nm and dried under ambient conditions to produce a free-standing membrane.

Preparation of vermiculite nanosheets and membrane fabrication: Bulk vermiculite crystals were exfoliated using an ion exchange method. Initially, 200 mg of vermiculite undergo reflux at boiling temperature with a saturated aqueous solution of NaCl for 24 hours, followed by multiple washes with DI water. The Na-exchanged washed sample is then refluxed with a 2 M aqueous LiCl solution at boiling temperature for 24 hours, followed by additional washing with DI water. Upon completion of the washing process, an aqueous dispersion with a concentration of 1 mg/ml is prepared using the washed product.

Free-standing vermiculite membranes are prepared through vacuum filtration of 40 ml of the 1 mg/ml vermiculite dispersion through a PTFE membrane with a pore diameter of 100 nm. After drying under ambient atmospheric conditions, the vermiculite membrane is peeled off from the support to obtain the free-standing vermiculite membrane.

Fabrication of Ionic Thermoelectric Devices: For the fabrication of i-TE devices a specific dimension (2 cm x 0.8 cm) of each respective membrane was cut and positioned onto a stage consisting of two glass slides measuring 2 cm x 2 cm. These glass slides were connected together with adhesive tape, maintaining an air gap of approximately 2 mm to prevent unintended heat transfer. The membranes for the measurements were affixed with two copper electrodes using conductive silver paste, ensuring a distance of 1.5 cm between them.

The fabricated thermoelectric device was then placed atop a stage comprising two Peltier devices, one serving as a heat source and the other as a heat sink. The temperature difference applied across the membrane was measured by positioning two K-type thermocouples, attached to a Testo 735 temperature measuring instrument, on the glass slides adjacent to the samples. A DC regulated power supply (METARAVI TM – RPS 30005) powered the Peltier devices, thereby maintaining the temperature gradient. The resulting thermovoltages were measured using a 2450 Keithley Sourcemeter.

The precautions were taken to minimize potential errors in temperature measurements. The magnitude of probable errors associated with temperature measurement positions was assessed by simultaneously measuring the temperature of the glass slides and the surface of the samples. This was done by systematically varying the temperature between 18 °C and 35 °C, as shown in Figure 4.1a and 4.1b. Typically, the temperature of the sample surface was found to be approximately 1±0.3 °C lower than that of the glass surface when the temperature of the glass surface exceeded the ambient temperature (~23 °C). Conversely, it was approximately 0.8±0.4 °C higher than the glass surface when the temperature of the glass surface was lower than the ambient temperature (Figure 4.1a). Similarly, the ΔT values measured between the hot and cold

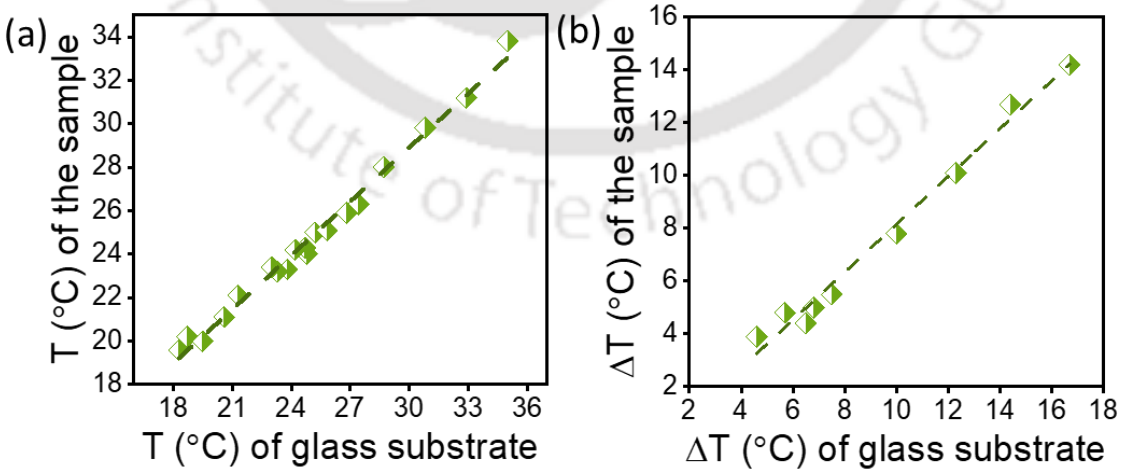

Figure 4.1: (a) Calibration curve for the temperature of the glass surface and temperature of the sample surface with respect to the glass surface. (b) Calibration curve for the temperature gradient in between the glass surfaces and temperature gradient across sample surface with respect to the glass surface temperature (schematic shown in Figure 2a).

zones of the sample surface were approximately ~1.9±0.5 °C lower than those measured on the glass surface (Figure 4.1b).

Fabrication of ionic thermopile: The ionic thermopile was assembled by connecting the Ni-PSS-M and Ni-AC-Cl-M-29 membranes (2 cm x 0.8 cm) in series on a stage composed of two glass slides. An air gap was maintained between the two glass slides to prevent unwanted heat transfer.

To harness additional power, the thermopile was constructed in such a manner where one side of both the Ni-PSS-M and Ni-AC-Cl-M-29 membranes (2 cm x 0.8 cm) was connected to a vermiculite membrane (2 cm x 0.8 cm). Integration of these membranes was achieved by introducing a water droplet of approximately 20 µl and allowing it to dry under ambient conditions. Upon completion of the drying process, one electrode was connected to the junction of Ni-PSS-M and vermiculite using conductive silver paste, while the other electrode was connected to the junction of Ni-AC-Cl-M-29 and vermiculite.

Similarly, to fabricate the thermopile with the nanofluidic vermiculite membrane, the same procedure was followed, except that the two electrodes were connected to the other side of the vermiculite membrane. One electrode was positioned on top of the Ni-AC-Cl-M-29 membrane, and the other was placed on top of the Ni-PSS-M membrane, as depicted in the inset of Figure 4.21h.

Fabrication of nanofluidic device: To fabricate the nanofluidic device, rectangular pieces of Ni-M (1.5 cm x 0.5 cm x 0.005 cm) and Ni-AC-M (1.5 cm x 0.5 cm x 0.0065 cm) were encapsulated within a PDMS elastomer. Two reservoirs for DI water and electrolyte were formed at both ends of the nanofluidic device, allowing the DI water and electrolyte within the reservoirs to come into contact with the membranes. The membranes were hydrated by placing them adjacent to DI water-filled reservoirs for 12 hours. Subsequently, ~0.3 ml of NaOH

electrolyte with a specific concentration (ranging from 10^{-6} M to 1 M) was added to the reservoirs and allowed to soak into the membranes for approximately 6 hours. After completing the soaking process, I-V curves were obtained for the particular concentration of NaOH electrolyte, repeating the procedure for other concentrations of NaOH electrolyte as well.

4.4. Characterizations: The morphological structures of $Ni(OH)_2$ membranes were examined using field emission scanning electron microscopy (FESEM) (Zeiss, model: Sigma), while the nanosheets of $Ni(OH)_2$ and Mg-Aminoclay were characterised via Field Emission Transmission Electron Microscopy (FETEM) (JEOL, Model: 2100F). The compositional analysis was conducted through Energy-dispersive X-ray analysis utilizing FESEM (Zeiss, model: Sigma). X-ray diffraction patterns were obtained using a Bruker D-205505 Cu-Kα radiation (λ = 1.54 Å) (Rigaku, model: Micromax-007HF). Additionally, IR spectroscopic analysis was performed using a Perkin Elmer (Spectrum Two) instrument. Zeta potential measurements for the aqueous dispersion of nanosheets were conducted with a Zetasizer instrument (Malvern, Nano-ZS90).

4.5. Result and discussions:

Freestanding β-$Ni(OH)_2$ membrane (Ni-M):

β-$Ni(OH)_2$ stands as a crucial layered material with significant relevance in alkaline rechargeable batteries. Its versatile applications extend to various fields including photocatalysis[18–21], electrocatalysis, electrosynthesis[22–24], supercapacitors[25–30] and electrochemical sensors.[30–33] For the exploration of β-$Ni(OH)_2$ as an ionic thermoelectric (i-TE) material, samples were prepared through the precipitation of Ni^{2+} ions (from nickel acetate tetrahydrate) using aqueous ammonia. The formation of β-$Ni(OH)_2$ nanosheets were verified

using FETEM image shown in Figure 4.2a. Vacuum filtration of the aqueous β-$Ni(OH)_2$ nanosheets yielded a freestanding membrane (Ni-M) as shown in the inset of the Figure 4.2b.

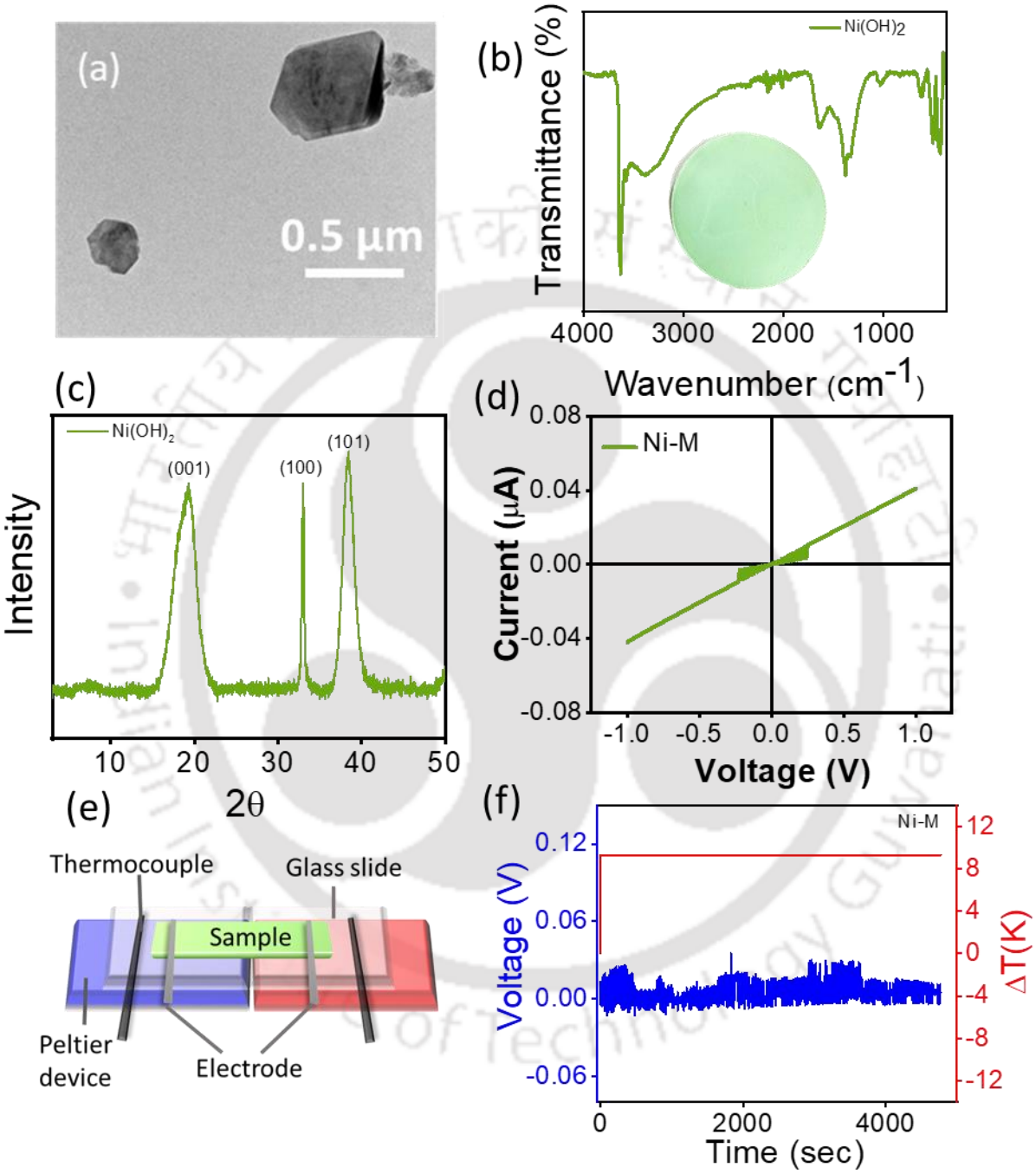

Figure 4.2: (a) FETEM image of a βi-$Ni(OH)_2$ nanosheets. (b) FT-IR spectra for Ni-M membrane, the inset represents a digital photograph of a freestanding Ni-M. (c) pXRD pattern of Ni-M. (d) The I-V curve recorded with Ni-M. (e) Schematic of the experimental setup used for the i-TE measurements. (f) Negligible thermoelectric response of Ni-M for the temperature gradient of 9 K.

The formation of the chemical composition of β-$Ni(OH)_2$ was additionally confirmed by FT-IR spectra and pXRD pattern shown in Figure 4.2b and c respectively. Nanofluidic devices comprising Ni-M, created by encapsulating a rectangularly cut piece of the lamellar membrane inside PDMS elastomers, exhibited negligible ionic transport (conductivity ~2.4 x 10^{-5} S/cm) even after 48 hours of immersion in water (Figure 4.2d). This ion-insulating property of Ni-M channels is attributed to the absence of intercalating ions and a narrow non-expansible interlayer space measuring 4.60 Å.[34,35] Because of this ion insulating property when an Ni-M was subjected to a temperature gradient using an experimental setup depicted in Figure 4.2e, no thermoelectric responses were recorded as shown in Figure 4.2f, therefore the material underwent further modifications.

Aminoclay doped β-$Ni(OH)_2$ membrane (Ni-AC-M):

To enhance the ionic conductivities of Ni-M, β-$Ni(OH)_2$ flakes underwent functionalization with synthetic clay sheets (Mg-aminoclay) derived from the reaction of 3-aminopropyltriethoxysilane and magnesium chloride in ethanol (experimental section 4.3)[36–38] The characterization of the prepared Mg-aminoclay samples is elaborated in Figure 4.3. The formation of synthetic clay nanosheets were verified from FETEM image depicted in Figure 4.3a and further confirmed from pXRD pattern and FTIR spectra shown in Figure 4.3e and f respectively. Aqueous dispersions of β-$Ni(OH)_2$ (15 mL, 10 mg/mL) and aminoclay (with varying amounts ranging from 17 to 57 wt%) were mixed, as depicted in Figure 4.3b, and subjected to vacuum filtration to produce freestanding membranes (Ni-AC-M). Digital photo and cross-sectional FESEM images illustrating the lamellar stacking of β-$Ni(OH)_2$ and aminoclay nanosheets are presented in Figure 4.3c and 4.3d, respectively. The presence of Mg-aminoclay in the composite of Ni-AC-M can be additionally verified from the EDX mapping shown in Figure 4.4. An enhancement of overall ionic conductivity was observed after the

incorporation of Mg-aminoclay within the β-$Ni(OH)_2$ nanosheets. The enhanced ionic conductivity of Ni-M following aminoclay intercalation (as revealed by the I-V curves in

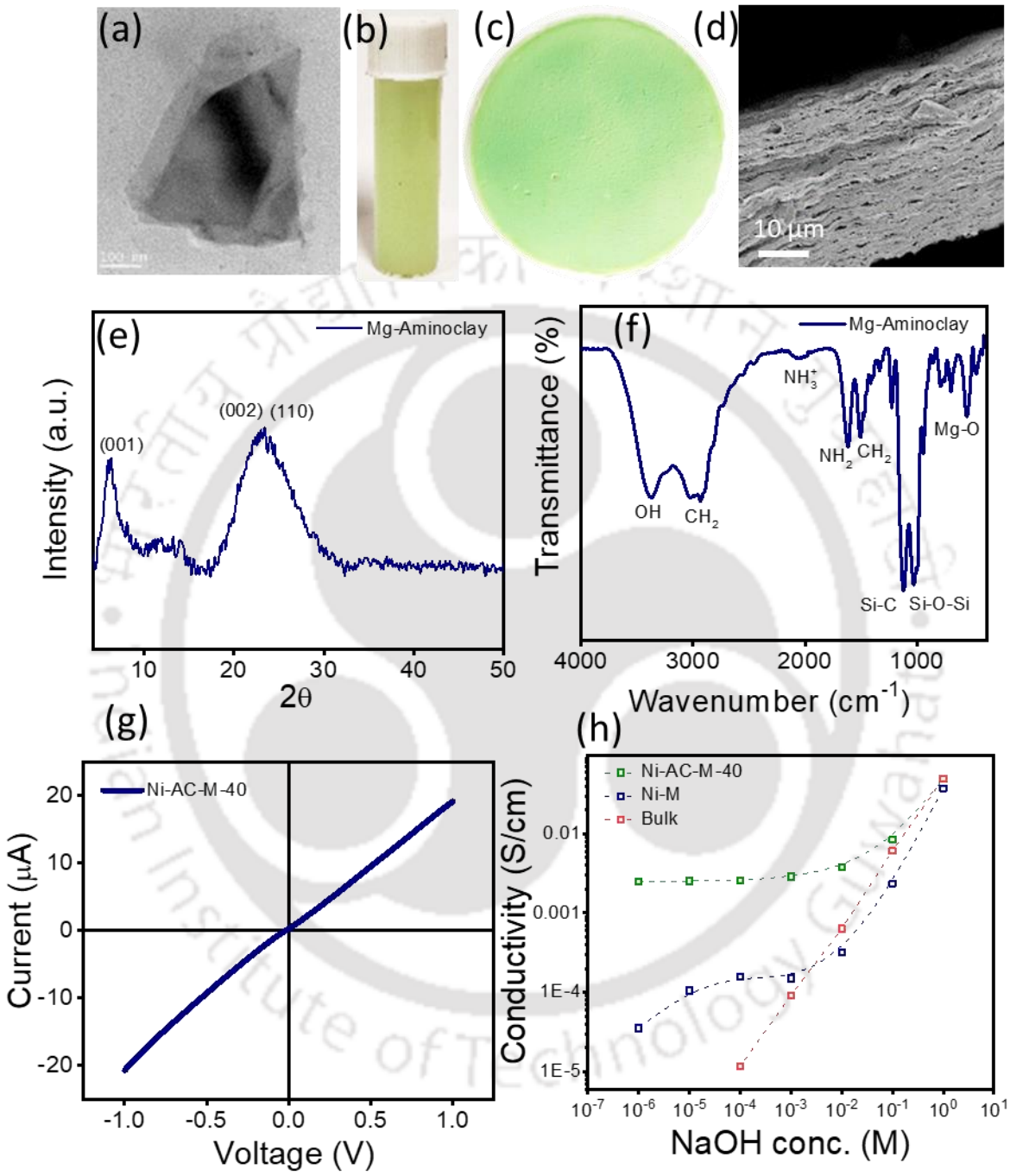

Figure 4.3: (a) FETEM image of a Mg-aminoclay nanosheets. Digital photographs of a (b) aqueous dispersion of βi-$Ni(OH)_2$ and Mg-aminoclay nanosheets, and (c) a freestanding Ni-AC-M-40. (d) Cross-sectional FESEM image of Ni-AC-M-40. (e) pXRD pattern, and (f) FT-IR spectra of Mg-Aminoclay. (g) I-V curve recorded with Ni-AC-M-40 nanofluidic device. (h) NaOH concentration vs ionic conductivity plot for Ni-M and Ni-AC-M-40 nanofluidic devices.

Figure 4.3g) is attributed to mobile OH^- ions and hydrophilic interlayer spaces. In the presence of aminoclay (2 mg/mL), the pH of DI water rose to approximately ~9.8. The plot of ionic conductivity vs. concentration of NaOH in Figure 4.3h further corroborates the presence of well-connected ultra-thin nanofluidic channels in Ni-AC-M-40. The IR spectra in Figure 4.5 highlights favourable chemical interactions between amino clay and β-$Ni(OH)_2$, such as hydrogen bonding between the –OH groups of β-$Ni(OH)_2$ and the $–NH_2$ groups of aminoclay, and the $–NH_2$ groups of aminoclay with the Ni^{2+} centers of β-$Ni(OH)_2$. Close inspection of the peak positions associated with NH_3^+ stretching and $–NH_2$ bending reveals a shift from 2050 cm^{-1} to 2108 cm^{-1}, and from 1611 cm^{-1} to 1635 cm^{-1}, respectively, for aminoclay and Ni-AC-M-40 membrane (Inset of Supporting Figure 4.5). The stretching frequencies of Ni-O for both

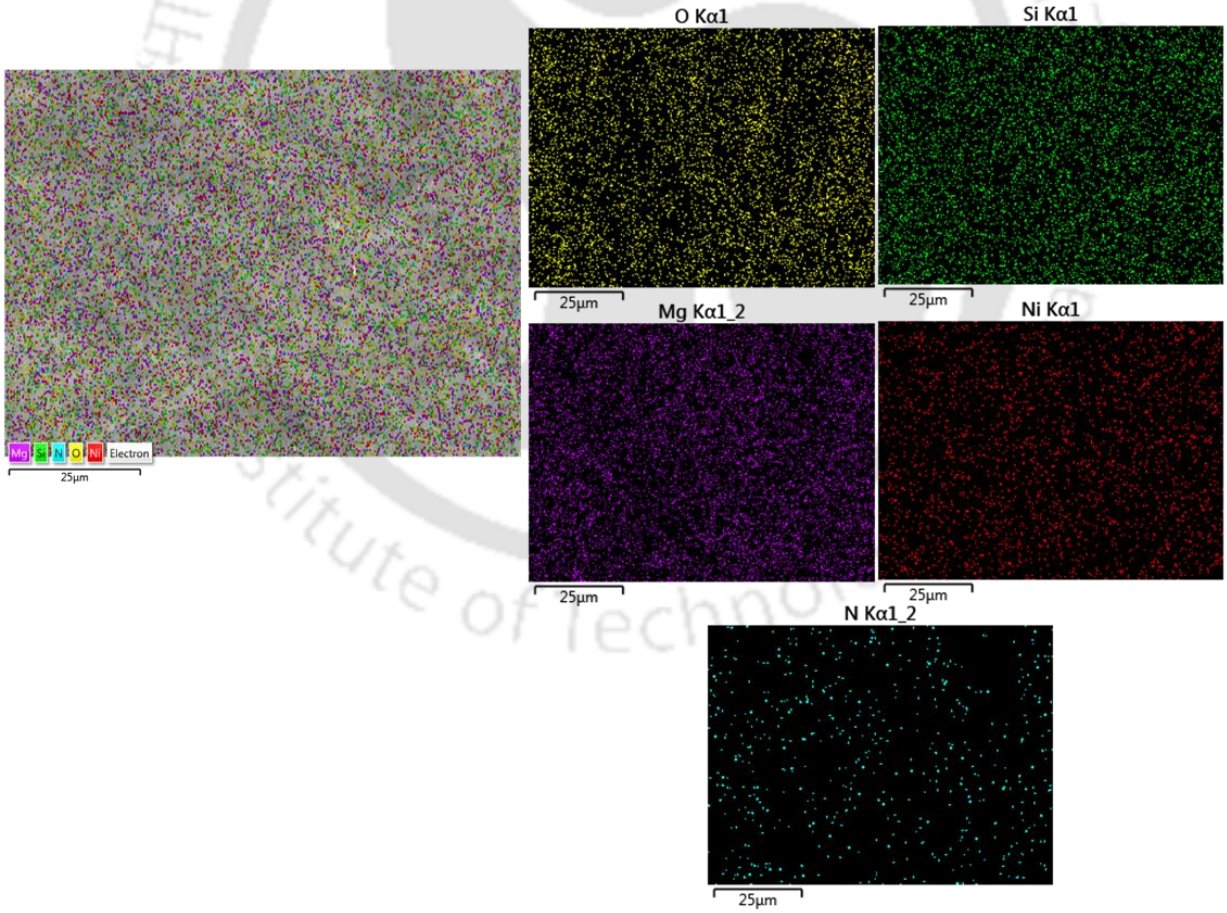

Figure 4.4: EDX mapping for the composite membrane Ni-AC-M-40

Ni-M and Ni-AC-M-40 membrane exhibit a downward shift from 506 cm^{-1} to 495 cm^{-1}, suggesting interactions between $–NH_2$ groups of aminoclay and Ni^{2+} centres of $Ni(OH)_2$.

Furthermore, the FT-IR spectra of $Ni(OH)_2$ reveal distinct peaks for hydrogen-bonded and non-hydrogen-bonded –OH stretching at 3374 cm^{-1} and 3631 cm^{-1}, respectively. However, in the case of the Ni-AC-M-40 membrane, the intensity of the IR peak for hydrogen-bonded –OH groups was notably higher compared to Ni-M, while the intensity for non-hydrogen-bonded –OH groups decreased. This observation indicates the presence of hydrogen bonding between –OH groups in β-$Ni(OH)_2$ and $–NH_2$ groups of aminoclay. The robust stability of Ni-AC-Ms in aqueous medium, evidenced by digital photos in Figure 4.6 after 50 days of soaking in water, underscores the strength of these chemical interactions.

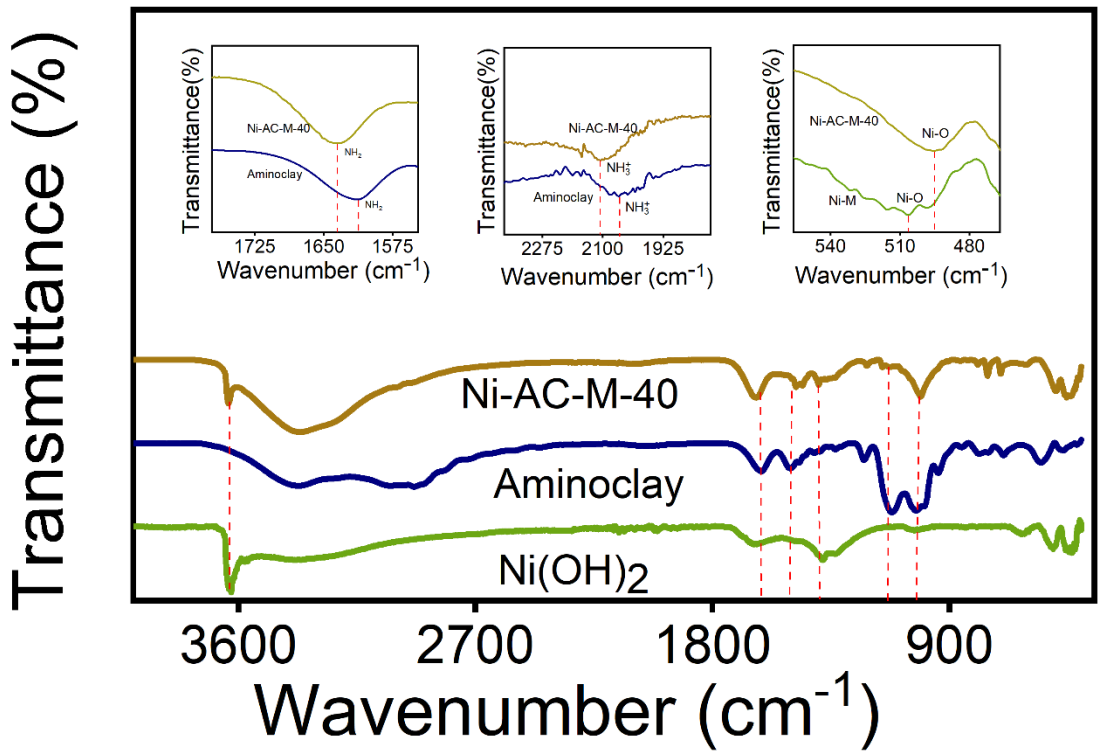

Figure 4.5: FT-IR spectra of $Ni(OH)_2$, Mg-Aminoclay and Ni-AC-M-40 membrane, (the inset IR spectra represents the shifts for IR peak positions for respective stretching and bending frequencies)

Ionic thermoelectric performance of Ni-AC-Ms:

Establishment of well-defined pathways with interconnected nanofluidic channels ensures a novel platform for i-TE studies. The i-TE performances of Ni-AC-Ms were investigated using an experimental setup outlined in Figure 4.2e. Upon exposure to a temperature difference (ΔT)

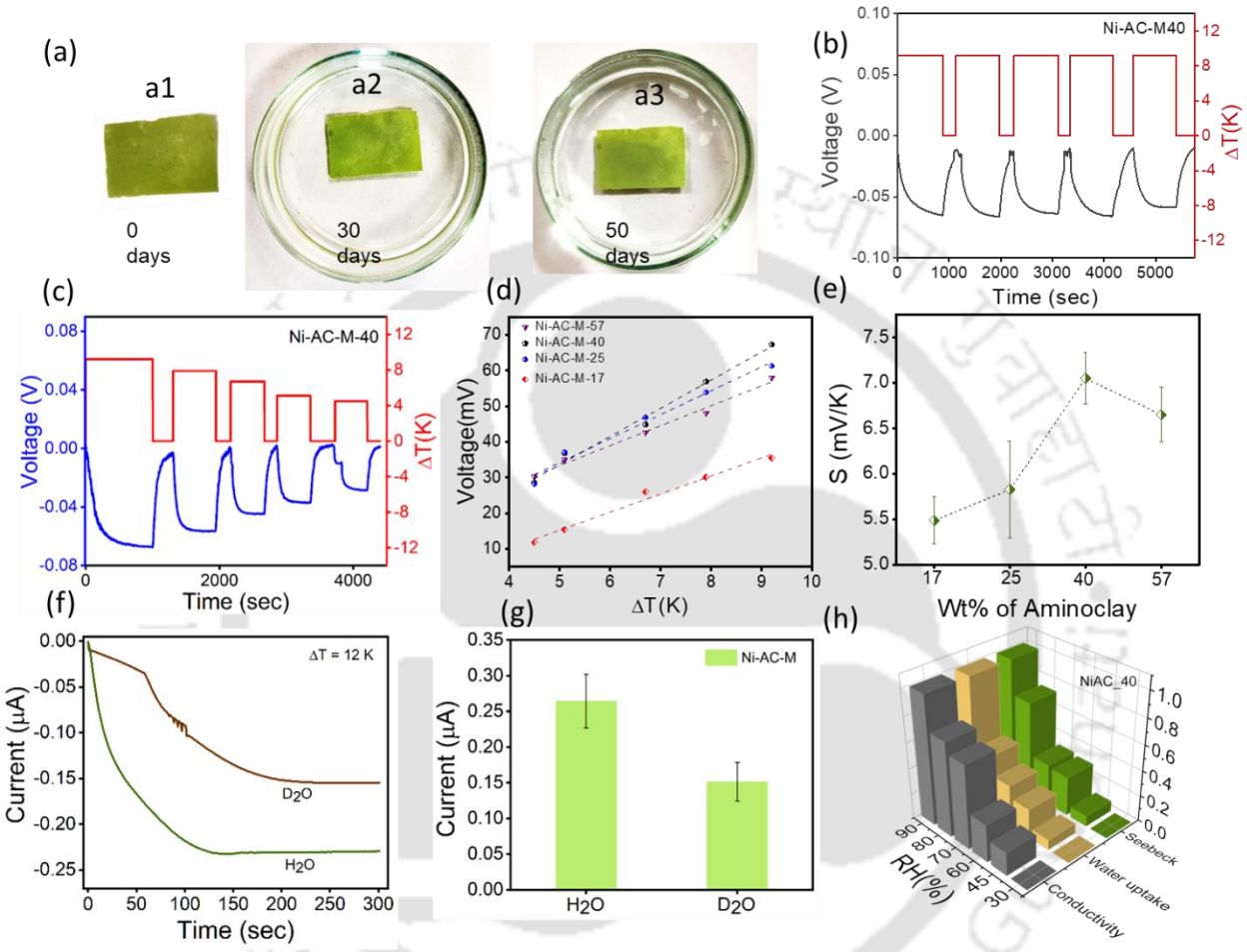

Figure 4.6: (a) Digital photograph of the Ni-AC-M-40 membrane (a1) before soaking in DI water, (a2) after 30 days of soaking in DI water, (a3) after 50 days of soaking in DI water. (b) Generation of thermovoltage of Ni-AC-M-40 at constant temperature gradient of 9 K. (c) Increment of the ionic thermovoltage with the increase of temperature gradient across Ni-AC-M-40. (d) Linear increment of the saturated thermovoltages with the temperature gradient across the Ni-AC-M. (e) Seebeck coefficients of Ni-AC-Ms with different wt% of aminoclay. (f) Generation of thermal current of H_2O-exposed Ni-AC-M-40 and D_2O-exposed Ni-AC-M-40 under a temperature gradient of 12 K. (g) Comparison of the thermal current of Ni-AC-M-40 with H2O and D2O under a temperature gradient of 12 K. (h) Simultaneous increment of water uptake, ionic conductivity and Seebeck coefficients for Ni-AC-M-40. Each of the measurements have been normalized with respect to the maximum value (water

of 9 K across the rectangular piece of Ni-AC-M-40, a negative thermovoltage was generated,

reaching saturation at – 67 mV within ~600 seconds (Figure 4.6b). Subsequently, upon removal of the temperature gradient, the thermovoltage began to decrease, approaching zero after approximately 290 seconds. The robustness of thermovoltage generation in Ni-AC-Ms was confirmed through repetitive temperature cycles, as evidenced by data up to the 5th cycle (see Figure 4.6b). Furthermore, Figure 4.6c and d illustrate that the generated thermovoltage increases with the escalating temperature gradient across the membrane. Similar condition was

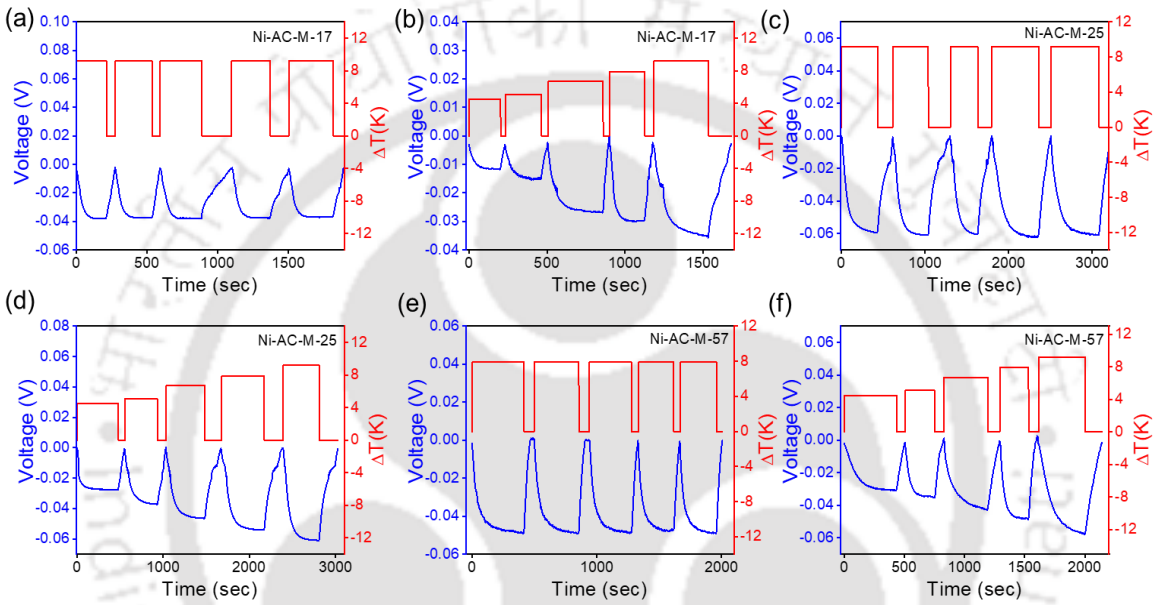

Figure 4.7: Generation of the thermovoltages by different Ni-AC-Ms.

applied to study the i-TE performance of other compositions of Ni-AC-Ms, revealing a linear increment of thermovoltages with increasing temperature gradient, as depicted in Figure 4.6d (respective thermovoltage curves are presented in Figure 4.7). With the application of the temperature gradient, the thermovoltage gradually increases and reaches a saturation level. The saturated ΔV vs ΔT plots, depicted in Figure 4.6d, were utilized to determine the Seebeck coefficients by fitting a linear line through the data points (R^2=0.98). Among all compositions, a maximum Seebeck coefficient of -7.04 ± 0.3 mV/K was observed for Ni-AC-M-40.

The generation of thermovoltages is attributed to the temperature gradient-driven diffusion (Soret effect) of mobile hydroxide ions (OH^-), originating during the hydration of amine groups of Mg-aminoclay in the presence of atmospheric water molecules (Figure 4.8). The Figure 4.8b schematically represents the generation of OH^- ions and migration under the influence of temperature gradient. To validate this hypothesis, all atmospheric water molecules surrounding Ni-AC-M-40 were replaced with D_2O through dehydration, followed by rehydration with the D_2O process. As anticipated, a reduction in the thermal current was

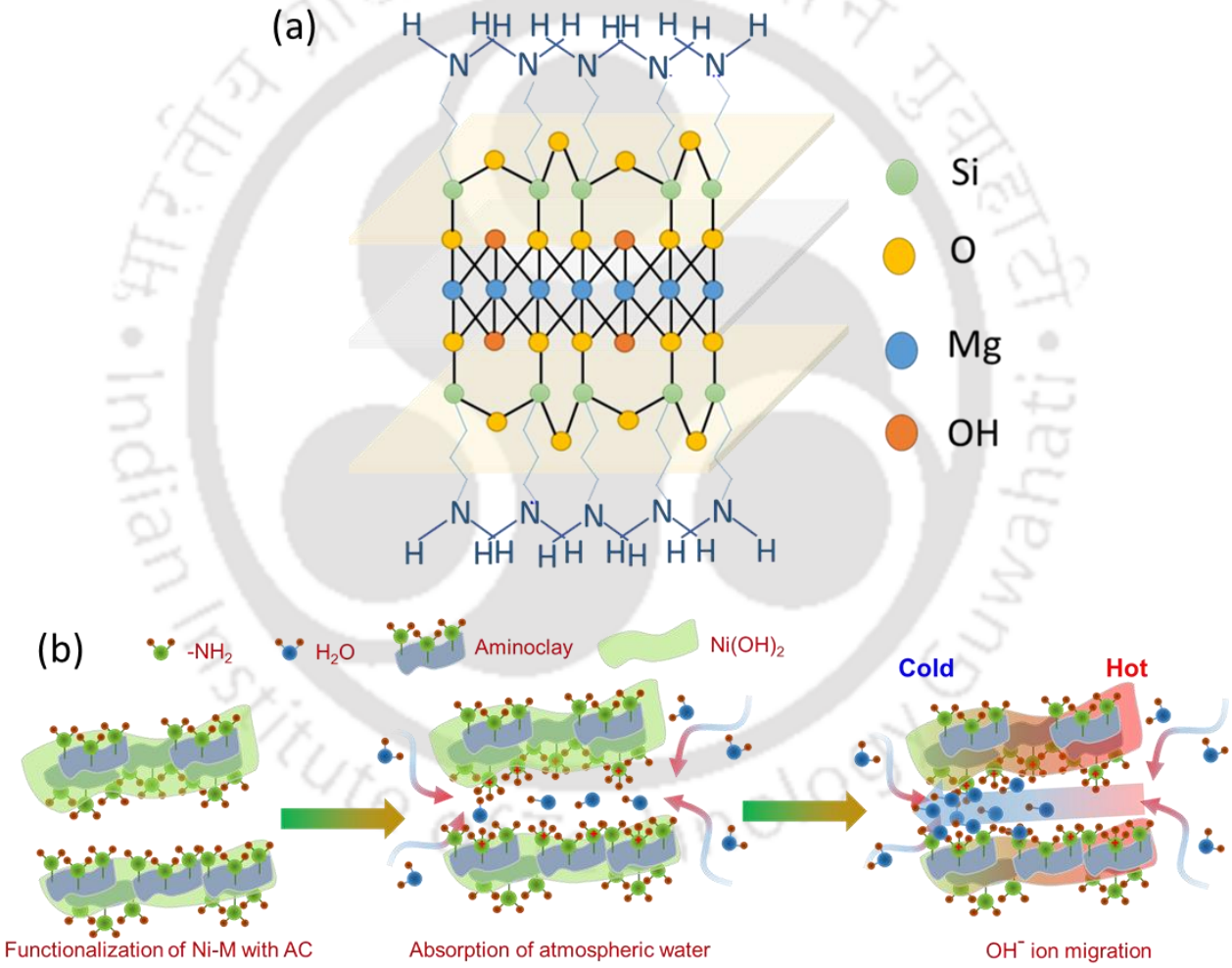

Figure 4.8: (a) Schematic of the structure of aminoclay. (b) Schematic representation of the absorption of water molecules by Ni-AC-M, formation of OH- ions and diffusion of OH- ions under temperature gradient.

observed with D_2O, as depicted in Figure 4.6f and g. Moreover, this thermal current returned to its original values upon re-exposure of Ni-AC-M-40 to H_2O molecules. The ratio of thermal

current for H_2O-exposed Ni-AC-M-40 to D_2O-exposed Ni-AC-M-40 was calculated to be 1.75. These findings support the hypothesis that the thermal diffusion of OH^- (or OD^-) ions is responsible for the thermovoltage. The increase in ionic conductivities and ionic Seebeck coefficients with increasing water uptake or relative humidity levels (RH) further corroborates this hypothesis of OH^- migration-based i-TE performance. Elevated humidity levels enhance the concentration of mobile OH^- ions through the dissociation of atmospheric water molecules, facilitating thermal diffusion of these OH^- ions through the 2D channels of Ni-AC-M, resulting in higher Seebeck Coefficient values (Figure 4.6h).

Ni-Cl-M membranes:

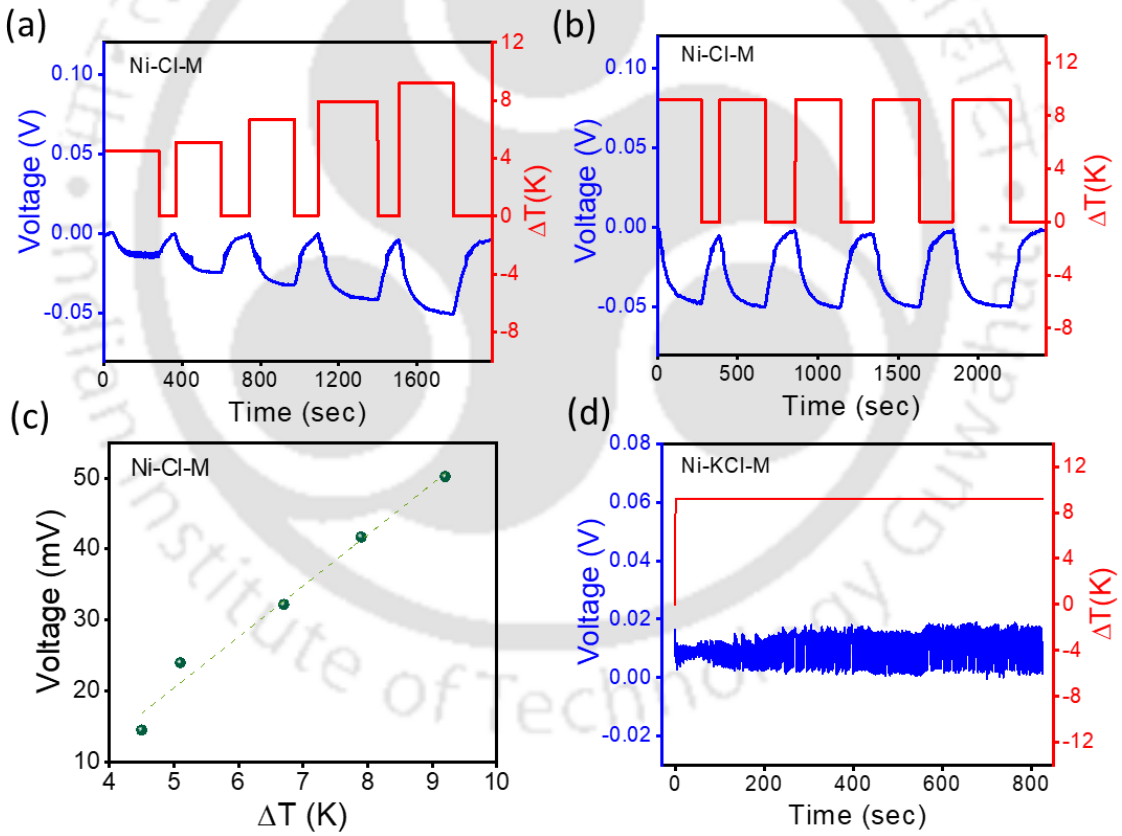

Figure 4.9: Generation of thermovoltage for Ni-Cl-M membrane (a) at varying temperature gradient (b) at constant temperature gradient. (c) Linear increment of the thermovoltage with respect to temperature gradient (d) negligible response with the temperature gradient across the Ni-KCl-M.

In the above section, it is observed that ion-insulating Ni-M channels could be converted into efficient ionic conductors by incorporating hygroscopic materials capable of in-situ generation of OH^- ions. Once loaded with ion-generating species, Ni-M channels became effective materials for ionic thermoelectricity (i-TE). To validate our hypothesis and further enhance the

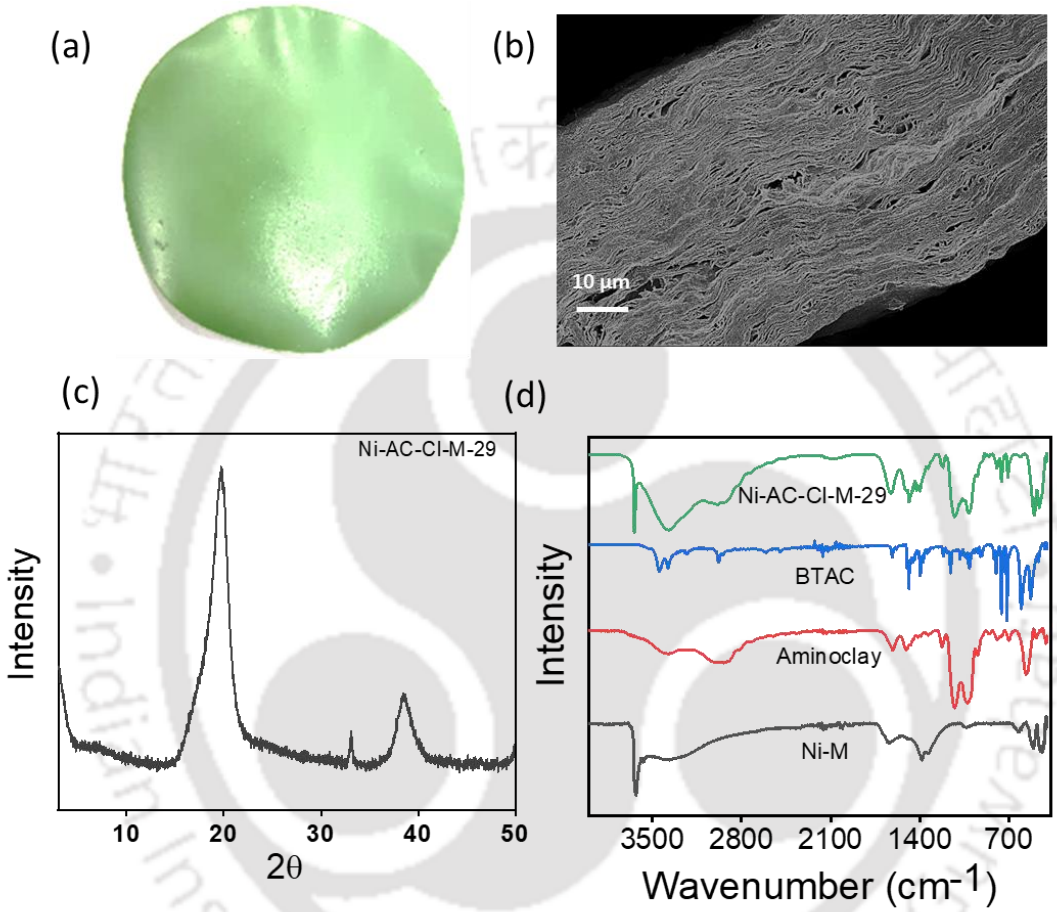

Figure 4.10: (a) a digital photograph of Ni-AC-Cl-M-29. (b) Cross-sectional FESEM image of Ni-AC-Cl-M-29. (c) pXRD pattern, and (d) FT-IR spectra of Ni-AC-Cl-M-29.

Seebeck coefficient, the thermoelectric (TE) experiments (Figure 4.9) were repeated by substituting Mg-aminoclay with Benzyltriethylammonium chloride (BTAC), another molecule capable of generating mobile anions. Typically, an aqueous mixture of β-$Ni(OH)_2$ and BTAC salt was vacuum-filtered through a PTFE membrane to prepare a freestanding membrane of β-$Ni(OH)_2$ loaded with BTAC (Ni-Cl-M) (see experimental section 4.3). The Ni-Cl-M exhibited

a negative Seebeck coefficient of -7.2 mV/K, attributed to the hygroscopic nature of BTAC and the significant difference in the sizes of the cationic and anionic groups (Figure 4.9 a, b and c). As suggested by Chen et al.[39] and Hu et al.[40], electrolytes with large cationic but smaller anionic groups are ideal for negative i-TE materials. Hence, the negative Seebeck coefficient of Ni-Cl-M is attributed to the hygroscopic nature of BTAC and the substantial difference in the sizes of the cationic and anionic groups. Furthermore, the Ni-M prepared with KCl (similar size of cationic and anionic groups) did not produce any thermovoltages under similar conditions (Figure 4.9d).

Ni-AC-Cl-M membranes:

Various possibilities for functionalizing Ni-M could create a new platform for enhancing and tuning i-TE parameters. For instance, a composite membrane was synthesized by incorporating BTAC (17, 23, 29, and 33%) into Ni-AC-M, named Ni-AC-Cl-M-17, Ni-AC-Cl-M-23, Ni-AC-Cl-M-29, and Ni-AC-Cl-M-33, respectively (experimental section 4.3). A digital image of

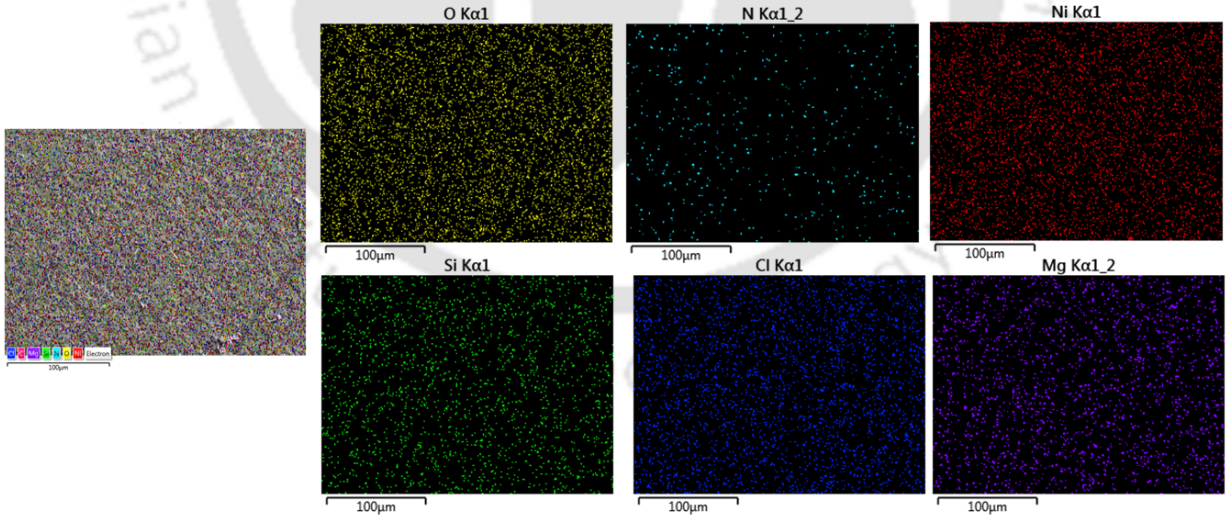

Figure 4.11: EDX mapping of Ni-AC-Cl-M-29 showing the homogenous distribution of all the elements.

the freestanding Ni-AC-Cl-M-29 membrane is shown in Figure 4.10a. The lamellar nature of

the composite membrane (Ni-AC-Cl-M-29) was verified from the cross-sectional FESEM image shown in Figure 4.10b. The composite membrane was additionally characterised with pXRD pattern and FT-IR spectra as shown in Figure 4.10c and 4.10d respectively and the presence of the Cl^- ions originated from BTAC salt is observed from the EDX mapping shown in Figure 4.11.

To determine the values of ionic conductivity, the I-V curves were recorded as illustrated in

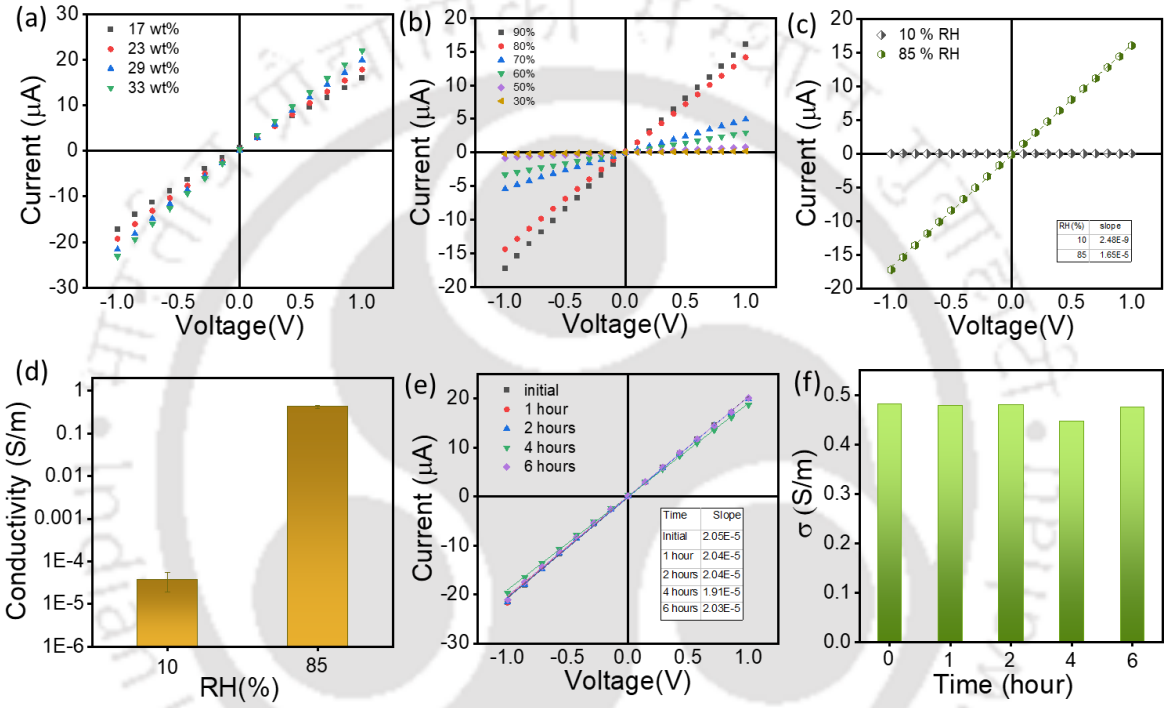

Figure 4.12: I-V curve of (a) different Ni-AC-Cl-Ms (with varying the wt% of BTAC salt), (b) Ni-AC-Cl-M-29 at different humidity levels, (c)Ni-AC-Cl-M-29 at 10% and 85% RH, (e) AC-Cl-M-29 at different intervals of time. Ionic conductivity values of Ni-AC-Cl-M-29 (d) at 10% and 85% RH, (f) at different intervals of time.

Figure 4.12. The conductivity (σ) was derived from the slopes of the respective I-V curves using the equation provided below (following existing literature references).

σ = slope x L/A

where,

L = length between the two electrodes, A= cross-sectional area of the membrane

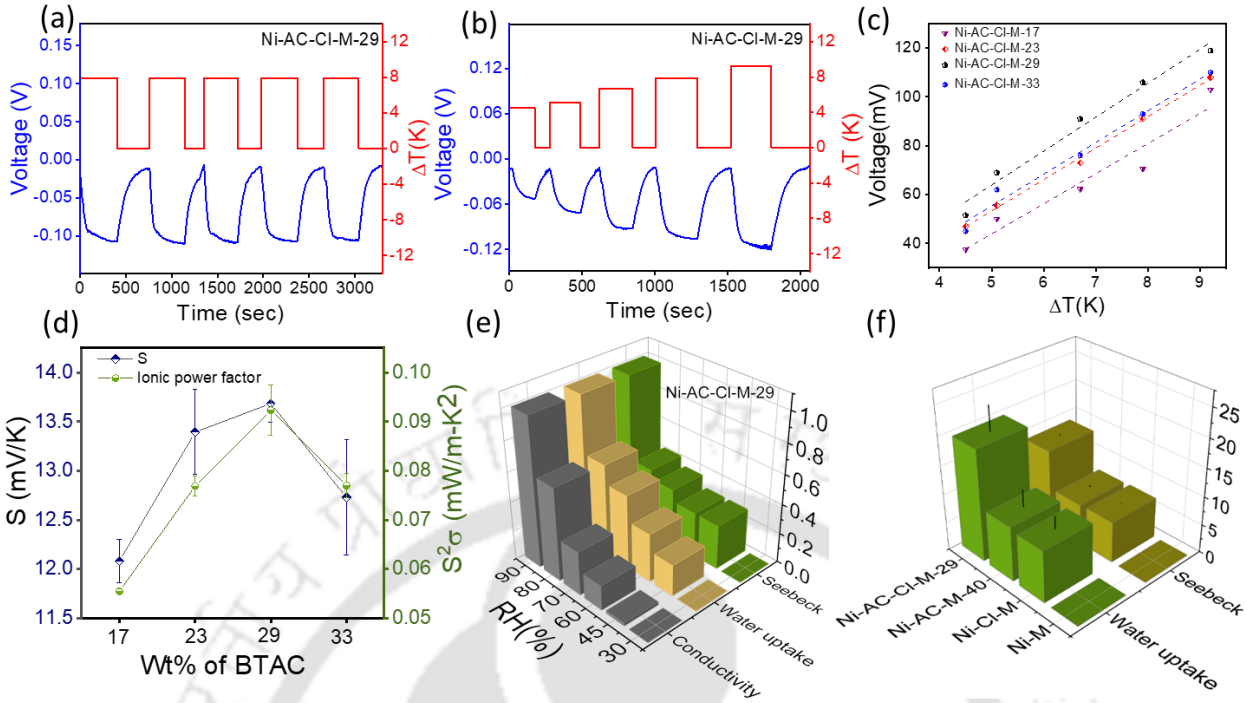

Figure 4.13: (a) Generation of thermovoltage by the Ni-AC-Cl-M-29 at ΔT = 8 K. (b) Generation of thermovoltage of Ni-AC-Cl-M-29 at variable temperature gradient. (c) linear increment of the saturated thermovoltage with respect to the temperature gradient for all of the Ni-AC-Cl-Ms. (d) Seebeck coefficients and ionic power factor of different Ni-AC-Cl-Ms (with varying the wt% of BTAC salt). (e) Simultaneous increment of water uptake, ionic conductivity and Seebeck coefficients for Ni-AC-Cl-M-29. Each of the measurements have been normalized with respect to the maximum value (water uptake (19.51 wt%), ionic conductivity (0.49 S/m), and Seebeck coefficient (13.7 mV/K)). (f) The concordant increment of Seebeck coefficient for Ni-M, Ni-Cl-M, Ni-AC-M-40 and Ni-AC-Cl-M-29 membrane with the water uptake capacity.

To comprehend the nature of conductivity (ionic or electronic), the I-V curves were recorded at varying relative humidity levels (RH % = 85 % and 10 %), as depicted in Figure 4.12c. The significant decrease in conductivity values (from 0.42 ± 0.03 S/m to 3.75 x 10^{-5}± 1.8 x 10^{-5}) at lower humidity levels indicates that ionic movement is the source of the observed conductivity (Figure 4.12d), as at lower humidity levels, the movement of ions are restricted due to the absence of water pathways. Moreover, to examine the time dependency of ionic conductivity, I-V curves were recorded at different time intervals (Figure 4.12e) and plotted in Figure 4.12f, revealing a nearly constant value over time.

The Ni-AC-Cl-Ms exhibited higher Seebeck coefficient values compared to Ni-AC-M and Ni-Cl-M. Notably, Ni-AC-Cl-M-29 displayed a thermovoltage of ~107 mV at ΔT = 8 K (Figure 4.13a), demonstrating repeatability up to the 5th cycle with similar ΔT, and a linear response with varying ΔT values (Figure 4.13b and c). The TE responses of other Ni-AC-Cl-Ms at constant and variable ΔT are presented in Figure 4.14. Among all Ni-AC-Cl-Ms, Ni-AC-Cl-29-M exhibited the highest Seebeck coefficient value of -13.7±0.2 mV/K (Figure 4.13d). Additionally, the ionic power factors ($S^2\sigma$) of all compositions were calculated based on earlier

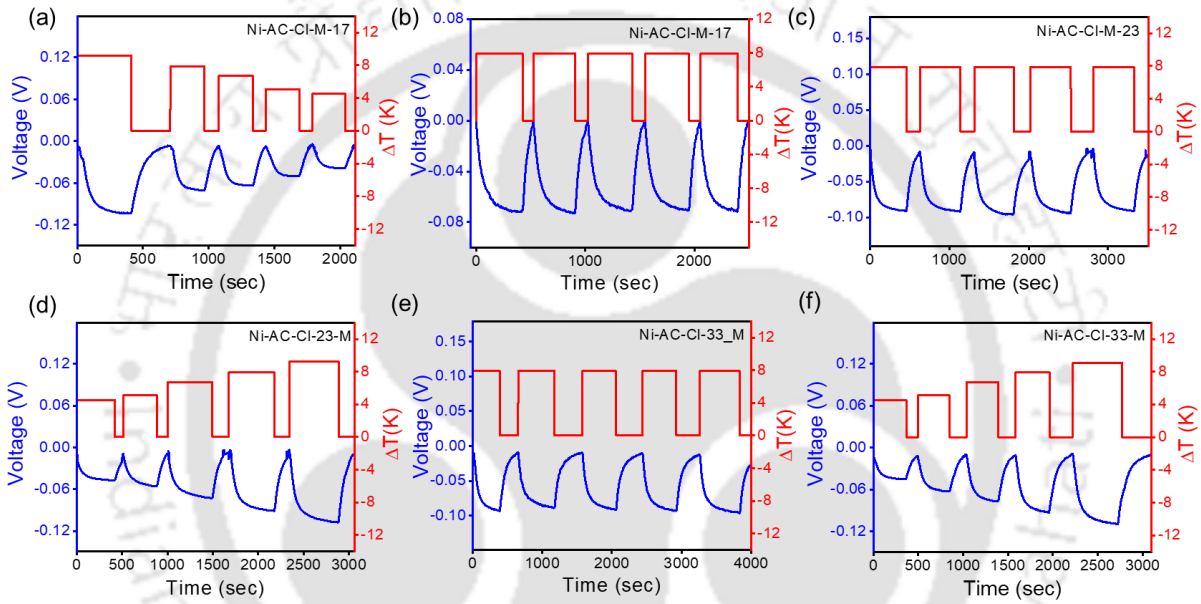

Figure 4.14: Generation of themovoltages for different composites of Ni-AC-Cl-Ms.

reports[8,12] and plotted in Figure 4.13d, where S^2 represents the square of the Seebeck coefficient and σ denotes the ionic conductivity (calculated from the I-V curves shown in Figure 4.12a). A maximum power factor of 0.09±0.005 mW/mK^2 was observed for Ni-AC-Cl-M-29. The importance of water molecules in the generation and enhancement of ionic thermovoltages is evident from the Figure 4.13e, where both the ionic conductivities and Seebeck coefficients of Ni-AC-Cl-M-29 increases with higher levels of water uptake at elevated relative humidity (RH%). The ionic conductivities in the Figure 4.13e were calculated from the I-V curves

presented in Figure 4.12b. The enhanced Seebeck coefficients in Ni-AC-Cl-Ms following the inclusion of both BTAC salt and Mg-aminoclay can be attributed to three main factors: (a) elevated ionic concentrations (OH^- and Cl^- ions), (b) increased water absorption (both BTAC

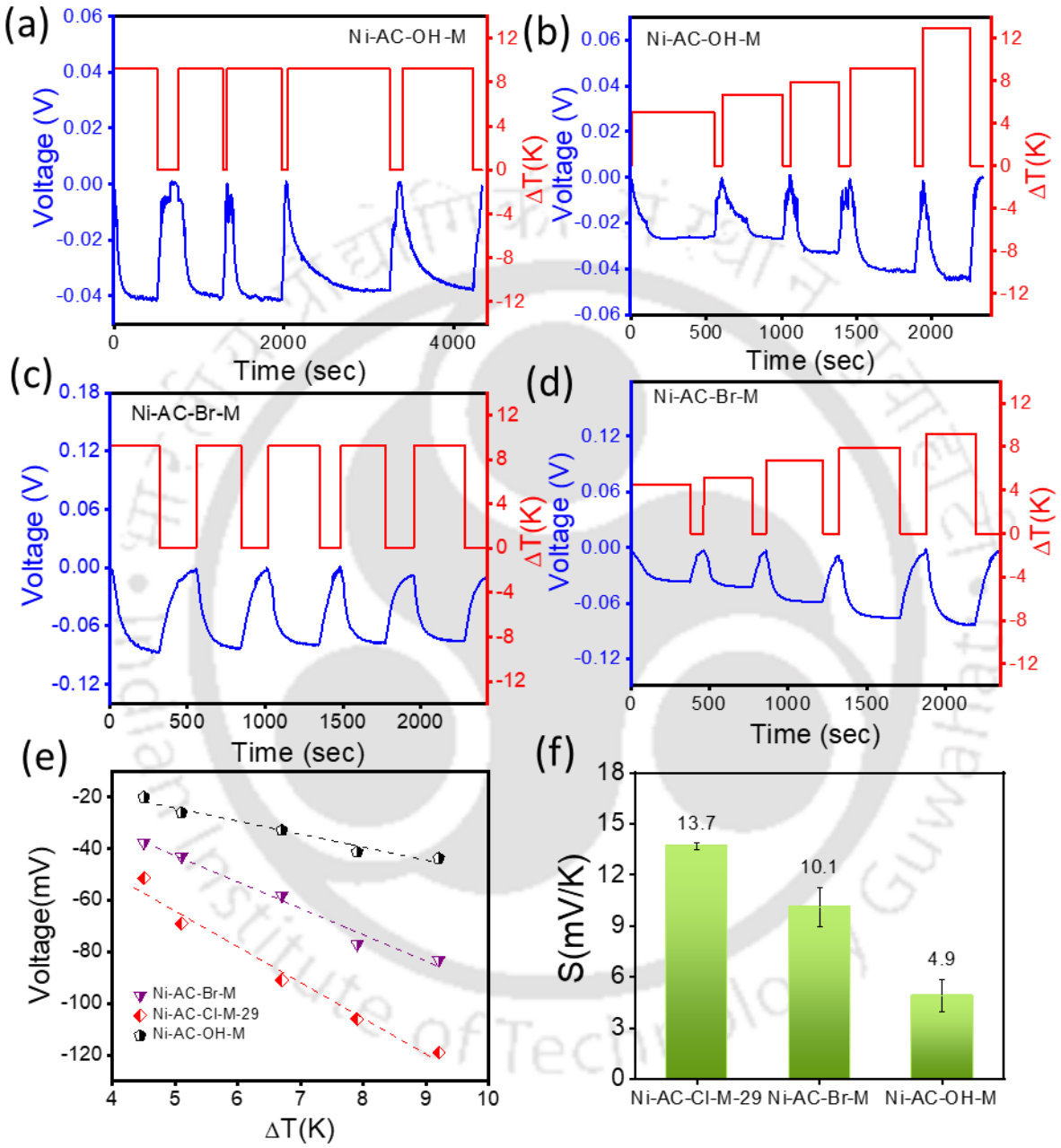

Figure 4.15: Thermovoltage of Ni-AC-OH-M (a) at constant temperature gradient, and (b) at variable temperature gradient. Thermovoltage of Ni-AC-Br-M (c) at constant temperature gradient, and (d) at variable temperature gradient. (e) Linear relationship in between saturated thermovoltage and temperature gradient for Ni-AC-Br-M, Ni-AC-Cl-M-29 and Ni-AC-OH-M. (f) Comparison of the Seebeck coefficients for Ni-AC-Br-M, Ni-AC-Cl-M-29 and Ni-AC-OH-M.

and Mg-aminoclay exhibit hygroscopic properties) (Figure 4.13f), and (c) the presence of 2D channels in Ni-AC-M, facilitating well-directed ion migration (Figure 4.3h).

Since the ionic thermoelectricity is believed to be originated from thermodiffusion of anions, the BTAC salt was substituted with Benzyltriethylammonium bromide (BTAB) and Benzyltrietylammonium hydroxide (BTAH) salts (Ni-AC-Br-M and Ni-AC-OH-M), and the resulting ionic thermoelectric responses were recorded as shown Figure 4.15a, b, c and d. The linear responses of the ionic thermovoltages with respect to that of ΔT are shown in Figure 4.15e. Remarkably, Ni-AC-Cl-M exhibited the highest Seebeck coefficient, followed by those with Br^- and OH^- ions (Figure 4.15f). This reliance of the Seebeck coefficient on the type of anions further supports our hypothesis of anion transport-based ionic thermoelectricity in Ni-M-based systems.

4.6. Long-time measurements:

In order to find out the stability of thermovoltages for a prolonged duration of time, the same were recorded for ~10000 seconds. As illustrated in Figure 4.16a, at ΔT = 8 K, the voltage reached saturation level within ~120 seconds and remained stable for about 10,000 seconds. However, the current values peaked at around 2.08 μA within ~240 seconds and gradually declined over time (Figure 4.16b). The decrease in ionic current can be attributed to the dehydration of the Ni-AC-Cl-M nanochannels and the saturation of ionic channels around the cold side of the electrode, impeding further diffusion of mobile ions.

The I-V characteristics recorded after applying ΔT = 8 K for 500 seconds confirm the separation of ions under the influence of the temperature gradient. As depicted in Figure 4.16c, at ΔT = 0 K, the I-V curve measured with Ni-AC-Cl-M-29 passes through the origin, indicating a homogeneous distribution of ions. However, following the application of ΔT (at 8 K, for 500 seconds), the I-V curve no longer intersects at the origin. Instead, it intersects at I = 2.26 μA

when V = 0 and at V = 125 mV when I = 0, as shown in Figure 4.16d. This characteristic of I-V response suggests the development of an ionic concentration gradient across the hot and cold zones.[41]

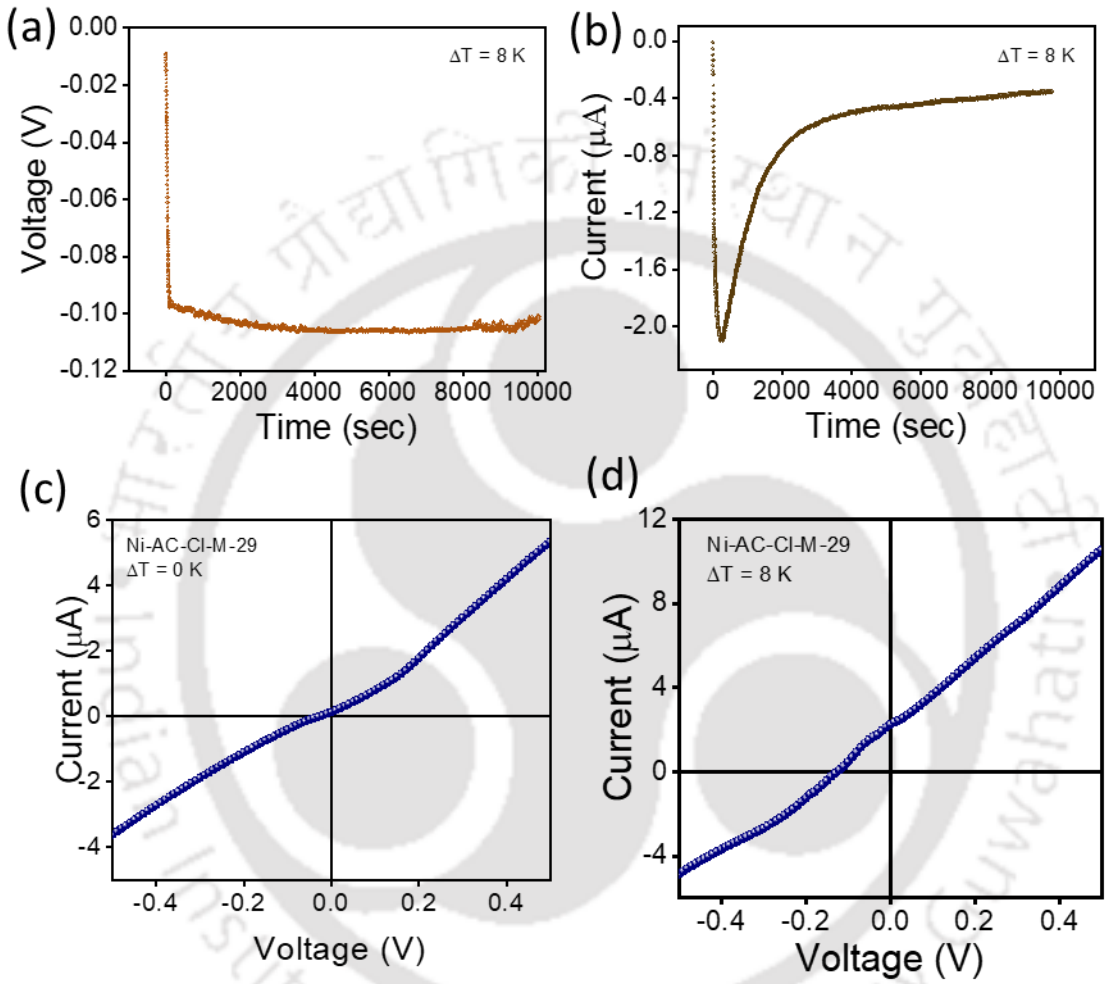

Figure 4.16: Generation of (a) voltage, and (b) current with Ni-AC-Cl-M-29 at a temperature gradient of 8 K for prolonged period of time. I-V curve for Ni-AC-Cl-M-29 (c) without, and (d) with temperature gradient of 8 K

4.7. High temperature stability:

Most of the i-TE materials studied so far are based on polyelectrolytes or ionic liquid based systems that are susceptible to instability at elevated temperatures and some of them may even fail under occasional temperature shocks. Conversely, numerous layered 2D inorganic materials are renowned for their high temperature stability. Leveraging this advantageous

characteristic, the membranes were evaluated for occasional temperature shocks. Ni-AC-Cl-M-29 was subjected to a muffle furnace at 200°C for 5 minutes, and thermovoltages were measured (Figure 4.17c). Remarkably, the heated membrane exhibited an almost identical Seebeck coefficient value (13.5 mV/K) compared to the pristine membrane (Figure 4.17c). The digital photographs depicted in Figure 4.17a further illustrate no visible signs of deterioration following the heat shock, corroborated by spectroscopic evidence presented in Figure 4.17b. Due to their enhanced thermal stability, i-TE materials of this nature hold promise for expanding application possibilities and facilitating advanced scientific studies.

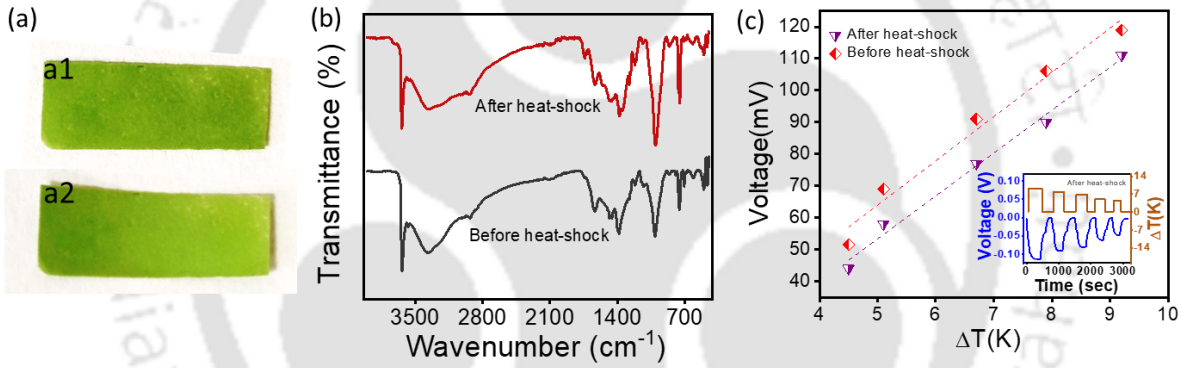

Figure 4.17: (a) Digital photograph of Ni-AC-Cl-M-29 before heat-shock (a1) and after heat shock (a2). (b) FT-IR spectra of Ni-AC-Cl-M-29 before and after heat shock. (c) Linear increment of the thermovoltages with temperature gradient of Ni-AC-Cl-M-29 before and after heat shock, the inset represents graph of thermovoltages at different temperature gradient.

4.8. Alteration of negative thermopower into positive:

So far, Ni-M has emerged as a promising platform for i-TE studies, showcasing the ability to fine-tune Seebeck coefficients by adjusting the nature and concentration of intercalated mobile ion generating species. While the inclusion of anion-generating materials like Mg-aminoclay and BTAC resulted in negative i-TE materials, the introduction of cation-generating materials should yield positive i-TE materials. As a validation of this concept, Ni-M was doped with

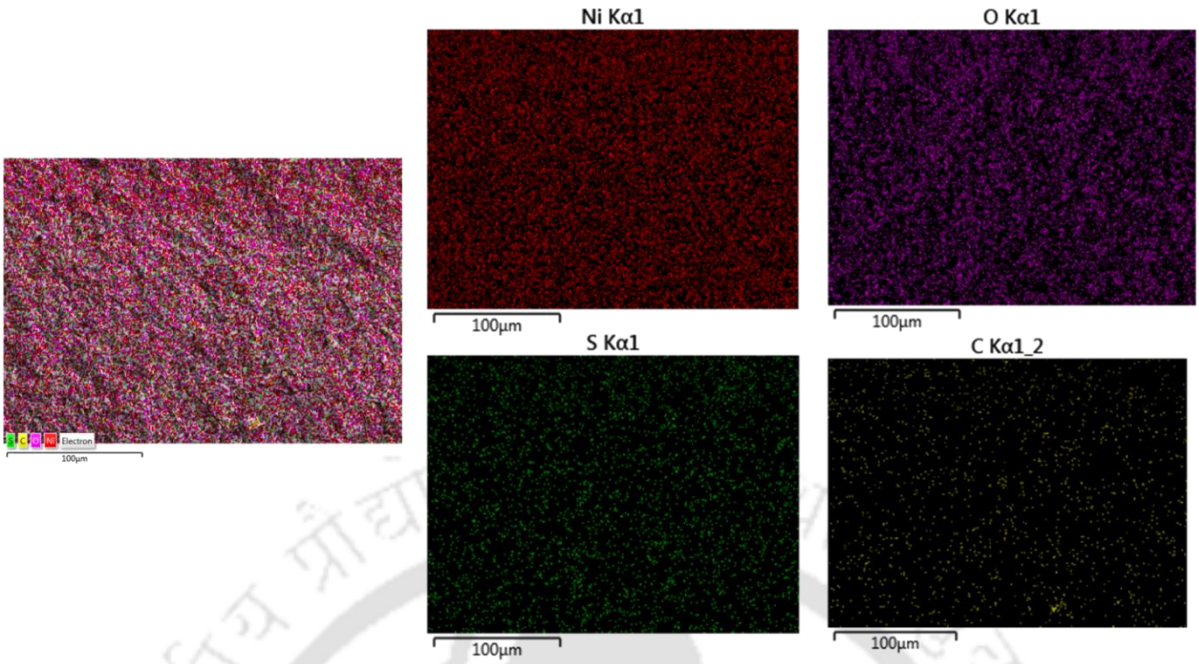

Figure 4.18: EDX mapping of the elements for Ni-PSS-M showing homogenous distribution of PSS molecules.

Poly(4-styrenesulfonic acid) (PSS) (Ni-PSS-M) through a process involving the mixing of aqueous solutions of PSS and β-$Ni(OH)_2$, followed by vacuum filtration of the mixture through a PTFE membrane (Experimental section 4.3). In the realm of ionic thermoelectricity, PSS is recognized as a positive i-TE polymer with notable hygroscopic and dissociative properties. In the presence of water, PSS releases a significant number of H^+ ions, capable of migration under

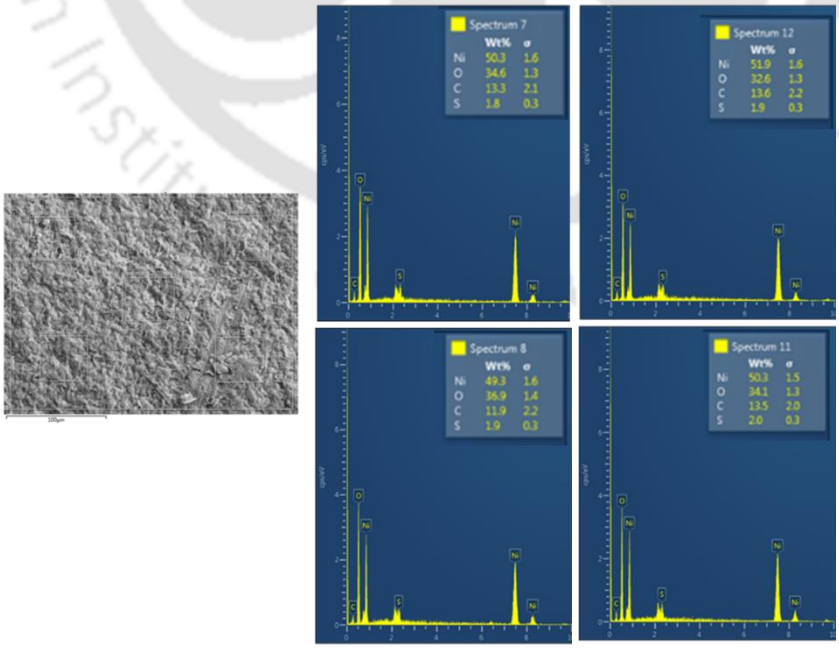

Figure 4.19: EDX analysis for the wt% of the elements present in Ni-PSS-M.

temperature gradients.[42] The uniform distribution of PSS molecules in the prepared Ni-PSS-M is evident from the EDX mapping and analysis presented in Figure 4.18 and 4.19 respectively.

The thermovoltages of Ni-PSS were measured using the experimental setup depicted in Figure 4.2e. As illustrated in the plots in Figure 4.20a and b, the thermovoltages recorded with Ni-PSS-M exhibited an opposite trend compared to Ni-AC-M, Ni-Cl-M, and Ni-AC-Cl-M, manifesting as positive values. A Seebeck coefficient value of +12 ± 1.9 mV/K was derived from the ΔV vs ΔT plot presented in Figure 4.20c. These observations validate our hypothesis regarding the tunability of Ni-M's Seebeck coefficients in both positive and negative directions through the introduction of suitable charge carriers.

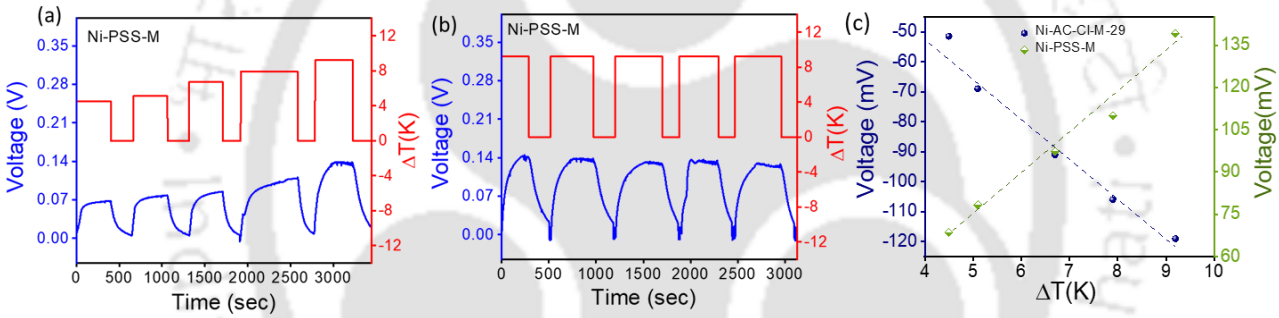

Figure 4.20: Generation of thermovoltage for Ni-PSS-M membrane (a) at variable temperature gradient and (b) at constant temperature gradient. (c) The thermovoltages as a function of ΔT attained from Ni-PSS-M and Ni-AC-Cl-M-29, respectively.

4.9. Applications:

Thermopile:

The transformation of the Seebeck coefficient from negative to positive through the doping of mobile cation generating species into Ni-M has introduced numerous innovative opportunities for developing advanced i-TE devices like thermopiles or temperature sensors. In thermopiles,

the integration of negative and positive i-TE materials in series leads to the generation of enhanced ionic thermovoltages. The schematic representation of an i-TE thermopile based on

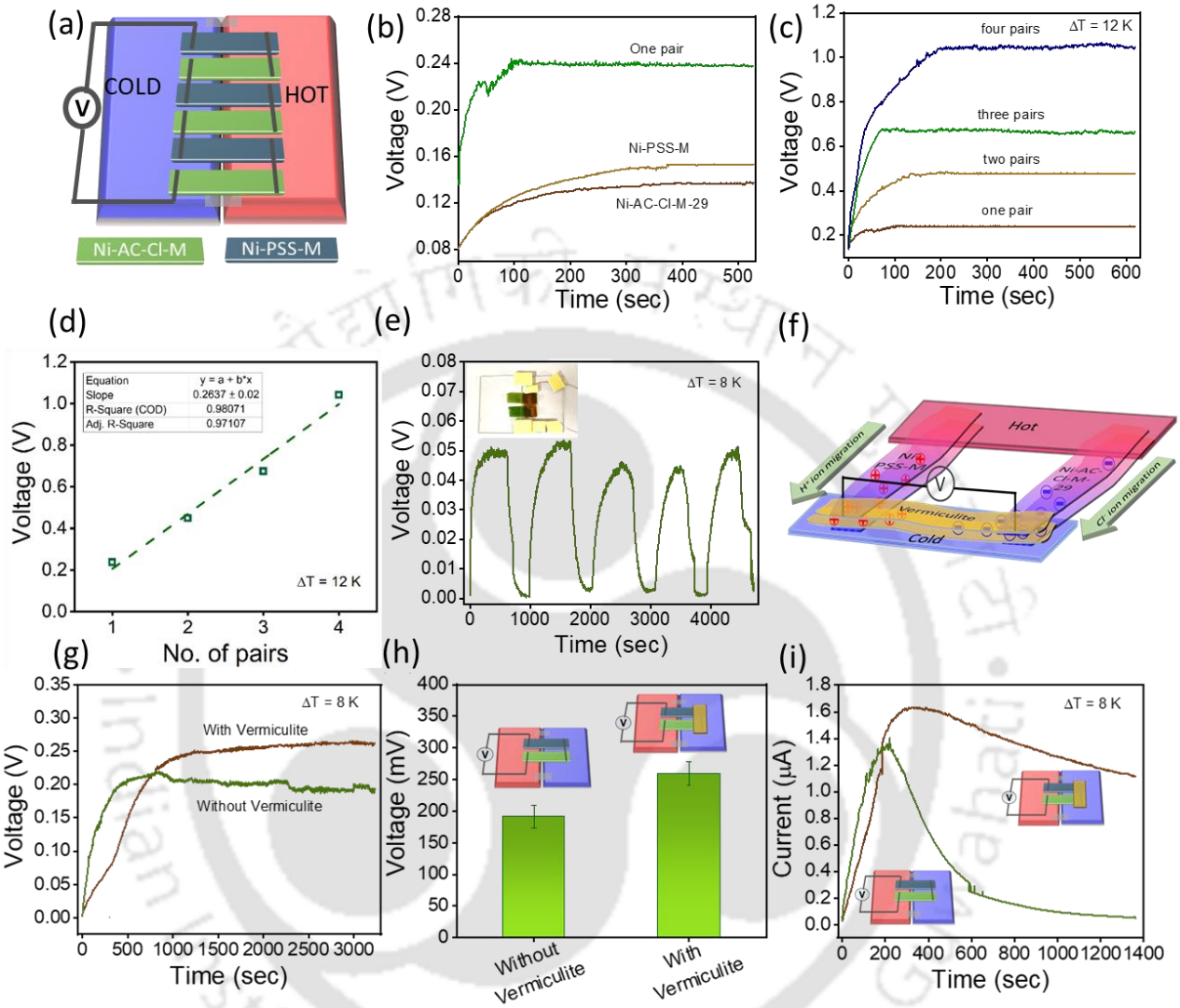

Figure 4.21: (a) Schematic illustration of the thermopile fabricated from Ni-AC-Cl-M-29 and Ni-PSS-M. (b) Comparison of the thermovoltages generated by Ni-AC-Cl-M-29, Ni-PSS-M and one pair of thermopile from these two membranes with a temperature gradient of 12K. (c) Thermovoltage generated with different pairs of thermopile. (d) Increment of thermovoltages with the increase of pairs of Ni-PSS-M and Ni-AC-Cl-M-29 3.9 thermopiles. (e) Thermovoltage generated when cold side of the Ni-AC-Cl-M-29 and Ni-PSS-M were connected through vermiculite membrane. (f) Schematic of a ionic thermoelectric device where Ni-AC-Cl-M-29 and Ni-PSS-M are connected using a vermiculite membrane in the colder side. (g) Thermovoltage generated from one pair of thermopile with and without the presence of vermiculite at $\Delta T = 8$ K. (h) Comparison of the thermovoltage generated from one pair of thermopile with and without the presence of vermiculite at $\Delta T = 8$ K, (the inset represents the schematic of the fabricated device). (i) Thermal current generated from one pair of thermopile with and without the presence of vermiculite at $\Delta T = 8$ K.

Ni-M variants is depicted in Figure 4.21a. As illustrated in Figure 4.21c, when connected in thermopiles, the thermovoltages generated by individual Ni-AC-Cl-M-29 and Ni-PSS-M devices are additive. This additive effect is evident in Figure 4.21b, where the individual thermovoltages of Ni-AC-Cl-M-29 and Ni-PSS-M (ΔT = 12 K) are compared with a series combination of both, resulting in nearly a twofold increase. With an increasing number of pairs of positive-negative i-TE membranes, the thermovoltages exhibited linear growth (Figure 4.21d). A thermovoltage of approximately 1 V was achieved using four pairs of positive-negative i-TE membranes, as shown in Figure 4.21c. It is worth highlighting that initially, the rate of increase of thermovoltages differs among various pairs of Ni-AC-Cl-M-29 and Ni-PSS-M. These variations may have originated from differences in the connections of nanofluidic membranes to the Cu wires via silver paste and inhomogeneity in the composite membranes. The duration needed to reach the saturated thermovoltage is dictated by the slowest device (Figure 4.22) as well as the quantity and quality of interfaces. Nonetheless, a nearly linear rise in voltages was observed with an increase in pairs (with an R^2 value of 0.98), indicating a strong linear correlation between the number of pairs and thermovoltages (as illustrated in Figure 4.21d). Thermopiles constructed from this combination of positive-negative i-TE materials can elevate voltages according to specific needs.

Drawing additional power from thermopiles:

A drawback of i-TE materials lies in their inability to allow charge carriers (ions) to flow into an external circuit upon reaching the electrodes. Consequently, in i-TE devices, ions tend to accumulate near the electrodes in the cold zone, impeding the continuous generation of electrical current when operated at a constant temperature difference. However, this drawback can be turned into an advantage by harnessing the accumulated charges to draw additional power. This is achieved by connecting the colder zones of positive and negative i-TE materials through an ion-conducting nanofluidic membrane, as illustrated in Figure 4.21f. To validate

this concept, one end of Ni-AC-Cl-M-29 was linked to the other end of Ni-PSS-M via a reconstructed vermiculite membrane (fabrication details discussed in section 4.3). As previously reported[43,44] freestanding membranes of water-soluble 2D nanosheets can be seamlessly connected through a water-assisted interfacial reorganization process.

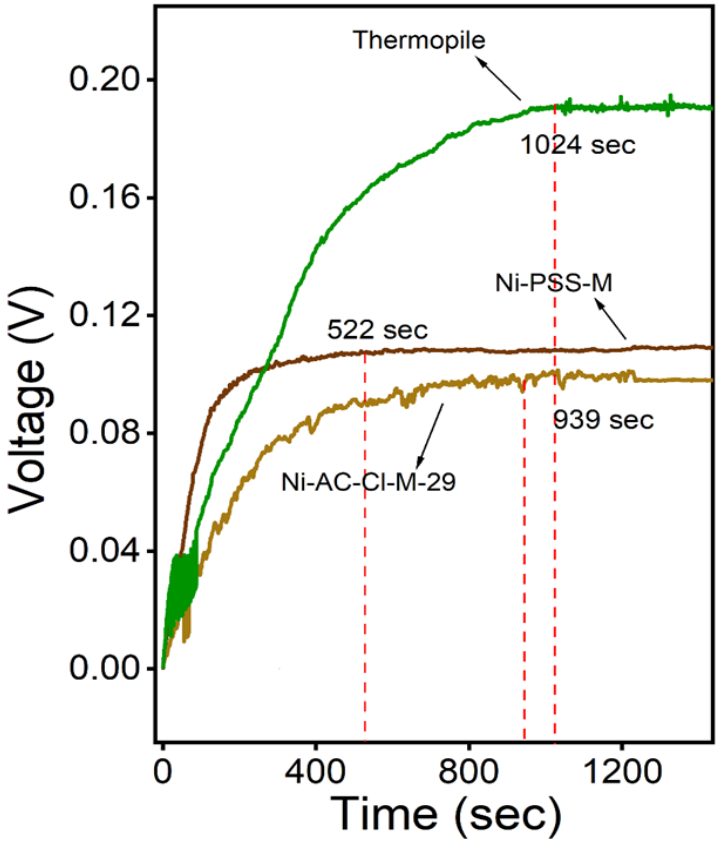

Figure 4.22: Different saturation time to attain the saturation voltage for Ni-AC-Cl-M-29, Ni-PSS-M and the thermopile composed of these two membranes.

Upon applying a ΔT, a potential difference between the cold zones of Ni-AC-Cl-M-29 and Ni-PSS-M emerged that diminishes once the temperature gradient was removed, as depicted in Figure 4.21e. This process can be repeated multiple times. The additional voltage generation process is ascribed to the accumulation of ions with opposite polarity towards the cold zones of negative and positive i-TE materials. Figure 4.21g and h further illustrated how the application of a reconstructed vermiculite membrane-based nanofluidic bridge enhanced the

overall device performance by ~50 mV at ΔT = 8 K. Notably, with the presence of nanofluidic bridge the rate of decrease in output current values under continuous operation significantly reduced, as shown in Figure 4.21i. A 23% reduction in current value after 1000 seconds of saturation (with the nanofluidic bridge) was observed compared to 92% (after 1000 seconds of saturation) without the application of the nanofluidic bridge (Figure 4.21i).

4.10. Conclusions:

In summary, our study highlights the potential of lamellar membranes fabricated from 2D nanomaterials as a promising platform for investigating i-TE properties. By strategically modifying atomically thin and well-ordered 2D nanochannels, a diverse range of i-TE materials with significant practical utility can be developed. Demonstrating this concept, we tuned the Seebeck coefficients of lamellar $Ni(OH)_2$ membranes from -13.7±0.2 mV/K to +12±1.9 mV/K by introducing appropriate dopant molecules such as Mg-aminoclay, organic halides, and poly(4-styrenesulfonic acid). Materials with such adjustable Seebeck coefficients hold immense promise for future applications, as the integration of dissimilar materials to fabricate complex devices is often challenging and their interfaces may not be compatible with varying environmental conditions. Further enhancements in the thermovoltage of lamellar nanofluidic membranes can be achieved by fine-tuning the channel dimensions, surface functionalization, ionic concentrations and through the incorporation of an another ion-conducting nanofluidic membrane. The high temperature stability is an another added advantage related to this classes of inorganic 2D lamellar membranes. Finally, the exploration of Ni-M-based i-TE materials opens up the way for investigating numerous other 2D materials with other interesting characteristics for i-TE-related studies.

4.11. References:

1 B. Chen, Q. Chen, S. Xiao, J. Feng, X. Zhang and T. Wang, *Sci. Adv.*, 2024, **7**,

eabi7233.

2 S. L. Kim, J.-H. Hsu and C. Yu, *Org. Electron.*, 2018, **54**, 231–236.

3 C. Cho, B. Kim, S. Park and E. Kim, *Energy Environ. Sci.*, 2022, **15**, 2049–2060.

4 M. Bharti, A. Singh, A. K. Debnath, A. K. Chauhan, K. P. Muthe, S. K. Gupta, K. Marumoto, T. Mori and D. K. Aswal, *Mater. Today Phys.*, 2021, **16**, 100307.

5 S. Park, B. Kim, C. Cho and E. Kim, *J. Mater. Chem. A*, 2022, **10**, 13958–13968.

6 S. X. Li, W. Guan, B. Weiner and M. A. Reed, *Nano Lett.*, 2015, **15**, 5046–5051.

7 B. Kim, J. U. Hwang and E. Kim, *Energy Environ. Sci.*, 2020, **13**, 859–867.

8 Z. Liu, H. Cheng, H. He, J. Li and J. Ouyang, *Adv. Funct. Mater.*, 2022, **32**, 2109772.

9 B.-R. Kim, G. Jeong, A. Kim, Y. Kim, M. G. Kim, H. Kim and Y.-J. Kim, *Adv. Energy Mater.*, 2016, **6**, 1600862.

10 H. Wang, D. Zhao, Z. U. Khan, S. Puzinas, M. P. Jonsson, M. Berggren and X. Crispin, *Adv. Electron. Mater.*, , DOI:10.1002/aelm.201700013.

11 B. Kim, J. Na, H. Lim, Y. Kim, J. Kim and E. Kim, *Adv. Funct. Mater.*, 2019, **29**, 1–8.

12 Z. A. Akbar, J. W. Jeon and S. Y. Jang, *Energy Environ. Sci.*, 2020, **13**, 2915–2923.

13 D. Zhao, A. Martinelli, A. Willfahrt, T. Fischer, D. Bernin, Z. U. Khan, M. Shahi, J. Brill, M. P. Jonsson, S. Fabiano and X. Crispin, *Nat. Commun.*, 2019, **10**, 1093.

14 S. Liu, Y. Yang, H. Huang, J. Zheng, G. Liu, T. H. To and B. Huang, *Sci. Adv.*, 2024, **8**, eabj3019.

15 S. Liu, Y. Yang, S. Chen, J. Zheng, D. G. Lee, D. Li, J. Yang and B. Huang, *Nano Energy*, 2022, **100**, 107542.

16 C. Chi, M. An, X. Qi, Y. Li, R. Zhang, G. Liu, C. Lin, H. Huang, H. Dang, B. Demir, Y. Wang, W. Ma, B. Huang and X. Zhang, *Nat. Commun.*, 2022, **13**, 221.

17 X. Wu, N. Gao, X. Zheng, X. Tao, Y. He, Z. Liu and Y. Wang, *ACS Appl. Mater. Interfaces*, 2020, **12**, 27691–27699.

18 D. Chen, Y. Xu, Y. Zhang, W. Sheng and G. Qian, *RSC Adv.*, 2021, **11**, 20479–20485.

19 S. Sun, Y. Feng, L. Pan, X. Zhang and J.-J. Zou, *Appl. Catal. B Environ.*, 2019, **259**, 118028.

20 J. Wang, Z. Wang and Z. Zhu, *Appl. Catal. B Environ.*, 2017, **204**, 577–583.

21 L. Mao, Q. Ba, X. Jia, S. Liu, H. Liu, J. Zhang, X. Li and W. Chen, *RSC Adv.*, 2019, **9**, 1260–1269.

22 W. Yang, X. Yang, B. Li, J. Lin, H. Gao, C. Hou and X. Luo, *J. Mater. Chem. A*, 2019, **7**, 26364–26370.

23 X. Zhu, X. Dou, J. Dai, X. An, Y. Guo, L. Zhang, S. Tao, J. Zhao, W. Chu, X. C. Zeng, C. Wu and Y. Xie, *Angew. Chemie Int. Ed.*, 2016, **55**, 12465–12469.

24 X. Chen, X. Zhong, B. Yuan, S. Li, Y. Gu, Q. Zhang, G. Zhuang, X. Li, S. Deng and J. Wang, *Green Chem.*, 2019, **21**, 578–588.

25 H. Li, S. Liu, C. Huang, Z. Zhou, Y. Li and D. Fang, *Electrochim. Acta*, 2011, **58**, 89–94.

26 J. Kang, F. Li, Z. Xu, X. Chen, M. Sun, Y. Li, X. Yang and L. Guo, *JACS Au*, 2023, **3**, 2660–2676.

27 H. B. Li, M. H. Yu, F. X. Wang, P. Liu, Y. Liang, J. Xiao, C. X. Wang, Y. X. Tong and G. W. Yang, *Nat. Commun.*, 2013, **4**, 1894.

28 X. Yi, H. Sun, N. Robertson and C. Kirk, *Sustain. Energy Fuels*, 2021, **5**, 5236–5246.

29 J. Yu, B. Wang, Q. Lu, L. Xiao, X. Ma, Y. Feng and Y. Qian, *Chem. Eng. J.*, 2023, **453**, 139769.

30 J. Yu, B. Wang, Q. Lu, L. Xiao, X. Ma, Y. Feng and Y. Qian, *Chem. Eng. J.*, 2023, **453**, 139769.

31 S. Guo, C. Zhang, M. Yang, Y. Zhou, C. Bi, Q. Lv and N. Ma, *Anal. Chim. Acta*, 2020, **1109**, 130–139.

32 B. Long, Y. Zhao, P. Cao, W. Wei, Y. Mo, J. Liu, C.-J. Sun, X. Guo, C. Shan and M.-H. Zeng, *Anal. Chem.*, 2022, **94**, 1919–1924.

33 Y. Zhang, D. Zheng, S. Liu, S. Qin, X. Sun, Z. Wang, C. Qin, Y. Li and J. Zhou, *Appl. Surf. Sci.*, 2021, **552**, 149529.

34 M. Wang, W. Ren, Y. Zhao, Y. Liu and H. Cui, *J. Nanoparticle Res.*, 2013, **15**, 1849.

35 S. Jiang, Z. Gui, G. Chen, D. Liang and J. Alam, *ACS Appl. Mater. Interfaces*, 2015, **7**, 14603–14613.

36 L. Fu, K. Kumara, R. Datta, K. Spyrou, G. Qi, A. Sardar, M. M. Khader, R. Zboril and E. P. Giannelis, *Appl. Mater. Today*, 2017, **9**, 451–455.

37 K. K. R. Datta, A. Achari and M. Eswaramoorthy, *J. Mater. Chem. A*, 2013, **1**, 6707–6718.

38 Y. Hwang, Y.-C. Lee, P. D. Mines, Y. S. Huh and H. R. Andersen, *Appl. Catal. B Environ.*, 2014, **147**, 748–755.

39 Q. Chen, B. Cheng, Z. Wang, X. Sun, Y. Liu, H. Sun, J. Li, L. Chen, X. Zhu, L. Huang, Y. Ni, M. An and J. Li, *J. Mater. Chem. A*, 2023, **11**, 2145–2154.

40 Y. Hu, M. Chen, C. Qin, J. Zhang and A. Lu, *Carbohydr. Polym.*, 2022, **292**, 119650.

41 X. L. Deng, T. Takami, J. W. Son, E. J. Kang, T. Kawai and B. H. Park, *Sci. Rep.*, 2014, **4**, 4005.

42 M. Jeong, J. Noh, M. Z. Islam, K. Kim, A. Sohn, W. Kim and C. Yu, *Adv. Funct. Mater.*, 2021, **31**, 1–7.

43 R. K. Gogoi and K. Raidongia, *J. Mater. Chem. A*, 2018, **6**, 21990–21998.

44 R. K. Gogoi, A. B. Neog, T. J. Konch, N. Sarmah and K. Raidongia, *J. Mater. Chem. A*, 2019, **7**, 10552–10560.

Chapter 5

Boosting of Moisture-Electricity Conversion by Robust Oxide-Hydroxide Nanofluidic Membranes with Light and Waste Heat

Summary

The conversion of moisture into electricity presents a promising avenue for renewable energy. In this chapter, we describe the development of a durable bilayer-moisture electric generator (BMEG), achieved through the fusion of oppositely charged nanofluidic membranes facilitated by water. The BMEG, crafted through the vacuum-assisted assembly of surface-functionalized two-dimensional (2D) vanadium pentoxide and β-nickel hydroxide sheets, efficiently converts moisture into electrical power. Unlike conventional moisture electric generators (MEGs) that produce short electric pulses, our BMEG delivers continuous power output for extended periods (a few months). Notably, its functionality remains intact even under extreme temperatures ranging from -195 to +200 °C, and after prolonged use exceeding three months. Furthermore, by refreshing and rehydrating connections, we successfully revived ~100% and 93% of the overused (80 days) BMEG's output current and voltage, respectively. Combining thermal diffusion (Soret effect) and photo-thermal heating, we amplified the BMEG's output voltage by up to 34% through the application of a temperature gradient (ΔT = 15 ºC), and approximately 23% by exposure to white light (7000 lux). With a straightforward assembly process, multiple BMEGs were interconnected to achieve an output voltage and current of up to 40 V and 45 µA, respectively. Additionally, we harnessed the BMEG's moisture sensitivity to develop self-powered moisture sensors

5.1. Introduction:

Moisture in the environment has emerged as a promising renewable energy source, with moisture electric generators (MEGs) at the forefront of this exploration.[1] These devices offer remarkable advantages, operating autonomously without additional fuel or water, eliminating the necessity for part replacements, and remaining unaffected by weather conditions. They operate seamlessly without moving components or human intervention.[2–5] According to estimates, the Earth's atmosphere contains several trillion gallons of water, with a significant amount of energy required to recycle this immense volume of atmospheric water approximately 40 times annually.[6] Harnessing even a fraction of this abundant energy could substantially contribute to sustainability efforts.

A majority of the research related to this field is primarily based on materials that have a gradient or asymmetric structure that demands continuous exposure to external pulses of moisture. For instance, a lot of focus was devoted to developing MEGs based on graphene oxide (GO) based materials that can have higher output.[7] However, the gradient based materials encounter challenges with maintaining continuous power output for extended periods. A bilayer moist electric generator (BMEG) can be a solution to this problem, which consists of two layers with contrasting surface charge properties. However, studies related to this class of materials are very limited.

Due to the several unique features such as high channel density, remarkable ionic conductivity, robustness, and simplicity in fabrication and scalability, nanofluidic membranes constructed through the assembly of inorganic 2D nanomaterials offer a multitude of potential applications. These applications span various fields including water treatment, energy harvesting, energy storage, and ionic thermoelectricity.[8–15] Therefore, these classes of materials can offer a promising platform to fabricated such BMEGs that can be tuned according to the necessities.

Indeed, by integrating other energy harvesting techniques such as ionic thermoelectricity with MEGs, the power output of these systems based on 2D materials can be further boosted.

5.2. Scope of the present investigation:

Considering the abundance of atmospheric water molecules in the form of moisture, moisture electric generators (MEGs) can have a promising future in the realm of energy harvesting. However, the majority of the materials studied so far have gradient-based structures, where inhomogeneity of the functional groups inside the gradient material develops a concentration gradient of ions, thereby generating an output voltage and current.[7,16–19] These classes of materials mostly develop transient responses of voltages that require continuous external pulses of moisture, thereby hindering the practical utility. Two layers with contrasting surface charge properties can also be fused together to form a bilayer known as a bilayer moist electric generator (BMEG) that can develop a continuous voltage for a prolonged duration. However, only a handful of works are related to this class of material.[3,20] This work initiates the utilisation of lamellar nanofluidic membranes to fabricate a BMEG that is primarily based on oxide and hydroxide materials. These classes of material offer enormous possibilities for surface tuning and intercalation of various ion-generating species. Unlike the majority of MEGs, the fabricated BMEG can develop continuous power output for a prolonged period of time without any external support of moisture. This work further demonstrates the hybridization of BMEG with the Soret effect highlighting the possibility of improving and tuning the BMEG output as per the necessity. The BMEG devices additionally sustain the extreme temperature variations without losing their intrinsic MEG properties, describing their potential application across a wide range of areas. The performance of these oxide- and hydroxide-based systems can be additionally revived by up to >90% after a prolonged continuous duration by simply renewing and rehydrating the connections. Considering several advantages such as thermal and chemical stability, robustness, surface tunability, possibility of hybridization with the Soret effect and

ability to recover from performance degradation over time, these classes of material hold great promise for advancing moisture-based energy harvesting technologies in future.

Material structure and properties:

The bulk form of vanadium pentoxide, V_2O_5, adopts an orthorhombic crystal structure, specifically belonging to the Pmmn space group.[27,28] This crystal structure is characterized by lattice parameters: a = 11.51 Å, b = 4.37 Å, and c = 3.56 Å. The physical layers within this structure are oriented along the (010) direction and consist of distorted VO_5 pyramids. These pyramids share edges and corners. Each elementary cell of this crystal structure contains two units of the chemical formula V_2O_5, totalling 14 atoms. Additionally, there are six planar layers of atoms, including four oxygen layers and two vanadium layers. The bulk structure of V_2O_5 can be exfoliated into individual layers and reconstructed to obtain interesting properties. V_2O_5 finds its utility in several fields, such as electrochemical energy storage, catalysis, gas sensors, electrochromic devices, biomedical applications and several applications related to energy generation.

Poly(4-styrenesulfonic) acid (PSS) is a polymer consisting of sulfonic groups (-SO_3H) that are typically attached to the benzene ring of the polystyrene backbone. Due to the presence of sulfonic groups, PSS shows ion conducting nature along with higher hygroscopicity. Due to its ion-conducting nature, it has been utilized in ion exchange resins, membrane separation processes, fuel cells and different energy harvesting techniques.

Nickel(II) hydroxide exists in two recognized polymorphic forms, denoted as α and β.[29] The α structure comprises layers of $Ni(OH)_2$ with intercalated anions or water molecules. On the other hand, the β form adopts a hexagonal close-packed arrangement of Ni^{2+} and OH^- ions. In the presence of water, the α polymorph tends to undergo recrystallization into the β form.[30] Besides the α and β polymorphs, various γ nickel hydroxides have been identified, characterized by

crystal structures featuring significantly larger inter-sheet distances. Nickel hydroxide was utilized in different fields such as in rechargeable nickel-metal hydride batteries as an active material in the positive electrode, catalysis, supercapacitors, water treatment processes, sensors etc.

Mg-aminoclay is a synthetic clay with the approximate composition $R_8Si_8Mg_6O_{16}(OH)_4$, where $R = CH_2CH_2NH_2$.[31] The structure of Mg-aminoclay typically consists of layers of magnesium ions (Mg^{2+}) sandwiched between layers of negatively charged silicate $(SiO_4)^{4-}$ tetrahedra. These layers are held together by electrostatic forces, with the positively charged magnesium ions balancing the negative charge of the silicate layers. Mg-aminoclay, owing to its unique properties, finds numerous applications across various fields. For instance, it can be utilized as an adsorbent, in catalysis, drug delivery processes, flame retardants, soil amendments etc.

Benzyltriethylammonium chloride (BTAC) is an organic quaternary ammonium salt containing a benzyl group in it. This quaternary ammonium salt finds its utility in several applications such as phase transfer catalyst, ion exchange resin, biocides and disinfectants, electroplating additive etc.

5.3. Experimental sections:

Materials: Nickel (II) acetate tetrahydrate ($Ni(CH_3CO_2H)_2.4H_2O$), Vanadium pentoxide (V_2O_5) and Magnesium chloride ($MgCl_2$) were purchased from SRL Pvt. Ltd., Liquor Ammonia solution and Poly (4-styrenesuphonic acid) (PSS) were purchased from Sigma-Aldrich, Hydrogen Peroxide was purchased from Finar Ltd., 3-aminopropyltriethoxysilane was purchased from Alfa-Aesar Pvt. Ltd. Ethanol was purchased from Changshu Hongheng Fine Co. Ltd. Benzyltrietylammoium chloride was purchased Avra Synthesis Ptv. Ltd. The copper electrodes were purchased from the local market. Silver paste was purchased from Alfa-Aesar Pvt. Ltd.

Preparation of $Ni(OH)_2$ nanosheets: To prepare a dispersion of Nickel (II) hydroxide ($Ni(OH)_2$), a solution was prepared by dissolving 0.35 gm of Nickel (II) acetate tetrahydrate ($Ni(CH_3CO_2H)_2.4H_2O$) in 30 ml of deionized (DI) water. Subsequently, 670 µl of 25% aqueous ammonia were added drop by drop to the solution while being stirred continuously. The stirring process was maintained for 24 hours, leading to the formation of a green precipitate. The precipitate underwent multiple washes with DI water. Finally, the $Ni(OH)_2$ precipitate was transferred into DI water to achieve the desired dispersion concentration of 10 mg/ml.

Preparation of V_2O_5 nanosheets: To prepare an aqueous dispersion of V_2O_5 nanosheets, bulk crystals of V_2O_5 with hydrogen peroxide (H_2O_2) in an ice bath maintained between 0 to 5 °C. Initially, 2.38 grams of V_2O_5 was combined with 25 ml of deionized water. Subsequently, 25 milliliters of 50% H_2O_2 was gradually added to the V_2O_5 dispersion, resulting in vigorous bubbling and the formation of a brown precipitate, which gradually transitioned into a gel-like substance. The resultant gel was then diluted with 150 ml of DI water and subjected to sonication for 30 minutes, ultimately yielding a V_2O_5 dispersion with a concentration of 15 mg/ml.

Preparation of $Ni(OH)_2$ membrane: A freestanding membrane of $Ni(OH)_2$ was fabricated by vacuum filtration of a prepared $Ni(OH)_2$ dispersion. The dispersion, with a concentration of 10 mg/ml, and a total volume of 15 ml underwent vacuum filtration through a PTFE membrane with a pore diameter of 0.1 µm. After filtration process, the membrane was dried under ambient atmospheric conditions, resulting in the formation of a freestanding $Ni(OH)_2$ membrane.

Preparation of V_2O_5 Membrane: To prepare V_2O_5 membrane a vacuum filtration process was employed to filter a 10 mL dispersion containing V_2O_5 nanosheets with a concentration of 15 mg/ml, using a PTFE membrane with a pore size of 100 nm. After filtration process, the

membrane was dried under ambient conditions, leading to the formation of a freestanding V_2O_5 membrane.

Preparation of V_2O_5 – PSS composite membrane (VO-PSS): Composite thin film membranes were effectively produced by mixing 10 mL of the V_2O_5 dispersion (15 mg/mL) with a suitable amount of PSS polymer. Various weight percentages of PSS (5, 10, 18, 31 wt%) were incorporated into the mixture. Afterward, the solution was sonicated for 20 minutes to achieve homogeneous dispersion. Following this, the solution was subjected to vacuum filtration using a PTFE membrane with a pore size of 100 nm. Finally, the membranes were dried to yield the composite freestanding membranes.

Preparation of Mg-Aminoclay: To prepare Mg-Aminoclay, a solution was prepared by dissolving 1.68 grams of Magnesium chloride ($MgCl_2$) in 40 grams of ethanol. Subsequently, 2.6 ml of 3-aminopropyltriethoxysilane was added dropwise to the solution with vigorous stirring. Stirring was continued for 24 hours to ensure complete reaction and product formation. The resulting white product was separated from the solution via centrifugation and then washed multiple times with ethanol to eliminate any impurities. Finally, the Mg-Aminoclay was dried at 40°C.

Preparation of $Ni(OH)_2$ and Mg-aminoclay composite membrane: Free-standing composite membranes comprising $Ni(OH)_2$ and Mg-aminoclay were prepared through a vacuum filtration process. Initially, 200 mg of Mg-aminoclay were mixed with 15 ml of a 10 mg/ml $Ni(OH)_2$ dispersion. The mixture was then sonicated for 20 minutes to ensure a homogeneous composite dispersion. Subsequently, the composite dispersion was subjected to vacuum filtration using a PTFE support with a pore diameter of 100 nm. The filtration process effectively separated the composite materials and formed freestanding composite membrane. Finally, the membrane was dried under ambient atmospheric conditions.

Preparation of composite membranes from $Ni(OH)_2$, Mg-aminoclay and Benzyltriethylammonium chloride salt (Ni-AC-Cl): The composite membranes consisting of $Ni(OH)_2$, Mg-aminoclay, and Benzyltriethylammonium chloride (BTAC) salt were prepared by keeping the amount of $Ni(OH)_2$ fixed at 150 mg (10 mg/mL) while varying the weight ratio of Mg-aminoclay and BTAC. The different weight ratios used were as follows:

Composition	Ratio	Actual weight
Mg-aminoclay:BTAC	1:4	50 mg of Mg-aminoclay and 200 mg of BTAC
Mg-aminoclay:BTAC	1:2	100 mg of Mg-aminoclay and 200 mg of BTAC
Mg-aminoclay:BTAC	1:1	200 mg of Mg-aminoclay and 200 mg of BTAC
Mg-aminoclay:BTAC	2:1	200 mg of Mg-aminoclay and 100 mg of BTAC
Mg-aminoclay:BTAC	4:1	200 mg of Mg-aminoclay and 50 mg of BTAC

These compositions of $Ni(OH)_2$, aminoclay, and BTAC salts were mixed and sonicated for 30 minutes to ensure a homogeneous mixture. Subsequently, the prepared mixture was vacuum-filtered through a PTFE membrane with a pore diameter of 100 nm. After filtration, the remaining part was dried in an ambient atmosphere and peeled off from the support to obtain the freestanding membrane.

Preparation of Al doped Zinc Oxide (AZO): AZO was prepared by following a previously reported procedure.[1] Initially, a solution of zinc acetate dihydrate was prepared by dissolving 11 grams of it in 80 mL of methanol at room temperature. Another solution was prepared by dissolving 0.0667 grams of aluminium chloride in 20 mL of methanol. These solutions were then combined to yield a clear, transparent solution. A 3 M NaOH solution was added dropwise in to the solution in order to obtain the white precipitate by adjusting the pH level at 11-12. The as prepared solution was kept in stirring for 24 hours. After that the solution was

hydrothermally treated at 200 °C for 12 hours followed by washing repeatedly for several times.

Preparation of $NiCo_2O_4$ coated carbon paper (Ni/C): The $NiCo_2O_4$ coated carbon paper were prepared from the precursors of $NiCl_2.6H_2O$, $CoCl_2.6H_2O$ and $CO(NH_2)_2$. Typically, 0.167 g of $NiCl_2.6H_2O$, 0.332 g of $CoCl_2.6H_2O$ and 0.168 g of $CO(NH_2)_2$ were dissolved in deionized water. The as prepared solution was transferred to a Teflon-lined autoclave along with the rectangular pieces of carbon papers. The hydrothermal process was continued for 12 hours at 150 °C. After completion of the hydrothermal process, the carbon papers coated with the intermediate products were then calcined at 400 °C for 2 hours to obtain the $NiCo_2O_4$ coated carbon paper.

Fabrication of Bilayer moist electric generator: The bilayer moisture-electric generator was assembled by pairing two rectangular pieces of VO-PSS (1.5 cm x 0.5 cm) and Ni-AC-Cl (1.2 cm x 0.5 cm) with a small amount of water (~20 µL). Typically, ~20 µL of deionized water was applied onto the surface of the VO-PSS, followed by placing the Ni-AC-Cl piece on top before the membranes dried. Once the fusion process was complete, the assembled device was allowed to dry, facilitating the adhesion of the two membranes. For electrical measurements, two copper electrodes were affixed to the device using conductive silver paste, with one electrode positioned on the top of the VO-PSS and the other on the top of the Ni-AC-Cl.

Fabrication of experimental setup for temperature gradient based experiments:

To set up the experiment, the constructed BMEG was positioned onto a stage formed by two glass slides, each measuring 2 cm x 2 cm. These slides were securely attached together using adhesive tape, creating an air gap of approximately 2 mm between them to prevent undesired heat transfer. The device was then connected to two copper electrodes using conductive silver paste.

Subsequently, the prepared thermoelectric device was placed above another stage containing two Peltier devices, with one serving as the heat source and the other as the heat sink. The temperature difference applied across the membrane was monitored using two K-type thermocouples connected to a Testo 735 temperature measuring instrument, which were positioned on the glass slides adjacent to the samples.

To maintain the desired temperature gradient, a DC regulated power supply (METARAVI TM – RPS 30005) was utilized to power the Peltier devices. The voltages generated were measured using a 2450 Keithley Sourcemeter, enabling precise assessment of the thermoelectric performance of the membranes.

5.4. Characterizations:

Various techniques were employed to comprehensively characterize the materials used in the study. Morphological analysis was conducted using a field emission scanning electron microscope (FESEM) (Zeiss, model: Sigma) to examine surface structures, while compositional analysis was performed through Energy-dispersive X-ray analysis using the same FESEM instrument (Zeiss, model: Sigma). X-ray diffraction (XRD) patterns were obtained with an X-ray diffractometer (Rigaku, model: Micromax-007HF). Infrared spectroscopic analysis was carried out using a Perkin Elmer (Spectrum Two) instrument to study molecular compositions, and atomic force microscopy (AFM) (Oxford, model: Cypher) was utilized to measure the height of individual nanosheets. Zeta potentials of different dispersions were determined using a Zetasizer instrument (Malvern, Nano-ZS90) to assess surface charge, while Field Emission Transmission Electron Microscope (FETEM) (JEOL, Model: 2100F) was employed to further characterize the nanosheets. Thermal images were captured using a Testo 872 Thermal camera to analyse heat distribution.

5.5. Result and discussion:

The bilayer moist electric generator (BMEG) investigated in this study were constructed by integrating membranes containing different intercalants and ionic charge carriers (VO-PSS and Ni-AC-Cl). To achieve this, a freestanding membrane capable of generating anions, named Ni-AC-Cl, was prepared by intercalating Mg-aminoclay and Benzyltriethylammonium chloride (BTAC) into the lamellar stacking of 2D β-$Ni(OH)_2$ flakes. The β-$Ni(OH)_2$ flakes were synthesized by precipitating Ni^{2+} ions from an aqueous solution of nickel acetate tetrahydrate through the addition of ammonia solution.[21] The Mg-aminoclay was obtained by reacting (3-aminopropyl) triethoxysilane with $MgCl_2$ in ethanol, while the BTAC salt was used as purchased.[22,23] The formation of individual nanosheets of both β-$Ni(OH)_2$ and Mg-aminoclay were confirmed from FETEM images shown in Figure 5.1a and b respectively. On the other hand, the cation-generating membrane, VO-PSS, was fabricated by reconstructing exfoliated 2D V_2O_5 flakes with Poly(4-styrenesulfonic acid) (PSS). The 2D V_2O_5 flakes were obtained by treating them with hydrogen peroxide.[24] The formation of individual nanosheets were confirmed from the AFM image shown in Figure 5.1c. Detail synthesis methods are elaborately discussed in the experimental section 5.3. The pXRD patterns of pristine β-$Ni(OH)_2$, V_2O_5 and their composite membranes were shown in Figure 5.1d and e.

Comparison of the FT-IR spectra of V_2O_5 with the composite of V_2O_5 and PSS (Figure 5.2a and b) suggest no chemical interactions among the V_2O_5 and PSS molecules as the IR peaks remains intake after incorporation of PSS molecules inside the layers of V_2O_5. The Figure 5.2c

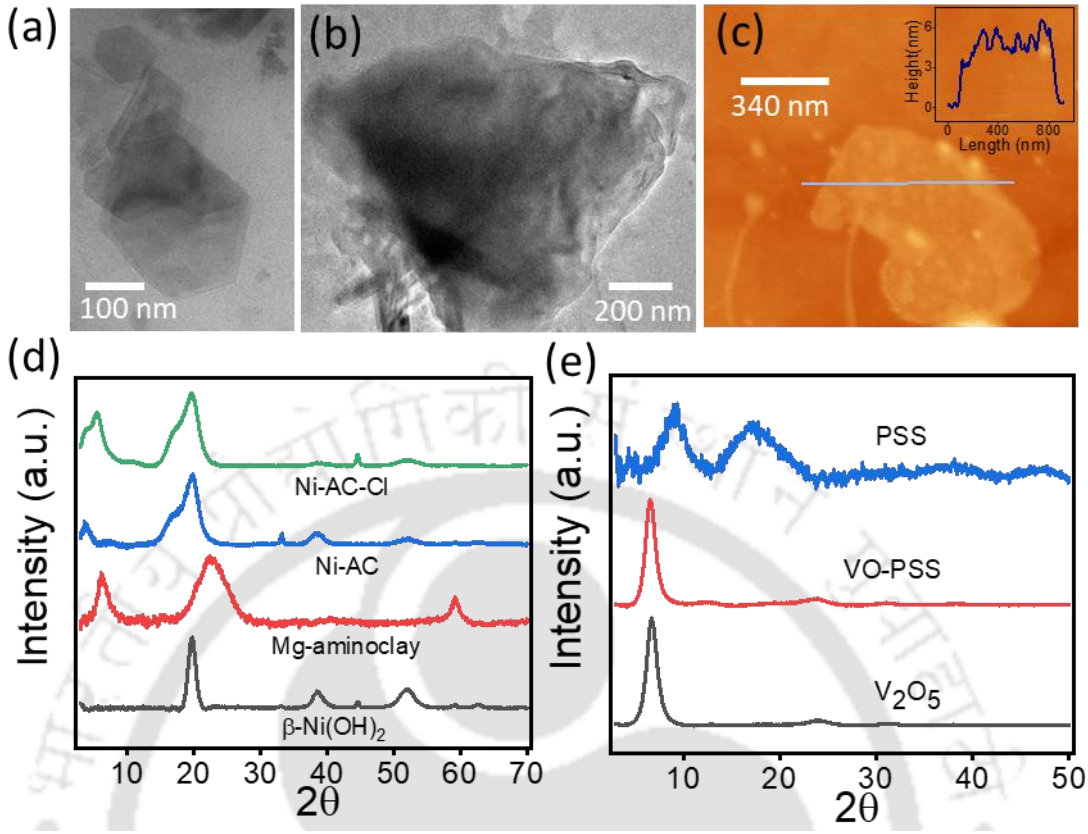

Figure 5.1: (a) TEM image β-($Ni(OH)_2$. (b) TEM image Mg-aminoclay. (c) AFM image of V_2O_5 nanosheet. (d) pXRD pattern of β-$Ni(OH)_2$, Mg-aminoclay, the composite of β-$Ni(OH)_2$ and Mg-aminoclay and the composite of β-$Ni(OH)_2$, Mg-aminoclay and benzyltriethylammonium chloride salt. (e) pXRD pattern of V_2O_5 membrane, composite membrane of V_2O_5 and PSS, PSS membrane.

represents different FT-IR peaks for Mg-aminoclay, and when compared with the composite of Mg-aminoclay and $Ni(OH)_2$ (Figure 5.2d) slight shift of the IR peaks were observed from 2089 cm^{-1} to 2120 cm^{-1} (Figure 5.2e) and from 1627 cm^{-1} to 1613 cm^{-1} (Figure 5.2f). The minute shift of these peak positions suggests the interactions among the Ni^{2+} of $Ni(OH)_2$ and –NH_2 groups of aminoclay as well as the hydrogen bonding among the –OH groups of $Ni(OH)_2$ and –NH_2 groups of Mg-aminoclay.

The anion-generating characteristic of Ni-AC-Cl was verified by the positive Zeta potentials of its components in aqueous dispersion, β-$Ni(OH)_2$ (+14.5±1.46 mV) and Mg-aminoclay (+21.58±2.66 mV), as shown in Figure 5.3b. Additionally, the pH of the aqueous dispersion of

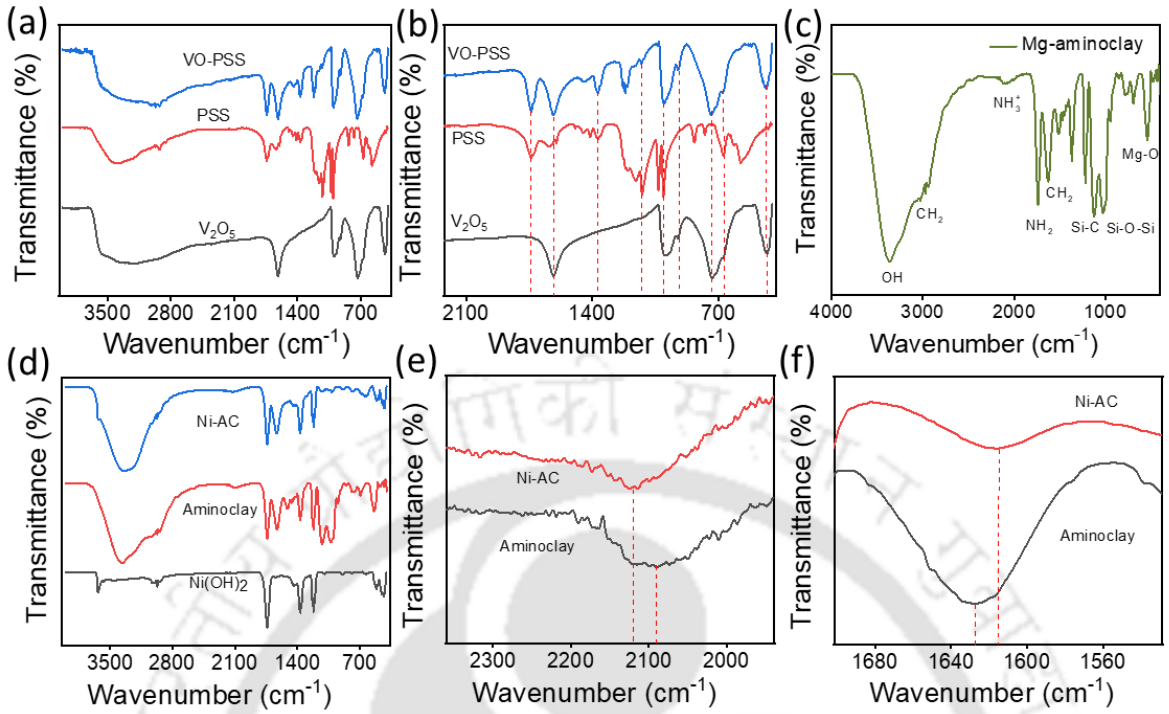

Figure 5.2: (a) FT-IR spectra of V_2O_5, PSS and the composite of V_2O_5 and PSS (VO-PSS). (b) Enlarged version of Figure 5.2a. (c) FT-IR spectra of Mg-aminoclay. (d) Comparison of the FT-IR spectra of $Ni(OH)_2$, Mg-aminoclay and composite of $Ni(OH)_2$ and Mg-aminoclay (Ni-AC). (e) and (f) Enlarged version of Figure 5.2d.

Mg-aminoclay was measured to be approximately ~9.8, attributed to the conversion of $-NH_2$ groups of Mg-aminoclay into $-NH_3^+$, leading to the release of mobile OH^- ions (Figure 5.3e). Moreover, due to the substantial difference in sizes, BTAC generates mobile anions (Cl^-) but relatively large static cations. Similarly, the negative Zeta potential of V_2O_5 nanosheets (- 42.5 ±1.2 mV) and PSS (-43.2±2.17 mV) confirms the cation-generating nature of VO-PSS (Figure 5.3b). Both PSS and V_2O_5 flakes are known to generate mobile protons by absorbing water molecules from the atmosphere.

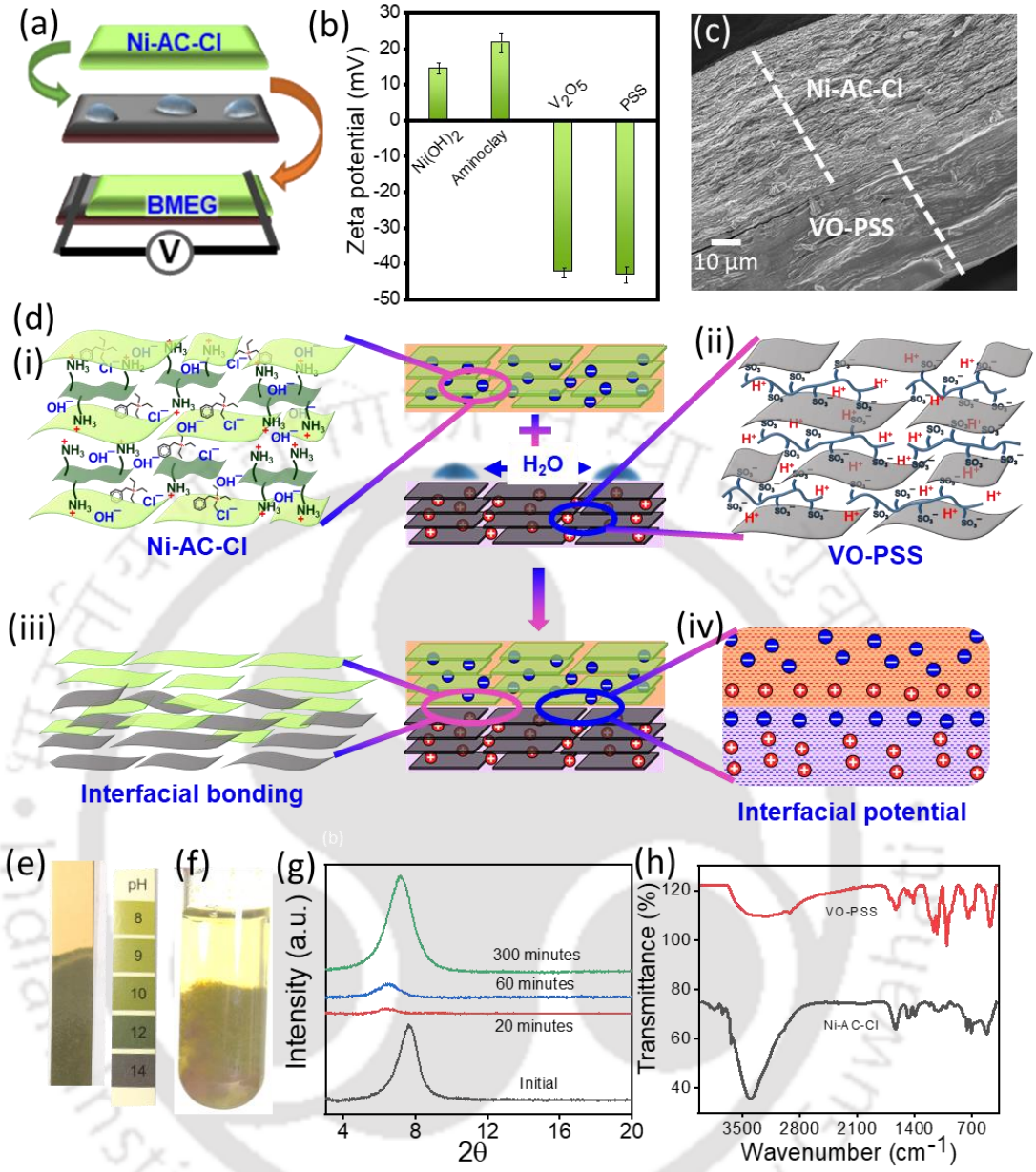

Figure 5.3: (a) Schematic representation of the fabrication of BMEG. (b) Zeta potential values of the components of BMEG β-($Ni(OH)_2$, Mg-aminoclay, V_2O_5 and poly(4-styrenesulfonic acid). (c) Cross-sectional FESEM image of thus fabricated BMEG showing two distinct layers of VO-PSS and Ni-AC-Cl. (d) Schematic representation of the interconnection VO-PSS and Ni-AC-Cl: d(i) structural representation of Ni-AC-Cl, d(ii) structural representation of VO-PSS, d(iii) interfacial bonding of VO-PSS and Ni-AC-Cl layers through intermixing of individual nanosheets, d(iv) schematic representation of the interfacial potential formed after formation of interfacial bonding. (e) Digital photograph of a pH indicator paper showing the basic nature of Mg-aminoclay solution. (f) A digital photograph to show the formation of agglomeration after mixing of oppositely charged aqueous dispersion of Ni-AC-Cl and VO-PSS. (g) In-situ pXRD pattern to demonstrate the swelling of VO-PSS membrane and regaining the original nature of VO-PSS membrane after different intervals of time. (h) FT-IR spectra of the swelling part of Ni-AC-Cl and VO-PSS membrane.

When a pressure is applied with a water droplet in between (Figure 5.3a), robust interfacial

bonding occurs between the strips of Ni-AC-Cl and VO-PSS, as illustrated schematically in Figure 5.3d(iii). As the components of both layers are highly hydrophilic and form aqueous dispersions, a portion of the surface components mix together upon the presence of water droplets, leading to the formation of strong interfacial bonds. This bonding mechanism is corroborated by in-situ pXRD and IR experiments (Figure 5.3g and 5.3h respectively). To examine the swelling of the VO-PSS membrane in the presence of a small amount of water, in-situ pXRD was conducted. Initially, pXRD was performed on the dry VO-PSS membrane, labeled as 'initial' in Figure 5.3g. To initiate the swelling process, a small amount of water was placed on the VO-PSS, and pXRD was recorded after 20 minutes, 60 minutes, and 300 minutes. The swelling reduces the level of crystallinity, leading to a decrease in peak intensity. This also results in an increase in d-spacing, confirmed by the shift of peak position towards the left side. Over time, the water gradually evaporates from the membrane, resulting in a slight increase in

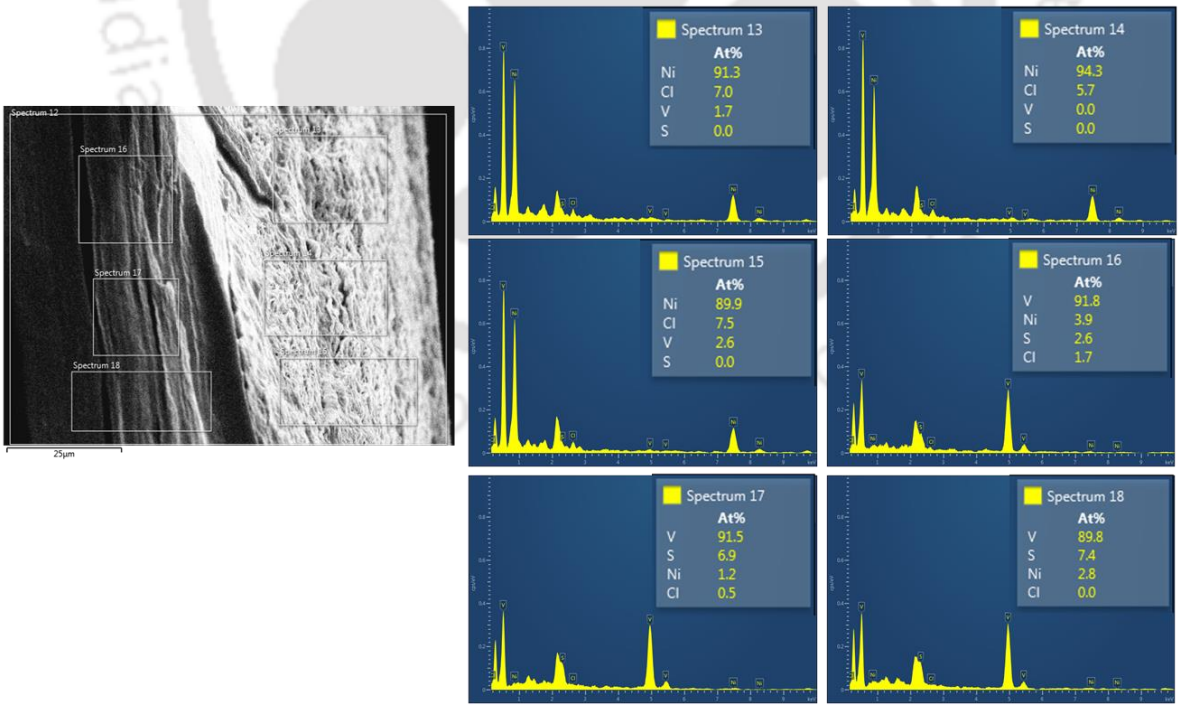

Figure 5.4: Atomic % of different elements on the cross-section of fabricated BMEG.

peak intensity. After 300 minutes, the water completely evaporates from the VO-PSS membrane, eventually restoring its original peak intensity and position.

For further confirmation, FT-IR spectra were recorded from the swollen part of the VO-PSS and Ni-AC-Cl membrane. Initially, approximately 40 µL of water was drop-casted onto the top of the VO-PSS and Ni-AC-Cl membrane. After ~15 minutes, the FT-IR spectra were recorded for the drop-casted water to observe whether it contained components of VO-PSS and Ni-AC-Cl after the swelling process. The observed spectra in Figure 5.3h suggest the presence of V_2O_5 and $Ni(OH)_2$, thus verifying the theory of interfacial mixing of the components of VO-PSS and Ni-AC-Cl during the device fabrication. Furthermore, as depicted in Figure 5.3f, when the aqueous dispersions of the Ni-AC-Cl and VO-PSS components were mixed, they rapidly bonded together, forming agglomerates and precipitates, thus confirming the presence of robust, attractive interactions. The cross-sectional FESEM image in Figure 5.3c reveals the lamellar arrangements of the nanosheets and the distinct layers of Ni-AC-Cl and VO-PSS. The presence of these two layers in the BMEG with the individual components were additionally

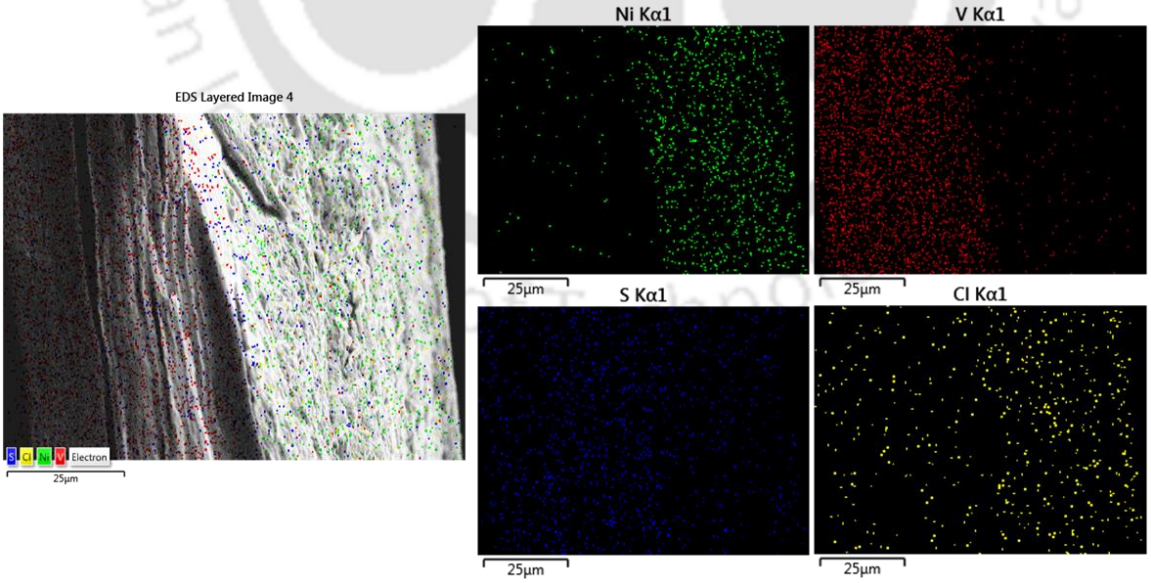

Figure 5.5: Elemental mapping of different elements on the cross-section of BMEG.

verified from elemental analysis and elemental mapping of EDX images shown in Figure 5.4 and 5.5 respectively.

When the two ends of the fabricated BMEG were linked to a sourcemeter instrument (schematic of Figure 5.3a), both output voltage and current were observed. Figure 5.6a illustrates the output voltage and current of the BMEG (comprising VO-PSS measuring 1.5 cm x 0.5 cm and Ni-AC-Cl measuring 1.2 cm x 0.5 cm) with time. The output voltage remained constant with the value ~610 mV for a duration of 10,000 seconds (Figure 5.6a). Conversely, the output current initiates at 27 µA and gradually diminishes over time, reaching saturation at ~3.16 µA after approximately 8,000 seconds (Figure 5.6a). Furthermore, voltage measurements were conducted over several days, showcasing its sustained stability (Figure 5.6b). At the steady state, the power density was computed to be 270 μWcm^{-3}. In the context of practical applications for moisture electric generators, the power density of these devices relative to their volume holds significant importance.

The sustained output voltage observed at the heterojunction of Ni-AC-Cl and VO-PSS is attributed to the establishment of an interfacial electric field between the two layers as depicted in Figure 5.3d(iv).[3,20,25,26] As previously discussed, the hygroscopic nature of Ni-AC-Cl and VO-PSS layers enables them to absorb water molecules from the atmosphere, leading to the generation of mobile anions and cations through the dissociation of surface functional groups. This phenomenon was experimentally validated by measuring the ionic conductivity of the layers under varying humidity levels. As depicted in Figure 5.7a, the conductivity of the layers increases with rising humidity levels, indicating a higher number of charge carriers. Analogous to semiconductor pn junctions, the diffusion of mobile ions is driven by concentration gradients across the interface. However, electrostatic attractions from the parent 2D flakes and repulsions from the opposing 2D flakes prevent their diffusion into the inner regions of the opposite layers, resulting in the localization of ions near the interface and the formation of an ionic double layer.

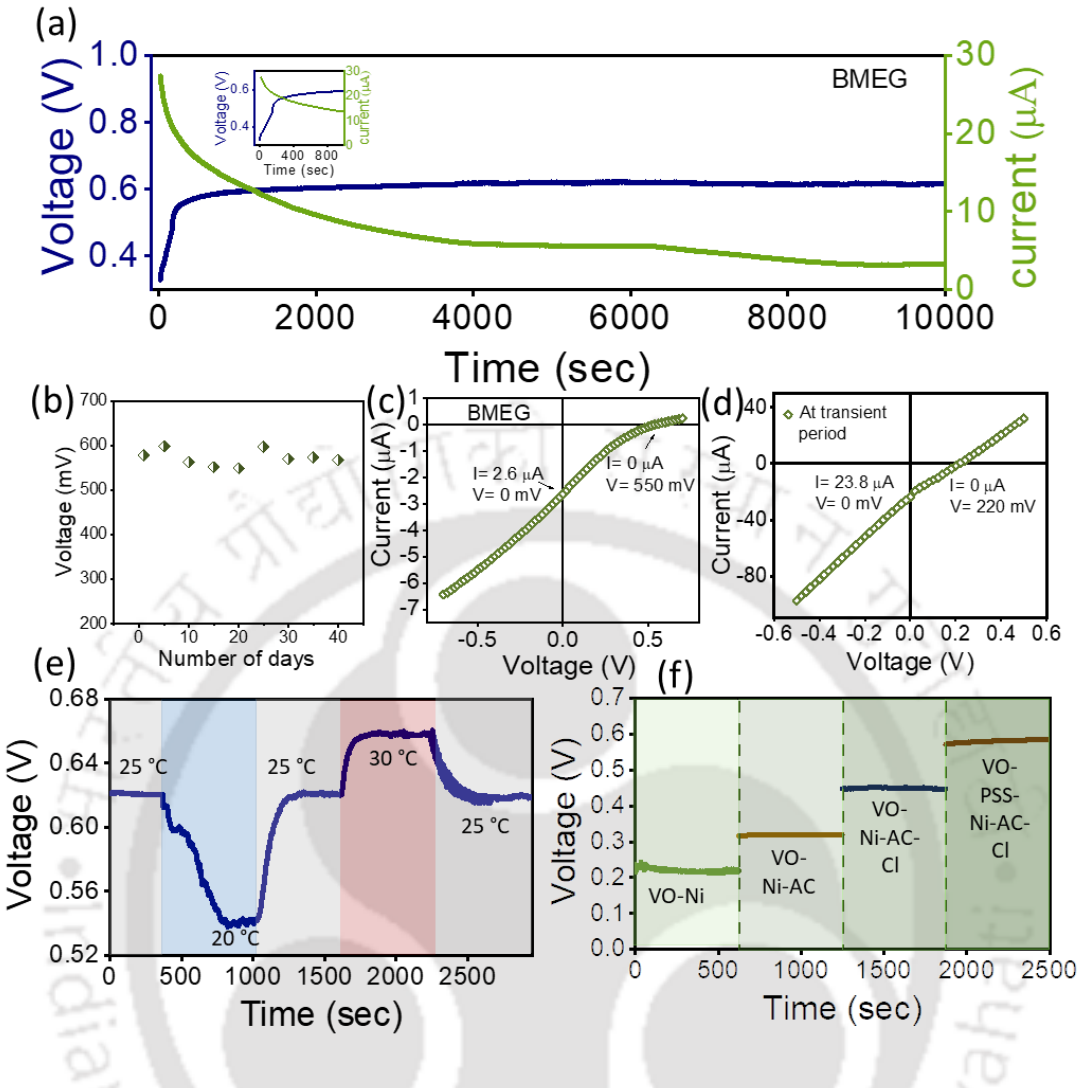

Figure 5.6: (a) Generation of voltage and current from thus fabricated BMEG. (b) Measurement of BMEG output voltage for several days. (c) I-V curve of the BMEG after attaining the saturation currents. (d) I-V curve of the BMEG at transient period. (e) BMEG output voltage at different temperatures. (f) The BMEG output voltage for different compositions of $Ni(OH)_2$ layer (pristine $Ni(OH)_2$: Ni, $Ni(OH)_2$ and Mg-aminoclay: Ni-AC, $Ni(OH)_2$, Mg-aminoclay and BTAC salt: Ni-AC-Cl) and for different compositions of V_2O_5 layer (pristine V_2O_5: VO, V_2O_5 and PSS: VO-PSS).

The resulting interfacial electric field is responsible for the prolonged voltage output of the BMEG. The establishment of a semiconducting pn junction-type heterostructure at the interface is supported by the asymmetry observed in the I-V curve, as shown in Figure 5.6c, where the current observed at -0.7 V is notably higher than that at +0.7 V. Moreover, a nonzero voltage (550 mV) was observed at zero current, and a nonzero current (2.6 μA) was detected at zero volts.

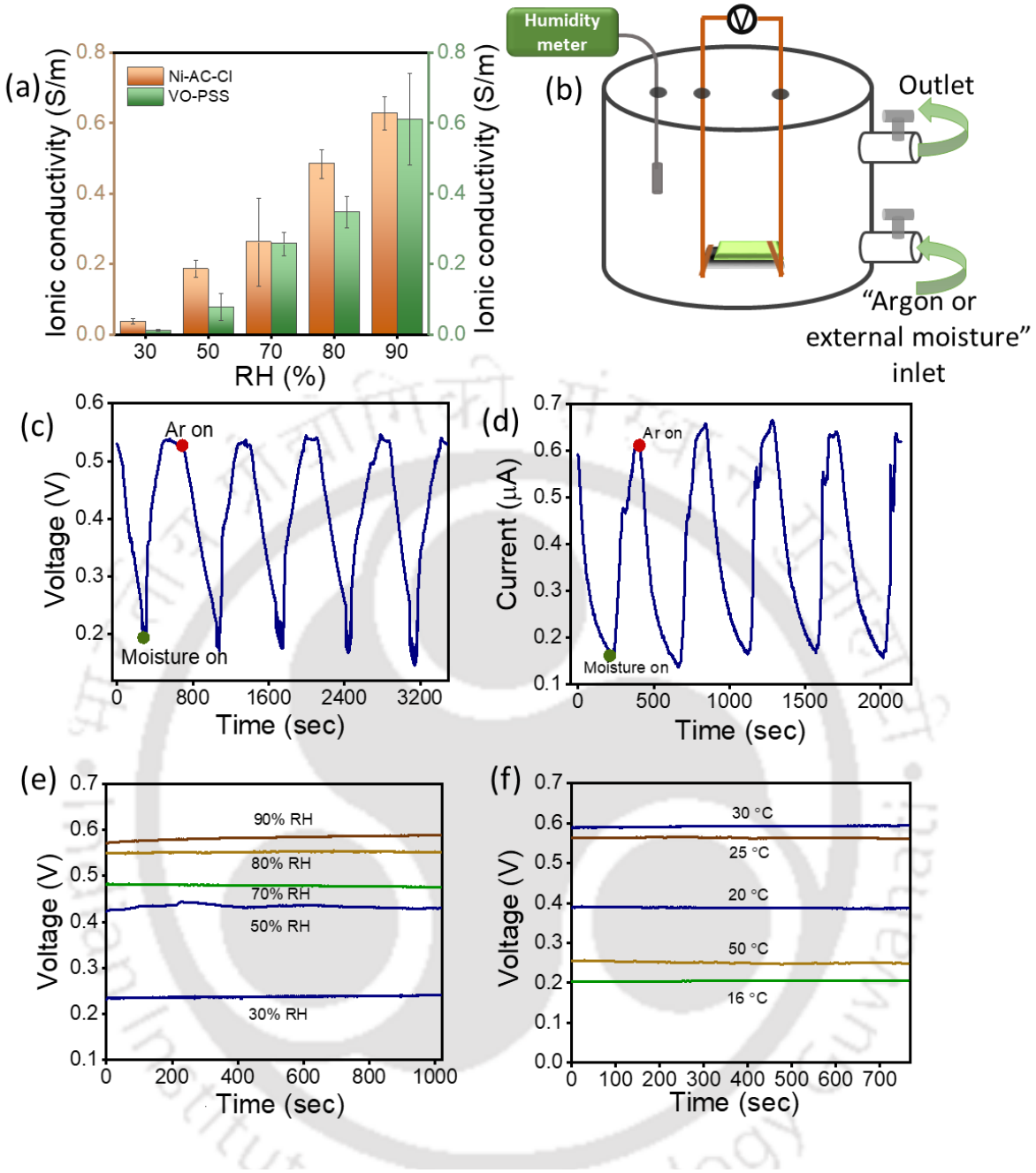

Figure 5.7: (a) Ionic conductivity values of Ni-AC-Cl and VO-PSS membrane at different relative humidity (RH). (b) Schematic illustration of the experimental setup for periodic insertion of external moisture or argon gas. (c) Periodic increment and decrement of BMEG output voltage upon exposure of external moisture and argon gas respectively. (d) Periodic increment and decrement of output current due to the exposure of external moisture and argon gas respectively. (e) Generation of voltage at different relative humidity. (f) Generation of voltage at different temperature on the BMEG.

During the transient period, a significant migration of ionic species from various regions of the membranes towards the interface results in a high ionic current and low voltage, as illustrated

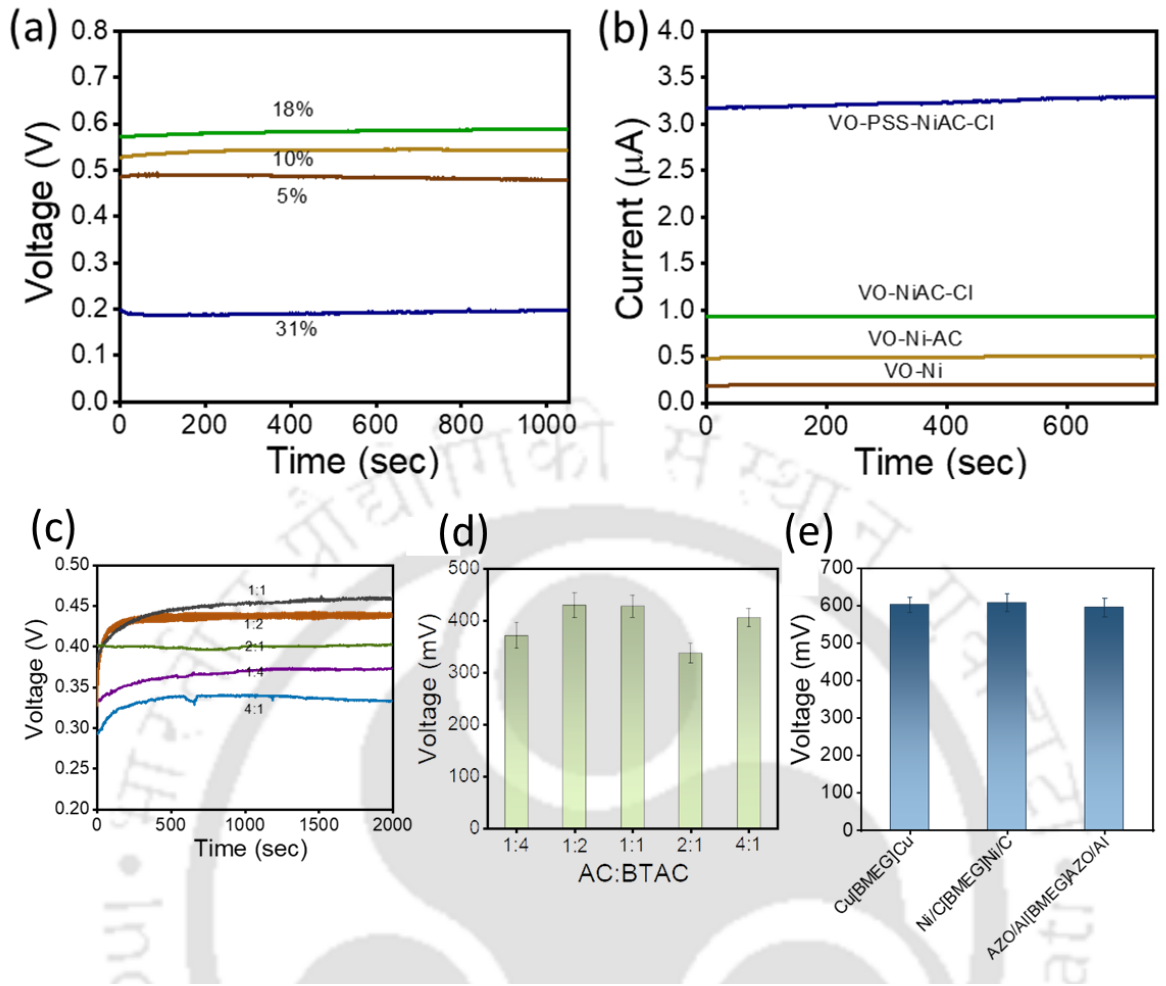

Figure 5.8: (a) The BMEG output voltage for different weight % of PSS. (b) The BMEG output current for different compositions of $Ni(OH)_2$ layer (pristine $Ni(OH)_2$: Ni, $Ni(OH)_2$ and Mg-aminoclay: Ni-AC, $Ni(OH)_2$, Mg-aminoclay and BTAC salt: Ni-AC-Cl) and for different compositions of V_2O_5 layer (pristine V_2O_5: VO, V_2O_5 and PSS: VO-PSS). (c) The BMEG output voltages for different weight ratio of Mg-aminoclay and BTAC salt. (d) The bar diagram for the comparison of the generated voltages for different weight ratio of Mg-aminoclay and BTAC salt. (e) MEG output with different electrode configurations.

in the inset of Figure 5.6a and 5.6d. As the ionic double layer begins to form, the potential difference gradually increases, while the output current gradually decreases until reaching a steady state after ~2000 seconds. In this steady state, both hygroscopic membranes continuously absorb water molecules from the atmosphere and ionize them through surface functional groups. The interfacial potential attracts ionic species towards the interface, where excess H^+ ions and OH^- ions combine to form water molecules, which then desorb from the system. This cycle of water molecule absorption and desorption continues for extended periods, converting atmospheric energy into electrical signals.

The significance of water molecule absorption was confirmed by replacing the humid environment with Ar gas and increasing the overall temperature of the system as depicted in Figure 5.7b, c, d and f respectively. The schematic representation of the experimental setup for periodic exposure of Ar gas and external moisture is shown in Figure 5.7b. Upon replacing humid air with Ar, both the output potential and current experienced a sharp decrease, followed by a rapid recovery upon reintroducing humid air. Similarly, increasing the temperature up to 30°C resulted in an increase in the output voltage from 620 mV to 657 mV, attributed to a favourable desorption process (Figure 5.6e). However, further temperature elevation hindered the absorption of atmospheric water molecules, leading to a sharp decrease in voltage output (Figure 5.7f). The importance of water desorption in the continuous generation of moisture electricity was further validated by lowering the overall system temperature to 20°C, resulting in a 13% reduction in output potential (Figure 5.6e). Furthermore, the dependence of the BMEG on humidity was confirmed by periodically increasing the relative humidity, resulting in a corresponding increase in BMEG output voltage, as shown in Figure 5.7e.

To explore the significance of mobile ion concentrations, BMEG devices were constructed using solely bare β-$Ni(OH)_2$ and V_2O_5 membranes without additional ion-generating additives. As anticipated, both output voltages and currents decreased from ~615 mV to ~230 mV and from about 3.15 μA to 0.2 μA, respectively (Figure 5.6f and Figure 5.8b). Likewise, when β-$Ni(OH)_2$ flakes were modified with anion-generating Mg-aminoclay while keeping the V_2O_5 layer unaltered, an improved output voltage of roughly 300 mV was observed compared to the pristine β-$Ni(OH)_2$ membrane. The incorporation of another anion-generating salt, BTAC, further increased the output voltage to approximately 450 mV (see Figure 5.6f). Additionally, optimization of the BMEG involved varying the weight ratios of Mg-aminoclay and BTAC salt, with the highest output voltage achieved at a ratio of 1:1 (as shown in Figure 5.8c and 5.8d). When the cation-generating V_2O_5 layer was supplemented with PSS molecules, the

BMEG's output voltage was further augmented, and the weight percentage of PSS molecules was finely adjusted to attain the optimal output, approximately 600 mV, for the specific composition of 18 wt% PSS, as illustrated in Figure 5.8a. Further, in order to verify that the energy is generated solely from the interaction of water, Cu electrodes does not have a specific role to play two different sets of electrodes were utilized ($NiCo_2O_4$ coated carbon paper (Ni/C) and Al doped ZnO and Al (AZO/Al)) instead of Cu that develops similar amount of potentials (Figure 5.8e) representing the moisture induced ions are the active components for generation of voltage across the MEG.

Performance of BMEG under temperature gradient:

In the preceding section, we established that the efficacy of BMEG relies on the concentration of mobile ions that create the ionic double layer at the interface of cationic and anionic membranes. The performance of BMEG can be further enhanced by tuning the interfacial potential via the thermodiffusion of ionic species, known as the Soret effect. In recent times, the Soret effect has garnered considerable attention for its potential in extracting electricity from low-grade waste heat sources.

As depicted in the diagram of Figure 5.9a, a BMEG was assembled by joining a 1.5 cm long VO-PSS strip with a 1.2 cm long Ni-AC-Cl strip, leaving one end of the VO-PSS strip (~0.3 cm) uncovered. Initially, the BMEG was subjected to a temperature gradient (ΔT) by positioning the uncovered section of VO-PSS on a hot Peltier device (temperature T_h), while the portion interfacing with Ni-AC-Cl was placed on a cold Peltier device (temperature T_c). At ΔT = 15 ºC (T_h = 33 ºC and T_c= 18 ºC), the output voltage exhibited an increase from 574 mV (at ΔT = 0 ºC) to 767 mV (ΔT = 18 ºC), as illustrated in Figure 5.9b. This rise in output potential is attributed to the heightened ionic concentration at the interface resulting from the thermodiffusion of ions from the hot to the cold zone, as depicted in the schematic in Figure

5.9d. To validate this proposition, the temperature gradient was reversed, wherein the temperature of the uncovered VO-PSS section was lowered (T_c = 18 ºC), while that of the overlapped part was raised (T_h = 33 ºC). In this arrangement, ions were compelled to

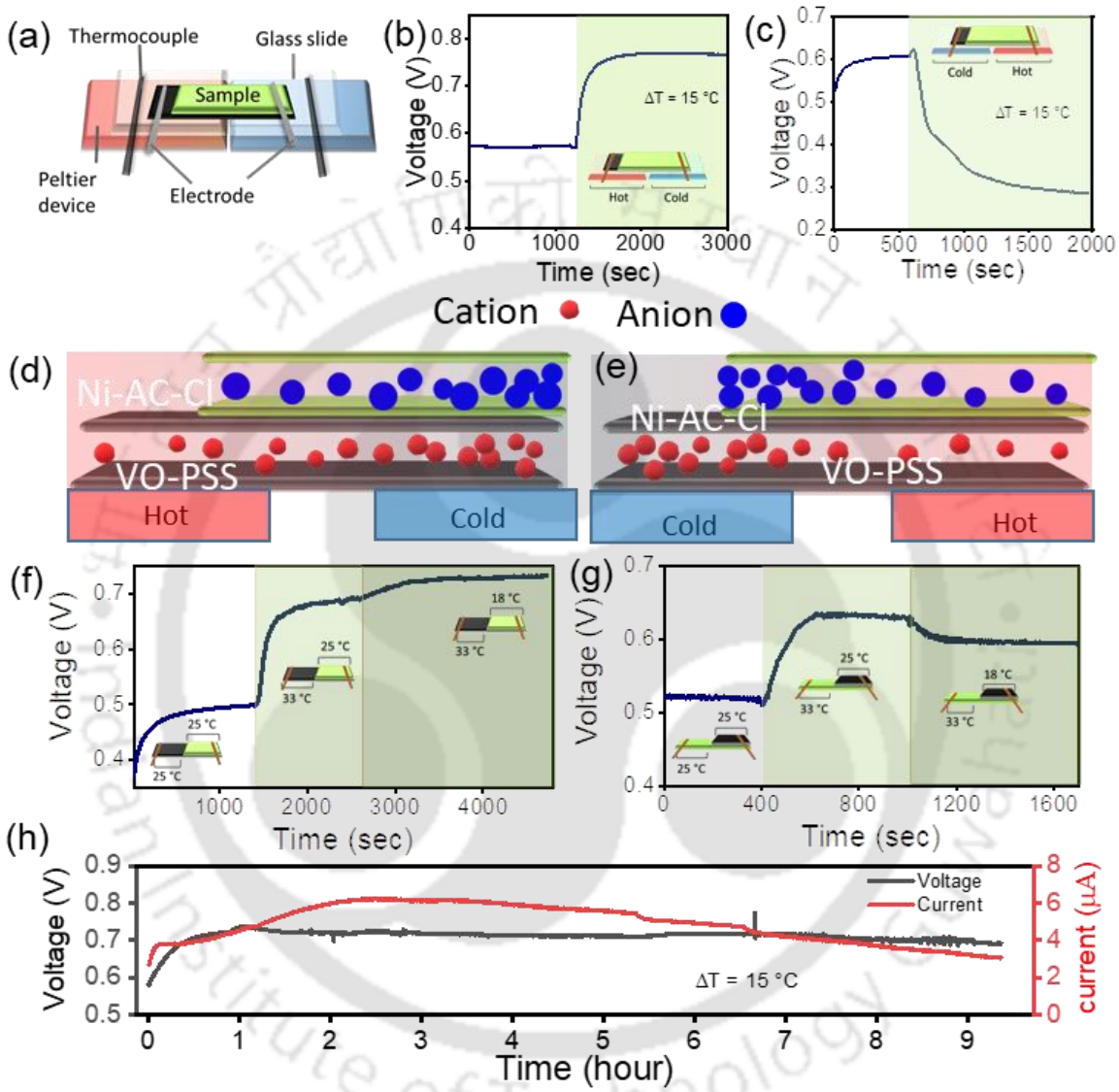

Figure 5.9: (a) Schematic of the experimental setup for temperature gradient based experiments. (b) Increment of the voltage output of BMEG under a temperature gradient of 15 ºC (T_h is towards the VO-PSS side and T_c is towards the Ni-AC-Cl side). (c) Decrease in the voltage output of BMEG under a temperature gradient of 15 ºC (T_h is towards the Ni-AC-Cl side and T_c is towards the VO-PSS side). Schematic representation of the diffusion of ions under the temperature gradient across the BMEG when (d) VO-PSS is exposed to high temperature and Ni-AC-Cl is exposed to low temperature, (e) Ni-AC-Cl is exposed to high temperature and VO-PSS is exposed to low temperature. Generation of voltage at two different temperature gradients when (f) the length of Ni-AC-Cl is half of VO-PSS membrane; (g) the length of VO-PSS is half of Ni-AC-Cl membrane. (h) Generation of current and voltage for longer period of time under a constant temperature gradient of 15 ºC.

thermodiffuse away from the interface, leading to a significant decrease in the output voltage (from ~600 mV to ~286 mV), as shown in Figure 5.9c.

To further validate the temperature-induced enhancements, another BMEG device was constructed by covering half of a 1.5 cm long VO-PSS strip with a 0.7 cm long Ni-AC-Cl strip. Due to the reduced overlapping area, this configuration exhibited slightly lower output current/voltage compared to that shown in Figure 5.9b (Figure 5.9f). Nevertheless, when subjected to a temperature gradient (ΔT = 8 ºC) favouring ion thermodiffusion towards the overlapping interface (T_h = 33 ºC, and T_c = 25 ºC), the output potential rose from 498 to 690 mV. Further increasing the temperature gradient (ΔT = 15 ºC) resulted in an output potential of ~730 mV. Another BMEG device with an alternative configuration was prepared by covering a portion of a 1.5 cm long Ni-AC-Cl strip with a 0.7 cm long VO-PSS strip of similar

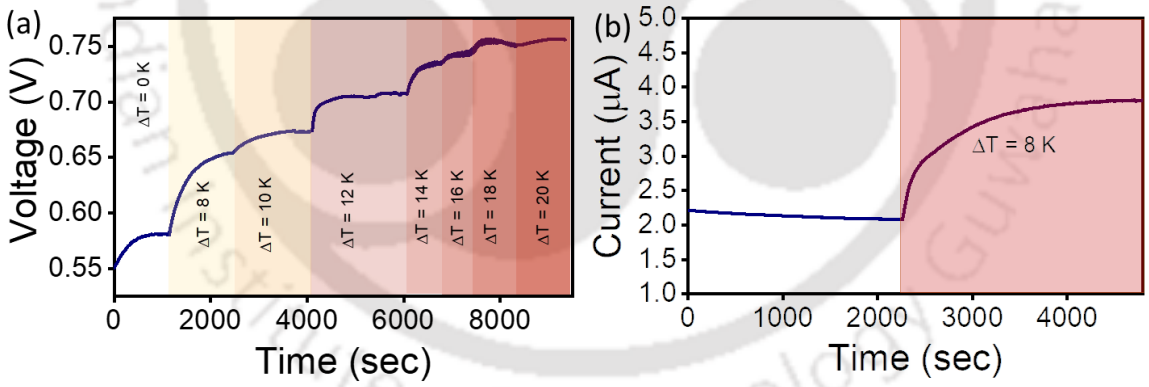

Figure 5.10: (a) Increment of the overall BMEG output voltage upon application of different temperature gradient across the BMEG. (b) Increment of the output current upon application of different temperature gradient across the BMEG.

width. Again, upon applying a temperature gradient (ΔT = 8 ºC) favouring ion thermodiffusion towards the interface (T_h = 33 ºC, and T_c = 25 ºC), the output potential increased from 519 mV to 630 mV. The voltage increment under different temperature gradients is depicted in Figure 5.10a, while the current increment is shown in Figure 5.10b. These findings could pave the

way for the development of unique platforms leveraging ubiquitous waste heat to enhance the power output of moisture electric generators for practical applications. As a proof of concept, Figure 5.9h illustrates continuous output current and voltage of a BMEG for nearly 10 hours under a constant ΔT = 15 °C. However, the output voltage declined when the temperature on the cold side (T_c = 18 ºC) was lowered to increase the temperature gradient, as shown in Figure 5.9g. This decline is attributed to the reduced dissociation and mobility of protons within the VO-PSS layer at lower temperatures.

Performance of BMEG under white light:

In the preceding section, we illustrated how exposing BMEG devices based on Ni-AC-Cl and VO-PSS to a temperature gradient can enhance their output performance. Exploiting ubiquitous and abundant white light offers another avenue to generate the required temperature gradient for this enhancement. Due to its darker colour, the VO-PSS strip absorbs more light and becomes hotter (34.5 ºC, 7000 lux) compared to the Ni-AC-Cl strip, which has a light green color (29.6 ºC, 7000 lux) (Figure 5.11d and e). Consequently, subjecting a BMEG device (VO-PSS dimensions: 1.5 cm x 0.5 cm x 0.005 cm, interfaced with Ni-AC-Cl dimensions: 0.8 cm x 0.5 cm x 0.006 cm) to uniform white light of 7000 lux intensity generates a temperature gradient (ΔT = 4.2 ºC) (Figure 5.11c). Figure 5.11b demonstrates an enhancement in the performance of the BMEG device with the light-induced temperature gradient. A schematic of the experimental setup is depicted in Figure 5.11a. Such light-driven moisture electric devices could offer alternative means to harness sustainable energy by simultaneously utilizing atmospheric water and light energy.

The output currents of the BMEG could be periodically increased from 0.5 µA to 5.8 µA by enlarging the exposed surface area from 0.5 cm^2 to 6 cm^2, as depicted in Figure 5.11f. This enhancement is attributed to the increasing number of charge carriers with the expanding

surface area. It's worth noting that the current values in Figure 5.11f were measured only after stabilization.

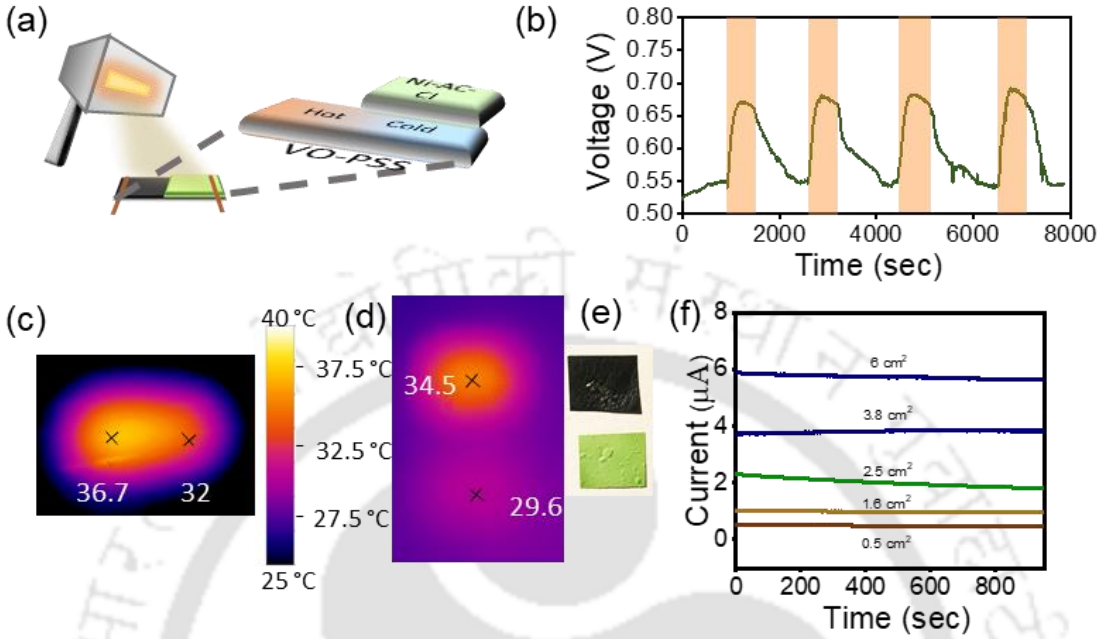

Figure 5.11: (a) Schematic representation of the illumination of white light over the fabricated BMEG. (b) Increment of the BMEG output voltages upon exposure to the white light. Thermal images of (c) BMEG and (d) individual VO-PSS and Ni-AC-Cl membrane under the expose of white light. (e) Digital photograph of the individual VO-PSS and Ni-AC-Cl membrane that are exposed to white light in Figure 4d. (f) Increment of the BMEG current output with the increase of total surface area.

High-temperature and Low-temperature stability:

Most previously reported MEGs have been constructed using polyelectrolytes, functionalized polymers, and oxygenated carbons. These MEGs typically require controlled operating conditions due to their susceptibility to functional degradation when exposed to harsh environments. Higher temperatures can lead to irreversible chemical alterations to oxygenated functional groups, gradient structures, and polymeric molecules, while materials with high water content, such as hydrogels or modified woods, may suffer physical damage at sub-zero temperatures. Notably, BMEGs crafted from robust inorganic 2D materials exhibit resilience to both high temperatures (up to 200 ºC) and low temperatures (-195 °C). Digital images of a

BMEG before and after exposure to heat shock (200 °C for 300 seconds) are presented in Figure 5.12a (a1 and a2), demonstrating the durability of the device at elevated temperatures.

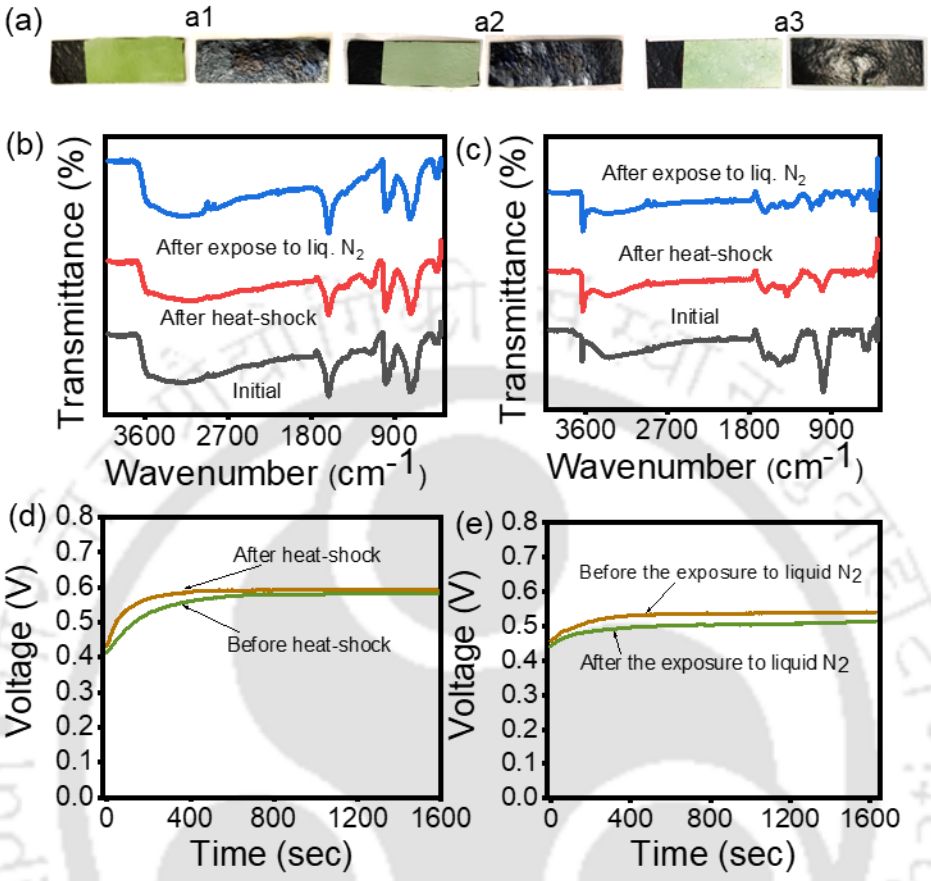

Figure 5.12: (a) Digital photograph of the top and bottom side of fabricated BMEG: at initial stage (a1), after heat-shock (a2) and after exposure of liquid N_2 (a3). The FT-IR spectra of (b) VO-PSS and (c) Ni-AC-Cl, before and after exposure of liquid N_2 and heat-shock. Generation of output voltage (d) before and after heat-shock; (e) before and after exposure of liquid N_2.

Similarly, the BMEG was immersed in liquid nitrogen (-195 °C) for approximately 5 minutes, as depicted in Figure 5.12a (a1 and a3). FT-IR spectra in Figure 5.12b and 5.12c confirm the unchanged chemical structures of the BMEG components during exposure to extreme temperatures. Graphs illustrating consistent output voltages before and after heat and cold shocks are shown in Figure 5.12d and Figure 5.12e, respectively. Any minor reduction in output potential may be attributed to the loosening of contacts between Cu wire/Ag pastes and

the membranes due to ice crystal deposition. The stability against extreme temperature variations highlights the versatility of this BMEG device for a wide range of applications.

Practicality of BMEG:

The parallelization of multiple devices is crucial for the practical implementation of moisture-electric generators in operating electronic devices. The seamless assembly of several BMEG devices is a primary criterion for their commercialization. As depicted in the schematic in Figure 5.13a, a large number of BMEG devices can be interconnected to aggregate the voltages and currents generated by each device. The plot of output voltage versus the number of devices in Figure 5.13b demonstrates that the output voltage linearly increases with the growing number of BMEG devices. An output voltage of approximately 40 V was achieved by connecting 200 BMEGs in series, and a current of up to 45 µA was recorded with 10 BMEGs in parallel connection, as shown in Figure 5.13c. The practicality of BMEG is further illustrated in Figure 5.13d, 5.13e where a calculator and LED light are powered using environmental humidity through an assembly of BMEGs.

Many previously reported MEGs suffer from inherent structural or active material-based shortcomings, leading to a decline in power output within days or weeks of operation. However, BMEGs based on inorganic 2D materials exhibit the ability to recover performance that has diminished during prolonged use. As illustrated in Figure 5.13f and 5.13g, after 80 days of continuous operation, the output voltages and currents of the BMEG decreased to approximately 410 mV (from an initial voltage of 610 mV) and 0.14 µA (from a saturated current of 3.16 µA), respectively. For the measurements of voltage Instead of maintaining a continuous connection to the sourcemeter, the MEG device was measured for approximately 2000 seconds for every alternative of 4 days over a span of 80 days and the voltages were recorded accordingly. This power depreciation is attributed to the loosening of device

connections and dehydration of the membranes, as chemical degradation of the inorganic

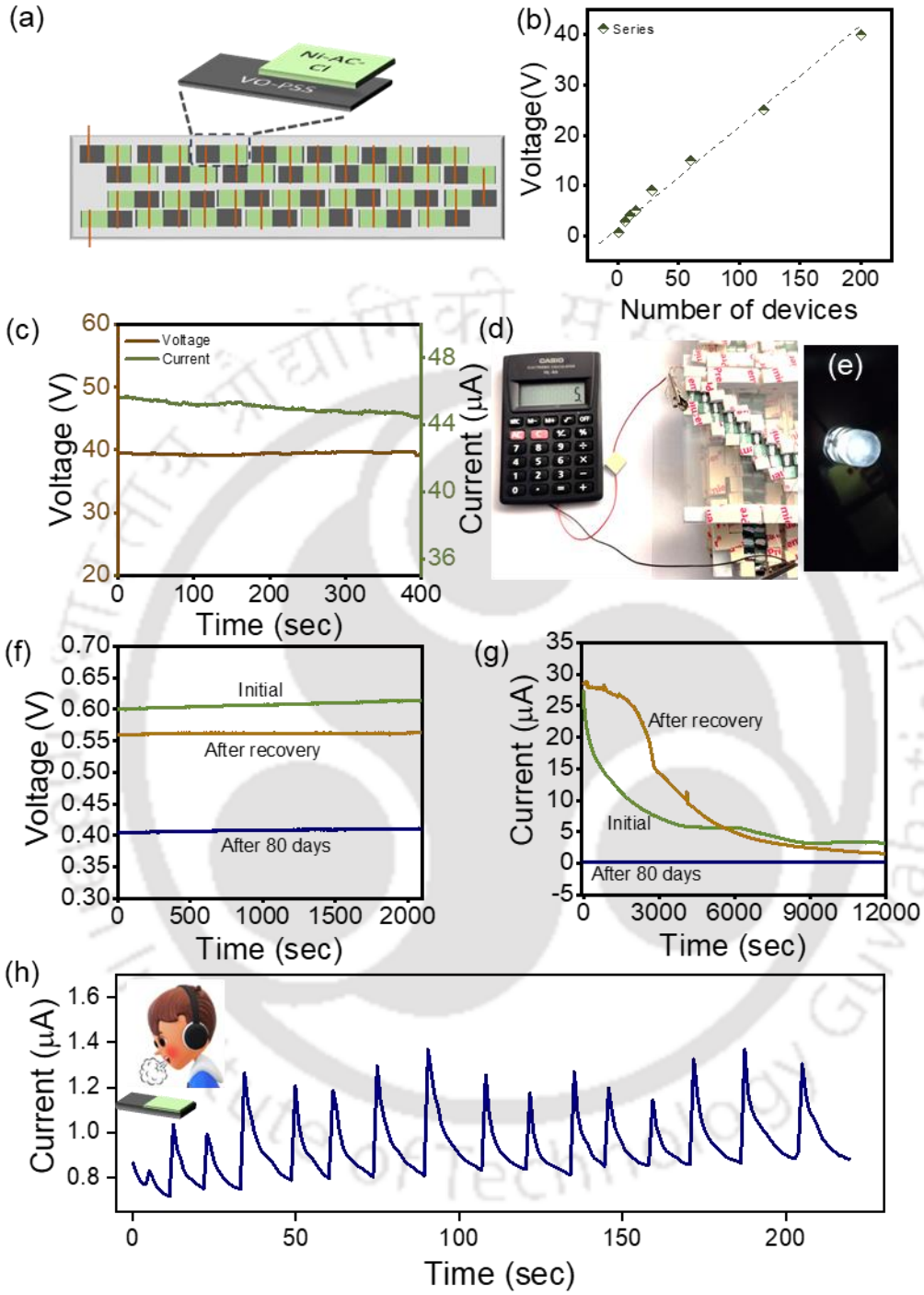

Figure 5.13: (a) Schematic representation of the connection of several BMEG devices. (b) Linear increment of the output voltage with the increasing numbers of devices. (c) The overall output voltage with 200 numbers of devices, and overall output current with 10 numbers of BMEG devices. Digital image of powering up (d) a calculator and (e) and LED with environmental moisture through BMEG devices. (f) Evaluation of the BMEG voltage variations after 80 days, in reference to the starting value (day 1) and after recovery (day 80). (g) Evaluation of the BMEG current variations after 80 days, in reference to the starting value (day 1) and after recovery (day 80). (h) Generation of electrical signal by the BMEG with respect to mouth air.

oxides and hydroxides at room temperature is unlikely. To restore the power output, the membrane connections with Cu wire were refreshed by applying fresh Ag-paste, and the membranes were rehydrated by adding a small droplet (~20 µL) of water at the junction of VO-PSS-M and Ni-AC-Cl-M. Remarkably, ~93% of the output voltage and 100% of the output current were regenerated within a few minutes (Figure 5.13f and 5.13g). This remarkable recovery capability of BMEG will undoubtedly enhance the practical utility, cost-effectiveness, and user-friendliness of moisture electric generators.

The sensitivity of BMEG to atmospheric water molecules can be further utilized as self-powered moisture sensors. As demonstrated in Figure 5.13h, BMEG responds to moist air coming from the mouth by generating electrical signals, suggesting the potential for developing self-powered devices for continuous diagnosis of abnormal physiological conditions, measuring respiration rate, detecting respiratory failure, and providing real-time human breath monitoring systems. Such BMEG devices can establish a novel platform for innovations in the field of medical appliances as self-powered biosensors.

5.6. Conclusion:

In conclusion, we have demonstrated the potential of employing atomically thin 2D nanomaterials derived from inorganic layered substances to create highly resilient, durable, and practically feasible moisture-to-electricity converters. In comparison to MEGs based on organic polymers or partially oxidized carbon, BMEG devices rooted in metal oxide and hydroxide exhibit exceptional durability and superior practicality. The junction potential occurring at the interface of nanofluidic layers containing oppositely charged mobile ions is responsible for the observed electrical signals in BMEGs, a phenomenon validated by manipulating the mobile charges via temperature gradients.

Unlike the short pulses typically observed with conventional MEGs, metal oxide and hydroxide-based BMEG devices deliver stable power output for extended periods, often lasting several months. The renewal and rehydration of connections enable the recovery of nearly 100% of the output current and 93% of the output voltage in layered materials-based BMEGs. A simple membrane fabrication and device assembly process can be utilized to connect multiple devices in series or parallel configurations, yielding the required power output for practical applications.

The power output of BMEGs can be tailored by exposing them to different intensities of white light and utilizing waste heat-driven temperature gradients. Moreover, BMEGs exhibit precise responsiveness to moisture, such as mouth air, suggesting the potential for developing highly resilient and self-powered moisture sensors. Given the abundance of inorganic layered materials and their surface-functionalized derivatives, exfoliated layered materials present numerous exciting opportunities for exploring and manufacturing moisture-electric generators for real-time applications.

5.7. References:

1 T. Xu, X. Ding, H. Cheng, G. Han and L. Qu, *Adv. Mater.*, 2023, **n/a**, 2209661.

2 Y. Cao, B. Xu, Z. Li and H. Fu, *Adv. Funct. Mater.*, 2023, **33**, 2301420.

3 T. Cai, L. Lan, B. Peng, C. Zhang, S. Dai, C. Zhang, J. Ping and Y. Ying, *Nano Lett.*, 2022, **22**, 6476–6483.

4 Y. Huang, H. Cheng, C. Yang, H. Yao, C. Li and L. Qu, *Energy Environ. Sci.*, 2019, **12**, 1848–1856.

5 M. Yang, Y. Hu, S. Zheng, Z. Liu, W. Li and F. Yan, *Adv. Sci.*, 2023, **10**, 2206071.

6 R. Li, Y. Shi, M. Wu, S. Hong and P. Wang, *Nano Energy*, 2020, **67**, 104255.

7 F. Zhao, H. Cheng, Z. Zhang, L. Jiang and L. Qu, *Adv. Mater.*, 2015, **27**, 4351–4357.

8 P. Deka, S. Roy, T. Jyoti Konch, B. Rani Bora, R. Gogoi, A. Bikash Neog, K. Sundararajan, S. Subbiah and K. Raidongia, *Chem. Eng. J.*, 2023, **469**, 143964.

9 P. Deka, V. K. Verma, A. Chandrasekaran, A. B. Neog, A. Bardhan, K. Raidongia and S. Subbiah, *J. Memb. Sci.*, 2022, **660**, 120884.

10 K. Saha, J. Deka and K. Raidongia, *ACS Appl. Energy Mater.*, 2021, **4**, 8410–8420.

11 J. Deka, K. Saha, R. Gogoi, G. K. Dutta and K. Raidongia, *ACS Appl. Electron. Mater.*, 2021, **3**, 277–284.

12 X. Wang, Y. Wang, M. Dong, Z. Fang, Y. Hu, K. Xue, Z. Ye and X. Peng, *Mater. Today Energy*, 2023, **34**, 101285.

13 Y. Wang, T. Yun, X. Wang, B. Yao, Z. Ye and X. Peng, *Mater. Today Energy*, 2023, **36**, 101359.

14 R. Gogoi, H. Madeshwaran, A. Ghosh, Y. Green and K. Raidongia, *Adv. Funct. Mater.*, 2023, **33**, 2301178.

15 R. Gogoi, A. Ghosh, P. Deka, K. K. R. Datta and K. Raidongia, *Mater. Horizons*, 2023, **10**, 3072–3081.

16 R. Zhang, M. Qu, H. Wang, M. Fan, Q. Chen, P. Tang and Y. Bin, *React. Funct. Polym.*, 2022, **181**, 105421.

17 H. Cheng, Y. Huang, F. Zhao, C. Yang, P. Zhang, L. Jiang, G. Shi and L. Qu, *Energy Environ. Sci.*, 2018, **11**, 2839–2845.

18 Y. Huang, H. Cheng, C. Yang, P. Zhang, Q. Liao, H. Yao, G. Shi and L. Qu, *Nat. Commun.*, 2018, **9**, 4166.

19 Y. Zhang, S. Guo, Z. G. Yu, H. Qu, W. Sun, J. Yang, L. Suresh, X. Zhang, J. J. Koh and S. C. Tan, *Adv. Mater.*, 2022, **34**, 2201228.

20 H. Wang, Y. Sun, T. He, Y. Huang, H. Cheng, C. Li, D. Xie, P. Yang, Y. Zhang and L. Qu, *Nat. Nanotechnol.*, 2021, **16**, 811–819.

21 R. K. Gogoi, A. B. Neog, N. Sarmah and K. Raidongia, *J. Mater. Chem. A*, 2019, **7**, 21157–21167.

22 L. Fu, K. Kumara, R. Datta, K. Spyrou, G. Qi, A. Sardar, M. M. Khader, R. Zboril and E. P. Giannelis, *Appl. Mater. Today*, 2017, **9**, 451–455.

23 K. K. R. Datta, A. Achari and M. Eswaramoorthy, *J. Mater. Chem. A*, 2013, **1**, 6707–6718.

24 R. K. Gogoi, A. B. Neog, T. J. Konch, N. Sarmah and K. Raidongia, *J. Mater. Chem. A*, 2019, **7**, 10552–10560.

25 W. Lu, T. Ding, X. Wang, C. Zhang, T. Li, K. Zeng and G. W. Ho, *Nano Energy*, 2022, **104**, 107892.

26 Y. Zhang, T. Yang, K. Shang, F. Guo, Y. Shang, S. Chang, L. Cui, X. Lu, Z. Jiang, J. Zhou, C. Fu and Q.-C. He, *Nat. Commun.*, 2022, **13**, 3484.

27 Nabavi, M., Sanchez, C. & Livage, J. Structure and properties of amorphous V2O5 . Philos. Mag. B 63, 941–953 (1991).

28 Hoppe, U., Kranold, R. & Gattef, E. An X-ray diffraction study of the structure of vitreous V2O5. Solid State Commun. 108, 71–76 (1998).

29 Delahaye-Vidal, A. & Figlarz, M. Textural and structural studies on nickel hydroxide electrodes. II. Turbostratic nickel (II) hydroxide submitted to electrochemical redox

cycling. J. Appl. Electrochem. 17, 589–599 (1987).

30 Hall, D. S., Lockwood, D. J., Bock, C. & MacDougall, B. R. Nickel hydroxides and related materials: a review of their structures, synthesis and properties. Proc. R. Soc. A Math. Phys. Eng. Sci. 471, 20140792 (2015).

31 Datta, K. K. R., Achari, A. & Eswaramoorthy, M. Aminoclay: a functional layered material with multifaceted applications. J. Mater. Chem. A 1, 6707–6718 (2013).

Chapter 6

Conclusions and Future perspective

6.1. Overview:

In conclusion, in this thesis work we initiates the development of a new class of ionic thermoelectric (i-TE) material that utilizes different reconstructed lamellar nanofluidic membranes. With through investigations of the unique characteristics of the membranes prepared in this thesis work, we have gained insights into the behaviour of ions at the nanoscale and their potential for thermoelectric applications. This advancement opens up new avenues for exploring and optimizing ionic thermoelectric materials, which holds promise for advancements in energy conversion and related technologies. Additionally, looking at the potential of these reconstructed membranes in the field of ionic thermoelectricity, it has been integrated with another newly emerged approach known as moist electric generators (MEG). The synergy between these two methodologies has markedly enhanced the overall power output of the MEG, paving the way for future advancements in this realm and overall fabrication of these classes of devices. One of the primary advantage that have been observed with these classes of material is their ability to withstand at high temperature stability without losing its original thermoelectric properties. Additionally, two of the i-TE material displayed water assisted healing property demonstrating its applicability in harsh conditions therefore, broadening the application areas in a wide horizon.

In chapter 2, an i-TE material was fabricated by reconstructing exfoliated naturally abundant clay minerals. The material was further modified through the surface functionalisation of the individual nanosheets into $–SO_3H$ groups, thereby elevating the overall performance. The study additionally dealt with the introduction of a photothermal material to create an intentional temperature gradient in order to harvest energy directly from white light. The fabricated device

can easily retain its thermopower at relatively lower humidity level through the introduction of a hydrogel as a coating on the i-TE material. The applicability of the fabricated i-TE device was further demonstrated in several areas such as fire-alarm, hot water steam, self-powered sensors etc.

As the formation of $–SO_3H$ groups significantly elevated the ionic thermopower of the clay material, in the chapter 3, a polyelectrolyte (poly(4-styrenesulfonic) acid (PSS)) containing the $–SO_3H$ was externally interchelated inside the nanochannels of V_2O_5. Nearly, 80% improvement of the ionic Seebeck coefficient was observed as compared to the pristine V_2O_5 nanofluidic membrane, after the incorporation of PSS molecules. The importance of nanoconfinements in the enlargement of ionic thermopower was thoroughly investigated by changing the morphologies of V_2O_5 nanosheets into nanobelts. Among different i-TE materials related to this class of nanofluidic membranes, a highest Seebeck coefficient of 26.3±0.7 mV/K was observed for the composite membrane of V_2O_5 and PSS. This work finally illustrates its practical versatility in diverse real-life scenarios, including the generation of ionic thermovoltage through direct exposure to a hot water kettle or infrared (IR) light, underscoring its role in paving the way for innovative advancements in ionic thermoelectric materials.

For the advancement of i-TE devices and its applications, the materials with both p-type and n-type characteristics are preferable. This chapter 4 was designed to develop a material that can be tuned to have both positive and negative Seebeck coefficient by changing the interchelated species from PSS to Mg-aminoclay. The ionic Seebeck coefficient can be further enhanced through the introduction of quaternary ammonium salts having disparity in the sizes of cations and anions. The successful acquisition of both p-type and n-type materials eventually facilitated the fabrication of an ionic thermopile capable of enhancing overall thermovoltages as needed. This study therefore opened up the possibility of tuning various classes of 2D materials for the development of ionic thermoelectricity across a multitude of applications.

In the previous chapters, lamellar nanofluidic membranes of both p-type and n-type behaviour have been developed. The p-type materials have the distinct property of generating mobile positive ions whereas the n-type materials are capable of developing mobile negative ions in the presence of atmospheric water molecules. The contrasting nature of these two materials can be utilized for the fabrication of a bilayer moist electric generator (BMEG) that is capable of developing a continuous output voltage. Therefore, in chapter 5 a BMEG was developed through the water assisted combination of V_2O_5 and $Ni(OH)_2$ based nanofluidic membranes. The BMEG outputs were further enhanced by creating a temperature gradient across the BMEG that specifically forces the ions to diffuse towards a specific direction (Soret effect). This phenomenon eventually helped in the tailoring of BMEG power outputs through the exposure of white light. The BMEG was finally applied for real time applications such as powering an LED, calculator and self-powered sensing devices.

Following the results of the previously reported i-TE materials a comparison table was constructed as shown in Table 1. Similarly, an another table was constructed for the comparison of different MEG studied so far as shown in table 2.

Table 1: Comparison of Seebeck coefficients of the fabricated i-TE materials with the existing literatures. We denoted thermodiffusion by TD and thermogalvanic by TG

Type	**Material**	**Seebeck coefficient (mV/K)**	**Reference**
TD(polyelectrolyte based)	PSSH	8	1
TD (polyelectrolyte based)	PSSNa	4	2
TD (polyelectrolyte based)	GO + PSSH	12.6	3
TD (polyelectrolyte based)	(PANI:PAAMPSA:PA	8.1	4

	SiO_2 nanoparticles+PANI:PAAMPSA:PA	17.37	
TD (polyelectrolyte based)	Pss-Ag	5	5
TD (polyelectrolyte based)	Nafion-Ag	-2	5
TD (polyelectrolyte based)	Nafion	4.2	5
TD (polyelectrolyte based)	S-PEEK	5.5	6
TD (polyelectrolyte based)	PDDAC	19	6
TD (polyelectrolyte based)	PVA-NaOH	-1	6
TD (polyelectrolyte based)	PVA-H_3PO_4	1.6	6
TD (polyelectrolyte based)	PEO–NaOH	11.1	7
TD (ionic liquid based)	EMIM:DCA/PVDF-HFP	25.4	8
TD (ionic liquid based)	WPU and EMIM:DCA	34.5	9
TD (ionic liquid based)	EMIM:DCA and PVDF-HFP	26.1	10
TD (ionic liquid based)	PU and EMIM:DCA	34.5	11
TD (ionic liquid based)	SiO_2 and EMIM:DCA	14.8	12
TD (ionic liquid based)	CPP-BMIM:Cl	32.7	13
TD (polymer composite)	PVDF-HFP, PC, NaTFSI	+20.2 to -10.2	14
TD (ionic hydrogel)	PAA-PEO-NaCl ionic hydrogels	3.26	15
TD (ionic hydrogel)	TOBC and LiTFSI	11.53	16
TD (zwitterionic polymer)	liquid metal (LM), waterborne polyurethane (WPU), and polyvinyl alcohol (PVA)	-12.8	17
TD (polymer)	PEDOT:PAAMPSA:PA	21.9	18
TD (ionic gel)	agarose, sodium dodecyl benzene sulfonate	41.8	19

TG	Guanidinium, urea into aqueous $[Fe(CN)_6]^{4-}/[Fe(CN)_6]^{3-}$	4.2	20
TG	$[Fe(CN)_6]^{4-}/[Fe(CN)_6]^{3-}$ with MWNT	1.4	21
TG	Guanidinium, $[Fe(CN)_6]^{4-}/[Fe(CN)_6]^{3-}$	3.73	22
TG + TD	gelatin-KCl-$FeCN^{4-/3-}$	17.2	23
TG	perchlorate electrolyte (Fe^{2+}/Fe^{3+})	1.76	24
TG + TD	KCl and $Fe(CN)_6^{4-}/Fe(CN)_6^{3-}$	17	25
TD (1-D nanochannel based)	PEO–NaOH in cellulose memmbrane	24	26
TG	I^-/I^{3-} in PNIPAM	-1.91	27
Our work (TD) (2D nanochannel)	Functionalised vermiculite	14.4	Our work
Our work (TD) (2-D nanochannel)	VO-M	14.5	Our work
	VO-PSS-18-M	26.27	
Our work (TD) (2-D nanochannel)	Ni-AC-Cl-M-29	-13.7	Our work
	Ni-PSS-M	12	

Table 2: Comparison of BMEG outputs with the existing literatures:

Active Material	Structure	Power density	Voltage output type/duration	Reference
Graphene Oxide	Gradient based	200 mW cm^{-3}	Transient	28
Graphene Oxide	Gradient based	168.3 µWcm^{-3}	Continuous/4 days	29
Graphene Oxide	Gradient based	32 mW cm^{-3}	Transient	30
Poly(4-styrenesulfonic acid)	Gradient based	0.85mW cm^{-3}	Continuous/2 days	31
Graphene Oxide	Gradient based	7 µWcm^{-3}	Continuous/5 days	32
Hydrogel and functionalised carbon	Gradient based	70 µW cm^{-3}	Continuous/7 days	33
Polypyrrole	Gradient based	69 µW cm^{-3}	Transient	34
Sodium Alginate	Gradient based	6.1 µW cm^{-3}	Continuous/10 hours	35
PAN/SDBS and PAN/DTAB nanofiber	Gradient based	11.4 µW cm^{-3}	Continuous/5 days	36
$Ti_3C_2T_x$ MXene	Gradient based	81.2 µW cm^{-3}	Transient	37
Graphene Oxide	Gradient based	1.5mW cm^{-3}	Transient	38
PSS-PVA	Gradient based	98.75µW cm^{-3}	Transient	39
Al^{3+} doped PPy	Gradient based	40 mW cm^{-3}	Transient	40
Wood	Bilayer	0.71 µW cm^{-3}	Continuous/ 1 day	41
PDDA/PSSH	Bilayer	0.9 µW cm^{-3}	Continuous/12 days	42
AAO	Bilayer	277 µW cm^{-3}	Continuous/30 days	43
PA/PC hydrogel	Bilayer	1.2 nW cm^{-3}	Transient	44
PVA/sodium alginate	Gradient based	0.55 mWcm^{-3}	Continuous/ 5 days	45
Protein	Gradient based	4 mW cm^{-3}	Continuous/62 days	46
$Ni(OH)_2$/ V_2O_5	Bilayer	270 µW cm^{-3} (without temperature gradient) and 580 µW cm^{-3} (with temperature gradient)	Continuous/80 days	Our work

6.2. Future perspective:

Despite making significant improvements, research on ionic thermoelectric materials (i-TEs) is still in its infancy, necessitating a deeper understanding and resolution of critical research gaps. Controversy arises when directly comparing i-TE parameters with those of electron/phonon transport-based thermoelectric (e-TE) materials, as the former relies on accumulated ion concentration differences and interactions among the components. Challenges such as inferior conductivity due to nonconductive components, slower ion dissociation and transfer, and susceptibility to external factors like temperature and humidity variations further complicate the landscape. Despite concerted efforts to address these challenges, risks such as dissipation and leakage persist during device assembly. Looking ahead, the future prospects for i-TE materials involve advancements in theoretical understanding, performance enhancement through innovative material discovery and device optimization, and the expansion of practical applications, ultimately affirming their potential as next-generation thermoelectric solutions. The important aspects should be addressed on the development of i-TE theories through digital modelling, logical prediction formula deduction, and the systematic strategies for performance optimization. Additionally, efforts should focus on improving i-TE performances by discovering novel materials, achieving a balance between thermoelectric and mechanical behaviours, and enhancing material stability. Furthermore, optimizing i-TE devices for capacitors, generators, sensors, and other practical applications will further solidify their position as a leading-edge TE solution.

The future of moisture-based electricity generators (MEGs) holds significant potential in sustainable energy technology. MEGs harness ambient humidity to generate electricity, offering a renewable and clean power source. Future advancements could focus on enhancing

the efficiency and scalability of these systems, allowing them to be integrated into various applications such as self-powered sensors, electronics, and grid-supporting devices. As material science progresses, new nanomaterials and surface designs may further improve water absorption and energy conversion rates. In a world increasingly concerned with reducing carbon emissions, moisture-based energy harvesting could provide a crucial, decentralized, and eco-friendly alternative, particularly in regions with high humidity. Moreover, combining MEGs with other renewable technologies could create hybrid systems, enhancing overall energy availability and resilience.

References:

1. Kim, S. L., Lin, H. T. & Yu, C. Thermally Chargeable Solid-State Supercapacitor. 1–7 (2016) doi:10.1002/aenm.201600546.
2. Wang, H. *et al.* Ionic Thermoelectric Figure of Merit for Charging of Supercapacitors. *Adv. Electron. Mater.* **3**, (2017).
3. Jeong, M. *et al.* Embedding Aligned Graphene Oxides in Polyelectrolytes to Facilitate Thermo-Diffusion of Protons for High Ionic Thermoelectric Figure-of-Merit. *Adv. Funct. Mater.* **31**, 1–7 (2021).
4. Akbar, Z. A., Jeon, J. W. & Jang, S. Y. Intrinsically self-healable, stretchable thermoelectric materials with a large ionic Seebeck effect. *Energy Environ. Sci.* **13**, 2915–2923 (2020).
5. Chang, W. B. *et al.* Harvesting Waste Heat in Unipolar Ion Conducting Polymers. *ACS Macro Lett.* **5**, 94–98 (2016).
6. Kim, S. L., Hsu, J. H. & Yu, C. Thermoelectric effects in solid-state polyelectrolytes. *Org. Electron.* **54**, 231–236 (2018).
7. Zhao, D. *et al.* Ionic thermoelectric supercapacitors. *Energy Environ. Sci.* **9**, 1450–1457 (2016).
8. Liu, Z., Cheng, H., He, H., Li, J. & Ouyang, J. Significant Enhancement in the

Thermoelectric Properties of Ionogels through Solid Network Engineering. *Adv. Funct. Mater.* **32**, 2109772 (2022).

9. Fang, Y. *et al.* Stretchable and Transparent Ionogels with High Thermoelectric Properties. *Adv. Funct. Mater.* **30**, 2004699 (2020).

10. Cheng, H., He, X., Fan, Z. & Ouyang, J. Flexible Quasi-Solid State Ionogels with Remarkable Seebeck Coefficient and High Thermoelectric Properties. *Adv. Energy Mater.* **9**, 1901085 (2019).

11. Xu, J. *et al.* Highly Stretchable PU Ionogels with Self-Healing Capability for a Flexible Thermoelectric Generator. *ACS Appl. Mater. Interfaces* **13**, 20427–20434 (2021).

12. He, X., Cheng, H., Yue, S. & Ouyang, J. Quasi-solid state nanoparticle/(ionic liquid) gels with significantly high ionic thermoelectric properties. *J. Mater. Chem. A* **8**, 10813–10821 (2020).

13. He, Y. *et al.* Ion–Electron Coupling Enables Ionic Thermoelectric Material with New Operation Mode and High Energy Density. *Nano-Micro Lett.* **15**, 101 (2023).

14. Chi, C. *et al.* Reversible bipolar thermopower of ionic thermoelectric polymer composite for cyclic energy generation. *Nat. Commun.* **14**, 306 (2023).

15. Fu, M. *et al.* Highly Stretchable, Resilient, Adhesive, and Self-Healing Ionic Hydrogels for Thermoelectric Application. *Adv. Funct. Mater.* **33**, 2306086 (2023).

16. Chen, L. *et al.* Super-stretching and high-performance ionic thermoelectric hydrogels based on carboxylated bacterial cellulose coordination for self-powered sensors. *Carbohydr. Polym.* **321**, 121310 (2023).

17. Ho, D. H. *et al.* Zwitterionic Polymer Gel-Based Fully Self-Healable Ionic Thermoelectric Generators with Pressure-Activated Electrodes. *Adv. Energy Mater.* **13**, 2301133 (2023).

18. Kim, D.-H., Akbar, Z. A., Malik, Y. T., Jeon, J.-W. & Jang, S.-Y. Self-healable polymer complex with a giant ionic thermoelectric effect. *Nat. Commun.* **14**, 3246 (2023).

19. Li, Q. *et al.* High Thermopower of Agarose-Based Ionic Thermoelectric Gel Through

Micellization Effect Decoupling the Cation/Anion Thermodiffusion. *Adv. Funct. Mater.* **33**, 2305835 (2023).

20. Duan, J. *et al.* Aqueous thermogalvanic cells with a high Seebeck coefficient for low-grade heat harvest. *Nat. Commun.* **9**, 1–8 (2018).

21. Hu, R. *et al.* Harvesting Waste Thermal Energy Using a Carbon-Nanotube-Based Thermo-Electrochemical Cell. *Nano Lett.* **10**, 838–846 (2010).

22. Yu, B. *et al.* Thermosensitive crystallization-boosted liquid thermocells for low-grade heat harvesting. *Science (80-.).* **370**, 342–346 (2020).

23. Li, Y. *et al.* 3D Hierarchical Electrodes Boosting Ultrahigh Power Output for Gelatin-KCl-FeCN4−/3− Ionic Thermoelectric Cells. *Adv. Energy Mater.* **2103666**, 1–10 (2022).

24. Kim, J. H. *et al.* Iron (II/III) perchlorate electrolytes for electrochemically harvesting low-grade thermal energy. *Sci. Rep.* **9**, 1–8 (2019).

25. Han, C. *et al.* T (5 , 6). **1098**, 1091–1098 (2020).

26. Li, T. *et al.* Cellulose ionic conductors with high differential thermal voltage for low-grade heat harvesting. *Nat. Mater.* **18**, 608–613 (2019).

27. Duan, J. *et al.* P-N conversion in thermogalvanic cells induced by thermo-sensitive nanogels for body heat harvesting. *Nano Energy* **57**, 473–479 (2019).

28. Zhao, F., Liang, Y., Cheng, H., Jiang, L. & Qu, L. Highly efficient moisture-enabled electricity generation from graphene oxide frameworks. *Energy Environ. Sci.* **9**, 912–916 (2016).

29. Cheng, H. *et al.* Spontaneous power source in ambient air of a well-directionally reduced graphene oxide bulk. *Energy Environ. Sci.* **11**, 2839–2845 (2018).

30. Huang, Y. *et al.* Interface-mediated hygroelectric generator with an output voltage approaching 1.5 volts. *Nat. Commun.* **9**, 4166 (2018).

31. Xu, T. *et al.* An efficient polymer moist-electric generator. *Energy Environ. Sci.* **12**, 972–978 (2019).

32. Huang, Y. *et al.* All-region-applicable, continuous power supply of graphene oxide composite. *Energy Environ. Sci.* **12**, 1848–1856 (2019).

33. Zhang, Y. *et al.* An Asymmetric Hygroscopic Structure for Moisture-Driven Hygro-Ionic Electricity Generation and Storage. *Adv. Mater.* **34**, 2201228 (2022).

34. Xue, J. *et al.* Vapor-Activated Power Generation on Conductive Polymer. *Adv. Funct. Mater.* **26**, 8784–8792 (2016).

35. Zhang, R. *et al.* Moist-electric films based on asymmetric distribution of sodium alginate oxygen-containing functional groups. *React. Funct. Polym.* **181**, 105421 (2022).

36. Sun, Z., Wen, X., Wang, L., Yu, J. & Qin, X. Capacitor-inspired high-performance and durable moist-electric generator. *Energy Environ. Sci.* **15**, 4584–4591 (2022).

37. Li, P., Su, N., Wang, Z. & Qiu, J. A Ti3C2Tx MXene-Based Energy-Harvesting Soft Actuator with Self-Powered Humidity Sensing and Real-Time Motion Tracking Capability. *ACS Nano* **15**, 16811–16818 (2021).

38. Zhao, F., Cheng, H., Zhang, Z., Jiang, L. & Qu, L. Direct Power Generation from a Graphene Oxide Film under Moisture. *Adv. Mater.* **27**, 4351–4357 (2015).

39. Wang, H. *et al.* Transparent, self-healing, arbitrary tailorable moist-electric film generator. *Nano Energy* **67**, 104238 (2020).

40. Chen, N. *et al.* MEG actualized by high-valent metal carrier transport. *Nano Energy* **65**, 104047 (2019).

41. Cai, T. *et al.* Bilayer Wood Membrane with Aligned Ion Nanochannels for Spontaneous Moist-Electric Generation. *Nano Lett.* **22**, 6476–6483 (2022).

42. Wang, H. *et al.* Bilayer of polyelectrolyte films for spontaneous power generation in air up to an integrated 1,000 V output. *Nat. Nanotechnol.* **16**, 811–819 (2021).

43. Zhang, Y. *et al.* Sustainable power generation for at least one month from ambient humidity using unique nanofluidic diode. *Nat. Commun.* **13**, 3484 (2022).

44. Lu, W. *et al.* Anion-cation heterostructured hydrogels for all-weather responsive electricity and water harvesting from atmospheric air. *Nano Energy* **104**, 107892 (2022).

45. Yang, S. *et al.* Green moisture-electric generator based on supramolecular hydrogel with tens of milliamp electricity toward practical applications. *Nat. Commun.* **15**, 3329

(2024).

46. Liu, X. *et al.* Power generation from ambient humidity using protein nanowires. *Nature* **578**, 550–554 (2020).